STRUCTURAL AND OPTICAL PROPERTIES OF PYROCHLORE STRUCTURED MATERIALS

Thesis

Submitted to

DELHI TECHNOLOGICAL UNIVERSITY

For the Award of the Degree of

DOCTOR OF PHILOSOPHY

By

UMANG

(2K18/PHDAP/508)

Under the Supervision of

Prof. Vinod Singh
Professor
Department of Applied Physics
Delhi Technological University,
New Delhi

Prof. Rinku Sharma
Professor
Department of Applied Physics
Delhi Technological University,
New Delhi

Department of Applied Physics

Delhi Technological University

Bawana Road, Delhi-110042

Dedicated to my parents and whole family, who have always loved me unconditionally and whose good examples have taught me to work hard for the things that I aspire to achieve.

Delhi Technological University

(Govt. of National Capital Territory of Delhi)

Shahabad Daulatpur, Bawana Road, Delhi-110042

DECLARATIONS

I ***Umang***, hereby certify that the thesis titled "***Structural and optical properties of pyrochlore structured materials***" submitted in the fulfilment of the requirement for the award of the degree of the Doctor of Philosophy is an authentic record of my research work carried out under the supervision of ***Prof. Vinod Singh*** and ***Prof. Rinku Sharma***. This work in the same form or any other form has not been submitted by me or anyone else earlier for any purpose. Any material borrowed or referred to is duly acknowledged.

Umang

(2K18/PHDAP/517)
Department of Applied Physics
Delhi Technological University
Delhi- 110042, India

Delhi Technological University

(Govt. of National Capital Territory of Delhi)

Shahabad Daulatpur, Bawana Road, Delhi-110042

CERTIFICATE

This is to certify that the thesis entitled "**Structural and optical properties of pyrochlore structured materials"** submitted by **Umang (2K18/PHDAP/508)** to Delhi Technological University (DTU) Delhi, India for the degree of Doctor of Philosophy, is a bonafide record of research work carried out by her under our supervision and guidance. This work embodied in this thesis has been carried out in the Nano Fabrication Laboratory, Department of Applied Physics Delhi Technological University (DTU), Delhi, India. The work of this thesis is original and has not been submitted in parts or fully to any other institute or university for the award of any other degree or diploma.

Prof. Vinod Singh
Professor
Department of Applied Physics
Delhi Technological University
Delhi- 110042, India

Prof. Rinku Sharma
Professor
Department of Applied Physics
Delhi Technological University
Delhi- 110042, India

Acknowledgement

First and foremost, I would like to thank my parents and my family who have been the sole reason of my mental, physical, and emotional sustenance throughput my pursuance of this degree. It is very difficult to put my thoughts into words because I owe so much to them. While writing this thesis I cannot help but remember my late grandfathers **Mr. Babu Ram** and **Mrs. Sona Devi**, who, since my childhood, instilled in me a proclivity to learn and made me aspire for an impeccable academic record. I cannot thank them enough for making me imbibe such great values. The love, pamper, support, encouragement, understanding and blessings of my parents gave me the strength to take up this work and complete it to the best of my ability. With heartful gratitude and love, I express my gratefulness to my father **Mr. Nafe Singh**, mother **Mrs. Kaushlya Devi**, sister **Mrs. Monika Jangra**, brother **Mr. Navdeep Singh**, my niece **Advika** and **Devyani,** my extended maternal and paternal family, my fiancé **Dr. Madhur Jangra** who have always been my pillars of strength and he enabled me to maintain a positive attitude in the final stage of my studies. I always thank all my beloved friends across the globe for sharing my happy and sorrow moments.

Thanks giving is a delightful job when sincerely expressed in words. Though these humble words, articulations and gratitude cannot really convey the deep feelings of my heart. While going through different stages during the last five years working in Delhi Technological University and specifically within the Nano Fabrication Laboratory (NFL), I take this opportunity to express my sincere thanks to those who helped me in this modest attempt of writing this thesis.

Prior to all, I would like to thank **Lord Shiva**, who showered constant blessings upon me and made me able to carry out the present study successfully.

I feel great honour in expressing my profound sense of gratitude, indebtedness and reverence to my supervisor **Prof. Vinod Singh**, Department of Applied Physics, Delhi Technological University, Delhi. It has been an honour to work under excellent, enthusiastic and distinguished supervisor. Their unremitting encouragement, constant help, meticulous supervision and constructive criticism throughout the course of my study for carving another milestone in my academic journey. Their immense knowledge of the subject, analytic gaze, farsightedness and perseverance were a constant source of inspiration during the course of this thesis work. I feel privileged to have worked under such a great supervision. I further show my sincere thanks to my joint supervisor **Prof. Rinku Sharma**, Dean Academic PG, Department of Applied Physics, DTU, for her valuable help and suggestions.

My heartfelt recognitions for **Prof. S.C. Sharma**, DRC member, Department of Applied Physics, DTU, my SRC & DRC committee members for their enduring support and appropriate propositions.

I would grab this opportunity to thank **Dr. Ashok Kumar**, Associate Professor, Deenbandhu Chhotu Ram University of Science and Technology (DCRUST), Murthal, Haryana and **Dr. Rajendra Singh Dhaka**, Associate Professor, Indian Institute of Technology (IIT) Delhi, for providing necessary facilities, giving valuable suggestions and discussion. All this proved as a leading light throughout pursuit of my studies and research endeavours.

I owe my sincere gratitude to **Dr. Pawan Kumar Kulriya**, Jawaharlal Nehru University (JNU), Delhi, for his timely advice and support.

It is my pleasure to express my sincere thanks to all the **faculty** members of Department of Applied Physics for their continuous encouragement and help during my research work. I am also grateful to my friends **Mr. Saroj Kumar Jha,** and other **technical and non-technical staff** for their timely support and cooperation whenever required.

Now it’s time to sincerely thank my dear former and present lab mates whose support helped in accomplished my work. It is my pleasure to thank **Mr. Kailash Chandra, Mr. Ashok Kumar, Ms. Priya, Mr. Anurag Sharma, Mr. Jasveer Singh, Ms. Shivani Sangwan, Mr. Hemendra Singh, Ms. Ankita Tondak, Mr. Praveen Kumar, Mr. Surya Pratap Singh, Mr. Ramesh Kumar Kulriya** for their support. I would also like to thank all the other scholars of Department of Applied Physics, Delhi Technological University, Delhi for their help and advice.

I wish to acknowledge the enjoyable company and suitable help rendered by my dear friends, **Mr. Anil Kumar, Mr. Srikanta Debta, Mr. Rohan Jaiswal, Mr. Chetan Awasthi,** for their help and support during this tenure. My special thanks to **Mr. Hemendra Singh, Mr. Aditya Sharma, Mr. Aman Kumar, Mr. Harender Mor, Mr. Lokesh Ahlawat, Mr. Ankush Dewan, Ms. Shilpa, Ms. Meena Parashar, Ms. Jyoti, Mr. Rajat Bajaj, Dr. Shadab Ahmed** with whom I have spent memorable time, who made my life easier and happier in Delhi Technological University.

I wish to express my sincere gratitude towards **Delhi Technological University** for extending all the necessary facilities and also for providing financial assistance in the form of Junior Research Fellowship and Senior Research Fellowship during the period of my Ph.D. course. I extend my gratitude to staff in Administration, Accounts, Store & Purchase, Library, and Computer Centre for their help and services during this tenure.

Finally, I wish to thank one and all for their timely interference into my life and making it happier and meaningful!!

Umang

PUBLICATIONS

A. Publications in international referred journals included in thesis.

1. **Umang Berwal**, Vinod Singh, and Rinku Sharma, "***Key role of Tb^{3+} doping on structural and photoluminescence properties of $Gd_2Ti_2O_7$ pyrochlore oxide***", Ceramics International, Volume 48, Issue 15, 1 August 2022, Pages 22266-22275, ***https://doi.org/10.1016/j.ceramint.2022.04.231*.**

2. **Umang Berwal**, Vinod Singh, and Rinku Sharma, "***Structural and optical studies on Dy^{3+} doped $Gd_2Ti_2O_7$ pyrochlore as white light emission***", Ceramics International, Volume 49, Issue 6, 15 March 2023, Pages 8897-8906, ***https://doi.org/10.1016/j.ceramint.2022.11.045.***

3. **Umang Berwal**, Vinod Singh, and Rinku Sharma, "***Effect of $Ce^{4+} \rightarrow Ce^{3+}$ conversion on the structural and luminescence properties of Ce^{4+} doped $Gd_2Ti_2O_7$ pyrochlore oxide***", Journal of Luminescence, Volume 257, May 2023, 119687, ***https://doi.org/10.1016/j.jlumin.2023.119687*.**

4. **Umang Berwal**, Vinod Singh, Rinku Sharma, Pawan Kumar Kulriya, and Ashok Kumar, "***Influence of Al^{3+} co-doped ions for the improvement of orange-reddish light emitting photoluminescence characteristics of $Gd_2Ti_2O_7:Eu^{3+}$ pyrochlore***", Ceramics International, Volume 49, Issue 21, Pages 34015-34024, 1 November 2023, ***https://doi.org/10.1016/j.ceramint.2023.08.098***.

B. Publication not included in this thesis:

1. Vinod Singh, Pawan K. Kulriya, Ashok Kumar, Ramesh Kumar, Priya Pradeep Kumar, **Umang Berwal**, Jasveer Singh, Kailash Chandra, and Kedar Singh, "***Hydrogen induced structural modifications in size selected Pd-Carbon core-shell NPs: Effect of carbon shell thickness, size and pressure***", International Journal of Hydrogen Energy, Volume 47, Issue 25, 22 March 2022, Pages 12642-12652, ***https://doi.org/10.1016/j.ijhydene.2022.01.245*.**

2. **Umang Berwal**, Vinod Singh, and Rinku Sharma, "***Structural Properties of TiS_2/MWCNTs Hybrid Nanostructures***", Proceedings of the International Conference on Atomic, Molecular, Optical & Nano Physics with Applications, Springer Proceedings in Physics book series (SPPHY, volume 271), ***https://doi.org/10.1007/978-981-16-7691-8_14*.**

3. *Ankita, **Umang Berwal**, Vinod Singh, **"Structural and optical properties of reduced graphene oxide***", International Conference on Nanotechnology: Opportunities and Challenges, 2022 (ICNOC-2022)/ Springer Nature Conference Proceedings, Accepted on May 6, 2023.

4. *Ankita, **Umang Berwal**, Vinod Singh, Yogendra Singh, and Satyendra Singh**, "Investigations of atomic disorder and grain growth kinetics in polycrystalline $Gd_2Ti_2O_7$",** 2nd International Conference on "Advanced Functional Materials and Devices" (AFMD-2023) / Springer Proceedings in Physics (Scopus Indexed), Accepted on June 5, 2023.*

C. Conference presentations:

1. **Umang Berwal**, Vinod Singh, and Rinku Sharma, "***Structural Properties of TiS_2/MWCNTs Hybrid Nanostructures***", Poster Number: 254, International Conference on Atomic, Molecular, Optical & Nano Physics with Applications (CAMNP 2019), New-Delhi, India. (**Best Poster Presentation Award**).

2. **Umang Berwal**, Vinod Singh, and Rinku Sharma, "***Role of Tb^{3+} doped $Gd_2Ti_2O_7$ pyrochlore oxide host for the fluorescence application***", 1st International Conference on Thin Films and Nanotechnology: Knowledge, Leadership & Commercialization ICTN-KLC 2021, 24-26 August 2021, New Delhi, India.

3. **Umang Berwal**, Vinod Singh, and Rinku Sharma, "***Role of Tb^{3+} doped $Gd_2Ti_2O_7$ pyrochlore oxide host for the fluorescence applications***", ICNOC2022: International Conference on Nanotechnology; Opportunities and Challenges, November 28-29, 2022, New Delhi, India.

4. **Umang Berwal**, Vinod Singh, and Rinku Sharma, "***Conversion Effect of $Ce^{4+} \rightarrow Ce^{3+}$ on the Structural and Optical Properties of Cerium Substituted $Gd_2Ti_2O_7$ Pyrochlore Oxide***" International Union of Materials Research Society (IUMRS-ICA 2022), December 19-23, 2022, Jodhpur, Rajasthan.

ABSTRACT

The main focus of this thesis is to examine the optical and structural properties of materials with rare earth ions doped pyrochlore structures that were created using the conventional solid-state approach. The main idea in the work is to enhance the luminescence phenomenon via doping of various rare earth ions in the host. It explores how the structural and optical properties of $Gd_2Ti_2O_7$ pyrochlore are affected by rare earth ions doping at both the A and B sites.

Numerous applications are now available because of the recent developments in solid-state lighting (SSL) technology. It is possible to create phosphor-based white LEDs with a single yellow phosphor and a blue LED chip, or with a combination of red, green, and blue phosphors stimulated by a UV LED chip. Low colour saturation, a lower colour rendering index (CRI), and an unstable colour temperature can result from the first method's red-green phosphor's reabsorption of blue light and the later method absence of a red component

In order to overcome these obstacles, single-phase phosphors doped with particular combinations of rare earth ions such as Dy^{3+}, Eu^{3+}, Ce^{3+}, Sm^{3+} etc. must be developed. This will enable the energy transfer necessary to produce white light emission. Furthermore, in order to enhance performance metrics such as correlated colour temperature (CCT), CRI, and luminous efficiency, new red phosphors are required..

Because of their adaptable physical, chemical, and luminous qualities, these phosphors are used in solar cells, biosensing, and other optoelectronic devices in addition to lighting. Phosphorus materials are often composed of a crystalline host matrix and an activator, or luminous centre. These materials are thought to be necessary for the development of white LED's and agricultural lighting systems. Due to the distinct luminous characteristics of rare earth ions,

inorganic phosphors activated by RE ions have been the preferred option for producing LEDs in recent decades. Transitions between the partially filled 4f energy levels of rare earth ions are made possible in these phosphors by the interaction between the orbitals of the rare earth ions and the oxygen atomic orbitals in the host, which produces unique luminous features.

Titanate pyrochlores are one of the many inorganic oxides that have acquired popularity for use in luminescent devices because of their good physical and chemical stability, wide range of excitation wavelengths, and abundance of bright colours. Pyrochlore oxides $Gd_2Ti_2O_7$ host are also reasonably priced, and their preparation techniques need less energy. Because of presence of rare earth ion at the A-site of pyrochlore structure $Gd_2Ti_2O_7$, the accommodation of another rare earth ion at the place of Gd is easier as the cation radii of various rare earths ions are nearly equal, these generate broadband visible light, which can enhance associated colour temperature and colour rendering. By regulating the energy transfer from Gd to rare earth ions, it is possible to get tunable visible emissions in rare earth-activated pyrochlore oxides, as recent studies have shown.

$Gd_2Ti_2O_7$ is renowned for its exceptional optical properties when doped with suitable rare earth ion, displaying quantum features along with amazing enhanced luminescence. This host may be made to emit various colours in the visible spectrum by adding the right rare earth ions, which makes it appropriate for LEDs used in agricultural lighting and general illumination applications. To accomplish the research goals, this work is divided into seven chapters that include comprehensive structural, and photoluminescence characterizations.

CONTENTS

LIST OF FIGURES

Figure No. ***Page No.***

Chapter - 1:

CHAPTER - 2:

CHAPTER - 3:

CHAPTER - 4:

CHAPTER - 6:

LIST OF TABLES

List of Abbreviations

SEM	Scanning Electron Microscope
XRD	X-Ray Diffraction
XPS	X-Ray Photoabsorption Spectroscopy
R_A/R_B	Ionic Radii Ratio
PL	Photoluminescence
RE	Rare earth
TRPL	Time Resolved Photoluminescence
GTO	$Gd_2Ti_2O_7$

Chapter 1
Introduction

The background of luminescence in pyrochlore-structured ceramics is concisely discussed in this chapter. Discussions are given regarding the fundamental ideas that underlie optical transitions in pyrochlore structures and the part of doping of rare earth play most important role for better luminescence results in terms of structural deformations. This chapter includes a summary as well as an explanation of the inspiration behind the present thesis project. Additionally, a brief overview of rare earth doped with pyrochlore structures is provided, including a variety of structural and optical properties. It also describes the goals of the research given here and investigates the significance of choosing pyrochlore structure ($Gd_2Ti_2O_7$) as host material. Furthermore, detailed literature survey concerning the rare earth doped materials and the basic principle behind the luminescence results are given. The organisation of the thesis is provided at the end of the chapter.

In today's world, energy becomes a very crucial part of our daily routine in life and its use increases day by day with the development of industrial area. Light is useful in daily lives and industrial area. Light uses a huge amount of total energy for its production. For high efficiency lighting devices energy saving and environment safety is required. Therefore, there is a need to improve optical properties for high efficiency lighting devices. So, in this thesis the title for research is "Structural and optical properties of pyrochlore structured materials".

The energy known as light is what enables us to experience visual impressions. Sunlight, which is a free and plentiful source of light, may be captured and turned into power. It is vital to create artificial light because not all emerging technologies can rely only on this natural light source. In general, incandescence and luminescence are the two basic ways that artificial light is produced.

1.1. Luminescence

When a substance is exposed to X-rays, ultraviolet or infrared radiation, electromagnetic radiation is released in the visible range, without heating the substance. This process is known as luminescence. Luminescence materials have widely studied due to their use in various applications in solid state lightings, computer and television screens, lasers, lamp phosphors, cathode ray phosphors, Plasma display panels, field emission displays, glass industry *etc.*[1–11]. A substance emitting light without being heated is said to be luminescent. It happens when electrons in atoms or molecules move from higher energy levels to lower energy states, releasing energy in infrared (IR), ultraviolet (UV), or visible region. When a substance absorbs energy from an outside source such as photons from a light source or electrons from an electrical current, subsequently releases that energy in form of light. The process of light emission is known as luminescence and the material showing this property is known as phosphors [12]. But the process of incandescence, involves heating a substance to extremely

high temperatures, which causes its atoms to vibrate and generate light. Consequently, luminescence is generally referred to as a 'cold' process in contrast to incandescence, which is sometimes referred to as a 'hot' process [13]. Incandescent bulbs emit light as a result of filament heating, which causes a large energy loss in the form of heat. Additionally, the lifespan of incandescent bulbs is only about 1000 hours, which is very less than that of compact fluorescent lights (6,000-15,000 h) and much less than the light-emitting diodes (LEDs), whose longevity can reach 50,000 hours [14]. Materials that undergo luminescence, offer improved efficiency because it is a cold process. In luminescence, the emission process can be started either internally or externally. The different luminescence mechanisms can be achieved by any kind of energy form like photoluminescence can be achieved by the UV radiation; cathodoluminescence is achieved by the energetic beam of electrons. Based on the source utilised to excite the material, the various luminescence processes can be categorised as shown below:

I. Cathodoluminescence:

Cathodoluminescence is a luminescence phenomenon that happens when an object is bombarded by high-energy electrons, emits light. It is a useful instrument for examining the microscopic characteristics of materials and is frequently employed in scientific analysis and materials characterization.

II. Electroluminescence:

When an electric current is passes through a substance, a phenomenon known as electroluminescence occurs. This light emission occurs when electrons in the material transitioning from higher energy states to lower energy ones, releases energy in the form of light particles (photons) [15]. Different light-emitting devices are built on electroluminescence, with Light Emitting Diodes (LEDs) serving as the most prevalent

and commonly utilised example. Modern electronics and lighting systems incorporate a variety of lighting and display technologies that are based on this phenomenon.

III. Photoluminescence:

Photoluminescence is a phenomenon in which a substance absorbs photon and then releases this energy again as visible light, ultraviolet light, or infrared light [16]. The light emission seen in various substances is caused by this process. There are various varieties of photoluminescence, including:

i. **Fluorescence:** In fluorescence, a substance absorbs photons of a specific energy (often UV or blue light) and immediately emits photons of lower energy (visible light). When the excitation source, such as UV light, is taken away, the emission immediately stops [17]. Examples include the components used in fluorescent lights and fluorescent dyes.

ii. **Phosphorescence:** Phosphorescence is a form of time-delayed fluorescence. The substance emits light after absorbing energy and does the same process till the excitation source is turned off. A glow-in-the-dark toy may continue to generate light after being exposed to light because of this delayed emission [18]. Before emitting energy as visible light, phosphorescent materials store energy in long-lived excited states.

iii. **Delayed fluorescence:** A less frequent type of photoluminescence is delayed fluorescence. The time between photon absorption and re-emission is briefly delayed in delayed fluorescence (microseconds to milliseconds). It has uses in organic electronics and photovoltaics and is frequently seen in various organic compounds.

iv. **Upconversion:** In a special process called upconversion photoluminescence, low-energy photons are absorbed and lead to the emission of higher-energy photons [19]. Materials for upconversion could be used in solar cells and imaging equipment.

v. **Downconversion:** Downconversion is the process by which high-energy photons are absorbed and then low energy photons are released [20]. This method is used to modify the wavelength of light generated by some luminous substances and phosphors, making them suited for use like colour conversion in LED technology.

vi. **Quantum dots:** Size-dependent photoluminescence is a property of nanoscale semiconductor quantum dots. The quantum dot emission colour can be adjusted by varying their size [21]. They are used in displays, lighting, and imaging for medical purposes.

IV. Radioluminescence:

When some materials are exposed to ionising radiation, radioluminescence occurs, which is the production of visible light or other electromagnetic radiation. The interaction of the radiation with the atoms or molecules in the substance results in this emission of light [22]. Radioluminescent materials are advantageous because of this property in a variety of scientific, medicinal, and industrial applications, particularly those involving the detection and measurement of ionising radiation.

V. Thermoluminescence:

Some materials exhibit a luminescent phenomenon called thermoluminescence that causes them to emit light when heated after being exposed to ionising radiation [23].

This method is used to analyse materials, particularly minerals and ceramics, in a variety of scientific and archaeological applications.

VI. Sonoluminescence:

A fascinating and extremely uncommon phenomena known as sonoluminescence occurs when microscopic gas bubbles in a liquid react to loud sound waves or ultrasound by ejecting brief bursts of light [24]. It continues to be a fascinating phenomenon that has stimulated research into its underlying mechanics and possible applications.

VII. Chemiluminescence:

A chemical reaction known as chemiluminescence results in the production of light without the release of heat. When chemical substances react, energy is released in the form of visible or ultraviolet (UV) light. It is seen in a wide range of natural creatures and has a wide range of real-world uses in disciplines like biology, analytical chemistry, entertainment, and safety [25].

VIII. Bioluminescence:

Living things can emit light through a chemical process occurring inside their bodies, a phenomenon known as bioluminescence. Numerous insects, fungi, marine organisms, and even a few terrestrial species exhibit this light emission [26]. These species use bioluminescence for a range of purposes, from luring in prey or mates to warding off predators and acting as camouflage.

IX. Mechnoluminescence:

A luminescent phenomenon known as mechanoluminescence occurs when certain materials are stressed or deformed mechanically and as a result generate light. This fascinating phenomenon can be seen in a variety of materials and has applications in materials science and stress research. Mechanoluminescence can take on a variety of forms, such as:

a) **Piezoluminescence:** One of the most prevalent forms of mechanoluminescence is piezoluminescence. Piezoluminescence is frequently linked to the dissolution of chemical bonds or the development of crystallographic flaws in the material as a result of stress [27]. Piezoluminescence is a phenomenon seen in quartz crystals and some organic substances.

b) **Tribo-luminescence:** It is the emission of light phenomenon produced by rubbing or friction of two surfaces. Electrons may move between the surfaces of two materials when they come into touch and are later separated, resulting in the release of photons. Common examples of materials that exhibit this form of mechanoluminescence are certain crystals, rocks, and adhesives.

c) **Fracto-luminescence:** When materials crack or fracture, this phenomenon is known as fracto-luminescence, and it results in the emission of light. A substance may fracture or develop microscopic fissures under stress. Light emissions are produced as a result of the creation and growth of these fissures [28]. In the investigation of material fracture and failure, this phenomenon is crucial.

Detailed type of Luminescence, excitation source and applications are shown in Table 1.

Table1: Types of Luminescence and applications.

Sr. No.	**Type of Luminescence**	**Excitation Source**	**Applications**
1.	Photoluminescence	Photons	Plasma display, Fluorescent Lamp
2.	Cathodoluminescence	High-energetic beam of electrons	Colour Monitors, T.V.
3.	X-ray Luminescence	X-ray	X-Ray Amplifier
4.	Thermoluminescence	Heat	Radiation dosimeter and dating
5.	Electroluminescence	Electric Field	LEDs, Electroluminescent displays
6.	Sonoluminescence	Ultrasound	Destruction of toxic chemicals
7.	Radio photoluminescence	α, β, γ	Detection of Radioactive Materials

1.2. Some essential terms:

(i) Absorption:

Absorption is the procedure by which a substance absorbs energy from an outside source, changing the internal energy of the system or state. Depending on the type of energy being absorbed and the characteristics of the absorbing medium, this energy absorption can have a variety of impacts. It is a basic concept having numerous applications in engineering, physics, chemistry, and biology.

(ii) Excitation:

An atom, molecule, or other physical system gets excited when energy is transferred to it, causing it to go from a lower energy state to a higher energy one [29]. Excitation is an important process in physics and chemistry. Depending on the characteristics of the system and the sort of energy involved, this process frequently results in a variety of observable outcomes.

(iii) Emission:

The emission process in a physical system involves the transfer of energy from an excited state to a lower energy state [29]. This procedure is crucial to many natural and artificial phenomena and has a wide range of real-world applications in multiple domains of science and technology. Types of Emission: Depending on the system's characteristics and the type of energy used, there are various types of emission processes. Typical forms of emission include:

a) **Spontaneous emission:** This takes place without outside interference. For instance, a photon is spontaneously released when an excited electron in an atom returns to its ground state. Natural occurrences like the starlight emission are caused by this process.

b) **Stimulated emission:** When an external photon interacts with an excited system, it triggers the release of a photon that is similar in wavelength, phase, and direction to the entering photon. This is known as stimulated emission. The operation of lasers is based on the idea of stimulated emission light.

(iv) Activators:

Activators are chemicals or impurities that are purposefully given to a host material in order to improve its luminescence or phosphorescence [30]. In order to control the emission of light from the host material, activators are essential. They are frequently employed in the creation of phosphors for a variety of luminous devices, displays, and lighting applications.

(v) Sensitizers:

Sensitizers are compounds that improve or raise a luminous or fluorescent material's sensitivity to external excitation sources, such as light or radiation [29]. They are used in the contexts of luminescence and fluorescence. Sensitizers increase the luminous material emission intensity by absorbing energy from the excitation source and then transferring it to material. Sensitizers are frequently employed in many different applications, such as luminous sensors and fluorescence microscopy.

(vi) Energy levels:

In the context of physics and quantum mechanics, energy levels refer to discrete, quantized energy values that a physical system may have. Quantized energy values known as energy levels define the permitted states of a quantum system. They are essential for comprehending how particles, especially electrons, behave in atoms, molecules, and solids, and are fundamental to quantum mechanics as well as many other fields of physics and chemistry.

(vii) Trap centers:

In terms of physics and materials science, trap centres are small areas or flaws that exist in a material and can have the ability to temporarily store charge carriers like electrons or holes (positive charge carriers). These trap centres are crucial for understanding a variety of electrical and optoelectronic devices of semiconductors, insulators, electrical and optoelectronic devices.

(viii) Fluxes:

The term "fluxes" usually refers to the flow or rate of photons (light) released by a luminous substance. This photon flux can be monitored in a variety of methods and is a crucial factor in describing luminous materials and their functionality. Since flux directly affects the functionality and efficiency of these devices, accurate flux assessment is crucial in many applications employing luminescent materials, from lights and displays to sensors and detectors [29].

(ix) Host:

A “host” matrix is the crystalline or amorphous structure that accommodates and envelops luminous species or activators in the context of luminescence, particularly in the field of materials science and solid-state physics. The behaviour and luminous properties of the substance are significantly influenced by the host matrix.

(x) Killers:

Killers or quenchers are substances or processes that decrease a material's capacity for luminescence [30]. In order to build sensors, improve materials, and explore molecular interactions, analytical chemistry, materials science, and biological research are just a few of the fields where an understanding of quenching mechanisms is crucial.

(xi) Energy transfer:

The process by which energy is transmitted between various entities within a luminous system is referred to as energy transfer. Energy transfer has the potential to affect the luminescent characteristics of the material, including light emission. Numerous energy transmission processes exist in luminescence, and they are essential in a variety of applications.

(xii) Relaxation:

The process by which an excited or perturbed system returns to its optimum or lower-energy state is known as relaxation [31]. Depending on the system and the kind of excitation, it entails the release or dissipation of extra energy collected during excitation and can take many different forms.

Jablonski diagram: The Jablonski diagram offers a graphic illustration of the energy transitions and changes that take place when light interacts with molecules. It aids scientists and researchers in chemistry and physics for understanding and making predictions about the behaviour of luminescent materials as well as the variables that affect their ability to emit and absorb light.

Most of the phosphors are composed of transparent crystalline host material and very small amount of impurity is induced into host lattice called activator [32]. When the excitation energy is absorbed then luminescent material emits radiation. The host matrix is excited only by the

high excitation energy. Only in the UV or Visible scale, direct excitation of the added impurity (activator) is possible [33]. The activator absorbs the excited radiation and goes to the excited state or some part of the excited radiation may be absorbed by the host material shown in Figure 1.1. Now the excited state came back to the original state by emitted radiation. The excited state energy can be used to excite the vibrations (phonons) of the host material. Due to these host lattice vibrations heat is produced which induces nonradiative transitions [34–36]. Some energy is absorbed by the host lattice which excites atoms to the excited state in the host material lattice and when it came back to ground state it gives emission [37]. In order to have efficient luminescence, nonradiative transitions should be suppressed.

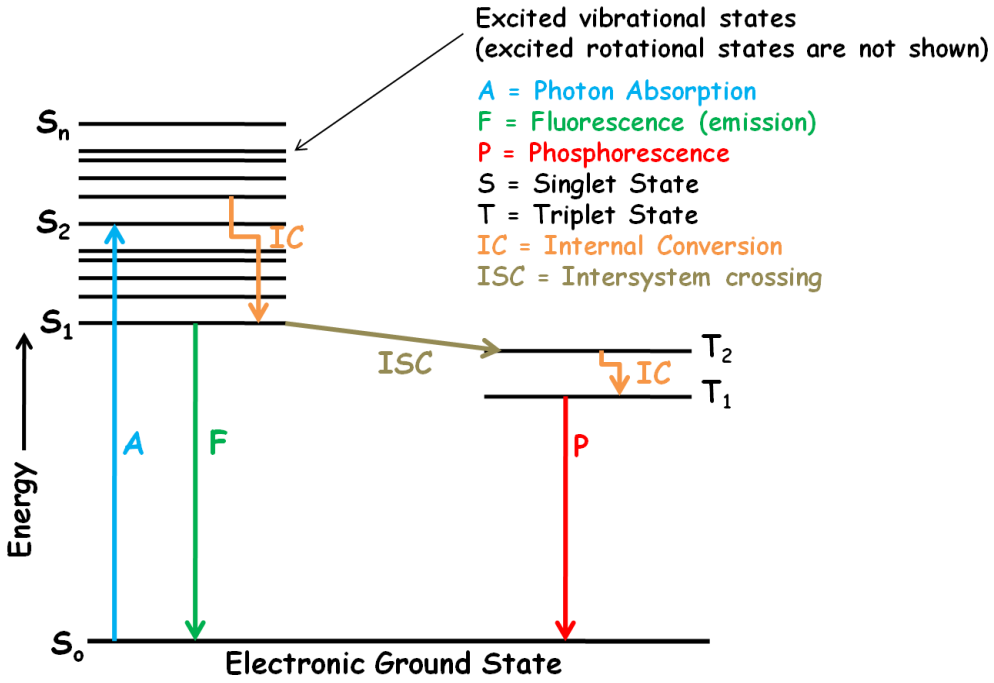

Figure 1.1: *Jablonski Diagram representation of energy states of a molecule and transitions.*

1.3. Phosphor and luminescence mechanism

The process of converting incident radiation energy into visible or infrared light is known as luminescence, and it is exhibited by luminescent materials (phosphors). Phosphor itself refers to a “light bearer” material. Phosphors typically consist of a host lattice, activators, and solid crystalline inorganic materials that have been lightly doped with impurities. The presence of

these activators, which can be lanthanide ions or transition metal ions, serves as the centre for luminescence, whereby luminous activities take place. Either within these activators or within the host lattice most of the radiation absorption takes place. Host excitation, phenomena wherein host lattices are capable of absorbing excitation energy from diverse sources. After exciting the host lattice, it releases energy in a variety of ways:

(i). The host lattice itself has the ability to release energy, producing a visual emission. This mechanism, which is seen in Figure 1.2 (a), is known as characteristic, pure, or host-sensitized luminescence. Vanadate and tungstate are two examples of host luminophores, which are phosphors that have this behaviour [38].

(ii). The host lattice have the ability to produce heat non-radiatively releasing the absorbed energy, as shown in Figure 1.2 (b).

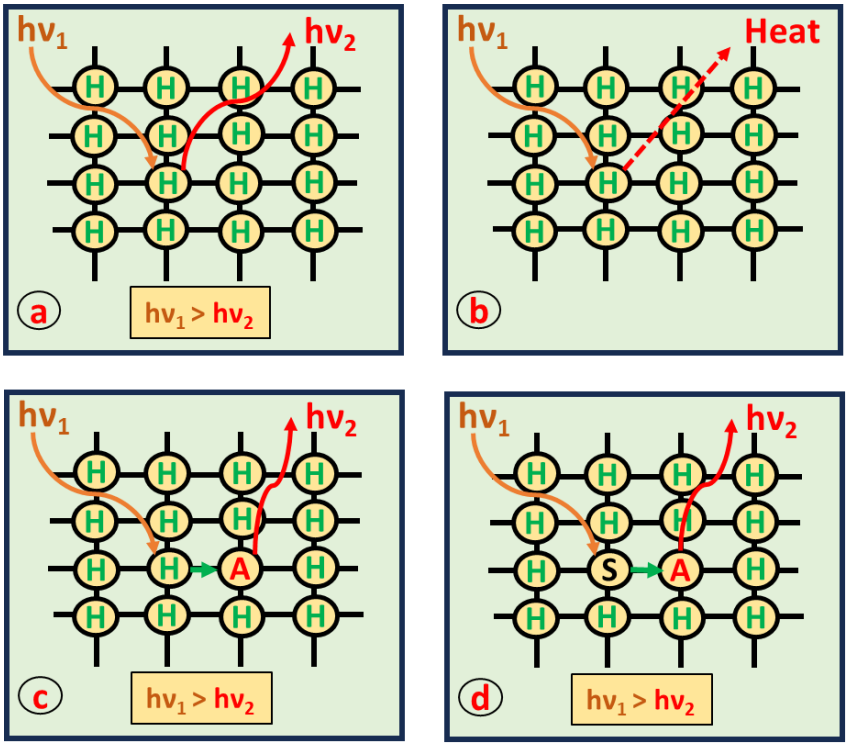

Figure 1.2: *Illustration of various processes, including (a) host-sensitized luminescence, (b) non-radiative relaxation, (c) host + activator luminescence, and (d) host + sensitizer + activator luminescence, involved in the absorption, transfer, and emission of energy in luminescent materials.*

(iii). The activator ion can receive energy from the host lattice. In this case, the activator is sensitised by the host lattice or sensitizer by means of energy transfer. The activator releases its energy after being excited to a higher energy level, going back to its ground state, and producing visible light. It is referred to as a quencher if the activator emits energy non-radiatively because it inhibits luminescence. Non-typical or impure luminescence are the terms used to describe this type of luminescence. Further division of impure luminescence into two groups: (a) host + activator, as shown in Figure 1.2 (c), in which the host absorbs the incident energy and activates the activator. (b) Host + Sensitizer + Activator, as shown in Figure 1.2 (d) [39], where the sensitizer absorbs the incident energy and passes it to the activator, which then emits the energy.

The direct excitation process [30] is when the excitation energy is directly absorbed by the activator ion and followed by either radiative or non-radiative emission. Stokes emission, which is characterised by a wavelength shift towards the red end of the spectrum, denotes lower energy, occurs when a high-energy photon is absorbed, causing the emission of a lower-energy photon. On the other hand, anti-Stokes emission occurs when two or more low-energy photons are absorbed, resulting in the emission of a high-energy photon. The wavelength shift towards the blue end of the spectrum, which denotes increased energy, is connected to anti-Stokes emission. Figure 1.3 (a) and (b) show these processes in graphic form, respectively [40].

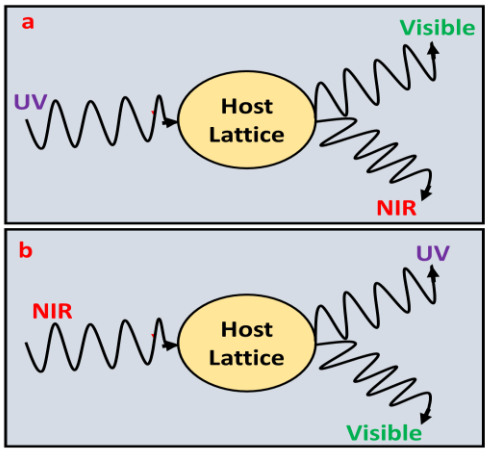

Figure 1.3*: (a) Down-conversion and (b) Up-conversion processes.*

1.4. Free ion spectra and selection rules:

The explanation of absorption and illumination are quite vital due to the reason that the vibration in the crystal field even when low temperatures are used to suppress it. Interaction between the absorption centres affects the spectrum. Therefore, it's necessary to analyse the properties of free ions of the crystal field. Coulomb interaction between the electrons and electron spin orbital interaction will affect the energy states of a free ion in crystal field.

LS scheme (Russell-Saunders) is applied for lighter molecules. In this scheme the energy levels are according to the total spin angular momentum (S) and total orbital angular momentum (L) in addition to the total angular momentum (J) where value of J= L+S [41]. According to the below convention the total angular momentum is denoted by:

L	**0**	**1**	**2**	**3**	**4**	**5**	**6**	**7**	**8**	**9**	**10**
Orbital	**S**	**P**	**D**	**F**	**G**	**H**	**I**	**J**	**K**	**L**	**M**

The spin multiplicity is given by the expression 2S+1 and it is written as prefix of the term symbol and the total angular momentum value J is written as suffix e.g. $^{5}D_{4}$ state having L=2, S=2 and J=4.

JJ-coupling scheme is used for the heavier elements due to the fact that in heavier elements Spin interaction dominates. The ground level of the ion is easily determined on the basis of Hund's rule if the electronic configuration of ion is known. On the basis of Hund's rule all the term values are allowed by the Pauli's principle that the lowest term having maximum multiplicity or the terms having maximum multiplicity with maximum value of L has lowest energy. For the electronic configuration having electrons in less than half-filled subshell has lowest spin orbit splitting with smallest J value and for the configuration having electrons in more than half-filled subshell the multiplets were inverted [42].

In the absorption and emission spectra electric dipole transition (ED) occurs with selection order $\Delta J=\pm1$ (not $0\leftrightarrow0$) and for LS coupling the selection rules are $\Delta S=0$, $\Delta L=0, \pm1$ (not $0\leftrightarrow0$). According to Laporte's rule the parity of the ionic state for an allowed transition must be changed. The half-life time for free ion of an excited state is approximately 10^{-8} sec if it allows transition to the energy state having low energy for emission in the visible or near visible region. If the half life time is 10^{-7} to 10^{-2}sec the transition is forbidden according to the concept of selection law for free electrons. Magnetic dipole (MD) and weak electric quadrupole (EQ) transitions will occur within the states having same parity. Selection law for the MD transitions are $\Delta J\leq1$, (not $0\leftrightarrow0$); $\Delta L\leq1$(not $0\leftrightarrow0$) and for the weak electric quadrupole transitions the selection rules are $\Delta J\leq2$ (not $0\leftrightarrow0,1$); $\Delta L\leq2$ (not $0\leftrightarrow0,1$). These rules are valid only for LS coupling.

1.5. Excitation and emission processes

The absorption spectrum may have broad or narrow absorption bands. The shape of the absorption band can be finding out by using configurational coordinate diagram and this diagram tells whether the luminescence is present or absent [43]. In the crystal matrix the potential energy is drawn as a function of coordinate r. The parameter r tells about the vibrational modes in which central metal ion is at rest and the surrounded atoms are oscillating with respect to one another. The vibrations are in symmetric stretching mode when central metal atom is at rest and the surrounded metal atoms are moving away and coming back from the metal atom at rest. Symmetric stretching mode is shown in the Figure 1.4.

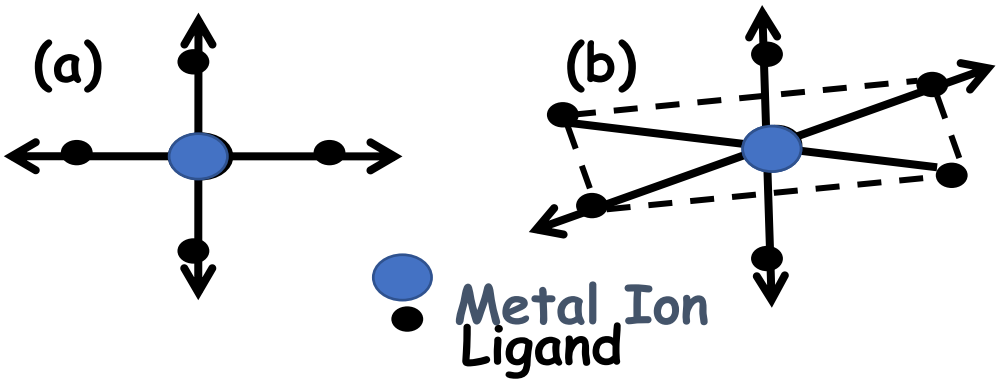

Figure 1.4: *Symmetrical & Asymmetrical Stretching.*

The coordinate r represents the metal atom at center and surrounded ligand distance. The configurational coordinate diagram considers only symmetrical stretching mode shown in figure 3. Due to the harmonic nature of the vibrational motion the ground and the excited states are parabolic. Vibrational states are represented by the horizontal lines. The r_0 represents the equilibrium distance of the lowest energy state (i.e. ground state) for lowest vibrational level. The equilibrium distance of the excited level r_e is distinct from the r_0 of the ground level due to distinct chemical bonding between the ground and excited level. Electron transition occurs at 0K to the excited state by absorbing the radiation and this process is shown by A→B in the Figure 1.5. The excited state losses energy to the lattice vibration with probability 10^{12} to 10^{13} sec^{-1} and for emission probability is 10^9 sec^{-1}. This is why electrons in the excited state goes from B→C (lower vibrational level) by dissipating heat until it reaches the equilibrium state before emission. The electron makes transition from the lowest vibrational level of the excited state to the ground energy state and thus emitting radiation shown by C→D. And D→A shows the relaxation process. The width of the absorption band is calculated from the difference Δr in between the two parabola of the excited and ground states. For large value of Δr the absorption band is broader. The coupling between the electrons and the vibrations of the center are calculated from the Δr difference. The vibrational level of the ground state may be at higher than zero at higher temperatures and this leads to the band broadening. The emission is always

at lower energy than the absorption due to the heat dissipation to the crystal lattice. The displacement of the emission from that of absorption is known as stokes shift. In the absorption spectrum the center is going to excited state but in the case of configurational coordinate diagram vertical transitions takes place because electrons moves faster than the nuclei. The nuclei take their appropriate positions later and this process is known as Frank-Condon principle [44].

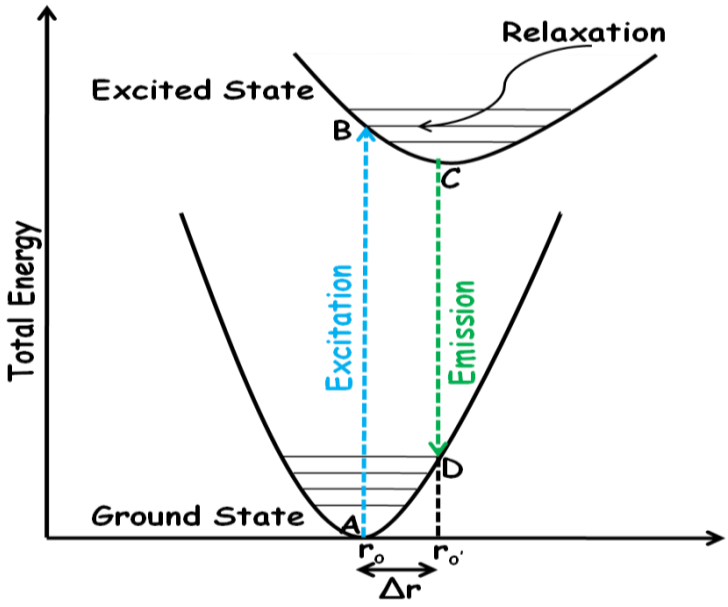

Figure 1.5: *Configurational Co-ordinate Diagram.*

1.6. Effect of crystal lattice:

Luminous characteristics of a material can be significantly influenced by its crystal structure. The crystal lattice has the following significant effects on luminescence:

a) **Emission Wavelength:** The energy levels of the electrons within a substance can be influenced by the crystal lattice. The quantization of the energy levels in a crystalline structure has an impact on the emission wavelength. The energy level configurations produced by various crystal lattices can change the wavelength of the light emitted [29].

b) **Emission Efficiency:** The crystal lattice can have an impact on luminescence efficiency, which is frequently assessed by the quantum yield. The total luminescence efficiency can be decreased by imperfections or defects in the lattice, which might open up non-radiative recombination routes for excited electrons [30].

c) **Emission Lifetime:** The lifetime of excited states can be impacted by the crystal structure. Short emission lifetimes can result from the host lattice ability to quickly quench excited states in some materials. Others may have longer emission lifetimes because the lattice shields the excited states from non-radiative processes [45].

d) **Stokes Shift:** The Stokes shift, or the energy difference between the absorption and emission wavelengths, can be influenced by the crystal lattice. A higher Stokes shift may result from a well-organized lattice, which shows effective energy transfer from absorbed to released photons [45].

e) **Host Material:** For luminous activators or dopants, the crystal lattice itself might act as the host material. The luminous characteristics, such as emission wavelength, efficiency, and longevity, can be considerably influenced by the host material selection [46].

f) **Crystalline Defects:** Impurities or vacancies in the crystal lattice can bring energy levels into the band structure, have an impact on luminescence. Depending on their type and density, these dopants may function as luminous centres or quenchers [29].

In conclusion, for different host lattice the optical properties of luminescent ion is also different due to the surrounding change of the luminescent ion. Optical properties for different host are different due to covalency and crystal field.

1.7. Luminescence of rare earth ions:

Rare earth elements are 17 in total number be composed of 15 lanthanides (La to Lu having atomic no. 71 and 79 respectively), and two more elements Sc and Y (atomic number 21 and

39). From Ce^{3+} to Lu^{3+} have 4f electrons. Sc^{3+}, Y^{3+}, La^{3+} and Lu^{3+} have no 4f electrons so they don't have electronic energy levels, therefore not showing luminescence process. The rare earths which have partially filled 4f electrons shows variety of well luminescent process in visible region, example Ce^{3+}, Eu^{3+} etc. Therefore, many of the rare earth elements could be used as luminescent centers in the phosphors. Rare earth ions can act as excellent for both host as well as dopants since they show different emission colours based on the 5d→4f and 4f→4f transitions [47].

Unique properties of rare earths:

Rare earth ions have special qualities that distinguish them apart from other optically active ions based on the distinctive interactions mentioned earlier. These distinctive characteristics include:

- The electromagnetic spectrum visible and near-infrared areas are both included in the range of spectral ranges where rare earth ions exhibit luminescence. They also have narrow spectral lines and long emission lifetimes [48].
- When stimulated by ligands, rare earth ions exhibit a substantial Stokes shift, which causes a sizable discrepancy between their excitation and emission wavelengths [49].
- The intra-configurational 4f-4f transitions within rare earth ions, which have low homogenous linewidths [50].
- They provide a range of energy levels that are excellent for optical pumping [51].
- For methodically examining their energy levels, transition intensities, and the dynamics of their excited states, there are widely recognised theoretical models available.

Both divalent and trivalent rare earth ions are incredibly useful in a variety of applications, especially in those involving biosensing, biomedical treatments, display technology, solar cells,

fingerprint recognition, indoor plant growth, and solid-state illumination, due to their intriguing qualities.

1.8. Optical transitions of rare earth elements:

Optical transitions are dependent on the rare earth element electronic configuration and on some more factors described below:

(i) f-f transition:

Rare earth ion doped materials display a variety of narrow spectral lines that are attributed to electronic transitions between $^{2S+1}L_J$ states and free ion levels or J-manifolds in the 4f subshell. These transitions are spin-prohibited and occurs in 4f orbitals of the same lanthanide ion. The host material in which activator ions are doped has no impact on the excitation or emission energies during f-f transitions. This is because the 5s and 5p electron shells are well shielded. As a result, these spectra have small line widths. A variety of transitions are produced when rare earth ions in the host material interact with incident light, including:

a) **Magnetic dipole transitions:** These transitions are produced when the magnetic field component of the incident light interacts with rare earth ions via a magnetic dipole mechanism. When charges are rotationally moved and the direction of rotation is maintained under inversion through a central point, magnetic dipole transitions take place. Transitions between states with the same parity are possible because of magnetic dipole transitions, which have equal parity and display even transformation under inversion [52]. Magnetic dipole transitions follow Laporte's selection rule:

$$|\Delta l| = \pm 1,\ |\Delta s| = 0,\ |\Delta L| \leq 0,\ |\Delta J| = 0;\ J = 0 \leftrightarrow 0 \text{ is forbidden}$$

b) **Forced electric dipole transitions:** These transitions happen when an electric dipole mechanism allows a rare earth ion to interact with the electric field component of incident

electromagnetic radiation. Forced electric dipole transitions have odd parity and odd transformation features under inversion. Since the beginning and end states of the $4f^n$ transition have the same parity, these transitions are often not allowed in rare earth ion doped materials. As a result, Laporte's selection rule ($|\Delta l| = \pm 1$, $|\Delta s| = 0$, $|\Delta L| \leq 6$, $|\Delta J| \leq 6$) limits electric dipole transitions. However, these transitions can be brought by non-centrosymmetric interactions between electronic states. Hypersensitive transitions are caused these transitions that are sensitive to the immediate surroundings of rare earth ions. These transitions, which are sometimes referred to as pseudo-quadrupole transitions, adhere to a set of selection conditions ($|\Delta S| = 0$, $|\Delta L| \leq 6$, $|\Delta J| \leq 6$). An uneven distribution of dipoles brought on by electromagnetic radiation in the presence of rare earth ions leads to hypersensitive transitions. The local field symmetry and the inhomogeneity of the dielectric medium surrounding rare earth ions both have an impact on the intensity of these transitions [53,54].

c) **Electric quadrupole transitions:** When quadrupole charges are shifted, electric quadrupole transitions take place. Four-point charges or two dipoles organised so that their net dipole moment is zero, making an electric quadrupole. In electric quadrupoles, parity is even. Electric quadrupole transitions are comparatively weaker than magnetic dipole and induced electric dipole transitions [55].

(ii) f-d transition:

In terms of parity, the transition of 4f electrons into the 5d subshell is allowed. The ligand field effect, however, has a significant impact on this transition, making it very sensitive to the environment around rare earth ions and contributing to its high intensity [56]. In contrast to the extremely narrow peaks seen in transitions between 4f-4f energy levels, these transitions,

which take place between $4f^n5d^0 \rightarrow 4f^{n-1}5d^1$ energy levels, produce a broad range of excitation and emission wavelengths. The Franck-Condon principle and the breakdown of the degeneracy of the 4f ground state are two phenomena that can be used to explain the wide spectrum of f-d transitions [56]. Spin-orbit coupling also causes the degeneracy of the 4f levels to be broken, leading to numerous levels. These transitions are stronger and broader than the f-f transitions and these transitions are also spin allowed and are observed in (Ce^{3+}, Pr^{3+}, Tb^{3+}, Yb^{2+}) rare earth ions [57,58]. The lowest band absorption of the divalent lanthanide is due to 4f→5d transition.

(iii) ***Charge transfer transition***:

In this type of transition one molecule transfers a fraction of charge to another molecule. These transitions have high energy and observed only for certain lanthanides. The charge transfer transition will shift towards the lower energies with increasing the oxidation state. Charge transfer band is known as ligand to middle metal charge transfer (LMCT). The position of charge transfer band is at lower energy for a lanthanide ion, if the background ligands are slighter electronegative. Further, there is a propensity to have the charge transfer band at lower energy side, when the background ligands are more in number [58,59].

1.9. Suitable dopant and host material:

Activators are mostly a dopant present in the crystalline host lattice in low concentration. The moderate concentration of dopants behaves as luminescent centers and the host material lattice serves a matrix to accommodate these luminescent centers at optimum positions. The rare earth elements are the best luminescent centers due to their ion-to-ion distance and spatial positioning. Most of the host lattice doped with rare earth showing emission of visible light under the excitation of near infra red radiation. Still for the better luminescent results a suitable position in the host lattice for the activators ions and dopant concentration occupy position

appropriately is needed. The lanthanide elements are mainly used as luminescent centers and these elements belongs to the VI period and III group having atomic no. in between 57 to 71 of the periodic table. The lanthanide elements having incompletely filled 4f shell and surrounded by the outer $5s^2$ and $5p^6$ orbitals and the energy levels were slightly shifted due to the surrounding environment and remains nearly invariable in the doped samples, regardless of the host material. The electronic configuration of rare earth elements is [Xe] $5d^0\ 6s^2\ 4f^n$ (n=0 to 14). The doping of the rare earth in the host matrix is most suitable in triply ionised state. Energy levels for any element have three terms, total spin angular momentum 'S', total orbital angular momentum 'L', and total angular momentum 'J'. Energy level splitting depends on the different kind of interactions such as coulombic, spin-orbit and crystal field interaction inside the host lattice and these are shown in Figure 1.6 and discussed below;

(i). Coulombic interaction:

This kind of interaction occurs due to the repulsion of electrons in the 4f orbitals of rare earth and it splits the energy level into ^{2S+1}L state with (2L+1) (2S+1) fold degeneracy. The term ^{2S+1}L splits in the order of $10^4 cm^{-1}$and this interaction is most eminent out of all the other interactions [60].

(ii). Spin-orbit interaction:

According to Russel-Saunders scheme, due to the strong coulombic interaction between total orbital angular momentum 'L' and total spin angular momentum 'S', forms total angular momentum 'J'. Due to the spin-orbit interaction the energy level splits into 2J+1 levels and denoted by $^{2S+1}L_J$ levels. The order of this kind of interaction is nearly $10^3 cm^{-1}$ [53].

(iii). Crystal field interaction:

The energy levels are further break up due to the interaction between ions and crystal field surrounding and causes stark splitting of $^{2S+1}L_J$ levels [61]. According to this degeneracy (2J+1)

is modified as (J+1/2) having odd number of ions, but degeneracy remains same (2J+1) for even number of ions and therefore it is finally represented by the term $^{2S+1}L_{J,\mu}$. In the crystal field interaction energy levels are separated by nearly 100 cm^{-1} [62].

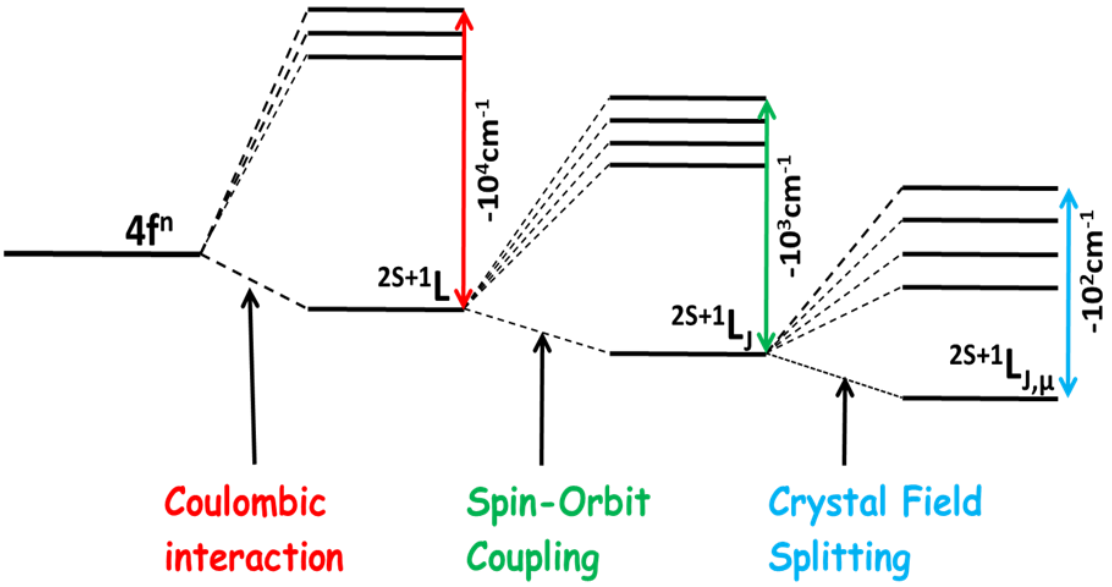

Figure 1.6: *Schematic diagram of interaction within the host inducing splitting*.

1.10. Pyrochlore oxides:

Rare earth pyrochlore oxides can have much importance in today's world due to their use in various fields, such as host for luminescence centers [63], catalysts [64], nuclear waste forms [65], high temperature pigments [66], ionic conductor [67], transparent ceramics [68], and water splitting [68]*etc*. Among ternary oxides, compound with popular formula $A_2B_2O_7$ belongs to a family of pyrochlore structure. Rare earth pyrochlore oxides are cubic and ionic in nature thus they add their selves to a variation of chemical substitution at A and B cationic position. Pyrochlore oxides have various physical properties since cation B is a transition metal atom with varying oxidation state and cation A is a rare earth element with inert lone pair of electrons. Lanthanum stannates ($La_2Sn_2O_7$) have studied due to extreme thermal and chemical stability and they are used as host matrix for phosphors and solid-state lasers as they can

accommodate rare earth ions in the octahedral site easily [69]. Rare earth pyrochlore oxide with formula $A_2B_2O_7$ will be used as host material for many luminescent based materials. Rare earth trivalent ions have novel optical properties of doped pyrochlore oxide samples. Among pyrochlore oxide rare earth titanates are used as phosphor materials due to strong luminescent, optical, magnetic, and electrical properties. The structural and optical properties are strongly related to each other in rare earth pyrochlore oxides [52].

1.11. Structure of pyrochlore oxide ($A_2B_2O_7$):

The general formula of pyrochlore oxide is $A_2B_2O_7$ having defect fluorite structure which is a part of the Fd3m space group. In pyrochlore oxide structure, A is the trivalent rare earth element (where A can be Gd^{3+}, Ln^{3+}, Nd^{3+} *etc*.) and cation B belongs to 3d, 4d or 5d element with suitable oxidation state (where B can be Ti^{4+}, Zr^{4+}, Hf^{4+} *etc*.). Rare earth pyrochlore oxide structure is a framework of fluorite structure (TiO_2). In fluorite structure cations (Ti) occupy the fcc lattice and oxygen ions are arranged in 8 tetrahedral positions but in the pyrochlore oxide structure A and B-cations are occupying the position 16d (½, ½, ½) and 16c (0,0,0) respectively and 1/8 anion sites are unoccupied. Because of the distinct arrangement of cations in pyrochlore oxide structure there are 3 kind of tetrahedral interstitial sites for oxygen atoms, 48f (x, 1/8, 1/8) position which coordinate 2 A^{3+} and 2 B^{4+} cations, 8a site which coordinates 4 B^{4+} cations, and 8b(3/8, 3/8, 3/8) site to coordinate 4 A^{3+} cations. In pyrochlore oxide structure there are 3 anion positions, 8a site of oxygen are empty due to which dislocation of 48f oxygen atoms from the middle of tetrahedral position are possible. Therefore, pyrochlore oxide composition is fully explained on the basis of positional parameter 'x' of 48f oxygen and value of this parameter ranges in between 0.3126 to 0.3751and two times the lattice parameter 'a' value [48,70]. There are simple rules to vary the positional parameter value 'x' which depends on the origin choice. X-ray and neutron structure analysis are used to find the value of

'x'. The strength of pyrochlore oxide structure is decided by the radii ratio of cation A (r_A) and cation B (r_B) (i.e. r_A/ r_B) ratio. The ionic radii ratio for $Gd_2Zr_2O_7$ is 1.46 and for $Gd_2Ti_2O_7$ its value is 1.75. The ionic radii ratio value ranges from 1.46 to 1.78 for stable pyrochlore oxide structure [48,70,71]. If the value of ionic radii ratio is less than 1.46 then the structure is changed into defect fluorite structure due to the easy swapping of 2 cations [72]. Pyrochlore basic crystal structure are shown in Figure 1.7.

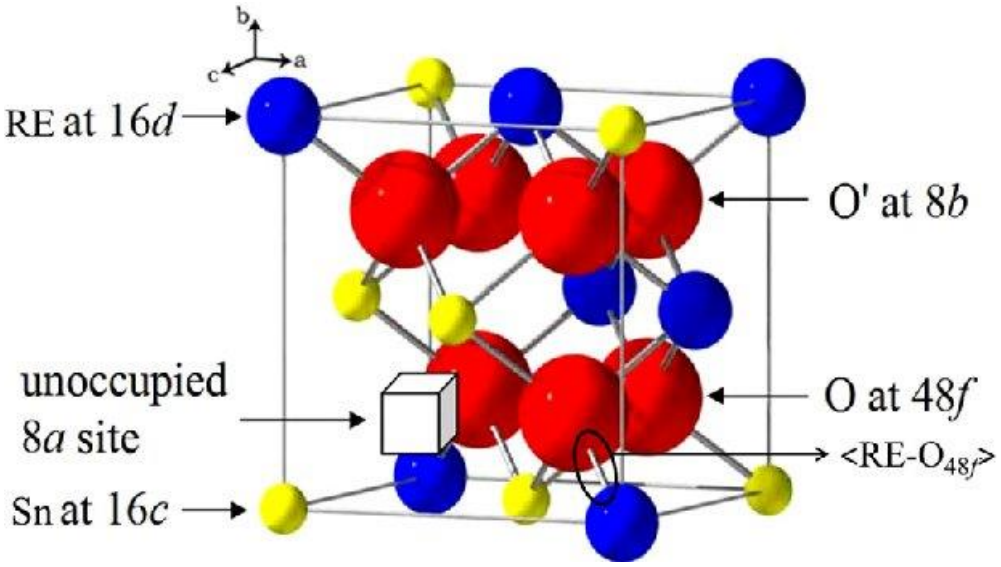

Figure 1.7: *Crystal Structure of 1/8th of a unit cell of pyrochlore oxide* [73].

1.12. Literature review:

The relevant literature survey related to luminescence properties, preparation method, various phosphors, rare earth ions as dopants, and applications are presented in Table 2.

Table 2: Literature survey related to optical and structural properties.

Host	**Preparation Method**	**Heat Treatment**	**Dopant**	**Purpose**	**Major Observation**	**Ref.**
$Gd_2Ti_2O_7$	Sol-Gel method	800-1100^{o}C	Eu^{3+} Dy^{3+}	Structural & Luminescent	Red and yellow emission line in visible range is observed	[74]

				properties study.	for $Gd_2Ti_2O_7$:Eu^{3+} or Dy^{3+}. An increase in the lifetime of PL transition is achieved in nanocomposite of silica at the same dopant concentration related to the $Gd_2Ti_2O_7$ doped Eu^{3+} rare earth.	
$Gd_2Ti_2O_7$	High energy ball milling and chloride salt flux method.	800-1000ºC	Un-doped	Band-gap, PL and NIR Reflection Properties study.	The band gap is increased from 2.77eV to 3.27eV through the addition of LiCl:CsCl flux for the nanocrystalline powder $Gd_2Ti_2O_7$. The phase purity and crystallinity of $Gd_2Ti_2O_7$ nanocrystalline powder prepared by LiCl:CsCl is high.	[75]
$Gd_2Zr_2O_7$	Chemical Co-precipitation method	800-1200ºC	Eu^{3+}	Structural and photolumine scence properties study	In $Gd_2Zr_2O_7$ host Eu^{3+} replacing Gd^{3+} show a strong PL intensity due to the f to f transition. There are no spectral changes with increasing the Eu^{3+} ion concentration. When $Gd_2Zr_2O_7$ is doped with Eu^{3+}, enhancement in the intensity of excitation peak increased	[76]

					therefore this material can be used as red light emitter.	
$Nd_2Sn_2O_7$	Solid state reaction technique	1350°C	Gd^{3+} Tb^{3+}	Structural, optical and electrical properties study	Change in the cubic structure and lattice parameter of $Nd_2Sn_2O_7$ is observed when doped with Gd and Tb. Therefore crystallite size and defect density decreases in $Nd_2Sn_2O_7$. Both Tb and Gd decrease the band gap and increase the electrical conductivity of $Nd_2Sn_2O_7$.	[77]
$Gd_2Ti_2O_7$	Sol-gel method	700-1000°C	Eu^{3+} V^{5+}	Effect of increasing calcination temperature on PL properties study.	MD transition ($^5D_0 \rightarrow {}^7F_1$) for Eu^{3+} doped Gadolinium titanate host pyrochlore is strongest but when $Gd_2Ti_2O_7$ doped with Eu^{3+} at A-site and V^{5+} at B-site then ED transition ($^5D_0 \rightarrow {}^7F_2$) is doming, therefore there is enhancement in the optical properties.	[78]
$Gd_2Ti_2O_7$	Sol-gel method	800-1000°C	Eu^{3+}	Structural and luminescence property study.	The MD transition ($^5D_0 \rightarrow {}^7F_1$) of $Gd_2Ti_2O_7$ doped with Eu^{3+} is because of the energy transfer from $Gd_2Ti_2O_7$ to Eu^{3+}. Both PL intensity and	[79]

					lifetime of Eu^{3+} increases with increment in temperature.	
$Gd_2Ti_2O_7$	Pechini-type polymerized complex route	880ºC	Eu^{3+} Sm^{3+}	Structural, luminescent and life time study.	The lifetime of $^4G_{5/2}$ state decreases with increasing Sm^{3+} content, from 5 ms to 2.4 ms. As Eu^{3+} ion concentration increases in the host, the lifetime of $^5D_0$ level decreases from 5.9 ms to 3.1 ms of Eu^{3+}	[54]
$Gd_2Ti_2O_7$	Sol-gel method	800ºC	Eu^{3+} V^{4+}	TGA, CIE, structural and optical property study.	On adding V^{4+} to B-site of $Gd_2Ti_2O_7$:Eu^{3+} the PL study show that the colour of emission changed from orange to pure red.	[80]
$Gd_2Ti_2O_7$	Sol-gel method	1000ºC	Eu^{3+} V^{5+}	Structural and Luminescent property study.	The intensity ratio of MD transitions to ED transitions is attributed due to the production of defects due to doping of V^{5+} at B-site in $Gd_2Ti_2O_7$:Eu^{3+}.	[81]
$Gd_2Ti_2O_7$	Sol-gel method	800ºC	Yb^{3+} Eu^{3+} Er^{3+}	Anti-counterfeiting study of Different color light	By controlling the doping concentration of Er^{3+} in host $Gd_2Ti_2O_7$ green to red emissions are obtained. When Eu^{3+} ions concentration	[82]

				emission in Yb/Er/Eu doped $Gd_2Ti_2O_7$ pyrochlore.	further increased then excitation-dependent multi-color emissions are achieved.	
$Gd_2Zr_2O_7$	Hydrothermal Method	600-1200^oC	Dy^{3+}	Structural and optical properties study of $Gd_2Zr_2O_7$:Dy^{3+} pyrochlore for lighting applications.	Emission intensity increases upto 2 mol% as Dy^{3+} dopant concentration is increased in the host but after that again decreases. Lifetime of the Dy^{3+} transitions decreases with increasing Dy^{3+} dopant.	[83]
$Gd_2Zr_2O_7$	Liquid–solid–solution phase transfer method	800^oC	Eu^{3+} Al^{3+}	Structural, luminescent and life time study.	Adding Al^{3+} in host increases the photon absorption of the host therefore improves emission of Eu^{3+} due to reduction of the local symmetry of Eu^{3+} and the energy transfer between Eu^{3+} and Al^{3+} hence decreases non radiative transitions.	[84]
$Gd_2Zr_2O_7$	Hydrothermal Synthesis	1000^oC	Tb^{3+}	Structural and optical study.	As Tb3+ ions doped in the host then emission intensity increases but at a particular concentration it again	[85]

					decreases due to concentration quenching. The Tb3+ ion doping results green emission at 545nm.	
$La_2Zr_2O_7$	Solid state method	1850°C	Gd^{3+}	Structural and optical study.	The energy level diagram of Gd^{3+} in $La_{2-x}Gd_xZr_2O_7$ system is simple and the transparent ceramics from x = 1.0, 1.2 and 1.6, reveal a wide transmittance range (0.45–6.0μm), which have many uses in scintillators hosts and high temperature optical materials.	[86]
$Gd_2Zr_2O_7$	Gel-combustion method	1400°C	Sm^{3+}	Structure and optical properties correlation study.	Due to doping of Sm^{3+} in the host $Gd_2Zr_2O_7$, energy transfers from $Gd_2Zr_2O_7$ to Sm^{3+} is reason for the orange-red emission domination over green emission. .	[87]
$Gd_2Zr_2O_7$	Urea combustion route	1000°C	Er^{3+} Yb^{3+}	Structural and Optical study.	Increase in the ratio of intensity, green to red emission from 26 to 93% band has been observed due	[88]

					to Yb^{3+} doping in $Gd_2Zr_2O_7:Er^{3+}$ samples because of the energy transfer from Yb^{3+} to Eu^{3+} therefore used in NIR to visible up conversion application.	
$La_2Zr_2O_7$	Chemical Co-precipitation method.	-----	Er^{3+}	Structural and photolumine scent properties study.	With increasing Er^{3+} concentration in the $La_2Zr_2O_7$ the intensity of emission transitions also increases upto concentration x= 0.025 to 0.005 but after this value if further Er^{3+} ion concentration increases then emission intensity decreases due to quenching.	[89]
$Y_2Ti_2O_7$	Combustion method	-----	Hf^{4+}	Structural, optical properties and rate of degradation study.	The band gap energy values are 3.8 and 3.1eV for $Y_2Ti_2O_7$ and $Y_2Ti_{1.5}Hf_{0.5}O_7$ respectively. Degradation rate are 40% and 19.5% for $Y_2Ti_2O_7$ and $Y_2Ti_{1.5}Hf_{0.5}O_7$ respectively.	[90]
$Gd_2Ti_2O_7$	Solid state reaction method	900°C	Te^{4+}	Structural study.	Due to doping of Te^{4+} in $Gd_2Ti_2O_7$ increase in the volume of TiO_6 octahedron is observed due to increment in	[91]

					the bond length of Ti-O. Shift in the Raman graphs to the higher frequency of E_g modes (related to O(2) sub-lattice) were observed. Also full width half maxima value of F_{2g} (related to O-Gd-O bonding) mode increases as Te^{4+} increases in the host matrix.	

1.13. Outcomes from the literature survey and motivation for the present work:

A photoluminescent material is always defined as a solid structure which absorbs ultraviolet radiation and emits electromagnetic radiation over thermal radiation. The luminescent materials are also called phosphors and always made up of host crystalline structure doped with a certain amount of impurity atoms, called activators. To make a better photoluminescent material, it is necessary that the incoming radiation is mostly absorbed by activators to emit electromagnetic radiation and should try to suppress the non-radiative transitions of the phonons of host structure [92]. To select a host matrix, we must understand that the optical properties of same activator ion are different for different host matrices. Rare earth based pyrochlore structured oxides were explored and investigated as host matrix to make a most efficient luminescent materials [63,93].Unlike metal ions, suitable electronic configuration of lanthanides (4f orbitals surrounded by the outer filled $5s^2$ and $5p^6$) makes them most relevant candidate as activators with surprisingly superior optical properties [94].The optical properties

of selected pyrochlore oxides can be enhanced by introducing defects with doping of rare earth ions at A-site and B-site of the pyrochlore oxide host. Rare earth elements are doped in the host to change the band gap of pyrochlore structured materials by introducing defect fluorite structure. Rare earth based pyrochlore structured oxides were explored and investigated as host matrix to make a most efficient luminescent materials. Several pyrochlore compositions, like, $Gd_2Ti_2O_7$, $Gd_2Zr_2O_7$, $Hf_2Ti_2O_7$, $Ln_2Ti_2O_7$, *etc.* were reported with an enhanced optical property by doping with suitable dopants like Tb, Eu, V, Sm, *etc.*[61,95–97]. Basically, photoluminescence (PL) intensity was found to be increased up to a certain extent of dopant and after that it again decreases because of concentration quenching. Therefore, the PL intensity of pyrochlore oxide can be enhanced up to a certain limit by adding suitable dopant at A-site and B-site. Furthermore, it has been found that the optical properties are strongly co-related with structural properties. Since pyrochlore is a derived from structure of less ordered defect fluorite structure and reported that the introduction of dopants with different charge states as a function of increasing annealing temperature would increase the distortion of inversion symmetry at A-cationic site. This makes a dominance of electric dipole transition over magnetic dipole transitions and finally, increases the PL intensity.

The $Gd_2Ti_2O_7$ is primarily selected for the present study on enhancement of photoluminescent properties with suitable rare earth ion dopants, because the developments of high-quality doped material would be defect free and ideal for practical applications. The use of pyrochlore oxides as host materials offers an interesting option to integrate their functional properties with luminescence. The large solubility for suitable dopant (Eu^{3+}, Tb^{3+}, Ce^{3+}, Dy^{3+} *etc*.) acting as luminous centers is advantageous for structural and optical study. In the present work we will select host lattice $Gd_2Ti_2O_7$, offers favourable characteristics such as high melting point, phase stability, chemical and thermal stability.

1.14. Objectives:

Main objectives of the present thesis are as follows:

- To synthesize single-phasic pyrochlore oxides ($A_2B_2O_7$) and co-relate its optical properties with structural properties.
- To study the effect of doping of rare earth elements at A-site in pyrochlore oxides on its optical and structural parameters.
- To study the effect of suitable dopant at B-site in pyrochlore oxides on its optical and structural parameters.
- To study the effect of suitable dopant at A-site as well as B-site simultaneously in pyrochlore oxides on its optical and structural parameters.

1.15. Thesis organisation:

The present thesis has been organized into different chapters as described below:

- **Chapter 1: Introduction**

  The background of luminescence in pyrochlore-structured ceramics is concisely discussed in this chapter. Discussions take place regarding the fundamental ideas that underlie optical transitions in pyrochlore structures and the part of doping of rare earth play most important role for better luminescence results in terms of structural deformations. This chapter includes a summary as well as an explanation of the inspiration behind the present thesis project. Additionally provided a brief overview of rare earth doped with pyrochlore structures that exhibit a variety of structural and optical properties. Furthermore, detailed literature survey concerning the rare earth doped materials and the basic principle behind the luminescence results were given. The organisation of the thesis is provided in the end of the chapter.

- **Chapter 2: Sample preparation and characterization tools**

  The second chapter focuses on natural phenomena and procedures related to the examinations used in this paper. It shows how single-phase polycrystalline samples are prepared using the conventional solid-state approach. Several modern materials characterisation methods, including X-ray diffraction (XRD), scanning electron microscopy (SEM), Raman spectroscopy, and X-ray Photoelectron Spectroscopy (XPS) were used for structural and microstructural studies. The optical properties of the rare earth doped pyrochlore oxides were investigated using, Photoluminescence spectroscopy, Life-time decay, UV-visible Spectroscopy, and CIE coordinates studies.

- **Chapter 3: Key role of Tb^{3+} doping on structural and photoluminescence properties of $Gd_2Ti_2O_7$ pyrochlore oxide**

  The main objective of this chapter is to investigate the relationship between the structural and optical properties $Gd_{2-x}Tb_xTi_2O_7$ ($0 \leq x \leq 0.16$). The samples are having a cubic pyrochlore structure, confirmed by using X-ray diffraction and Raman spectroscopy Through analysis of UV absorption patterns, the band-gap of the host matrix $Gd_2Ti_2O_7$ is found to be 2.26 eV. From the photoluminescence results, the bands at 489 nm, 545 nm, 585 nm, and 623 nm, which correspond to the doping-induced transitions at $^5D_4 \rightarrow {}^7F_{6,5,4,3}$. An ideal doping concentration of x = 0.12, a bright green emission line at 545 nm is observed, corresponding to the $^5D_4 \rightarrow {}^7F_5$ dominant transition of terbium ions. The results indicate the possible use of a Tb^{3+}-doped $Gd_2Ti_2O_7$ composition as a luminous material, with an ideal doping concentration of 6 mol% of Tb^{3+} ions.

  The content of this paper is published as "***Key role of Tb^{3+} doping on structural and photoluminescence properties of $Gd_2Ti_2O_7$ pyrochlore oxide***", Ceramics International,

Volume 48, Issue 15, 1 August 2022, Pages 22266-22275, *https://doi.org/10.1016/j.ceramint.2022.04.231*.

- **Chapter 4: Structural and optical studies on Dy^{3+} doped $Gd_2Ti_2O_7$ pyrochlore as white light emission**

  The solid-state process approach was used to create a range of GTO pyrochlore samples, $Gd_{2-x}Dy_xTi_2O_7$ (where x = 0.5, 1.0, 1.5, 2.0, and 2.5 mol%). The Fd3m space group single-phase nature of all samples was discovered using XRD, Raman spectroscopy, and photoluminescence spectroscopy. Two strong emission bands with centres at 484 nm (blue) and 581 nm (yellow) were observed at an excitation wavelength of 347 nm, which correspond to the $^4F_{9/2} \rightarrow {}^6H_{15/2}$ and $^4F_{9/2} \rightarrow {}^6H_{13/2}$ transitions, respectively. The Y/B ratio is near unity for the optimum Dy^{3+} concentration (2.0 mol%), indicating a mixture of yellow and blue emission bands that combined generate white light. These results show the potential use of Dy^{3+} substituted GTO pyrochlore samples as luminous components in wLED applications.

  The content of this paper is published as "***Structural and optical studies on Dy^{3+} doped $Gd_2Ti_2O_7$ pyrochlore as white light emission***", Ceramics International, Volume 49, Issue 6, 15 March 2023, Pages 8897-8906, *https://doi.org/10.1016/j.ceramint.2022.11.045*.

- **Chapter 5: Effect of $Ce^{4+} \rightarrow Ce^{3+}$ conversion on the structural and luminescence properties of Ce^{4+} doped $Gd_2Ti_2O_7$ pyrochlore oxide**

  Solid-state reaction technique is used in this study to create several pyrochlore oxides, $Gd_2Ti_{2-x}Ce_xO_7$, with doping concentrations of x = 0, 0.04, 0.08, 0.12, and 0.16. Conventional methods like X-ray diffraction and Raman spectroscopy verified that the synthesised samples displayed a pyrochlore structured phase. The investigation of the

effects of Ce^{4+} to Ce^{3+} conversion on the structural and luminous properties is the main goal of this chapter. The unit cell expanded more and strain accumulated more in the reduced samples with pyrochlore structures. The oxidation state of the oxygen anions as well as the cations of Gd and Ti are examined using X-ray photoelectron spectroscopy (XPS). In comparison to the unreduced samples, it is observed that the Ce^{4+} to Ce^{3+} conversion produced better results in the PL emission and excitation. At 4% doping concentration for the cerium dopant, concentration quenching effects are observed. This work offers insightful information on the potential use of Ce^{4+} to Ce^{3+}: $Gd_2Ti_2O_7$ for the synthesis of blue LED chips used in the creation of WLEDs.

The content of this paper is published as "***Effect of Ce^{4+}→Ce^{3+} conversion on the structural and luminescence properties of Ce^{4+} doped $Gd_2Ti_2O_7$ pyrochlore oxide***", Journal of Luminescence, Volume 257, May 2023, 119687, *https://doi.org/10.1016/j.jlumin.2023.119687*.

- **Chapter 6: Influence of Al^{3+} co-doped ions for the improvement of orange-reddish light emitting photoluminescence characteristics of $Gd_2Ti_2O_7$:Eu^{3+} pyrochlore**

  In this chapter main focus is to study the enhanced luminescence emission and corelation of structural and optical properties for a series of powdered samples of $Gd_{1.92}Ti_{2-x}O_7$:$Eu_{0.08}Al_x$ with Al^{3+} doping (where x = 0, 0.02, 0.04, 0.06, & 0.08). Raman spectroscopy analysis revealed that high intensity vibrational bands displayed a blue shift upon the introduction of Al^{3+} substitution in the $Gd_{1.92}Eu_{0.08}Ti_2O_7$ host lattice, the purity of the produced samples was confirmed using X-ray diffraction analysis. Photoluminescence results show that the Al^{3+} doped $Gd_{1.92}Eu_{0.08}Ti_2O_7$ pyrochlore oxides have prominent orange-reddish emission spike at 588 nm caused by the $^5D_0 \rightarrow {}^7F_1$ transition, as well as emission peaks at 612 nm coming from the trivalent europium

ions' $^5D_0 \rightarrow {}^7F_2$ transition. The measured CIE coordinates (x = 0.622 and y = 0.351), which are dependent on the emission profile under 322 nm excitation, closely matched those of the commercial phosphor $Y_2O_2S:Eu^{3+}$. The results show that the Al^{3+} doped $Gd_{1.92}Eu_{0.08}Ti_2O_7$ pyrochlore oxides used as orange-reddish emitting components in luminous devices.

The content of this paper is published as "***Influence of Al^{3+} co-doped ions for the improvement of orange-reddish light emitting photoluminescence characteristics of $Gd_2Ti_2O_7:Eu^{3+}$ pyrochlore***", Ceramics International, Volume 49, Issue 21, Pages 34015-34024, 1 November 2023, *https://doi.org/10.1016/j.ceramint.2023.08.098.*

- **Chapter 7: Summary and Future Scope**

In this chapter, significant outcomes of this thesis were presented. This chapter provides an overview of the fundamental concept behind the structural and optical outcomes. Lastly, future scope of this work is discussed in detail as rare earth ion doped $Gd_2Ti_2O_7$ hold immense potential for usage in the production of WLEDs.

Chapter 2

Sample preparation and characterization tools

The second chapter focuses on the preparation of various rare earth ions doped pyrochlore oxide series using solid state reaction method. Single-phase polycrystalline samples are prepared using the conventional solid-state approach and several modern materials characterisation methods, including X-ray diffraction (XRD), scanning electron microscopy (SEM), Raman spectroscopy, and X-ray Photoelectron Spectroscopy (XPS) were used for structural and microstructural studies. The optical properties of the rare earth doped pyrochlore oxides were investigated using, Photoluminescence spectroscopy, Life-time decay, UV-visible Spectroscopy, and CIE coordinates studies.

2.1. Solid state reaction method:

Due to the rising demand for functional materials, material synthesis has taken enormous significance. Traditional solid-state synthesis method was the main techniques used for the sample series. Numerous thermodynamically stable samples were prepared using this technique. Diffusion in solid-state reactions is a naturally slow process that adheres to Fick's law of diffusion [98]:

$$\frac{dx}{dt} = \frac{k}{x} \ldots\ldots\ldots (2.1)$$

Here, ‘t’ stands for time, ‘k’ is a constant, and ‘x’ is the degree of reaction (thickness of the product layer). Not all ions and molecules are immediately available for the reaction in a solid-state reaction, in contrast to reactions that take place in solutions. The reaction, however, only happens when the reactants are in close proximity to one another. The subsequent progress of the reaction depends on the diffusion of one or both reactants via this product layer after a product layer has formed at the interface between the reactants. During this diffusion process, electro-neutrality must be maintained. The size of the diffusing ions, the structure of the reactants and the product, the reaction temperature, the existence of defects, and the sample’s characteristics are some of the variables that affect the diffusion of reactants [99]. The process by which items are created in the solid-state method are well represented in Figure 2.1.

In this process, solid reactants such as oxides or carbonates are repeatedly ground and annealed at high temperatures, usually for a long time, before being mechanically mixed [100]. This method involves a multi-step heating process with continuous grinding and pelletizing. The reaction starts off quickly but slows down as the reactants must diffuse through the generated product layer in order to come into contact.

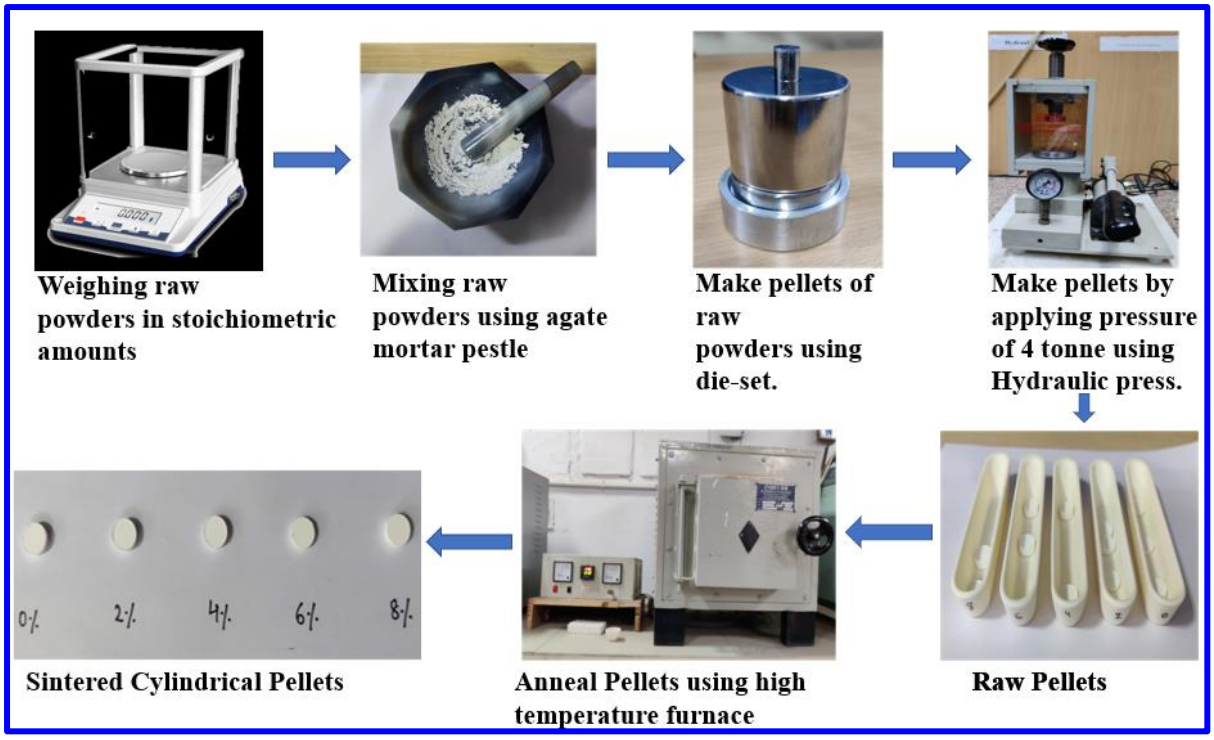

Figure 2.1: *Solid state reaction method.*

Influencing variables for the solid-state reactions:

a) **Temperature:** Temperature is the crucial parameter in solid-state processes as solids normally do not react at room temperature within standard time scales. These reactions must be driven by high temperatures. Solid-state processes require the understanding of both kinetic and thermodynamic considerations. Kinetics examines the rate at which the reaction develops, and the thermodynamics determines if a reaction is possible or not. Only at temperatures above 1100 °C the reaction begins, and it may even take several days of heating to 1300 °C to finish.

Nucleation and growth are the two steps that solid-state processes normally go through. At the recognized nucleus site, there is a large amount of structural reorganisation during the nucleation stage. The atoms and ions in the solid lattice are basically immobile at ambient temperature. However, for a reaction to take place, reactant particles must move in the direction of one another, occupying nearby void spaces to create a product layer. As a result,

high temperatures are required to provide these atoms and ions with enough energy to diffuse into one another. The development of this layer starts after the formation of the product nuclei. This phase is significantly more difficult because, as the product layer at the interface becomes thicker, atoms must diffuse over greater distances in order to contribute to the production of the product. Ion diffusion towards one another is directly responsible for solid-state processes. Further reaction proceeds more slowly because the diffusion rate reduces as the product layer thickness grows. The melting point, phase transition, and decomposition temperature of one of the reactants are some of the variables that influence the choice of a suitable temperature.

b) **Area of contact between the reacting solids:** The reactivity of solids is highly influenced by their surface area, which plays a crucial role in solid-state processes. The process of pelletizing a well-ground mixture of powders increases the contact area between reactants. Cold-pressed pellets typically have a porosity of between 30 % to 40 % and a density that falls between 65 % and 75 %. Hot pressing can minimise porosity by tightens up the fit between the particles through combining pressure and temperature. This densification process can take several hours. The nucleation process becomes more evident as the contact area between reactants grows, which speeds up the pace at which products are formed. In essence, the reaction is sped up by expanding the contact surface.

c) **Defects and vacancies**: Defects, vacancies, and interstices in the crystal lattice can also affect how quickly a solid-state reaction occurs. The diffusion of ions throughout most of the crystal is directly related to the reaction speed. The mobility of ions is increased by defects, vacancies, and interstices, which raises the total rate of the reaction.

Advantages of solid-state reaction method:

The solid-state reaction technique is advantageous for the synthesis of materials and compounds as it has the following benefits:

(i) **Thermodynamic Stability:** Solid-state processes are excellent for creating materials and molecules that are thermodynamically stable. They can create goods that are less prone to breakdown or phase changes.

(ii) **Purity:** Because there are no solvents used in this process that could add contaminants, it often produces highly pure products.

(iii) **Diverse Materials:** A variety of materials, such as ceramics, semiconductors, superconductors, and others, can be used with it.

(iv) **Simple:** This technique is quite easy to use and economical as it does not require complicated machinery or significant processing,.

(v) **High Temperature Reactions:** Solid-state reactions enable high-temperature synthesis, which is sometimes necessary for some materials and properties.

(vi) **Control:** Scientists have good control over the reaction rate..

(vii) **Homogeneity:** Mechanical mixing and grinding produce homogeneous products with consistent compositions in solid-state processes.

(viii) **Customization:** To customise the properties of the final product, reaction parameters, such as temperature, time, and grinding techniques, can be changed.

(ix) **Research and Development:** In several areas, including materials science, chemistry, and nanotechnology, solid-state reactions are essential for research and development.

Drawbacks of solid-state reaction method:

The mixing and grinding processes might introduce non-uniform composition and localised changes in stoichiometry, which is a typical drawback of this approach. Increased

contamination from the grinding media may result from prolonged grinding times. Additionally, this procedure requires high temperatures and lengthy annealing durations this is because solid-state synthesis needs the movement of these species over greater distances via diffusion due to the naturally constrained closeness of the reacting species. As a result, high temperatures are required, which produces goods of large and rough surfaces. Such goods are difficult to process and might not be appropriate for many real-world uses.

2.2. Important factors for experimental work:

Several crucial factors need to be taken into mind before starting an experiment involving solid-state reactions:

a) **Collect Data of Reactants:** Compile essential data, such as the reactant's melting and decomposition temperatures and vapour pressures. Understanding how the reactants will behave under various circumstances requires the knowledge of these data.

b) **Use Pellets for Heating:** Pellet forms are advantageous while heating the reactants. The reactants have a larger surface area of contact, improving reactivity when heated in forms of pellets.

c) **Appropriate Atmosphere:** Selecting the appropriate atmosphere, considering the specific needs and stability of the reactants are desired. The reaction outcome can be considerably influenced by the choice of atmosphere.

d) **Selection of the Crucible Material:** The selection of the crucible material is important. Even at the high temperatures of the reaction, it should be chemically inert towards both the reactants and the result. Platinum and Al_2O_3 are two materials frequently found in crucibles.

e) **Optimise Heating Temperature:** Optimizing the heating temperature for the compound with the lowest melting point or decomposition temperature is important.

These issues can improve the accuracy and effectiveness of solid-state reaction experiments.

2.3. Chemicals required:

Several kinds of chemicals are required for the synthesis of rare earth ions doped pyrochlore oxide materials, including a host lattice, activators, sensitizers, fuels, and a few fluxes. The oxide structures examined in this thesis were synthesised using the chemicals listed below in Table 2.1.

Table 2.1: Chemicals required to produce various rare earth ion doped $Gd_2Ti_2O_7$ pyrochlore oxide samples in the pursuit of this thesis.

Sr. No.	Chemical Name	Chemical Formula	Purity	CAS No.
1.	Gadolinium oxide	Gd_2O_3	≥ 99.99% purity, Sigma Aldrich	12064-62-9
2.	Titanium (IV) oxide	TiO_2	≥ 99.99% purity, Sigma Aldrich	1306-38-3
3.	Terbium (III) oxide	Tb_2O_3	≥ 99.99% purity, Sigma Aldrich	12036-41-8
4.	Dysprosium (III) oxide	Dy_2O_3	≥ 99.99% purity, Sigma Aldrich	1308-87-8
5.	Cerium (IV) oxide	CeO_2	99.95% purity, Sigma Aldrich	1306-38-3
6.	Europium Oxide	Eu_2O_3	99.9% purity, Sigma-Aldrich	1308-96-9
7.	Aluminium Oxide	Al_2O_3	99.5% purity, Sigma-Aldrich	1344-28-1

2.4. Instrumental details and characterization strategies:

2.4.1. Structural characterization tools:

To understand the features of the synthesised phosphors and optimising their usage as luminous materials in lighting devices require careful characterization. These phosphors are characterised using standard instruments and an analysis of their morphology, structure, and luminescence behaviour is required. The following sections of this chapter provide more structural details on the instruments and methods employed for the categorization.

2.4.1.1. X-ray diffraction:

The most common and efficient method for figuring out the phase and crystal structure of materials that have been synthesised is X-ray diffraction, or XRD. Electromagnetic waves having wavelengths in the angstrom range are called X-rays, and they are used to pierce materials to reveal structural details. Typically, X-ray wavelengths utilised in XRD vary from 0.50 to 2.50 angstroms [101].

The periodic arrangement of atoms in a three-dimensional lattice is exhibited by crystalline materials. The unit cell is the fundamental structural unit of a crystal. Translational vectors a, b, and c specify the lengths of the edges in this lattice, and angles α, β, and γ characterise the relationships between these vectors and the positions of the atoms in the lattice. Seven crystal systems, further subdivided into 14 Bravais lattices, are used to classify crystalline solids [102].

Basic principle:

When the wavelength of an X-ray coincides with the inter-planar spacing in a periodic lattice, X-ray diffraction (XRD) takes place. X-ray diffraction is then produced by this lattice acting as a diffraction grating. The structural arrangement of atoms within a crystal can be studied using the exact match between the X-ray wavelength and the inter-planar spacing.

The fundamental principle of X-ray diffraction is Bragg's Law. Atoms are arranged in a three-dimensional arrangement in a crystal lattice to form parallel planes with a particular interplanar spacing, represented by the letter 'd'. Electromagnetic radiation is reflected by the crystal's surface and internal planes when it strikes the lattice at specific angles. The reflected beams form constructive interference through interaction. A collection of atoms with interplanar spacing 'd' arranged in parallel planes is seen in Figure 2.2(a). Consider a monochromatic beam shining at an angle of θ on the lattice, with a wavelength of λ. When two reflected rays have a path difference that is an integer multiple of the wavelength λ, constructive interference takes place.

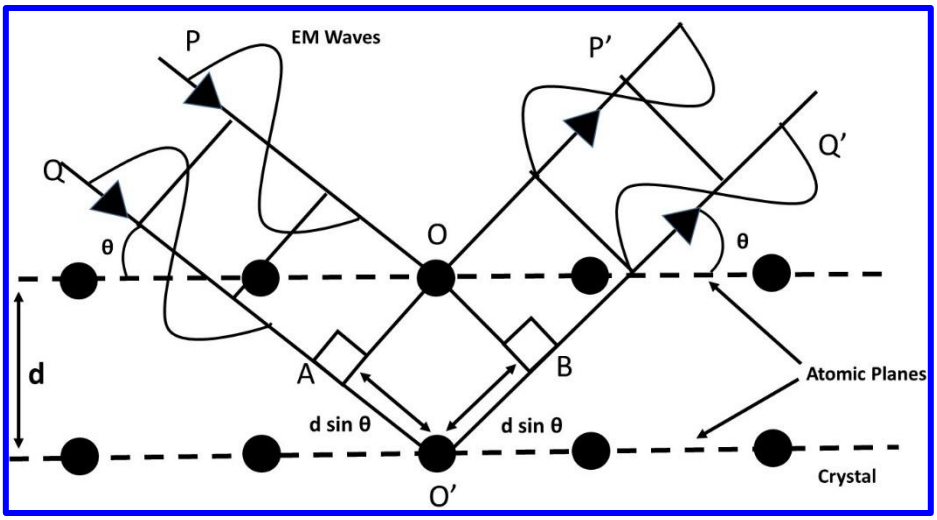

Figure 2.2: *Visualization of Bragg's Diffraction phenomenon occurring when X-rays interact with crystal planes.*

The formula for AO′+O′B, which represents the difference between rays P′ and Q′, is

$$AO'+O'B = d\sin\theta + d\sin\theta.$$

The path difference must be an integer multiple of the wavelength nλ, where n is an integer, in order for constructive interference to occur [101]. Consequently, we obtain:

$$2d\sin\theta = n\lambda.$$

Bragg's law, is the name given to the above relation. The intensities of the scattered waves are gathered as a function of angle in order to obtain the diffraction pattern. This interference pattern and diffraction peaks show the existence of many phases and their corresponding lattice structures.

Powder diffraction:

An X-ray tube, a sample holder, and an X-ray detector are the three primary parts of an X-ray diffractometer. The X-rays were produced by the X-ray tube, having a specific wavelength. As shown in Figure 2.3, the crystal sample is positioned at any angle about the incident X-ray beam by rotating it along an axis that passes through the geometric centre of the spectrometer. The X-ray detector function is to measure the intensity of the diffracted X-rays. It can also be rotated around the geometric centre of the spectrometer to get a desired angular location. The crystal is positioned so that it meets the requirements for diffraction, making sure that its reflecting surfaces make an angle of θ with the X-ray beam that is incident [102].

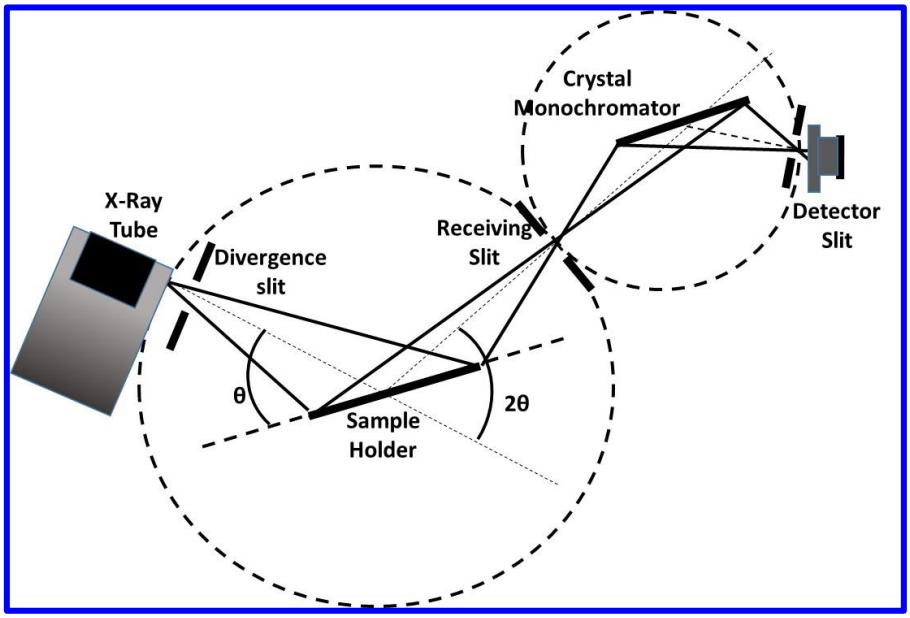

Figure 2.3: *Schematic representation of the data collection setup for XRD.*

When a sample is finely powdered, the individual crystals employ every possible orientation about the incident X-ray beam. The diffracted beams arise from this process create a cone-shaped radiation that is released from the sample. There are three main, statistically measurable aspects of a powder diffraction pattern given below:

(a) d-spacings: An important characteristic of the atomic arrangement is the separations between crystal lattice planes.

(b) Intensities: These reveal detailed arrangement of crystalline phases as well as the strength of the diffracted X-rays.

(c) Line profiles: These provide information about the diffraction lines width. A powder diffraction pattern's lines have a finite width at half maximum, and the width grows with the size of the particles.

The average crystallite size of a powdered sample can be measured using the powder diffraction method, which relies on the line broadening in the diffraction pattern.

Crystallite size and structural analysis:

Every crystalline substance has a distinct diffraction pattern that can be used as a fingerprint to determine its phase. When evaluating the pure phase development of a material under analysis, researchers frequently consult standard diffraction patterns issued by groups such as the international crystallographic diffraction data (ICDD) or the joint committee on powder diffraction standards (JCPDS). Peaks that differ from the reference data are usually regarded as contaminants and could be distinct phases of crystals. The XRD instrument used for sample characterization is well shown in Figure 2.4.

Figure 2.4. *XRD machine of Bruker company with Model-D8-advance setup.*

There are several uses for X-ray diffraction, such as:

Qualitative phase analysis: It determining which phases are contained in a given substance.

Determination of strain and size of crystallites: Evaluating internal strains and the size of the crystalline domains.

Orientation of crystalline materials: Determining how a sample's crystals align in different directions.

Determination of atomic number and position: Giving details regarding atom placement within a crystal lattice.

Determination of lattice parameters: XRD patterns can be used to calculate crystallite size using the Debye-Scherrer formula given below [103];

$$D = \frac{K\lambda}{\beta \cos\theta} \ldots \ldots \ldots (2.2)$$

Where, 'D' is the crystallite size, 'k' is the form factor (is usually 0.94 for cubic particles), the wavelength of the X-rays employed is 'λ', the diffraction peak full width at half maximum is represented by 'β', and the Bragg's diffraction angle is represented by 'θ'.

The Williamson-Hall (WH) method is an additional technique for estimating crystallite size [104].

$$\beta_{hkl} \cos\theta = \frac{0.94 * \lambda}{D} + 4\varepsilon \sin\theta \ldots \ldots \ldots (2.3)$$

where 'ε' represents the lattice strain. The crystallite size and micro-strain can be calculated by plotting a straight-line graph between $\beta_{hkl}\cos\theta$ along y-axis and $\sin\theta$ values on X-axis. The values of crystallite size 'D' and micro-strain 'ε' can be calculated by the y-intercept and slope values respectively from straight line WH plot. Scherrer formula also used to determine the crystallite size but the basic difference between WH and scherrer formula is that in case of scherrer formula the average crystallite size depends on $1/\cos\theta$ value, but in case of WH method crystallite size depends on $\tan\theta$ values.

Rietveld analysis:

Hugo Rietveld created the Rietveld method, which uses information from powder X-ray diffraction to characterise crystalline materials. Reflections defines the pattern in X-ray diffraction; these are quantified as intensities at particular angles. Many facets of the material's structure are revealed by the miller indices (hkl) connected to these reflections.

The Rietveld approach iteratively refines a theoretical line profile using a least-square fitting analysis. The process of refining is carried out repeatedly (10 cycles) until the computed pattern closely resembles the data obtained in experiments. The objective is to reduce the discrepancy

between the diffraction data seen and an artificially calculated crystal structure, considering the experimental factors. Specialised Rietveld refinement software, such as Full Prof Suite, can be used to fine-tune important parameters, including background, peak shape, and lattice parameters. This approach is very useful for the following reasons:

1. Quantitative Phase Analysis: It determines how much of each phase is there in a sample.

2. Microstructural Analysis: Determining the crystalline domain's strain and size.

3. Texture Analysis: Analysing a material's preferred crystal orientation.

4. Residual Stress Analysis: Examining a material's inherent tensions.

The Rietveld method uses known data, including reflection positions, cell size, space group symmetry, intensities, and atomic positions, to determine the crystal structure with accuracy [75]. Using a least-squares fitting technique, these parameters are refined to yield accurate values that characterise the structure of the material.

2.4.1.2. Raman spectroscopy:

Raman spectroscopy is an effective analytical method for the identification and non-destructive characterisation of chemical substances. It is based on the Raman scattering phenomenon, which occurs when photons interact with a sample, rotational and vibrational transitions within the sample's molecules change their energy [105]. Below a thorough explanation of its fundamental principle, advantages, drawbacks, and applications are given:

Basic principle:

- Incident light: The first step in Raman spectroscopy involves a monochromatic light source, usually a laser, incident on a sample.

- Scattering interaction: Most of the incident photons experience elastic scattering, sometimes referred to as rayleigh scattering, when they interact with the sample. The energy (and wavelength) of the scattered photons in rayleigh scattering are constant with the incident photons.
- Inelastic scattering: A small proportion of incoming photons experience inelastic scattering, also known as Raman scattering. In this process, interactions with the vibrational and rotational modes of the molecules in the sample cause some photons to lose energy (a Stokes shift) and others to gain energy (an anti-Stokes shift).
- Raman wavelength: A spectrum is created from the energy shifts in the raman-scattered photons; this spectrum usually shows the intensity of scattered light along the x-axis and raman shifts (frequency or wavenumber differences) along the y-axis. The vibrational and rotational modes found in the molecules of the sample are reflected in these shifts [106].

  The raman instrument of 532 nm WITec Alpha 300RA raman microscope setup is shown in Figure 2.5.

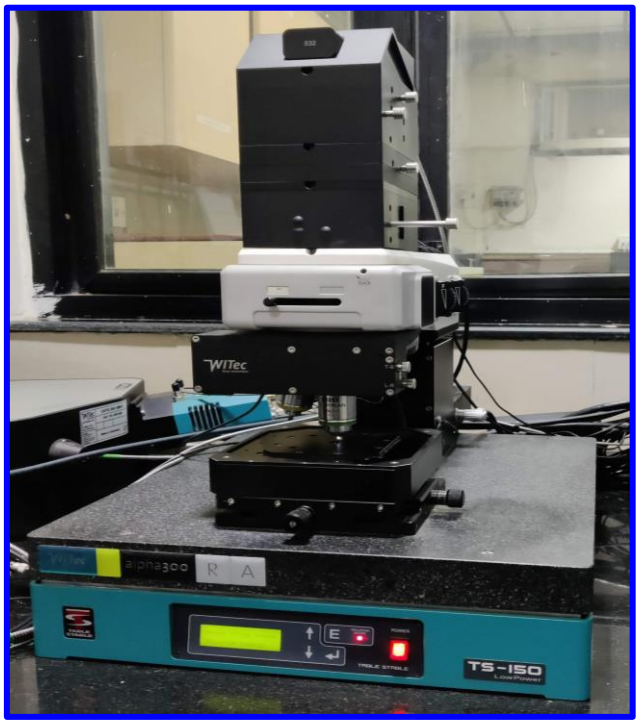

Figure 2.5: *532 nm in the WITec Alpha 300RA Raman microscope setup.*

Advantages:

- Chemical specificity: Compound identification is made possible by the raman spectroscopy and gives information regarding molecular structure and chemical composition.
- Non-destructive: It is non-destructive technique, therfore it can be used to analyse valuable or delicate material.
- Versatility: Raman spectroscopy has a wide range of applications in chemistry, materials science, biology, and pharmaceuticals, as well as in gases, liquids, and solids.
- Water insensitivity: Raman is less susceptible to water influence than some other methods, such as infrared spectroscopy.

Disadvantages:

- Weak signal: Raman signals are weak therefore; only low concentration samples can be detected through this spectroscopy.
- Fluorescence interference: It is ideal for samples that does not fluoresce because the sample fluorescence can frequently unclear raman signals.
- Sample Damage: Samples, especially delicate or organic materials, may be harmed by the high laser power in raman spectroscopy.
- Time-consuming: The weak signal in raman spectroscopy, which sometimes longer exposure durations, can make data acquisition time-consuming.

Applications:

- Chemical Analysis: The identification of organic and inorganic chemicals is one of the many applications of raman spectroscopy in chemical analysis.

- Material Characterization: Polymers, ceramics, minerals, and other materials are studied using this method.
- Pharmaceuticals: Drug analysis and quality control are two areas where raman spectroscopy is used in the pharmaceutical sector.
- Biology: Biomolecules, cells, and tissues are studied using raman spectroscopy in biology.
- Forensics: Material identification in forensic science is accomplished via raman spectroscopy.
- Environmental Analysis: Pollution analysis and environmental monitoring are done with the raman spectroscopy.

2.4.1.3. Scanning electron microscopy (SEM):

It is an extremely useful and adaptable instrument that can be used to collect detailed data at various magnifications regarding the microstructure and surface topography of materials. With incredibly high magnification, this tool is used to study the topography of specimens and record surface-specific compositional details. Scanning electron microscopy is a powerful microscopy method that may be used to see the surface morphology and collect comprehensive data regarding the composition and topography of a variety of materials. SEM produces greatly magnified images by sweeping a concentrated electron beam across a sample surface, detecting the released or backscattered electrons [107]. The following are the fundamental ideas, uses, benefits, and drawbacks of SEM:

Basic principle:

The collection of secondary electrons emitted when the specimen surface interacts with a precisely focused electron beam is the basic idea behind the imaging process. One way to make

the surface of non-conductive materials conductive is to add a very thin layer of carbon, gold, or gold-palladium. The specimen is placed on a metallic platform and scanned across the surface after its surface has been made conductive. A thermal emission source, such as a heated tungsten filament or a lanthanum hexafluoride crystal set on a tungsten filament, is usually the source of the electron beam. The electron beam is produced by an electron cannon at the top of the microscope, and it is directed by a vacuum vertical column. As the beam approaches the specimen, condenser lenses and electromagnetic fields around the vacuum column focus it. By collecting secondary electrons, the electron probe moves across the specimen surface in a two-dimensional pattern to create an image for scanning electron microscopy. Point-by-point construction of the SEM image is made possible by electromagnetic scan coils, which are regulated by a scan generator. When the specimen interacts with the primary electron beam, secondary electrons are released from it. At every point in the scanned region, an electron detector typically a Photomultiplier tube, detects these expelled secondary electrons. An electron signal intensity is shown as brightness on a cathode ray tube. Two ways of imaging are possible: backscattered electrons are used in the second mode, and secondary electron signals are used in the first. The secondary and backscattered electrons are collected by detectors, and the magnified signal is shown on a screen. SEM produces enlarged images by using electrons as opposed to light [108]. The figure 2.6 shows the schematic diagram.

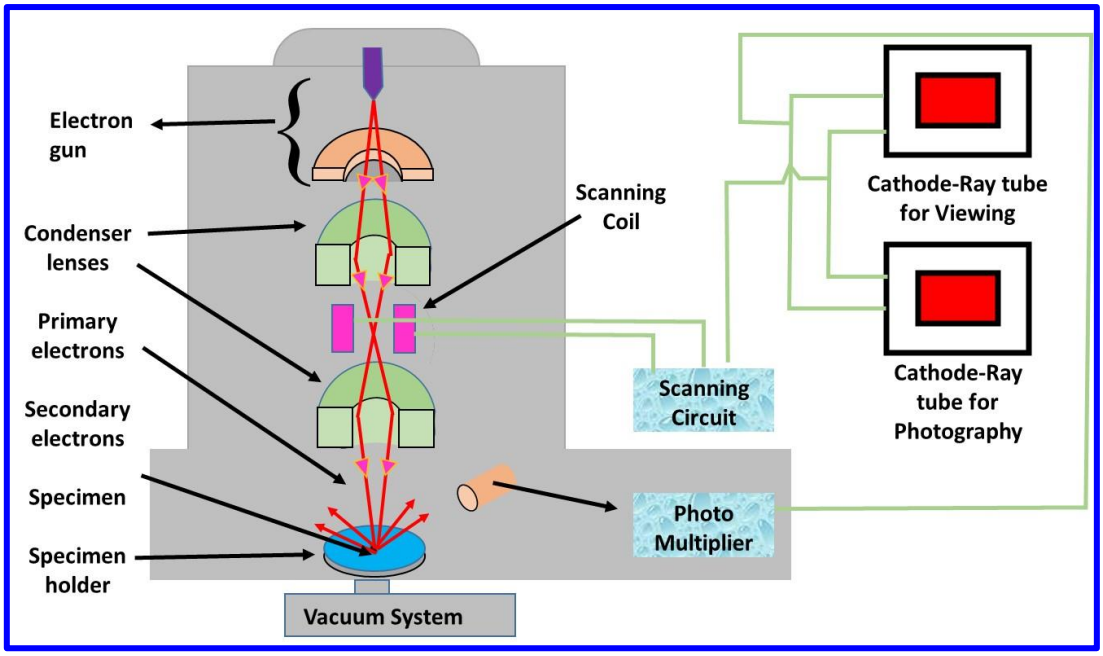

Figure 2.6: *Diagram showing the basic parts and configuration used for SEM apparatus.*

- A high-energy electron beam, usually accelerated to 1 to 30 kilovolts, is used in SEM.
- A variety of interactions are caused by the primary electron beam being focussed onto the sample surface.
- These interactions include backscattered electrons, characteristic X-rays, and secondary electrons released from the sample surface.
- Detectors pick up these emissions and produce signals that are utilised to produce analytical data or pictures.
- SEM generates high resolution, 2D and 3D pictures with a deep field of view.

SEM analysis:

By adjusting the electron probe scan width, one can change the SEM image's magnification. The formula M = D/d, where 'D' is the width of the monitor screen on which the image is displayed, 'd' is the electron probs scan width, and 'M' is the magnification, can be used to

determine the magnification of the scanned image [107]. A drop in scan width occurs when the magnification is increased because the monitor's size is constant, and vice versa. Particle size distribution and associated statistical analysis can be carried out by processing SEM pictures. The topography (surface look and texture), morphology (particle shape, size, and arrangement), composition, atomic arrangement, and degree of disorder are only a few of the features that these photos can reveal. The MIRA-II TESCAN Field emission SEM machines are the tools utilised for morphological observations; they are shown in Figures 2.7.

Figure 2.7: *MIRA-II TESCAN Field emission scanning electron microscopy setup.*

Applications:

- Material Science: Examining the structures and surfaces of materials.
- Nanotechnology: Defines nanomaterials and nanoparticles.
- Biology: The study of organisms, tissues, and cell structures.
- Geology: Examining the mineral and rock compositions.
- Electronics: Analysing components and integrated circuits.

- Forensics: Microstructure analysis and tracing evidence.
- Pharmaceuticals: Assessing particle and drug delivery methods.
- Metallurgy: Evaluation of microstructures and metal alloys.

Advantages:

- High Resolution: Offers finely detailed photos with a high resolution.
- Surface Sensitivity: Shows composition and topography of the surface.
- Depth of Field: Provides a wide field of view for 3D pictures.
- Elemental Analysis: Capable of conducting elemental analysis using energy-dispersive X-ray spectroscopy (EDS).
- Non-destructive: Analysis and imaging is non-destructive.
- High Magnification: Enables a high magnification for inspection at a small scale.
- Versatile: Fits with a variety of materials and uses.

Disadvantages:

- Vacuum requirement: In order to image, samples need to be coated to make them conductive, requires vacuum environment.
- Sample preparation: Preparing a sample takes time.
- 2D imaging: SEM doesn’t form 3D images it produces 2D images.
- Complex operation: Needs operators with advanced skills.
- Limited to surface: SEM only offers surface data; little information about depth is available.
- Expense: The cost of purchasing and maintaining an instrument might be high.

Because of its outstanding imaging capabilities and analytical potential, SEM is a flexible and extensively utilised tool in many scientific and industrial domains.

2.4.1.4. X-Ray photoelectron spectroscopy (XPS):

Electron spectroscopy for chemical analysis (ESCA), commonly referred to as X-ray photoelectron spectroscopy (XPS), is a potent analytical method for figuring out the chemical state, electronic structure, and elemental oxidation state, of especially surfaces. Below is a brief explanation of its functions, benefits, drawbacks, and applications:

Working principle:

1. Excitation: X-ray photons, which are usually produced by a monochromatic X-ray source, are incident on a material surface in order to operate XPS. The material electrons are impacted by these intense X-rays.

2. Emission: An electron in the sample may be ejected from its energy level by an X-ray photon colliding with it, and this process is known as photoionization.

3. Detection: Photoelectrons are the electrons released during photoionization. After that, these photoelectrons are collected and examined.

4. Energy Analysis: An electron energy analyser is used to determine the photoelectrons kinetic energy. This energy has a direct relationship to the sample electron binding energy.

5. Analysis: XPS offers details on the elemental composition, chemical state, and electronic structure of the sample surface by evaluating the kinetic energy and the quantity of expelled photoelectrons at different binding energies [109,110].

Advantages:

- Elemental composition: XPS can precisely ascertain a material's top few nanometres elemental composition.
- Chemical state: It offers details of the oxidation states, chemical states, of many elements.

- Surface sensitivity: XPS is perfect for examining the uppermost atomic levels because of its great surface sensitivity.
- Quantitative analysis: It makes it possible to analyse sample components quantitatively.
- Non-destructive: It can be used to analyse valuable or sensitive materials as XPS doesn't cause any damage.
- Broad applicability: It finds use in several disciplines, including as biology, chemistry, physics, and materials science.

Applications:

- Material characterization: A wide range of materials, including metals, polymers, ceramics, and semiconductors, can have their composition and physical characteristics studied using XPS.
- Investigating surface chemistry, which encompasses adsorption, corrosion, and catalysis, is a valuable use of surface chemistry.
- Thin film analysis: XPS is used in the study and creation of thin films.
- Biomaterials: It is applied to the research of biomaterials and helps to characterise surfaces functionalized with biomolecules.
- Semiconductor Industry: XPS is essential for thin-film quality control and analysis in the semiconductor sector.
- Environmental analysis: This method is used to examine contaminants on surfaces in environmental science.

Drawbacks:

- Limited depth: The application of XPS for bulk investigation is limited by its limited probing depth, which is usually a few nanometres.

- High vacuum environments are necessary for this approach, which restricts the examination of volatile or organic materials.
- Time-consuming: XPS data collecting might time consuming, particularly when mapping samples or scanning across a large energy range.
- Instrument Cost: The acquisition and maintenance of XPS instruments can be costly.

In conclusion, X-ray photoelectron spectroscopy is a useful and adaptable instrument for surface investigation that is frequently employed in a variety of academic and professional settings where an understanding of the chemistry and composition of the surface is essential.

2.4.2. Optical characterization tools:

For numerous crucial reasons, optical characterization technologies are required in industry, scientific research, and other domains. Optical characterization instruments are critical to the advancement of science, quality control, environmental protection, safety and security, and the development of novel technologies in a variety of fields and sectors. Here in this section various characterization tools are discussed in detail and they are as follows.

2.4.2.1. UV-Visible absorption spectroscopy:

UV-Visible spectrophotometer, is a multipurpose analytical tool for determining how much visible and ultraviolet (UV) light a chemical material absorbs. It is extensively used for both qualitative and quantitative investigation of chemicals in many different domains. Here is comprehensive information about UV-Visible spectroscopy, covering its fundamentals, benefits, drawbacks, and uses;

Basic principle:

a) The Beer-Lambert rule [111], which stipulates that the absorbance 'A' of a solution is exactly proportional to the concentration of the absorbing species 'C', the sample path length 'l', and the molar absorptivity 'ε', is the foundation of UV-Visible spectrophotometry.

$$A = \varepsilon Cl \ldots \ldots \ldots (2.4)$$

A portion of visible or UV light that enters a sample is absorbed by it. The level of concentration and chemical arrangement of a substance determine how much of the light is absorbed.

The spectrophotometer measures the transmitted light's intensity 'I' and the incident light's intensity 'I_0'. It determines absorbance 'A' using the formula,

$$A = -\log(I/I_0),$$

b) The band-gap can be determined by extraploting the linear region of the graph drawn between $(\alpha h\nu)^{1/n}$ vs $h\nu$. The obtained expression is known as tauc plot can be explained by the following relation [112],

$$(\alpha h\nu)^{1/n} = k\left(h\nu - E_g\right) \ldots \ldots \ldots (2.5)$$

Here 'α' is the absorption coefficient; 'hν' is the photon incident energy, 'n' is nature of the transition, 'E_g' is the band gap energy, and 'K' is the energy independent constant. Value of n = 1/2 for direct allowed transitions and n = 2 for indirect allowed transitions. Pyrochlore oxides have indirect band gap. UV-Visible spectrophotometer of Jasco company with Model V-770 setup is shown in Figure 2.8.

Figure 2.8: *UV-Visible spectrophotometer of Jasco company with Model V-770 setup.*

Advantages:

- Quantitative analysis: A common method for quantitative analysis is UV-Visible spectrophotometry, used to determine concentrations in a range of materials.
- High sensitivity: It is extremely sensitive to even minute concentrations of chemicals that absorb light.
- Wide application range: The UV-Visible spectrum includes visible (400-750 nm) and UV (200-400 nm) areas.
- Quick and non-destructive: It is appropriate for routine analysis because it is non-destructive and gives data quickly.
- Wide applicability: Applied in medicines, food and beverage testing, environmental analysis, chemistry, and biochemistry, among other fields.

Disadvantages:

- Limited information: UV-Visible spectroscopy does not reveal the identity of absorbing chemicals, it only reports their presence and concentration.
- Interference: Measurement inaccuracies may be caused by background contaminants, scattering, or other substances.

- Solvent dependency: The selection of solvent and solvent impurities may have an impact on the outcomes.
- Narrow application range: Although UV-Visible has a wide range of applications, its analysis is restricted to substances that absorb within this range.

Applications:

- Quantitative analysis: In chemistry, biology, and environmental science, UV-Visible technique is frequently utilised for the quantitative determination of analytes.
- Pharmaceuticals: It is essential to pharmacokinetics, quality assurance, and drug development.
- Life Sciences: Used in experiments for cell viability, enzyme kinetics, and DNA and protein analysis.
- Environmental analysis: Air, water, and soil contaminants are measured using UV-Visible spectroscopy.
- Food and beverage: Used to evaluate the content and quality of food and drinks.
- Colour analysis: UV-Visible is utilised in the paint and textile sectors to ascertain colour properties.
- Material science: It facilitates the investigation of material optical characteristics and electrical transitions.
- Astronomy: To ascertain the makeup of celestial bodies, UV-Visible spectroscopy is utilised in astronomical studies.

2.4.2.2. Photoluminescence:

A flexible, non-invasive, and effective analytical method for examining the sample light-emitting properties, is photoluminescence (PL) spectroscopy. This technique is investigating

the phenomena related to light emission from a sample upon photoexcitation. When light is released, its wavelength and intensity are plotted to create a photoluminescence spectrum. Concurrently, an excitation spectrum is acquired through the observation of a certain, pre-established emission band within a specified wavelength range. The emission spectrum is then created using the bands found in the excitation spectrum. The vertical axis of these two spectra shows the photoluminescence intensity, and the horizontal axis shows the wavelength fluctuations. The excitation and emission spectra are thus combined to form the photoluminescence spectrum [20].

Instrumentation:

Three essential parts make up the spectrophotometer: a sample holder, a detector, and an excitation source. Instead of providing a line spectrum, the excitation source is selected to offer a continuous spectrum. For this purpose, a Xenon lamp is usually used since it emits light that is both high-intensity and somewhat continuous above 220 nm in wavelength. Figure 2.9 shows Jasco-8300 fluorescence spectrometer with xenon lamp setup for UV absorption measurements. The assembly includes an excitation monochromator with wider aperture diffraction gratings to collect the brightest excitation light and this might increase the spectrofluorometer sensitivity. The prepared sample is placed into the sample holder and exposed to light from the excitation monochromator. The emission monochromator then collects luminous light in a targeted manner.

To measure the fluorescence intensity, a photomultiplier tube (PMT) or another light detector is used. PMTs are regarded as good current sources and are acknowledged for their superior spectral response. However, the non-uniform radiation spectra and unstable light production of xenon lamps lead to increased noise and signal distortion. A light-source compensation method is used to solve this problem. To monitor and adjust the part of the excitation light, a PMT with

a reference cell is placed next to the excitation monochromator in this configuration. The detector is then fed the adjusted signal again. By choosing the wavelength scan mode along with a high-voltage PMT setup, with low or medium scan speed and utilising excitation and emission slit widths of 0.1 nm, the excitation and emission spectra are recorded at room temperature. One uses a pulsed excitation source for time-resolved photoluminescence (TRPL). Temperature-dependent photoluminescence (TDPL) involves heating the sample to a higher temperature and taking photoluminescence measurements at different temperatures.

Figure 2.9: *Jasco-8300 fluorescence spectrometer with Xenon lamp.*

Here is a thorough overview of photoluminescence, including its benefits, drawbacks, and uses:

Basic principle:

The basis principle of photoluminescence is that a material absorbs photons and then emits them back in the form of light. A sample electron is stimulated to higher energy states when it is subjected to photons with energies higher than its bandgap. As these excited electrons settle back to their ground state, they release energy again in the form of photons. The material distinctive emission spectrum is produced by photons that are released with longer wavelengths and lower energy than those that are absorbed.

Advantages:

- Sensitivity: Photoluminescence is extremely sensitive and capable of identifying minute quantities of substances.
- Specificity: It offers details on the composition, electrical structure, and material flaws.
- Non-destructive: It can be used to analyse fragile material as it is non-destructive.
- Quantitative analysis: When applied in accordance with the right principles, it permits quantitative analysis.
- Broad range of application: Useful in semiconductors, materials science, biology, chemistry, and more.

Disadvantages:

- Preparing the sample: Sample preparation can take a lot of time, and for some materials, like cryogenic temperatures is required.
- Interference: Measurements may be tampered by background signals or sample contaminants.
- Instrument complexity: Expensive and sophisticated equipment may be needed for advanced photoluminescence measurements.
- Photobleaching: With repeated stimulation, fluorescent dyes can deteriorate over time and lose some of their luminosity.

Applications:

- Material characterization: Investigates the characteristics of nanomaterials, quantum dots, and semiconductors.
- Biology: It is used in bioimaging for molecular and cellular research, including fluorescent biomolecule tagging.

- Semiconductor Industry: Essential to optoelectronic device development and quality assurance.
- Solar cells: Used to evaluate and enhance photovoltaic devices efficiency.
- Pharmaceuticals: Used in quality assurance and medication development.
- Quantum computing: Investigating solid-state system quantum states.
- Environmental monitoring: Identifying and measuring contaminants in the environment.

2.4.2.3. CIE (Commission Internationale de l'Éclairage):

A mathematical representation of human colour vision is the CIE diagram, sometimes referred to as the CIE XYZ colour space, or the CIE 1931 colour space. It is employed to map and standardise the way the human eye interprets colour. The CIE diagram purpose and operation are as follows:

Reasons of using the CIE diagram:

a) Colour standardisation: Colour descriptions and representations can be standardised with the help of the CIE diagram. It serves as a global standard for describing the colour.
b) Colour matching: This is a crucial aspect of colour matching that makes it possible to reproduce colours accurately in a variety of settings, including printing, photography, and display technologies.
c) Colour quality control: The CIE diagram is used for quality control in the manufacturing and design industries to make sure that designs and products adhere to intended colour standards.
d) Lighting Design: Knowing the colour attributes of light sources is helpful in lighting design as it facilitates the creation of lighting environments with certain colour attributes.

How CIE diagram works:

- Colour matching functions: These functions explain how the human eye interprets colour and are the foundation of the CIE diagram. On the diagram, these functions are shown as curves.
- Tristimulus values: X, Y, and Z are commonly used as tristimulus values in the CIE system to determine colour. The amounts of the three primary colours required to match a particular colour perception are represented by these values.
- Chromaticity diagram: A chromaticity diagram is a two-dimensional depiction of colour that is similar to the CIE diagram. It has a border in the shape of a horseshoe that symbolises every colour that is visible. Colours that fall under this range are regarded as physically achievable.
- Chromaticity coordinates: Chromaticity coordinates are used to define a colour using the CIE diagram. These coordinates frequently represented by the symbols x and y, where a colour is located in the diagram. A colour position and saturation are represented by its chromaticity coordinates, but not its brightness, or luminance.

2.4.2.4. Time resolved photoluminescence (TRPL):

TRPL is an analytical method and tool for examining a material luminescence characteristics over incredibly brief periods of time. It is especially useful for studying the dynamics of excited states in luminous materials, offering insights into phenomena like phosphorescence, fluorescence, and charge carrier recombination in semiconductors. Here are specific details regarding the TRPL instrument.

Basic Principle:

The basis of TRPL is the measurement of a sample time-dependent photon emission after it has been excited by a light pulse. The material produces photons as it transitions from an excited state to the ground state when it is excited. The TRPL technique records the duration of luminescence decay, which provides insights into many processes like as recombination, energy transfer, and the lifetimes of excited stated [113].

Parts of an instrument for TRPL:

a) Pulsed excitation source: Typically, TRPL uses a pulsed laser or another type of light source that can produce excitation pulses with very short time, usually between femtoseconds (10^{-15} seconds) and nanoseconds (10^{-9} seconds).

b) Sample holder: To reduce scattering the sample being studied inside the sample chamber for effective light-matter interactions.

c) Detector: The released photons are picked up by a very sensitive detector, like a streak camera or photomultiplier tube. The reaction time of the detector is in line with the experiment intended time resolution.

d) Delay generator: The laser excitation and detector are concurrently triggered by a delay generator, which allows for fine temporal control of the measurements. Time-resolved measurements at delay times can cause stimulation.

The instrument used for this measurement is shown in Figure 2.10.

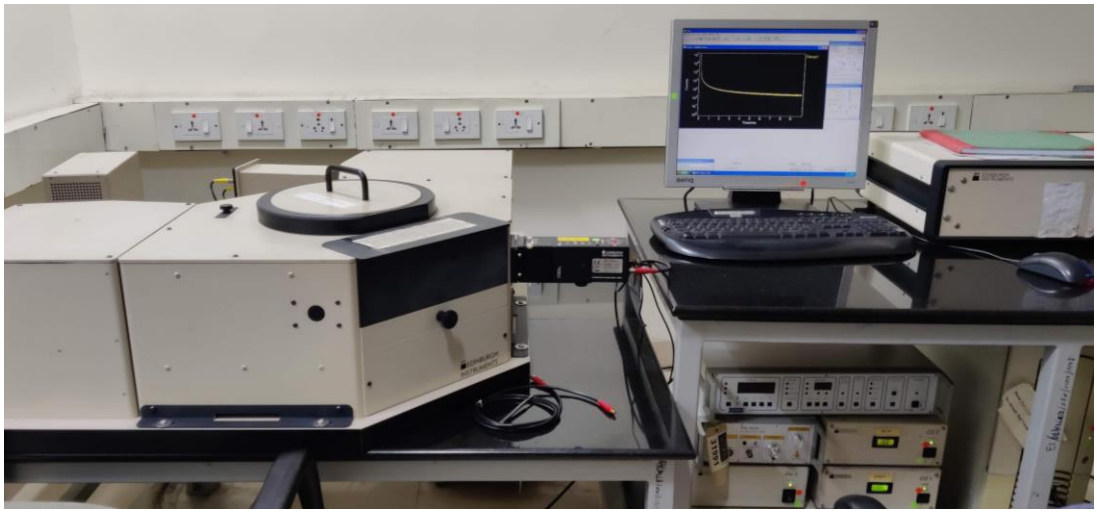

Figure 2.10: *TRPL machine of Horiba company with model DeltaFlex01-DD.*

Advantages:

- Ultra-high time resolution: The time resolutions available with TRPL sensors can capture incredibly fast phenomena, like fluorescence lifetimes that last less than a nanosecond.
- Probing complicated dynamics: TRPL can provide light on a variety of complicated dynamics, such as charge carrier recombination in materials and energy transfer.
- Materials characterization: Useful for describing photoluminescent materials, optoelectronic devices, and semiconductors.
- Mechanical insights: It makes it possible to examine photophysical processes in depth, which helps to comprehend the characteristics and behaviour of materials.

Disadvantages:

- Complex instrumentation: Operating TRPL instruments requires a high level of knowledge and might be expensive to set up.
- Sample constraints: Not all materials can be examined using TRPL, and samples need to be appropriate for time-resolved measurements.

- Data analysis: Dealing with multi-exponential decay curves, luminescence processes making data analysis challenging.

Applications:

- Semiconductor research: By examining the recombination kinetics of charge carriers in semiconductors, TRPL sheds light on the effectiveness and performance of semiconductor devices.
- Development of solar cells: It helps the dynamics of charge carriers in photovoltaic materials.
- Bioimaging: TRPL can be utilised for fluorescence lifetime imaging in biology and medicine, which enables label-free and non-invasive imaging of biological materials.
- Materials science: The photophysical characteristics of luminous materials, such as quantum dots and phosphors, are examined using TRPL.

Chapter 3

Key role of Tb^{3+} doping on structural and photoluminescence properties of $Gd_2Ti_2O_7$ pyrochlore oxide

The main objective of this chapter is to investigate the relationship between the structural and optical properties $Gd_{2-x}Tb_xTi_2O_7$ ($0 \leq x \leq 0.16$). The samples were having a cubic pyrochlore structure, confirmed by using X-ray diffraction and Raman spectroscopy Through analysis of UV absorption patterns, the band-gap of the host matrix $Gd_2Ti_2O_7$ was found to be 2.26 eV. From the photoluminescence results, the bands at 489 nm, 545 nm, 585 nm, and 623 nm, which correspond to the doping-induced transitions at $^5D_4 \rightarrow {}^7F_{6,5,4,3}$. An ideal doping concentration of x = 0.12, a bright green emission line at 545 nm was found, corresponding to the $^5D_4 \rightarrow {}^7F_5$ dominant transition of terbium ions. The results indicate the possible use of a Tb^{3+}-doped $Gd_2Ti_2O_7$ composition as a luminous material, with an ideal doping concentration of 6 mol% of Tb^{3+} ions.

3.1. Introduction:

Several research groups have focused their investigations on luminescent materials over the last few decades. Luminescence materials have widely studied due to their various applications in solid-state light sources [10], computer and television screens, lasers [6,8,9], Hg-free lamp phosphors [3], cathode ray tube (CRT) phosphors [4,5], Plasma display panels (PDP) [1], field emission displays [7], optical thermometer in medical field [2] *etc*. Mostly, inorganic phosphors are composed of crystalline host material doped with very small amount of impurity atoms, called activators. To make a good phosphor, the selection of host lattice and luminescent centres is very important or in other words, the largest ratio of radiative to irradiative transitions and the distribution of absorption and emission spectra are the main parameters to make a best phosphor [114]. Unlike metal ions, suitable electronic configuration of lanthanides (4f orbitals surrounded by the outer filled $5s^2$ and $5p^6$) makes them most relevant candidate as activators with surprisingly superior optical properties [94]. Therefore rare-earth based lattice structures and rare-earth ions (REI's) are the excellent candidate for both hosts and activators (luminescent centres), respectively since they show different colours of emission based on the 5d→4f and 4f→4f transitions [47]. The lanthanide elements are main contenders for being utilized as the activators with partially occupied 4f shell which is surrounded by the outer $5s^2$ and $5p^6$ orbitals. Due to this shielded $4f^N$ shell configuration of REI's, their energy levels are not much influenced by the surrounding environment irrespective of the host structure except a very slight shift in the positions and a small change in relative intensities of their spectral lines. To make a better photoluminescent material, it is necessary that the incoming radiation is mostly absorbed by activators to emit electromagnetic radiation and the non-radiative transitions of the phonons of host structure are suppressed [92]. To select a host matrix, we have to understand that the optical properties of same activator ion are different for different host matrices. Here rare-earth based pyrochlore structured oxides were explored and

investigated as host matrix to make a most efficient luminescent materials [63,93]. Among ternary oxides, compound with popular formula $A_2B_2O_7$ belongs to a family of pyrochlore structure where A^{3+} and B^{4+} are cations. Rare earth pyrochlore oxides can have much importance in today's world due to their use in various fields, such as host for luminescence centers [63], catalysts [64], nuclear waste forms [115], high temperature pigments [66], ionic conductor [67], transparent ceramics [68], and water splitting [68] *etc.* Rare earth based pyrochlore oxides are cubic and ionic in nature thus their adoptability towards the variation of chemical substitution at A and B cationic position is very high. Pyrochlore oxides have various physical properties due to the fact that cation B is a transition metal atom with varying oxidation state and cation A is a REI with inert lone pair of electrons. The stability strength of pyrochlore oxide structure is described by the radii ratio of cation A (r_A) and cation B (r_B) (i.e., r_A/ r_B) ratio. The ionic radii ratio for $Gd_2Zr_2O_7$ is 1.46 and for $Gd_2Ti_2O_7$ its value is 1.75. The ionic radii ratio value ranges from 1.46 to 1.78 for stable pyrochlore oxide structure [48,70,71]. If the value of ionic radii ratio is less than 1.46 then the structure is changed into defect fluorite structure due to the easy swapping of two cations [72]. These properties of pyrochlore oxides attracts different research groups to explore its applications in the preparation of best luminescent materials. Lanthanum stannates ($La_2Sn_2O_7$) have studied due to extreme thermal and chemical stability and they are used as host matrix for phosphors and solid-state lasers as they can accommodate rare-earth ions in the octahedral site easily [69]. Rare earth trivalent ions have novel optical properties of doped pyrochlore oxide samples. Several pyrochlore compositions, like, $Gd_2Ti_2O_7$, $Gd_2Zr_2O_7$, $Hf_2Ti_2O_7$, $Ln_2Ti_2O_7$, *etc.* were reported with an enhanced optical property by doping with suitable dopants like Tb, Eu, V, Sm, *etc.* [61,95–97]. Among different pyrochlore compositions, rare earth titanates were used as phosphor materials due to easy incorporation of trivalent rare earth ions as activator at the A-site (due to nearly same ionic radii), strong luminescent, optical, magnetic, and electrical properties [105,116–

119]. Some research groups were investigated the enhancement of optical properties of $Gd_2Ti_2O_7$ by doping of rare earth ions; namely Eu^{3+}, Er^{3+}, and Dy^{3+} at A-site [79,96,120–123]. Garbout *et al.*, were synthesized $Gd_{2-x}Eu_xTi_2O_7$ oxides using solid-state method and found the lattice expansion on replacing the Gd^{3+} (1.053 Å) by Eu^{3+} (1.066 Å). They have also reported the enhancement of photoluminescence ((PL) properties and explained this phenomenon by introduction of defects due to increasing $r(REI^{3+})/r(Ti^{4+})$. Although the compositions with more than 50 % Eu^{3+} showed the luminescence quenching [96]. Pang *et al.*, were also used trivalent europium rare earth ion as reactant and synthesized the thin film of Eu^{3+} doped $Gd_2Ti_2O_7$. The concentration quenching was observed in the solid solution with Eu^{3+} higher than 9 at.% [79]. Furthermore, Zeljka Antic *et al.* have prepared trivalent europium doped $Gd_2Ti_2O_7$ crystalline pyrochlore thin film, at calcination temperatures more than 1000℃ by using pulsed laser deposition (PLD) approach and study the temperature effect on luminescent properties. They observed that with temperature increment up to 1100℃, complex but better luminescent spectrum of crystalline thin films were observed. Also, after deposition, asymmetry emission ratio increases at temperature 1100℃ due to crystal lattice expansion and therefore trivalent rare earth europium ions were symmetrically distributed into the host lattice $Gd_2Ti_2O_7$ [120]. Ting *et al.*, prepared Er^{3+} ions doped $Gd_2Ti_2O_7$ host lattice at the A-site with various concentrations; 0.1, 1, 5, 10, 15, or 20 mol%, using conventional sol-gel method and they noticed that PL intensity was increased up to doping concentration of 10 mol% of trivalent Er^{3+} ions annealed at a temperature 1100℃ for 1 hour. PL intensity further decreases for 15 and 20 mol% doping of Er^{3+} due to concentration quenching effect (because of the Eu^{3+}-Eu^{3+} ion distance decreases) [121]. Thus, these groups were reported the rare earth doped $Gd_2Ti_2O_7$ as best host material for phosphors. Therefore, optical properties of selected pyrochlore oxides can be enhanced by introducing defects with the doping of rare earth ions at A-site of the pyrochlore oxide host. It can be concluded from the literature survey that the REI's are doped

in the host with ideal pyrochlore structure *i.e.,* $Gd_2Ti_2O_7$ to enhance the PL properties of pyrochlore structured materials by introducing defect fluorite structure. Here $Gd_2Ti_2O_7$ pyrochlore oxide was primarily selected for the present study on enhancement of photoluminescent properties with suitable rare earth ion dopants, because of the developments of high-quality doped material would be defect free and ideal for practical applications. Terbium ions (Tb^{3+}) are used as the most supreme green light emitting luminescent activators (dopant) for various phosphors since it has an intense emission around wavelength of 544 nm with very high intensity, which is adjacent to the theoretical optimal wavelength for the green section of three primary colour centers [93]. Since the cationic radii for Gd^{3+} and Tb^{3+} are 1.053 Å and 1.040 Å, respectively. Therefore r_{Gd}/r_{Ti} and r_{Tb}/r_{Ti} are 1.740 and 1.719 respectively which shows that the doping of Tb^{3+} ions in $Gd_2Ti_2O_7$ host matrix does not affect basic pyrochlore structure. Here in the present research work, we prepared pellets by the doping of Tb^{3+} rare earth trivalent ion as activator in the host $Gd_2Ti_2O_7$ lattice, using solid-state reaction method. The pellets of pristine $Gd_2Ti_2O_7$ and doped with 2%, 4%, 6%, and 8% of Tb^{3+} were studied by using characterization techniques like, X-ray diffraction spectroscopy (XRD), Micro-Raman analysis and Field Emission Scanning electron microscopy (FESEM), UV-Visible spectroscopy, and PL spectroscopy.

3.2. Experimental section:

3.2.1. Sample preparation:

The Tb^{3+} doped $Gd_{2-x}Tb_xTi_2O_7$ pyrochlore ternary oxides with x = 0%, 2%, 4%, 6%, and 8% were obtained by using a facile solid-state reaction route. In this method stoichiometric amount of high purity (Sigma Aldrich ~ 99.99% pure) AR-grade raw powders Gd_2O_3, TiO_2 and Tb_2O_3 were preheated for 3 hours to remove moisture and extra volatile impurities. Stoichiometric number of raw powders are given in Table 3.1. After preheating all the powders were

stoichiometrically weighed and ground intimately to obtain homogeneity using mortar and pestle. Powdered mixture of powders was pelletized using hydraulic press and dye set by applying a pressure of 4.5 Torr.

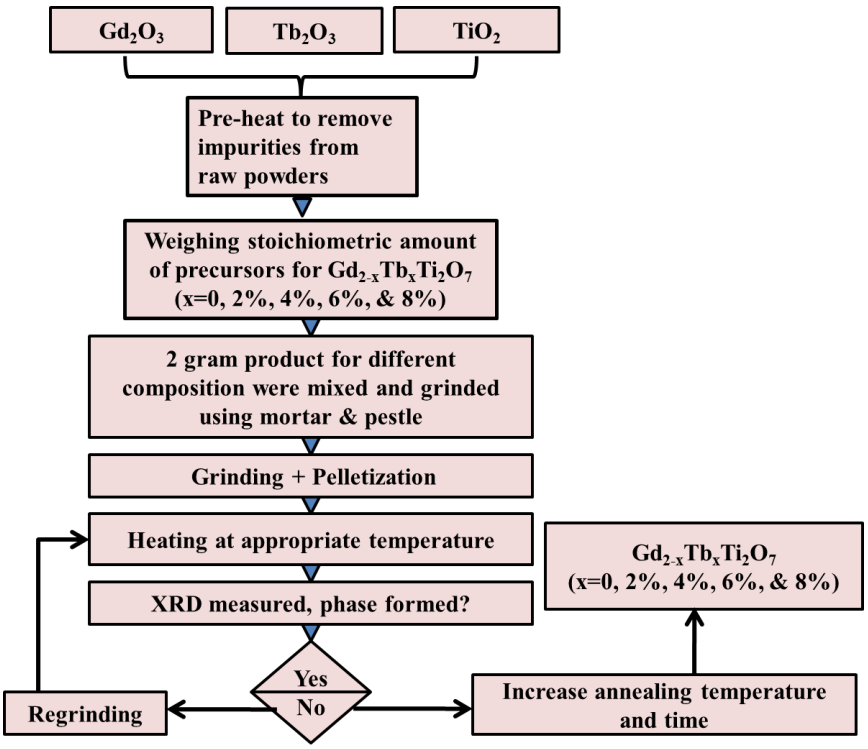

Figure 3.1. *Flow Chart for the synthesis of Tb^{3+} doped $Gd_2Ti_2O_7$ pyrochlore host matrix.*

Cylindrical pellets were heated initially at a temperature of 1200 ℃ for 24 hours duration using high temperature box furnace. The procedure of pelletizing and grinding was repeated again and again unless we get desired pure phasic structure of pyrochlore ternary oxide. For second heating protocol, all the pellets were re-grounded and pelletized again and heated at temperature 1250 ℃ for 36 hours. To remove defects and to achieve pellets of high density, all the pellets were finally sintered at a high temperature of 1300 ℃ for 48 hours of duration using box furnace with heating rate 5 ℃/min and colling rate 2 ℃/min respectively. A flow chart for the synthesis of various doping concentration of Tb^{3+} doped $Gd_2Ti_2O_7$ pyrochlore host matrix is shown in Figure 3.1.

Table 3.1. Concentration of salts used in synthesis of $Gd_2Ti_2O_7$ doped with Tb^{3+} series.

Doping level (x)	**$Gd_{2-x}Tb_xTi_2O_7$**	**Gd_2O_3 (gram)**	**TiO_2 (gram)**	**Tb_2O_3 (gram)**
0	$Gd_2Ti_2O_7$	1.3947	0.6146	0
0.04	$Gd_{1.96}Tb_{0.04}Ti_2O_7$	1.3588	0.6110	0.028
0.08	$Gd_{1.92}Tb_{0.08}Ti_2O_7$	1.3324	0.6116	0.056
0.12	$Gd_{1.88}Tb_{0.12}Ti_2O_7$	1.3045	0.6115	0.084
0.16	$Gd_{1.84}Tb_{0.16}Ti_2O_7$	1.2766	0.6114	0.112

3.2.2. Characterization of Tb^{3+} doped $Gd_2Ti_2O_7$ pyrochlore oxide:

The structural investigation of all the finally sintered pellets with different doping concentration of terbium were examined using X-ray diffraction technique. The XRD patterns of all the pellets were recorded on XRD machine of Bruker company (Model-D8-advance) in the range of angle 2θ from 10^o to 75^o using a step of 0.02^o and scan speed 0.5^o min^{-1} with Cu diode K_α radiation of wavelength λ = 1.5406 Å at DTU, New Delhi. All the finally sintered pellets were examined through Field emission scanning electron microscopy (FESEM-MIRA-II, TESCAN), at IUAC, New Delhi. Raman patterns for all the pellets were recorded using a laser of excitation wavelength 532nm using the WITec Alpha 300RA raman microscopy equipped with a 50× objective lens, at JNU, New Delhi. Absorption spectra for pristine $Gd_2Ti_2O_7$ was examined on an UV-Visible spectrophotometer of Jasco company (Model V-770) at DTU, New Delhi. PL excitation patterns and emission spectrum for all the samples with various doping concentration of terbium were observed with a Jasco-8300 fluorescence spectrometer at room temperature using Xenon lamp.

3.3. Results and discussion:

3.3.1. Structural analysis through XRD:

X-ray diffraction for all the powdered samples $Gd_{2-x}Tb_xTi_2O_7$ with varying the value of x = 0.04, 0.08, 0.12, and 0.16, annealed at 1300°C for 48 hours were recorded and depicted in Figure 3.2(a). A series of XRD patterns for all the samples were recorded in the 2θ range from 10° to 75° to obtain all pyrochlore superstructural peaks. The most recognizable XRD patterns containing two types of diffraction maxima. For first type of XRD peaks having high intensity peaks with miller indices (222), (400), (440), (622), (444), and (800) centered at 2θ values 30.48°, 35.34°, 50.78°, 60.35°, 63.42°, and 71.30°, respectively were represents basic fluorite structure on which pyrochlore structure was build. Furthermore, the second kind of highly ordered super-structure of pyrochlore oxide with low intensity peaks were found at 2θ values 15.15°, 29.16°, 38.62°, 46.41°, and 53.28° having miller indices planes (111), (311), (331), (511), and (531), respectively, represented by star (*) mark shown in Figure 3.2. All the samples belong to cubic crystal structure with Fd-3m space group. For all the different compositions of dopant (Tb^{3+}), crystalline single phase cubic structure of pyrochlore were formed without any second phase which are in good agreement with the published results [124]. Therefore, doping of Tb^{3+} at the A-site into host $Gd_2Ti_2O_7$ does not distorted the crystal structure which indicated that the trivalent rare earth ion Tb^{3+} have been correctly accumulated within the host matrix $Gd_2Ti_2O_7$ in place of Gd^{3+} lattice position [125]. This perfect pyrochlore structure for the synthesized solid-solution can be explained on the basis of ratio of cationic radii r_A/r_B, which can be calculated using the following relation,

$$\left[\frac{r_{Gd,Tb}}{r_{Ti}}\right] = \left[\frac{r_{Gd} \times atomic\ \% + r_{Tb} \times atomic\ \%}{r_{Ti}}\right] \ldots\ldots\ldots (3.1)$$

Where $r_{Gd} = 1.0530$ Å, r_{Tb} =1.0400 Å and $r_{Ti} = 0.6050$ Å as the ionic radius for the trivalent and tetravalent cations with considering their coordination number. The calculated values of ratio of ionic radii are written in Table 3.2 which decreases from 1.7405 to 1.7388 on increasing Tb^{3+} concentration. An enlarged view of diffraction patterns (peak centered around 30.48° angle) within 2θ range 30° to 31° was separately plotted in Figure 3.2(b) to show the shifting in diffraction patters as a result of doping. The most dominant diffraction peak (222) was slightly shifted towards higher angle side with increment of the Tb^{3+} trivalent rare earth ion in the $Gd_2Ti_2O_7$ host pyrochlore matrix as guided by a dotted line from bottom to top in Figure 3.2(b). This peak shifting is related to the decreasing lattice constant or to the shrinkage of host lattice [84]. Since the cationic radius of Tb (1.040 Å) is smaller than the cationic radius of Gd (1.053 Å), hence the lattice parameter slightly decreases from 10.1508 Å to 10.1451 Å, on the substitution of terbium in place of gadolinium. It shows that on adding Tb at the A-site of host $Gd_2Ti_2O_7$ matrix, no phase changes were observed.

From the XRD patterns of different composition of Tb^{3+} in host at A-site, various parameters are calculated like, cationic radii ratio 'r_A/r_B', lattice parameter 'a', volume 'V', crystallite size 'D', and strain 'ε' and tabulated in Table 3.1. From XRD patterns average crystallite size and strain can be calculated for both pristine host $Gd_2Ti_2O_7$ as well as Tb^{3+} doped samples using following Williamson Hall (WH) relation;

$$\beta_{hkl} \cos\theta = \frac{0.94 * \lambda}{D} + 4\varepsilon \sin\theta \ldots\ldots\ldots (3.2)$$

Here 'β_{hkl}', 'ε', and 'λ' represents the Full Width Half Maximum (FWHM) of the first five dominating XRD peaks corresponding to their θ values, micro lattice strain related to the synthesized pyrochlore oxide samples, and wavelength of the X-rays used in XRD machine (1.5046 Å) respectively. The factor 0.94 represents the value of structure factor for spherical crystals having cubic symmetry and 'D' represents crystallite size.

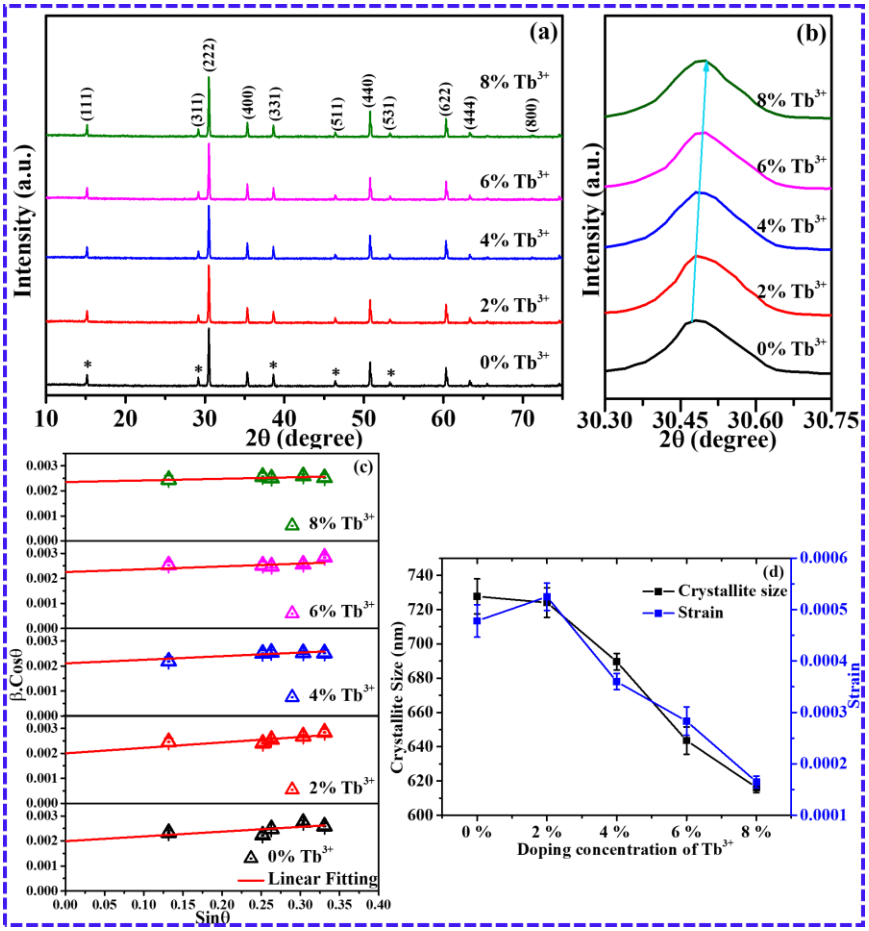

Figure 3.2. *(a). A set of XRD spectra for undoped and Tb^{3+} doped samples of $Gd_2Ti_2O_7$, (b). peak shifting in (222) peak, (c). WH plot and (d). Variation in the values of crystallite size and strain with doping concentration of terbium.*

To find the crystallite size and micro-strain for pristine and Tb^{3+} doped pyrochlore host matrix $Gd_2Ti_2O_7$, a straight-line graph is plotted between $\beta_{hkl}\cos\theta$ on y-axis and $\sin\theta$ values on X-axis as shown in Figure 3.2 (c) for all the compositions. The values of crystallite size 'D' and micro-strain 'ε' can be calculated by the y-intercept and slope values respectively from straight line WH plot. Scherrer formula also used to determine the crystallite size but the basic difference between WH and Scherrer formula is that in case of Scherrer formula the average crystallite size depends on $1/\cos\theta$ value, but in case of WH method crystallite size depends on $\tan\theta$ values [126]. From the WH plots for all compositions, the observed intercept and slop are reported in Table 3.2. The crystallite size and strain were calculated from the observed values of intercept

and slope respectively. It was observed that the value of crystallite size decreases from 727.7 ± 4.3 Å to 616.2 ± 4.3 Å. Furthermore, it was observed that with increasing Tb^{3+} content in $Gd_2Ti_2O_7$ host matrix, the value of both crystallite size and strain continuously decreases which is shown by Figure 3.2(d). The doped Tb^{3+} ion in the host $Gd_2Ti_2O_7$ at Gd^{3+} cationic site is in a very small concentration from 2% to 8%. Therefore, crystallite size and strain are decresaed very slightly.

Table 3.2. The structural parameters for undoped and doped samples of $Gd_2Ti_2O_7$ calculated from XRD results.

Doping level	**$Gd_{2-x}Tb_xTi_2O_7$**	**r_A/r_B**	**Intercept**	**Slope**	**Crystallite Size in Å**	**Strain**
0	$Gd_2Ti_2O_7$	1.7405	0.00199 ±0.00033	0.00191 ±0.00012	727.7 ± 4.3	0.00048 ± 0.00003
0.04	$Gd_{1.96}Tb_{0.04}Ti_2O_7$	1.7401	0.00200 ±0.00030	0.00210 ±0.00011	724.1 ± 4.0	0.00053 ± 0.00002
0.08	$Gd_{1.92}Tb_{0.08}Ti_2O_7$	1.7396	0.00210 ±0.00018	0.00144 ±0.00026	689.6 ± 3.2	0.00036 ± 0.00004
0.12	$Gd_{1.88}Tb_{0.12}Ti_2O_7$	1.7392	0.00225 ±0.00031	0.00113 ±0.00011	643.6 ± 2.7	0.00028 ± 0.00001
0.16	$Gd_{1.84}Tb_{0.16}Ti_2O_7$	1.7388	0.00235 ±0.00012	0.00066 ±0.00005	616.2 ± 2.6	0.16 00001

3.3.2. FESEM analysis:

The FESEM micrographs of pristine samples of $Gd_{2-x}Tb_xTi_2O_7$ (x = 0.04, 0.08, 0.12, and 0.16) annealed at 1300℃ were depicted in Figure 3.3(a-e). Grain size for all the synthesized

compositions were studied under high magnification of the order of 20,000 times. These FESEM micrographs were analyzed through ImageJ software. All FESEM images show almost equal grain size distribution in the range of 400 nm to 1400 nm. It was observed that all the samples have spherical agglomerated particles with almost equal free space. Although all samples have shown very compact morphology at the surface. The exact grain size was found to be 0.82 ± 0.04 µm, 0.81 ± 0.01 µm, 0.82 ± 0.02 µm, 0.79 ± 0.01 µm, and 0.78 ± 0.02 µm for the samples $Gd_2Ti_2O_7$, $Gd_{1.96}Tb_{0.04}Ti_2O_7$, $Gd_{1.92}Tb_{0.08}Ti_2O_7$, $Gd_{1.88}Tb_{0.12}Ti_2O_7$ and $Gd_{1.84}Tb_{0.16}Ti_2O_7$, respectively as shown in Figure 3(f-j). Thus, it was found that all the samples have almost equal grain size. The micrographs corresponding to all composition show almost similar void volume which provides an indirect information about nearly same bulk density. The information of almost equal grain size and bulk density convey by micrographs can be validated by same heating protocol for the whole series. Although, on comparing the micrographs of pure host and 8% Tb^{3+} doped host, the doping has introduced some structural distortion which did not induce any significant change in grain size and surface morphology as studied in FESEM analysis of the series $Gd_{2-x}Tb_xTi_2O_7$ (x = 0.04, 0.08, 0.12, and 0.16). Furthermore, all the elements (Gd, Ti, Tb, and O) are uniformly distributed as represented by the elemental mapping through energy dispersive x-ray analysis (EDX) and shown in Figure 3.3 (k-n) for the last composition $Gd_{1.84}Tb_{0.16}Ti_2O_7$ (x = 0.16). Thus, EDX analysis concludes that the all compositions have uniform distribution of the dopant (Tb^{3+}) throughout the host lattice $Gd_2Ti_2O_7$.

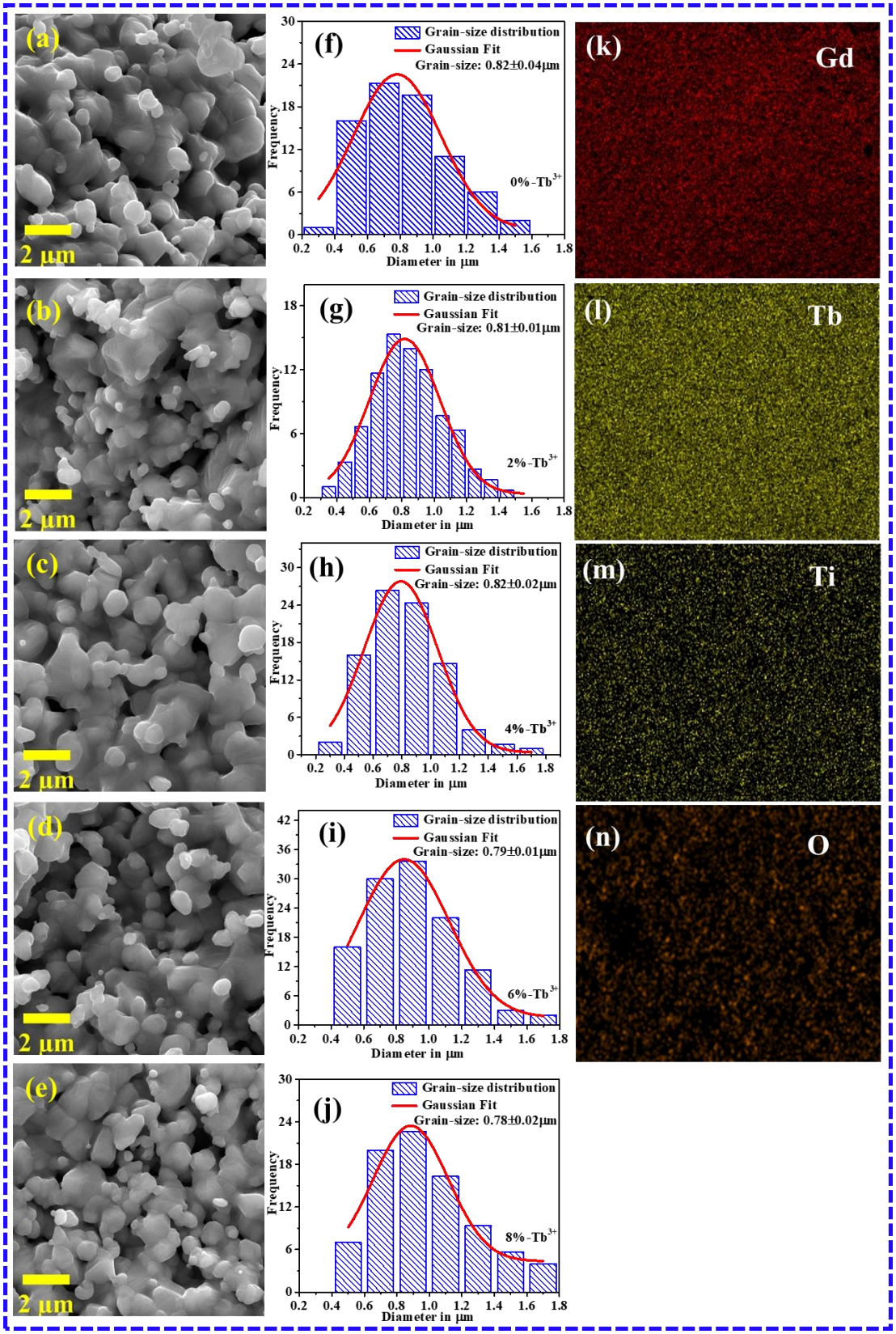

Figure 3.3. *(a-e). FESEM micrographs and (f-j). Corresponding grain size histogram for the samples of* $Gd_{2-x}Tb_xTi_2O_7$ *(x = 0.04, 0.08, 0.12, and 0.16). The elemental mapping is shown in (k-n) for the last composition* $Gd_{1.84}Tb_{0.16}Ti_2O_7$ *(x = 0.16).*

3.3.3. Raman spectroscopic analysis:

For micro-structural analysis of vibrations of Tb^{3+} doped $Gd_2Ti_2O_7$ samples, raman patterns were collected at room temperature in the wavenumber range of 100-1000 cm^{-1} for $Gd_2Ti_2O_7$ host and various concentrations of Tb^{3+} doped $Gd_2Ti_2O_7$ samples. Figure 3.4 (a) shows a series of raman spectra for undoped and doped compositions and Figures (b, c, d, e, and f) show the deconvoluted spectrum into various vibrational active modes of pyrochlore structures. The raman patterns of all the various concentration of Tb^{3+} doped $Gd_2Ti_2O_7$ having the same pattern as that of undoped $Gd_2Ti_2O_7$ pyrochlore host. All the raman patterns shows that Tb^{3+} were completely dissolved in $Gd_2Ti_2O_7$ host without too much structural distortion which is in good agreement with the XRD outcomes. General formula, $A_2B_2O_7$, pyrochlores with Fd-3m space group have generally six raman active modes and seven infrared active modes [127]. The pyrochlore structure with Fd-3m space group have only six raman active modes at the brillion zone center: $\Gamma = A_{1g} + E_g + 4T_{2g}$ [78]. These all modes of vibrations are due to motion of oxygen atom only because cation A and B motion give rise to non active vibrational raman modes. Raman vibrational modes of $Gd_{2-x}Tb_xTi_2O_7$ with varying the value of x = 0.04, 0.08, 0.12, and 0.16 were tabulated in Table 3.3. Five vibrational active modes ($A_{1g} + E_g + 3T_{2g}$) are due to the oxygen vibrations centered at 48f site of 'O', while the sixth vibrational mode T_{2g} is due to the oxygen vibration centered at 8b site of 'O'[128]. The most intense band at frequencies around (209-213) cm^{-1}, (310-312) cm^{-1}, (516-517) cm^{-1}, are due to the F_{2g}, E_g and A_{1g} modes, respectively, and all these three most intense bands as shown in Figure 3.4 have good agreement with the published studies [129]. The remaining three Raman peaks of F_{2g} modes are difficult to identify due to their small intensity. The most intense band around frequency 311 cm^{-1} is due the bending of O-Gd-O mode and results from the contribution of two modes i.e E_g and F_{2g} modes and the peak around 516 cm^{-1} is due to the internal stretching of Gd-O mode of A_{1g} vibrations. Less intense peaks observed at wavenumber nearly 212 cm^{-1}, and 545

cm^{-1} are due to the remaining F_{2g} modes of vibration. A very small intensity peak around wavenumber 450 cm^{-1} is due to the trace amounts of TiO_2 [130]. Peak around wavenumber 685 cm^{-1} are due to the Ti-O stretching and distortion of TiO_6 octahedra [129]. As we observed from the XRD data that the value of cationic radii ratio of cation A and cation B decreases from 1.7045 to 1.7388 and the value of lattice constant also decreases slightly from 10.1508 Å to 10.1451 Å as we increasing the Tb^{3+} on the A-site at the place of Gd in the pyrochlore structure. Therefore, as lattice constant decreases the value of force constant between the various raman bands increases. Force constant increment implies that the value of bond length also decreases and therefore the lattice shrinks. The most intense intensity peaks around 311 cm^{-1} and 516 cm^{-1} slightly shifts towards higher wavenumber side. Therefore, as Tb^{3+} is added to $Gd_2Ti_2O_7$ host lattice at the place of Gd the raman peaks shows blue shift, due to the reason of decreasing bond length Gd-O with increasing terbium concentration in host lattice. The bond length decrement produced by doping terbium at the place of gadolinium can be interpreted by the production of cation anti-site defects. Intensity peaks of raman patterns are directly related to the structural ordering and disordering for pyrochlore host lattice. Thus, Raman spectroscopic analysis of Tb^{3+} doped $Gd_2Ti_2O_7$ samples concludes that the pyrochlore structure is present in all synthesized samples without showing any structural departure on the doping of terbium ion except some peak shifting.

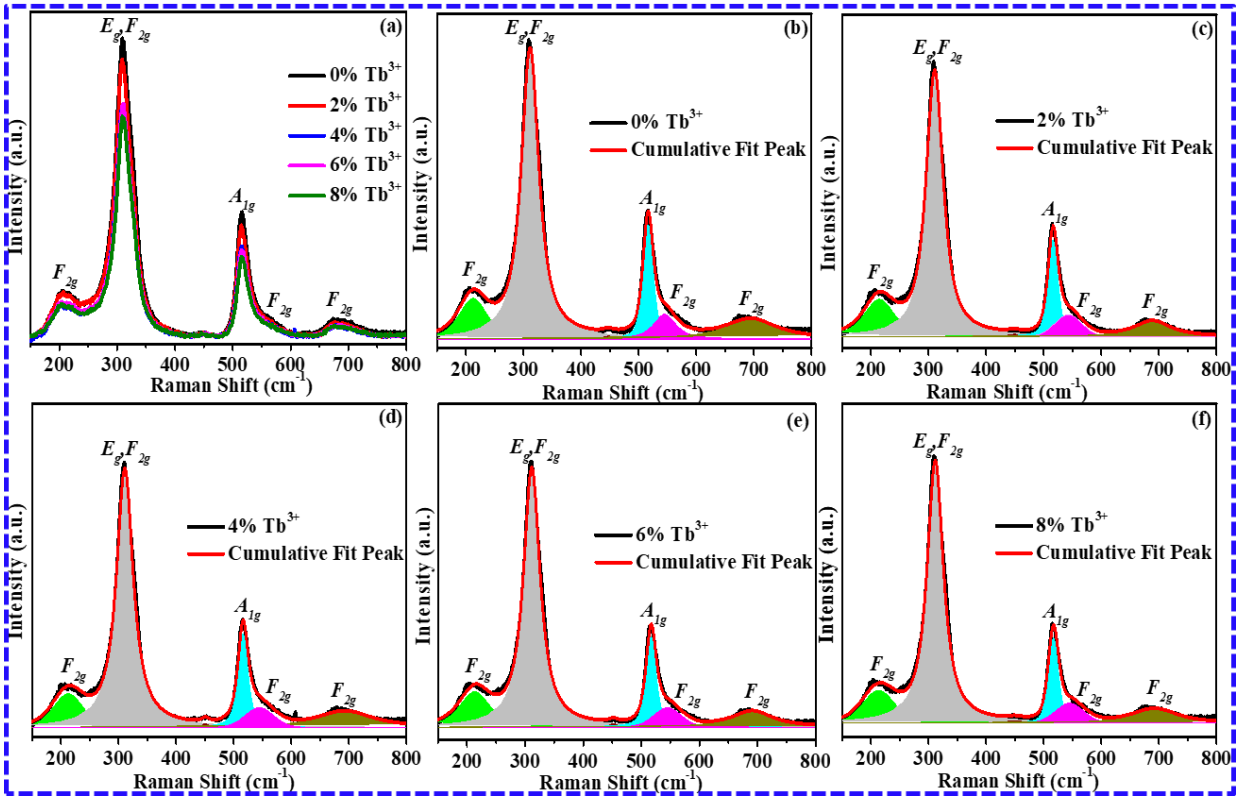

Figure 3.4: *(a). A set of Raman spectra for undoped and Tb^{3+} doped samples of $Gd_2Ti_2O_7$ and (b-f). cumulative peak fitting for all compositions.*

Table 3.3: Peak shifting in raman for Tb^{3+} doped $Gd_2Ti_2O_7$.

Doping	**Tb^{3+} doped $Gd_2Ti_2O_7$ (Peak Shifting $\Delta\omega$ cm^{-1})**					
	1st Peak	**2nd Peak**	**3rd Peak**	**4th Peak**	**5th Peak**	**6th Peak**
0 %	0.0	0.0	0.0	0.0	0.0	0.0
2 %	0.3 B	0.7 B	3.2 R	0.1 R	5.8 R	2.8 B
4 %	1.5 B	1.1 B	1.9 R	0.4 B	4.8 B	3.4 B
6 %	1.9 B	0.4 B	6.2 B	0.5 B	0.5 R	7.8 B
8 %	2.5 B	1.0 B	3.7 B	0.2 B	0.5 R	2.7 B

3.3.4. UV-Visible spectroscopic analysis:

UV-Visible absorption patterns for undoped $Gd_2Ti_2O_7$ host pyrochlore oxide sample were recorded within the wavelength range 200-700 nm and depicted in Figure 3.5 (a). It is the noble technique for the determination of band-gap. It is clearly visible from the UV spectrum that the powder of $Gd_2Ti_2O_7$ shows around 32 % optical absorbance. A sharp high intensity absorption peak for undoped sample ($Gd_2Ti_2O_7$) was observed in the UV region at 362 nm due to intrinsic transitions of host matrix $Gd_2Ti_2O_7$. This optical absorbance is stretched in the UV region around 325-425 nm. The band-gap can be determined by extraploting the linear region of the graph drawn between $(\alpha h\nu)^{1/n}$ vs $h\nu$. The obtained expression is known as Tauc plot can be explained by the following relation [131],

$$(\alpha h\nu)^{1/n} = k\left(h\nu - E_g\right) \dots\dots\dots (3.3)$$

Here 'α' is the absorption coefficient; 'hν' is the photon incident energy, 'n' is nature of the transition, 'E_g' is the band gap energy, and 'K' is the energy independent constant. Value of n = 1/2 for direct allowed transitions and n = 2 for indirect allowed transitions. Pyrochlore oxides have indirect band gap so we select n = 2 and the tauc plot for the undoped sample of $Gd_2Ti_2O_7$ is shown in Figure 3.5 (b).

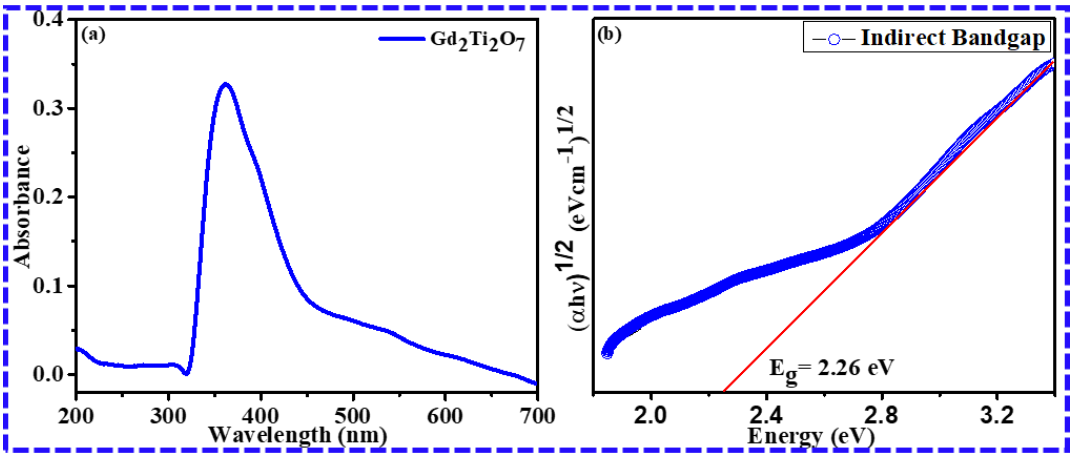

Figure 3.5. *UV-Visible Absorption pattern and tauc-plot for the undoped sample $Gd_2Ti_2O_7$.*

Therefore, using tauc plot, band-gap is calculated by extrapolating linear portion of the $(\alpha h\nu)^{1/2}$ versus hν curve and the extrapolating line hits on the energy axis at the value of 2.26 eV. Hence, the prepared sample of $Gd_2Ti_2O_7$ has band-gap of 2.26 eV.

3.3.5. PL spectroscopic analysis:

Terbium ion is a popular activator which provides intense photoluminescence in the 450-650 nm region for a large number of ceramic compounds. Generally, terbium is stable trivalent ion (Tb^{3+}) state, used as an activator of green emission as it has a sharp high intensity emission peak around 545 nm. Luminescence phenomenon of a material is monitored by using PL results. PL properties were illustrated in Figure 3.6 for host $Gd_2Ti_2O_7$ and in Figure 3.7 for Tb^{3+} doped $Gd_2Ti_2O_7$. An excitation band was recorded by selecting the emission of Tb^{3+} transition ($^5D_4 \rightarrow {}^7F_5$) at a wavelength of 545 nm for the host $Gd_2Ti_2O_7$ (shown in Figure 3.6 a) and various Tb^{3+} doped $Gd_2Ti_2O_7$ compositions (shown in Figure 3.7 a). From the excitation result, a broad band is observed in the wavelength range from 305 nm to 380 nm peaking at ~375 nm that can be attributed to the f → d transitions of 4f shell of Tb^{3+} in the excitation, which is in good agreement with the previous results [63]. An improvement in the excitation intensity peak is observed with the terbium ion doping in the host lattice of $Gd_2Ti_2O_7$. The Gd-O charge transfer band and the general f-d transition lines of the terbium ion at the longer wavelength region have not been observed due to their relatively week intensity compared to strong $Gd_2Ti_2O_7$ host excitation band in undoped samples. Furthermore, emission spectrum of terbium doped and undoped samples of $Gd_2Ti_2O_7$ was recorded at the excitation wavelength of 375 nm. An emission peak around 439 nm is observed in the emission band of the host $Gd_2Ti_2O_7$ due to the presence of Gd^{3+} ion at cationic lattice in pyrochlore oxide.

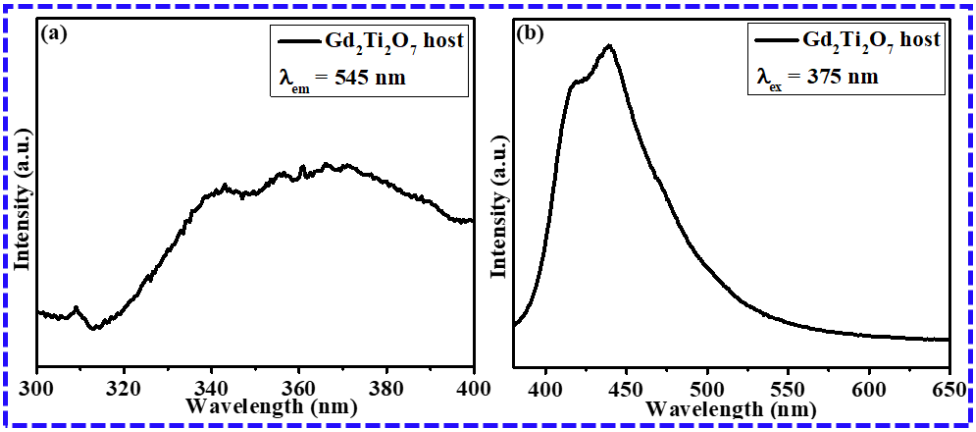

Figure 3.6: *(a) Exciation and (b) Emission patterns for host $Gd_2Ti_2O_7$.*

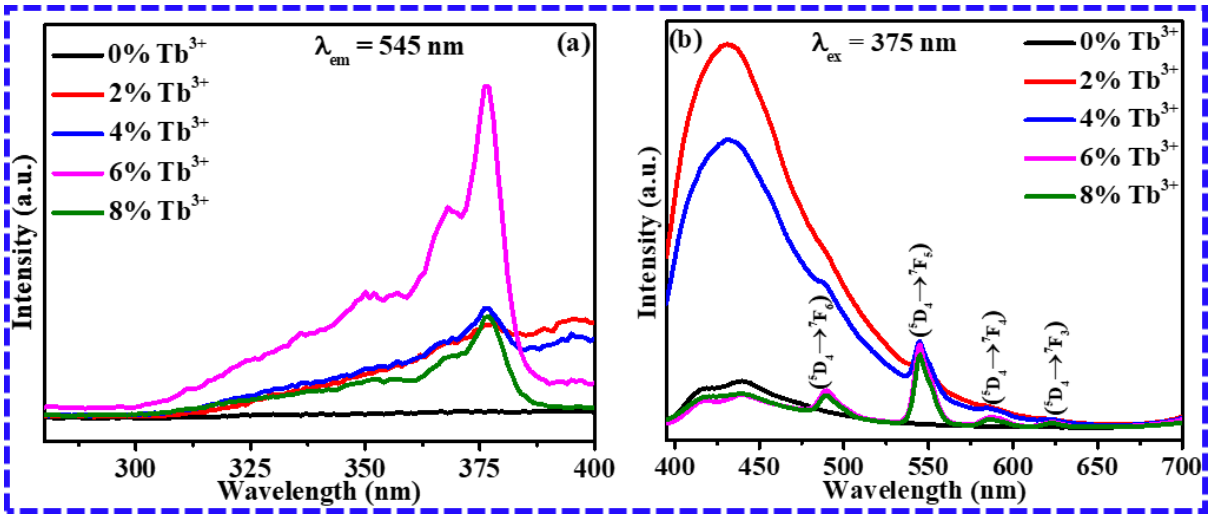

Figure 3.7. *(a) Excitation (λ_{em} = 545 nm) and (b) Emission (λ_{ex} = 345 nm) pattern of $Gd_2Ti_2O_7$ doped Tb^{3+} for various concentrations.*

Emission spectra of Tb^{3+} doped $Gd_2Ti_2O_7$ samples were monitored in the wavelength range 395 nm to 700 nm by using excitation wavelength (λ_{ex}= 375 nm), shown in Figure 3.7 b. It can be noted from the Pl emission bands of Tb^{3+} doped compositions consist of the dominant transitions at 489 nm, 545 nm, 585 nm, and 623 nm.

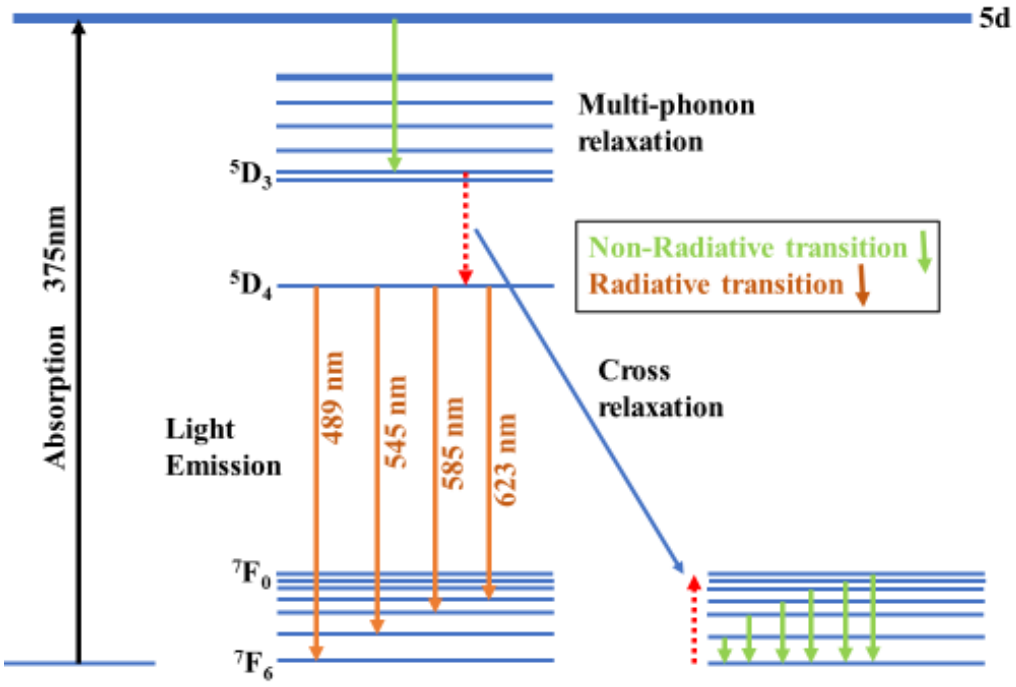

Figure 3.8. *Tb_2O_3 energy level diagram.*

A schematic diagram for optical energy transitions of terbium ion is represented in Figure 3.8. Trivalent ion Gd^{3+} have no tendency to give out luminescence spectrum in visible region. When Tb^{3+} ion doped into the $Gd_2Ti_2O_7$ host lattice and excited to low wavelength, the energy is absorbed by the host lattice and deliver it to Tb^{3+} ions. With increasing Tb^{3+} doping, at the low wavelength firstly intensity peak at 439 nm increases until all the energy being transferred. Excessive doping of Tb^{3+} ions into the host lattice doesn't increase the intensity and the host lattice $Gd_2Ti_2O_7$ reduces the absorbed energy by the process of charge transfer, hence the peak intensity at the low wavelength 439 nm decreases over the maximum saturation limit of 4% Tb^{3+} doping. Further for 6% terbium doping, an electron under excitation of 375 nm goes into the 5d localised band first and returns back to $^5D_3$ energy level non-radiatively [132]. Due to high concentration of Tb^{3+}, $^5D_3$ to $^5D_4$ transition is resonant with the $^7F_6$ to $^7F_{0,1}$ transition. The energy from the $^5D_3 \rightarrow {}^7D_4$ transition may be taken up by a neighbouring ion *via* a cross relaxation process [57]. As the doping concentration of terbium ion at the A-site is further increased, then peaks at 489 nm ($^5D_4 \rightarrow {}^7F_6$), 545 nm ($^5D_4 \rightarrow {}^7F_5$), 585 nm ($^5D_4 \rightarrow {}^7F_4$), and

623 nm ($^5D_4 \rightarrow {}^7F_3$) are appeared due to the transition from $^5D_4 \rightarrow {}^7F_{6,5,4, \text{ and } 3}$ trivalent Tb^{3+} in the $Gd_2Ti_2O_7$ pyrochlore phosphor. The emission line $^5D_4 \rightarrow {}^7F_5$ (high intensity green line), at 545 nm, is dominating over the other emission lines. This is due to the fact that for even higher doping concentration of trivalent terbium ion in the host $Gd_2Ti_2O_7$, there is absence of blue emission since cross relaxation give rise to an enhancement in the population of the $^5D_4$ state at the loss of $^5D_3$ state [132]. The emitting green light intensity increases with doping of Tb^{3+} in $Gd_2Ti_2O_7$ host up to 6%, after that again decreasing with further doping of Tb^{3+} due to the concentration quenching effect [97]. The distance between the terbium ions decreases when the ion concentration increased up to (6% Tb^{3+}) a maximum limit. As the distance between the Tb^{3+} ions decrease, energy transfer between the two Tb^{3+} ions are easy, therefore, due to this non-radiative transition results. Hence the emission intensity is decreased for 8% Tb^{3+} doping in host $Gd_2Ti_2O_7$. It is evident from PL studies that the $Gd_2Ti_2O_7$ pyrochlore oxide can be used as host matrix for Tb-fluorescence with a suitable doping concentration of 6%.

3.4. Conclusion:

Pyrochlore structured $Gd_2Ti_2O_7$ doped Tb^{3+} samples were successfully prepared by solid-state reaction method followed by a multistage heating protocol. XRD and Raman patterns at room temperature were used for the confirmation of crystalline pyrochlore phase present in all the finally heated pellets. XRD traces revealed that samples annealed at temperature 1300°C exhibited all the diffraction peaks pertaining to single-phase $Gd_2Ti_2O_7$ and $Tb_2Ti_2O_7$ with cubic structure of pyrochlore with space group symmetry Fd-3m. The crystallite size changes from 727.7 nm (for $Gd_2Ti_2O_7$) to 616.2 nm (for 8% Tb doping) and the lattice parameter slightly decreases from 10.1508 Å to 10.1451 Å with doping of Tb^{3+} ions at A-site of the host matrix. FESEM micrographs of all the samples consist of agglomerated spherically shaped particles having the diameter of the order of micron. Further, Raman patterns shows that Tb^{3+} were

completely dissolved in $Gd_2Ti_2O_7$ host without too much structural distortion which is in good agreement with the XRD outcomes. Also most intense raman peaks at 311 cm^{-1} and 516 cm^{-1} slightly shifts towards higher wavenumber side (blue shift), due to the decrement of bond length Gd-O with terbium doping in host lattice. The bond length reduction is due to the production of cation anti-site defects. Optical study using UV-spectroscopy provides a value of indirect band-gap for $Gd_2Ti_2O_7$ as 2.26 eV. From PL results, emission band of the host $Gd_2Ti_2O_7$ consists of an intense transition at 439 nm attributed to Gd^{3+} ion. Moreover, the emission band of Tb^{3+} doped samples consist of four transitions 489 nm ($^5D_4 \rightarrow {}^7F_6$), 545 nm ($^5D_4 \rightarrow {}^7F_5$), 585 nm ($^5D_4 \rightarrow {}^7F_4$), and 623 nm ($^5D_4 \rightarrow {}^7F_3$) in the visible region which are related to transitions among the levels in Tb^{3+} dopant. It is concluded from the PL results that green light emission of the Tb^{3+} ion is dominating by $^5D_4 \rightarrow {}^7F_5$ transition in host matrix due to energy transfer from host to Tb^{3+} ions upon excitation at λ_{em} = 545 nm. Thus, the PL studies explore the application of Tb doped $Gd_2Ti_2O_7$ up to a maximum concentration of 6% as green phosphor with the visible emission peaks without undergoing any phase transition or structural distortion.

Chapter 4

Structural and optical studies on Dy^{3+} doped $Gd_2Ti_2O_7$ pyrochlore as white light emission

The solid-state process approach was used to create a range of GTO pyrochlore samples, $Gd_{2-x}Dy_xTi_2O_7$ (where x = 0.5, 1.0, 1.5, 2.0, and 2.5 mol%). The Fd3m space group single-phase nature of all samples was discovered using XRD, Raman spectroscopy, and photoluminescence spectroscopy. Two strong emission bands with centres at 484 nm (blue) and 581 nm (yellow) were observed at an excitation wavelength of 347 nm, which correspond to the $^4F_{9/2} \rightarrow {}^6H_{15/2}$ and $^4F_{9/2} \rightarrow {}^6H_{13/2}$ transitions, respectively. The Y/B ratio is near unity for the optimum Dy^{3+} concentration (2.0 mol%), indicating a mixture of yellow and blue emission bands that combined generate white light. These results show the potential use of Dy^{3+} substituted GTO pyrochlore samples as luminous components in wLED applications.

4.1. Introduction:

Over the past few years, the trivalent rare earth ions doped materials with electronic transition within 4f orbitals were extensively explored due to their potential application in the field of material science, chemistry, physics, and chemical sciences due to their important role in applications like optical fibre [133], planar waveguides [134], compact micro-chip lasers [56], solid state lasers [62], cathode ray tube [135], field emission display [136], white light emitting diodes [137] and florescent tubes [138] *etc.* Researchers has been focused much on the white light emitting diodes (w-LEDs) in the solid-state lighting field despite of fluorescent lamps due to their excellent advantages such as small size, energy saving, high energy efficiency, robustness, longer life times, environmental friendliness, and high brightness [139–142]. The designing of a new high efficiency luminescent device for the production of w-LEDs with improved performance can be achieved by selecting appropriate host and trivalent rare earth ions. There are two methods to obtain white light from solid state lighting device [143] (SSLD) *via* **(i)** RGB-LEDs (free from phosphor) method in which devices providing red, green and blue colours are efficiently mixed together to illuminate white light, **(ii)** phosphor integrated SSLD uses an ultra violet (UV)/ near ultra-violet (NUV) light. The limitation of first method is the adjustment of power supply for each LED in accordance to balance the efficient mixing and emission intensity of individual colour. While the serious problem with second method of phosphor integrated SSLD is colour dependence, blue-yellow colour separation poor colour rendering index (the illuminated objects colour do not have their true colour) *etc.* [144].

Also, the UV/NUV LEDs with multiple colours emitting phosphors is an alternative way to form white light emission with good colour rendering index due to ease of colour mixing and control but this method also has serious drawback such as low luminescence efficiency due to blending of red, green and blue emitting phosphors [145]. Hence for the fabrication of wLEDs using UV/NUV LEDs, single phase phosphor is necessary to avoid above problem. Various

approaches are used to make white light emission from single host lattice by **(a)** doping single rare earth ion, **(b)** doping of more than one rare earth ions, **(c)** co-doping of various ions and controlling emission *via* energy transfer process, and **(d)** controlling the defect formation through ion concentration.

Ternary pyrochlore oxides are considered to be suitable host for better luminescent active ions because of its high melting point, and very good solubility of rare earth ions despite of their chemical and physical properties [146]. Pyrochlore oxide structures with general formula $A_2B_2O_7$ have several potential applications such as ionic/electric conductors [147], catalysts [148], radioactive waste management [149], and have proven to be suitable host material for the enhancement of luminescence properties [150] of florescent centers in various domains of scientific technology and instrumentation due to their excellent optical, magnetic, electrical, and dielectric properties [151].

Cubic Pyrochlore oxides $A_2B_2O_7$ (eight molecules per unit cell), are a derivative of fluorite structure having Fd3m space group with two types of cations at A-site and B- site. The cations at A-site are large sized rare earth ions having 3+ covalency and B-site contains smaller sized cations like titanium, zirconium *etc.* with 4+ covalency. A-site cations are 8-fold coordinated to oxygen anion and located within distorted cubic coordination polyhedron (contains 6 equally spaced anion oxygens at a slightly shorter distance from central cation) and the B-site cations are 6-fold coordinated which is located within distorted octahedron (contains all the six anions at equal distances from the central cations) due to the removal of oxygen atoms. Two types of oxygen sites were illustrated by Wyckoff positions 48f and 8b for pyrochlore structures. In the Wyckoff notation 48f, oxygen has (x, 0.5, 0.5) position coordinated to two rare earth cations A^{3+} and two B^{4+} cations. For the another 8b Wyckoff notation, oxygen is located at (0.375, 0.375, 0.375) in a tetrahedron coordinated to only rare earth A^{3+} cations [119]. Pyrochlore structures has one positional parameter ‘x’ and its value ranges within 0.309 - 0.355 and lattice

parameter of nearly ~10 Å. The phase stability of pyrochlore structures were explained on the behalf of relative cationic radii ratio of cation A and B, *i.e.*, r_A/r_B. For the stable pyrochlore oxide structures the value if cation radii ratio lies within 1.460 to 1.80 [48].

The addition of trivalent rare earth ions to these hosts can improve the chemical durability and luminescence intensity. In various type of host, pyrochlore ternary oxide $Gd_2Ti_2O_7$ (GTO) paved the significant role and improvement over the other oxides, phosphate and fluoride glass systems [152]. GTO have a very intact pyrochlore structure. The larger cationic radii ratio 1.75 will provide a larger flexibility of accommodating of different trivalent lanthanide ions without undergoing into phase transformation or phase segregation [115]**.** Apart from structural and chemical flexibility, GTO have a suitable localized environment for strong luminescent, optical, magnetic, and electrical properties [116,118]**.** By varying the Dy^{3+} rare earth ion concentration in the host a strong variation of the yellow/blue intensity ratio can be attained [153]. The present work focuses on the investigation of structural and luminescent properties of trivalent rare earth ion Dy^{3+} doped GTO pyrochlore host with different concentration of Dy^{3+} substitution. The cationic radii ratio r_{Gd}/r_{Ti} and r_{Dy}/r_{Ti} are obtained as 1.7405 and 1.6975, respectively which means the maximum concentration of Dy^{3+} (for 2.5%) at the place of gadolinium cation (A-site) does not affect the basic pyrochlore structure. Moreover, the luminescent results of this host for various Dy^{3+} concentration were recorded and related to the structural properties. The rare earth ions were used to generate different colours like Eu^{3+} (at 616 nm having $^5D_0$-$^7F_2$ transition producing red colour [154]), Tb^{3+} (high intensity PL emission at 545nm is due to $^5D_4$-$^7F_5$ producing green light [150]), Er^{3+} (the emission peaks are green at 545 nm due to $^4S_{3/2}$-$^4I_{15/2}$ optical transitions and red at 647nm due to $^4F_{9/2}$-$^4I_{15/2}$ transition [155]), Sm^{3+} (the most intense emission peak at 606 nm is due to $^4G_{5/2} \rightarrow {}^6H_{7/2}$ transition of samarium ion producing orange light [87]) *etc*. but Dy^{3+} ion generate two different colours; blue (486 nm, $^4F_{9/2}$-$^6H_{15/2}$) and yellow (576 nm, $^4F_{9/2}$-$^6H_{13/2}$) [156]. The intensity of

$^4F_{9/2}$-$^6H_{13/2}$ is hypersensitive to the host matrix while the transition $^4F_{9/2}$-$^6H_{15/2}$ is insensitive to its local environment. Thus, Dy^{3+} ion is the most suitable dopant to establish a relation between local environment and emitted Y/B colours ratio and therefore, the substitution of Dy^{3+} at the place of Gd^{3+} in the host have a lot of importance over other rare earth ions for the generation of white light [157]. Hence, Dy^{3+} is selected as the suitable dopant for the particular host. In the present manuscript, a series of Dy^{3+} substituted GTO single phasic pyrochlore oxide samples have been successfully prepared through solid state reaction method to explore its use as potential phosphor for white LEDs by studying structural and luminescence properties in details using XRD, SEM, Raman spectroscopy, and PL spectroscopy provided CIE chromaticity coordinates. In the present work, the optical studies coupled with structural analysis conclude that the optimum concentration of Dy^{3+} substituted GTO series is found to be 2.0 mol% which is having an intact pyrochlore structure and CIE coordinate set for this pyrochlore composition lies in the standard cool white light calorimetric point.

4.2. Experimental details:

4.2.1. Synthesis:

Polycrystalline pyrochlore oxide series of Dy^{3+} substituted GTO with various doping concentration of Dy^{3+} substitution (where x = 0.5, 1.0, 1.5, 2.0, and 2.5 mol%), have been synthesized by using conventional solid state reaction technique. In this method initially AR grade raw precursors namely, Gadolinium (III) oxide (Gd_2O_3) (≥99.99% purity, Sigma Aldrich), Dysprosium (III) oxide (Dy_2O_3) (≥99.99% purity, Sigma Aldrich), and Titanium (IV) oxide (TiO_2) (≥99.99% purity, Sigma Aldrich), were taken into stoichiometric ratios and then thoroughly mixed and grounded multiple times using agate mortar pestle [158], and a systematic step wise flowchart for the preparation of Dy^{3+} substituted GTO series is shown in Figure 4.1.

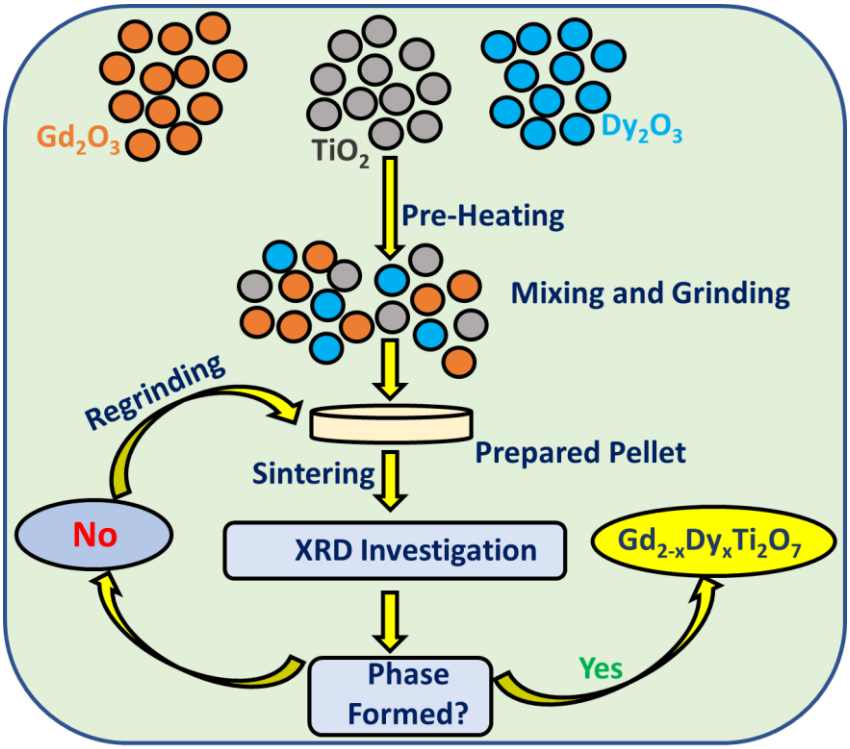

Figure 4.1. *Synthesis process for pure and Dy^{3+} substituted GTO samples.*

Rare-earth ion-based oxides get easily oxidized due to their higher reactivity towards CO_2 and water in the exposure of atmospheric environment. Hence, to avoid excess moisture and volatile impurities, all the AR grade powders were placed in alumina crucibles and essentially pre-heated in a programmable muffle furnace at a temperature of 800 ℃ for the time duration of 5 hours. After pre-heating step, stoichiometric ratios of all the AR grade pure reagents Gd_2O_3, Dy_2O_3, and TiO_2 were accurately measured using weighing machine (Shimadzu, Model Number: D307030200) to prepare a batch of 3-gram sample for each composition and is reported in Table 4.1.

Table 4.1. Weight of raw powders of Gd_2O_3, Dy_2O_3, and TiO_2 used for the synthesis of 3-gram batch of $Gd_{2-x}Dy_xTi_2O_7$ series.

Dy^{3+} (%)	**$Gd_{2-x}Dy_xTi_2O_7$**	**Gd_2O_3 (gram)**	**TiO_2 (gram)**	**Dy_2O_3 (gram)**
0	$Gd_2Ti_2O_7$	2.0824	0.9176	0
0.5 %	$Gd_{1.99}Dy_{0.01}Ti_2O_7$	2.0718	0.9175	0.0107
1.0 %	$Gd_{1.98}Dy_{0.02}Ti_2O_7$	2.0612	0.9174	0.0214
1.5 %	$Gd_{1.97}Dy_{0.03}Ti_2O_7$	2.0506	0.9173	0.0321
2.0 %	$Gd_{1.96}Dy_{0.04}Ti_2O_7$	2.0399	0.9172	0.0428
2.5 %	$Gd_{1.95}Dy_{0.05}Ti_2O_7$	2.0293	0.9171	0.0535

After weighing stoichiometric amounts of all the precursors, all were mixed and grounded properly for 9 hours using agate mortar pestle with ethanol as dispersed medium to form uniform and homogeneous final powdered product. The finely grounded products were transformed into the pellets of 10 mm diameter and 2 mm thickness, using hydraulic machine by exerting a pressure of 4 tons using a stainless-steel die-set of 10 mm diameter. Now all these pellets were kept in alumina crucible and then heated in a programmable muffle furnace at three temperatures of 1200 ℃, 1250 ℃ and 1300 ℃ for 24 hours, 36 hours, and 48 hours, respectively with a heating rate of 5 ℃/min and cooling rate of 2 ℃/min, and these steps were represented well by Figure 4.1. Series of final product of $Gd_{2-x}Dy_xTi_2O_7$ (x = 0, 0.01, 0.02, 0.03, 0.04, and 0.05) were formed through multi-step solid state method from the initial raw powders Gd_2O_3, Dy_2O_3, and TiO_2 following the reaction (4.1);

$$(1 - 0.5 * x).Gd_2O_3 + (0.5 * x).Dy_2O_3 + TiO_2 \xrightarrow{1200\,℃\,(24\,hours),\ 1250\,℃\,(36\,hours),\ 1300\,℃\,(48\,hours)} Gd_{2-x}Dy_xTi_2O_7$$

$$(x = 0, 0.01, 0.02, 0.03, 0.04, and\ 0.05) \ldots\ldots\ldots (4.1)$$

4.2.2. Characterization tools:

Structural investigation for the complete series of Dy^{3+} substituted GTO was evaluated *via* X-ray diffraction (XRD). Crystalline phases were investigated by plotting the XRD data within range $10° \leq 2\theta \leq 80°$ (step-size of 0.02°, and scanning rate 0.5°/min) using a CuK_{α} source of wavelength $\lambda = 1.54056$ Å in a D8-Advance Brucker XRD machine at Delhi Technological University (DTU), New Delhi. Raman spectroscopy for all the samples were recorded using a Nd: YAG laser source of wavelength 532 nm using WiTec alpha 300 RA system with a 50× objective lens at Jawaharlal Nehru University (JNU), Delhi. For the complete series, photoluminescence (PL) excitation and emission were examined through a Jasco-8300 fluorescence spectrometer coupled with Xenon lamp, at DTU, New Delhi. The measurements were performed at room temperature.

4.3. Results and discussion:

4.3.1. X-ray Diffraction:

Room temperature XRD for the as synthesized series of Dy^{3+} substituted GTO with various concentration of Dy^{3+}, has been performed through XRD and were well described by Figure 4.2 (a). All the compositions having the same XRD patterns and were marked by miller indices. Pyrochlores oxides have cubic crystal structure with cell parameter nearly ~10 Å lattice parameter (a = b = c), and belongs to Fd-3m space group. Pyrochlore structure have two types of intensities; The high intensity XRD peaks with even miller indices (222), (400), (440), (622), (444), and (800) at the 2θ value ~ 30.42°, 35.31°, 50.75°, 60.35°, 63.43°, and 74.75 respectively, were represents basic fluorite structure on the other hand low intensity XRD peaks with odd miller indices (111), (311), (331), (511), and (531) at the 2θ value ~ 15.18°, 29.15°, 38.67°, 46.38°, and 53.32° respectively, represents the highly ordered pyrochlore superstructure (marked by a club (♣) in Figure 4.2 (a)). The XRD patterns for all the

compositions have single phase pyrochlore structure without any impurity peak which confirms the complete dissolution of Dy^{3+} ions into the GTO host and also substitution of Dy^{3+} at the Gd^{3+} doesn't affect the crystal structure and the stability of each composition was confirmed by the following r_A/r_B cationic radii ratio (4.2);

$$\left[\frac{r_{Gd,Dy}}{r_{Ti}}\right] = \left[\frac{r_{Gd} \times atomic\ \% + r_{Dy} \times atomic\ \%}{r_{Ti}}\right] \ldots\ldots\ldots (4.2)$$

Here, value of cationic radii for Gd (1.053) is larger as compared to the cationic radii of Dy ion (1.027), therefore the ratio of r_A/r_B goes on decreasing from 1.7405 (0 % Dy^{3+}) to 1.7396 (2.5 % Dy^{3+}) for maximum substitution. As the value of Dy ion is smaller as compared to gadolinium ion therefore there is nearly negligibly small shift of XRD peaks towards the lower angle 2θ side with increasing concentration of dysprosium ion.

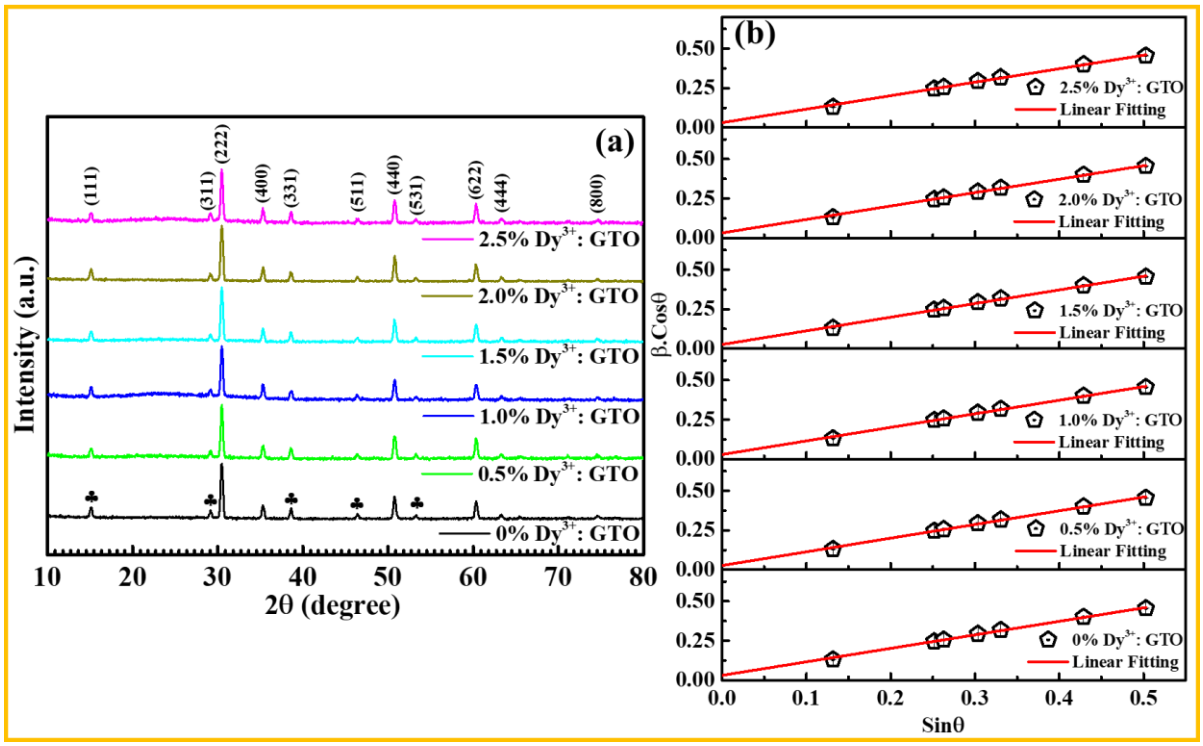

Figure 4.2. *(a) XRD patterns for pure and Dy^{3+} substituted GTO, and* ***(b)*** *WH-Plot for all the compositions.*

The strain and crystallite for all the compositions of Dy^{3+} substituted GTO were calculated by using Williamson-hall plot (WH-P) formalism as given below *via* equation (4.3);

$$\beta_{h,k,l} \cos\theta = \left(\frac{K \times \lambda}{D}\right) + 4\varepsilon \sin\theta \ldots\ldots\ldots (4.3)$$

The value of factor K (structure factor) is 0.94 for the cubic crystal structures and 'D' is the average crystallite size. The parameter '$\beta_{h,k,l}$' represents the full width of diffraction half maxima (FWHM) of first seven dominating high intensity XRD peaks and '2θ' is the diffraction angle corresponding to xrd diffraction peaks. Here 'λ' (1.5406 Å) is the wavelength of CuK_{α} source and parameter 'ε' is the lattice micro-strain related to the pyrochlore ternary oxide samples. To find the values of parameters 'D' and 'ε' for the complete Dy^{3+} substituted GTO series, a graph (straight-line) is plotted between $\beta_{h,k,l}$ cos θ (along y-axis) and sin θ (along x-axis), as shown by WH-P in Figure 4.1 (b) [159], and results were given in Table 4.2. As on increasing Dy^{3+} concentration, the cationic radii ratio (r_A/r_B) is changed only by less than 0.1 %. It is very clear that this small amount of Dy^{3+} substitution is not going to affect the phase forming sintering temperature and therefore, the structural properties depict insignificant changes as reported in Table 4.2. The calculated crystallite size as well as lattice strain does not significantly vary as a function of Dy^{3+} concentration.

Table 4.2. Structural parameters measured for undoped and Dy^{3+} substituted GTO for all compositions *via* XRD results.

Dy^{3+} (%)	**$Gd_{2-x}Dy_xTi_2O_7$**	**r_A/r_B**	**Crystallite Size (D) in Å**	**Strain**
0%	$Gd_2Ti_2O_7$	1.7405	46.744 ± 0.007	0.214±0.004
0.5 %	$Gd_{1.99}Dy_{0.01}Ti_2O_7$	1.7403	53.654 ± 0.008	0.217±0.005
1.0 %	$Gd_{1.98}Dy_{0.02}Ti_2O_7$	1.7401	49.764 ± 0.008	0.215±0.005
1.5 %	$Gd_{1.97}Dy_{0.03}Ti_2O_7$	1.7399	59.590 ± 0.008	0.216±0.005
2.0 %	$Gd_{1.96}Dy_{0.04}Ti_2O_7$	1.7397	44.448 ± 0.007	0.213±0.004
2.5 %	$Gd_{1.95}Dy_{0.05}Ti_2O_7$	1.7395	46.44 ± 0.008	0.214±0.004

For more structural investigations all the compositions were further refined by Rietveld refinement with FullProf Suite software. Linear interpolation between a set background point with refinable heights, was used to refine background with number of ten cycles, and for fitting experimental data pseudo-Voigt function was used for each composition. During refinement instrumental parameter, lattice constant, shape parameter, scale factors, occupancies, and oxygen 48f positions parameters were also fixed for every refinement and the occupancies of Gd and Ti ions didn't change much in the refinement step. The degree of disorder parameter 'x' of 48f oxygen anion and lattice parameter were calculated for complete series of Dy^{3+} substituted GTO. Rietveld refinement plot for all the compositions with increasing content of Dy^{3+} ions at the place of Gd^{3+} were depicted by Figure 4.3 and lattice parameter, Braggs factor (R_B), volume (V), weight factors R_{wp} and $R_{exp,}$ and goodness of fitting (χ^2), were tabulated in Table 4.3. In refined plot for each composition, black circle represents experimental intensity data, red line represents the refined intensity/observed intensity, blue line represents the

difference experimentally observed and calculated intensities, and the green perpendicular line symbol represents Bragg's peak positions. For all the refined compositions, the value of goodness lying within 1.0 to 2.0 value, that represents best fitting. On increasing the Dy^{3+} cation at A-site in GTO, the value of lattice parameter doesn't show any change up to two decimal places which is the accuracy of XRD detector with 0.02 step size. These results show that the substitution of smaller sized cation at the A-site with very small amount is not going to made any significant change in unit cell of GTO even for 2.5 % doped composition. Since x-parameter of 48f oxygen atoms approaches to 0.3125, the composition will acquire a perfect pyrochlore structure. Therefore, the decreasing value of O48f from 0.3269 to 0.3242 as on increasing Dy^{3+} content shows that the crystalline unit cell is trying to acquire a more ordered pyrochlore structured cell [28].

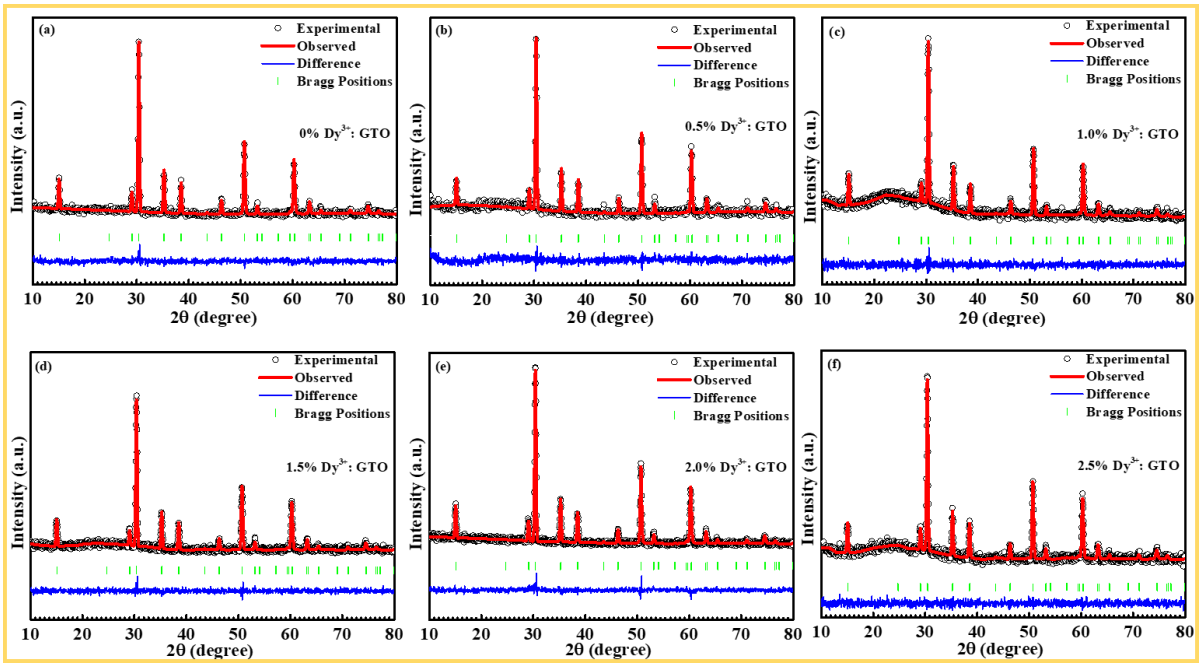

Figure 4.3. *Rietveld refinement plot for pure and Dy^{3+} substituted GTO for all compositions.*

Table 4.3. Rietveld refinement structural parameters for the diffraction patterns of Dy^{3+} substituted GTO for complete series.

Dy^{3+} (%)	**Composition ($Gd_{2-x}Dy_xTi_2O_7$)**	**Lattice Parameter (Å)**	**48f oxygen 'x' parameter**	**R_P**	**R_{wp}**	**R_{exp}**	**χ^2**	**V (Å^3)**
0 %	$Gd_2Ti_2O_7$	10.18	0.3269	43.7	26.0	24.0	1.176	1055
0.5 %	$Gd_{0.99}Dy_{0.01}Ti_2O_7$	10.18	0.3268	62.9	33.3	29.7	1.255	1055
1.0 %	$Gd_{0.98}Dy_{0.02}Ti_2O_7$	10.18	0.3240	59.5	31.4	31.2	1.016	1055
1.5 %	$Gd_{0.97}Dy_{0.03}Ti_2O_7$	10.18	0.3259	48.1	26.8	26.0	1.062	1055
2.0 %	$Gd_{0.96}Dy_{0.04}Ti_2O_7$	10.18	0.3311	37.7	22.9	20.7	1.223	1055
2.5 %	$Gd_{0.95}Dy_{0.05}Ti_2O_7$	10.18	0.3242	56.1	30.7	31.0	1.026	1055

4.3.2. *micro*-Raman spectroscopic analysis:

The Raman vibrational bands for the Dy^{3+} substituted GTO for all the compositions have been found in the frequency range 150-800 cm^{-1}, and were well represented in Figure 4.4. Detailed group study of pyrochlore structure $A_2B_2O_7$ suggesting the presence of six vibrational Raman active modes; one A_{1g}, one E_g and four T_{2g} and in all these six vibrational modes only oxygen atom position is displaced [160]. Figure 4.4 (a-f) represents the deconvoluted Raman spectra of $Gd_{2-x}Dy_xTi_2O_7$ powders at increasing concentration of Dy^{3+} with x=0.01, 0.02, 0.03, 0.04, and 0.05 containing various vibrational modes.

$$\Gamma = A_{1g} + E_g + 4T_{2g}$$

In the pure GTO sample and Dy^{3+} substituted GTO with various concentrations of Dy^{3+}, all the vibrational bands are in good agreement with the previous results. It was observed that Dy^{3+}

ions get completely dissolved in the host GTO without creating structural distortion. Out of all the six active Raman bands, the A_{1g} and E_g vibrational modes are originating due to parallel polarization spectra, on the other hand T_{2g} vibrational bands are formed due to perpendicular polarization [160]. Among these 4 T_{2g} vibrational modes, only one T_{2g} mode is due to O_{8b} oxygen atom while the other three T_{2g} modes are due to O_{48f} oxygen atom vibrations [127]. Raman spectra have five intense Raman bands (~210 cm^{-1}, ~312 cm^{-1}, ~517 cm^{-1}, ~548 cm^{-1}, and ~680 cm^{-1}). Most intense Raman band consists of two vibrational modes E_g and T_{2g} (with very close wave number) and formed due to the O-Gd-O bending mode, centered around ~312 cm^{-1} [127]. Other remaining three T_{2g} vibrational bands were found to be centered around ~210 cm^{-1}, ~548 cm^{-1}, and ~680 cm^{-1} respectively. The peak centered at ~517 cm^{-1} corresponds to the A_{1g} mode, originating due to relative vibrations of internal Gd-O stretching mode. With the introduction of Dy^{3+} ions, it was found that a very less intense band around ~447 cm^{-1} appeared due to the TiO_2 trace amount [150]. The cationic radii ratio r_A/r_B decreases with the Dy^{3+} ion substitution in GTO host from 1.7405 to 1.7396 and the introduction of smaller cation would reduce the size of GTO unit cell or in other words, substitution of Dy ion made an enhancement in force constant within the bands. Therefore, due to increasing force constant or decreasing bond length, all the bands shifted slightly towards higher wavenumber side *i.e.,* blue shifting but the shifting is within error and the Raman results. Although these small substitution concentrations are not induced significant structural changes as they have not been observed through XRD. The observed Raman vibrational bands and their corresponding wave numbers for the Dy^{3+} substituted GTO pyrochlore series were well depicted in Table 4.4 with increment of Dy^{3+} ions.

Table 4.4. Observed Raman Vibrational bands and their respective peak position.

Sample	Peak Positions					
	1st Peak	**2nd Peak**	**3rd Peak**	**4th Peak**	**5th Peak**	**6th peak**
0% Dy^{3+}	207.97±0.7	312.19±0.1	448.92±0.5	517.47±0.2	548.47±2.9	681.03±1.8
0.5% Dy^{3+}	208.37±0.8	312.26±0.1	449.32±0.9	517.51±0.2	548.45±3.3	680.87±1.8
1.0% Dy^{3+}	209.62±0.8	312.33±0.1	450.19±4.7	517.38±0.2	550.24±3.5	679.51±1.8
1.5% Dy^{3+}	210.21±0.7	313.51±0.1	448.57±2.3	518.47±0.2	548.79±2.6	682.46±1.7
2.0% Dy^{3+}	210.15±0.6	313.67±0.1	448.32±3.1	518.80±0.2	551.10±3.0	681.78±1.9
2.5% Dy^{3+}	210.51±0.9	313.21±0.1	446.94±4.2	518.17±0.2	549.25±3.0	679.40±2.1

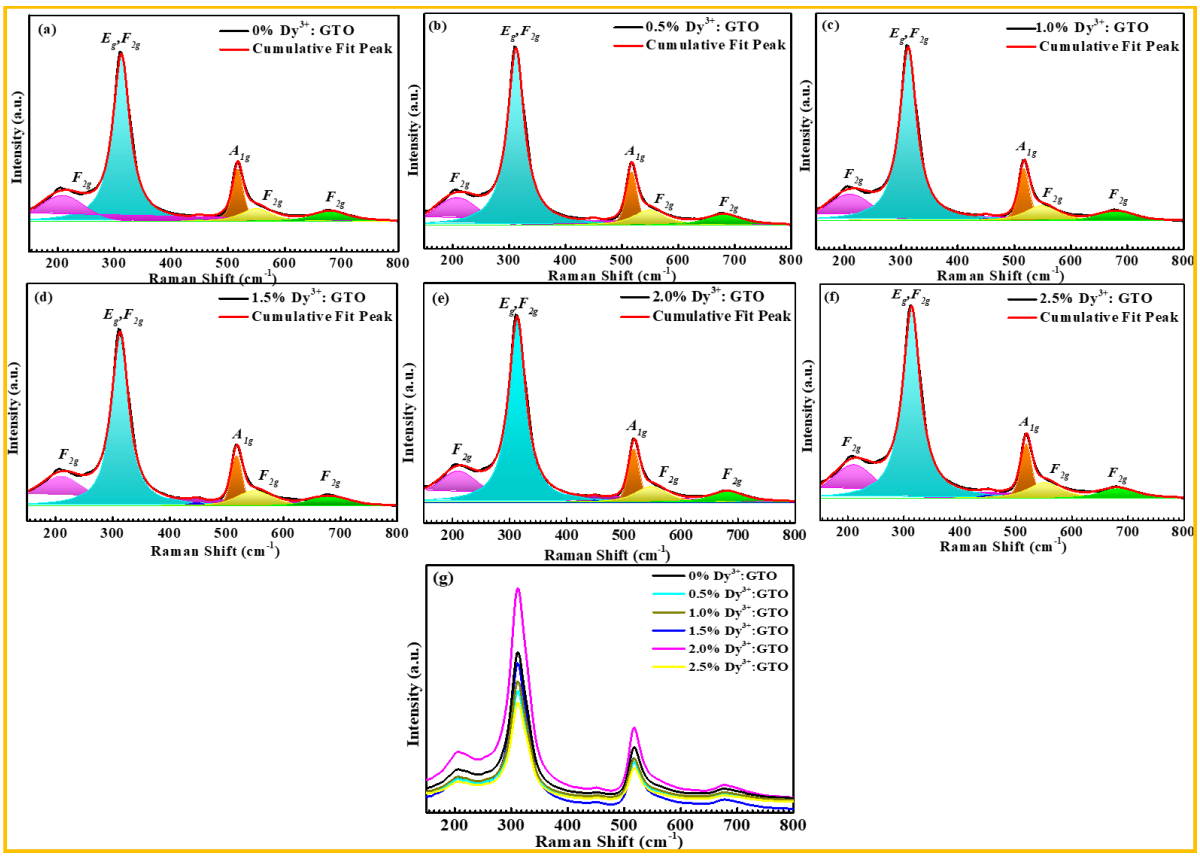

Figure 4.4 *(a-f). Deconvoluted Raman spectra for pure GTO and Dy^{3+} substituted GTO series and (g) Comparative Raman Spectra for complete series of samples.*

4.3.3. Photoluminescence (PL) spectroscopy:

In consequence of Dy^{3+} substitution through PL analysis, the PL excitation (EX) spectra and the PL emission (EM) spectra of trivalent ion Dy^{3+} substituted GTO with various concentrations (0.5%, 1.0%, 1.5%, 2.0%, and 2.5%) are well depicted by Figure 4.5 & 4.6. Figure 4.5 represents the photoluminescence EX-spectra in the spectral range from 280 to 400 nm for the complete series of Dy^{3+} substituted GTO along with pure GTO pyrochlore oxide by selecting emission wavelength of 484 nm. The EX-spectra contain six sharp bands centered around 322 nm, 347 nm, 352 nm, 361 nm, 380 nm, and 389 nm due to the intra band 4f to 4f transition from ground state $^6H_{15/2}$ to various excited states $^6P_{3/2}$ + $^4M_{17/2}$, $^6P_{7/2}$, $^6P_{5/2}$ + $^4I_{11/2}$, $^4I_{13/2}$ + $^4F_{7/2}$, $^4G_{11/2}$, and $^4I_{15/2}$ respectively [15,29–31].

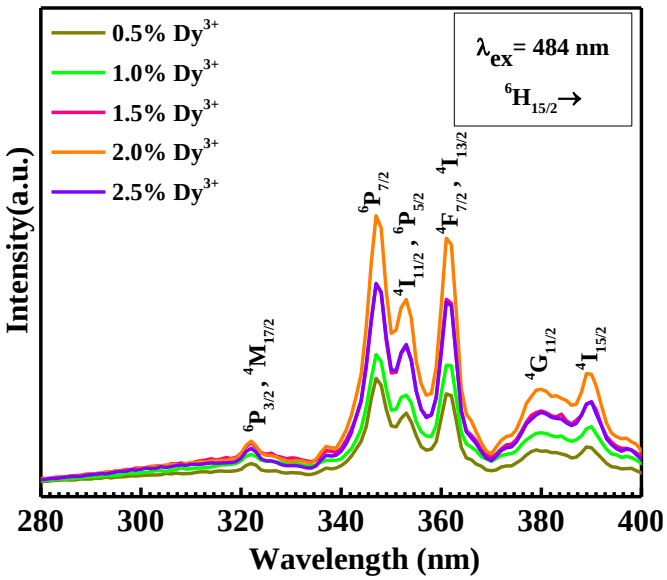

Figure 4.5. *EX-spectra of Dy^{3+} substituted GTO at the place of Gd^{3+}.*

The strongest excitation band $^6P_{7/2}$ is centered around ~347 nm and the second strongest excitation band $^4I_{13/2}$ + $^4F_{7/2}$ is appeared at ~360 nm. Hence, to plot PL emission results, 347 nm wavelength has been selected as excitation wavelength among all the excitation peaks. Figure 4.6 represents the EM-spectra plotted in the spectral region 370 nm to 650 nm for the complete series of Dy^{3+} substituted GTO pyrochlore oxide with various concentration of Dy^{3+}

cations (0%, 0.5%, 1.0%, 1.5%, 2.0%, and 2.5%) by fixing excitation wavelength of 347 nm. The EM-spectra for pure sample (GTO: represented by black line) has emission band around ~ 428 nm due to the Gd^{3+} ions present in the pure host GTO [150]. The complete EM-spectra contains three bands and among these bands two strong intensity bands centered around 484 nm and 581 nm, which can be assigned due to the $^4F_{9/2} \rightarrow {}^6H_{15/2}$ and $^4F_{9/2} \rightarrow {}^6H_{13/2}$ transitions, respectively and the less intense band appeared at the wavelength of 456 nm arising due to the $^4I_{13/2} \rightarrow {}^6H_{13/2}$ transition of Dy^{3+} ions. The emission peaks at 484 nm and 581 nm indicate that the Dy^{3+} cation could behave as luminescent centers and the holes and electrons generated by the host GTO recombined at the localized Dy^{3+} centers which transfers the excitation energy to the Dy^{3+} cations [164]. From many studies it was noticed that the transition peak centered around 581 nm (yellow) wavelength is frequently significant due to localized position of Dy^{3+} ion with low-symmetry without inversion center while the blue emission (484 nm) shows more strength than the yellow one when it occupied the high symmetry local site with an inversion center [146].

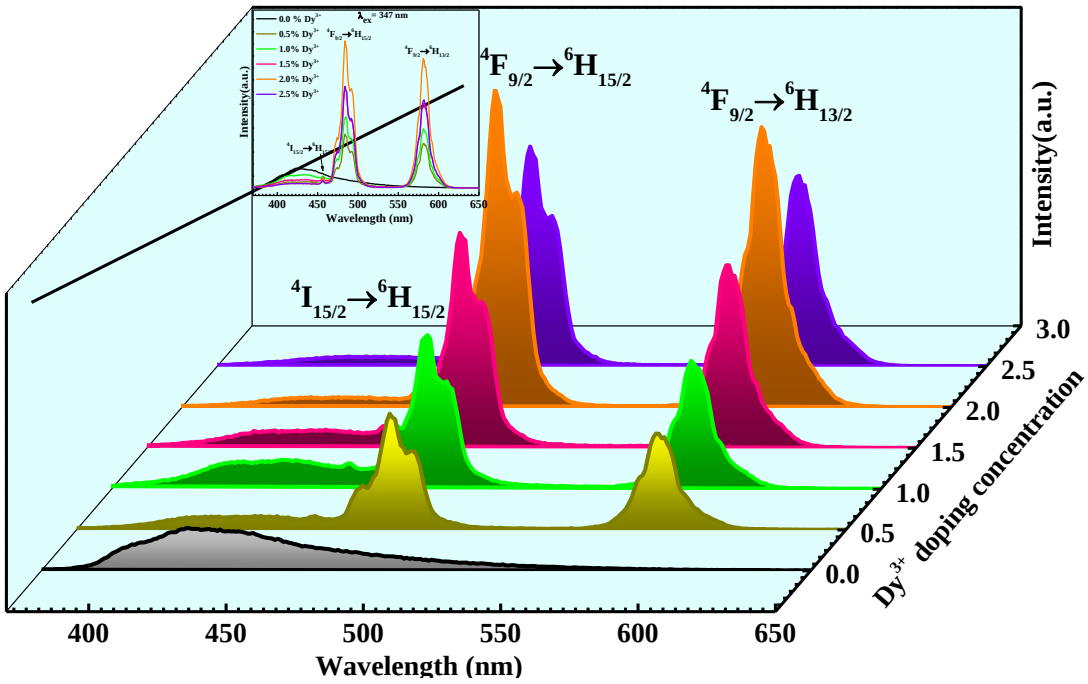

Figure 4.6. *EM-spectra of Dy^{3+} substituted GTO at λ_{ex} = 347 nm.*

The peak at 484 nm with $^4F_{9/2} \rightarrow {}^6H_{15/2}$ transition corresponds to magnetic dipole and its emission intensity is independent of crystal field of GTO and on the other side the transition peak $^4F_{9/2} \rightarrow {}^6H_{13/2}$ at 581 nm (yellow) belongs to a forced electric dipole transition [145]. When active Dy^{3+} located at local site with low symmetry without the inversion centre in host GTO, the emission band at 484 nm *i.e.,* blue is more prominent in the complete emission spectra as compared to the other transition peak at 581 nm (yellow) [165,166]. In the host GTO pyrochlore oxide, two types of cations Gd^{3+} and Ti^{4+} are present. The Dy^{3+} ions are supposed to occupy Gd^{3+} sites due to having same valance state. This can be explained as the size of Dy^{3+} (1.027) ions are smaller than the Gd^{3+} (1.053) ions therefore the Dy^{3+} ions can easily occupy the Gd^{3+} sites in GTO with low symmetry and it is in good acceptance with the results found by XRD analysis. From Figure 4.6 it is clearly noticeable that the emission intensity first increases with an increment of Dy^{3+} cations in GTO at the place of Gd^{3+} site, up to to a maximum content of 2.0% mole of Dy^{3+} ions, but beyond 2.0% of Dy^{3+} in GTO, the emission intensity gradually decreases (for 2.5% of Dy^{3+}) due to the well-known concentration quenching effect (caused by non-radiative energy transfer). This is due to the reason that as the amount of Dy^{3+} ion increases, the distance between luminescent centers decreases which can cause the non-radiative energy transfer. Energy transfer process from the one Dy^{3+} ion to another Dy^{3+} ion, in the present work depends on the critical distance (D_c) between the Dy^{3+}-Dy^{3+} cations. According to Blasse [167,168], the critical distance between adjacent Dy^{3+} ions could be calculated through the following expression (4.4);

$$D_c = 2 \times \left(\frac{3V}{4\pi x_c n}\right)^{\frac{1}{3}} \ldots\ldots\ldots (4.4)$$

Here, 'V' represents the unit cell volume calculated through the Rietveld refinement measurements, the term 'x_c' denotes the optimum concentration of the Dy^{3+} ions, and 'n' represents the number of cations per unit cell. From experimental data analysis it was observed

that for the optimized concentration x_c = 0.04, V = 1055 Å^3, and n = 8. For the current system the value of critical distance is found to be 18.4680 Å. According to Van Uitert the energy transfer is associated with the phenomenon of exchange energy, re-absorption of radiation, and multiple interactions [169]. Out of these all interactions the exchange interaction is responsible for the energy transfer for the forbidden transition and the critical distance for this should be shorter than 3-5 Å [168]. In present study, the value of critical distance between adjacent Dy^{3+} ions are found to be greater than 5 Å, therefore multipolar interactions will play important role in this case rather than exchange interactions.

The luminescence intensity 'I' and the mole fraction of the activator ions 'x' could be corelated to each other through the following expression (4.5) [170];

$$\log\left(\frac{I}{x}\right) = -\frac{Q}{3}\log(x) + A \ldots\ldots\ldots (4.5)$$

Here, 'A' is a constant and the quantity 'Q' is the type of interaction between the rare-earth ions. If the value of Q come out to be 6, 8 and 10, then the interactions corresponding to electric dipole-dipole, dipole quadrupole, and quadrupole-quadrupole respectively [55]. The relationship between log(I/x) and log(x) plotted along y-axis and x-axis respectively for the Dy^{3+} substituted GTO with various concentrations under the excitation wavelength of 347 nm wavelength were well represented by Figure 4.7. The value of 'Q' parameter is come out to be 4.05 which is close to 6 indicates that the effect of concentration quenching in the Dy^{3+} substituted GTO is due to the electric dipole-dipole interaction [55].

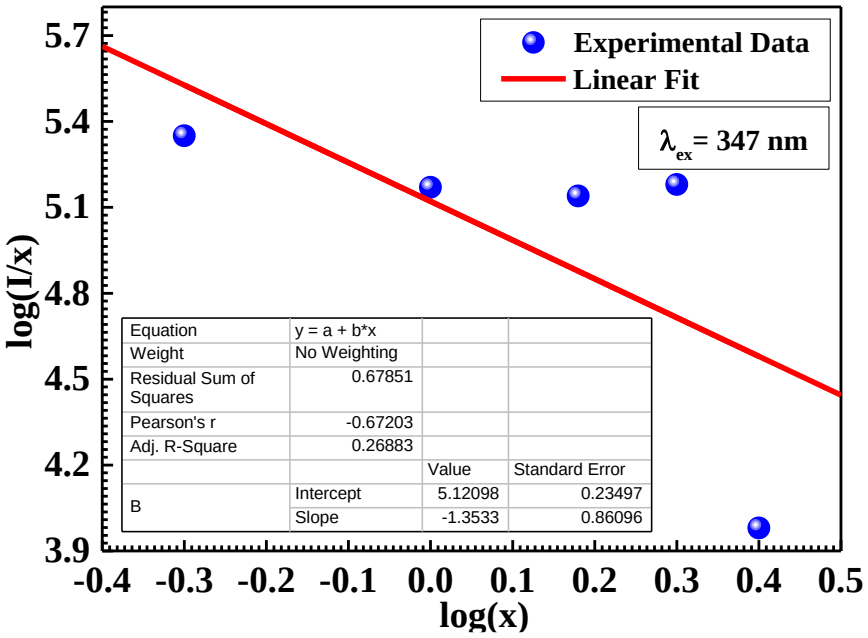

Figure 4.7. *Relationship of log(I/x) with log(x) for complete series of Dy^{3+} substituted GTO under 347 nm excitation.*

The Yellow/blue (Y/B) ratio for the Dy^{3+} substituted GTO pyrochlore oxide has been studied with respect to function of Dy_2O_3 concentration and it is important for white light emission. The degree of covalence between the Dy^{3+}-O^{2-} ions can be identified by the Y/B ratio. Greater value of Y/B ratio indicating the good degree of covalency between dysprosium and oxygen ions. For the excitation wavelength 347 nm, the value of Y/B ratio for the complete series of Dy^{3+} substituted GTO for concentrations 0.5 %, 1.0 %, 1.5 %, 2.0 %, and 2.5 %, were calculated and tabulated in Table 4.5, were found to be nearly close to unity, indicates the stability of the colour coordinates for all concentrations. The value of Y/B ratio increases with increasing Dy^{3+} up-to 2.0 mol % and then decreases for further increment of Dy^{3+}. The results are in accordance to the known Dy^{3+} ions doped single-phase $BaNb_2O_6$ phosphors [145], Dy^{3+} doped ZnO [156], and Dy^{3+} doped $Mg_2Al_4Si_5O_{18}$ phosphor [166]. We conclude that the Y/B ratio and CCT provide a basis for the design of efficient white phosphor for displays and WLED's.

Table 4.5. Y/B ratios, x and y CIE chromaticity coordinates, and CCT for Dy^{3+} substituted GTO with various doing concentration of Dy^{3+} ions.

λ_{ex} = 347 nm			
X (Dy^{3+} concentration in mol%)	**Yellow/Blue (Y/B) Ratio**	**(x, y) coordinates**	**CCT (K)**
0.5 %	0.8346	(0.31730, 0.31024)	6385.51
1.0 %	0.8383	(0.32988, 0.31403)	5638.77
1.5 %	0.8507	(0.32780, 0.32651)	5732.52
2.0 %	0.8753	(0.34959, 0.35381)	4844.95
2.5 %	0.8671	(0.34217, 0.34587)	5102.82

Figure 4.8, depicts the systematic energy level diagram consisting excitation, emission, resonance energy transfer, and cross-relaxation processes involved in Dy^{3+} substituted GTO. The radiation excites the Dy^{3+} ions by using energy of 347 nm (upward black arrow represents excitation line) and then relaxes to the energy state $^4F_{9/2}$ via non-radiative transfer (denoted by downward green arrow) and then emitting three visible light emission lines 456nm ($^4I_{13/2}\rightarrow{}^6H_{13/2}$), 484 nm ($^4F_{9/2}\rightarrow{}^6H_{15/2}$), and 581 nm ($^4F_{9/2}\rightarrow{}^6H_{13/2}$) radiatively from $^4F_{9/2}$ energy levels. The possible non-radiative transitions could be due to resonance energy transfer corresponds to transition from $^4F_{9/2}+{}^6H_{15/2} \rightarrow {}^6H_{15/2}+{}^4F_{9/2}$ and cross relaxation channels such as ($^4F_{9/2}+{}^6H_{15/2}\rightarrow{}^6F_{11/2}$, $^6H_{9/2}+{}^6F_{5/2}$), ($^4F_{9/2}+{}^6H_{15/2}\rightarrow{}^6F_{9/2}$, $^6H_{7/2}+{}^6F_{5/2}$) and ($^4F_{9/2}+{}^6H_{15/2}\rightarrow$ $^6F_{1/2}+{}^6F_{11/2}$,$^6H_{9/2}$) are well represented by CRC1, CRC2, and CRC3 respectively.

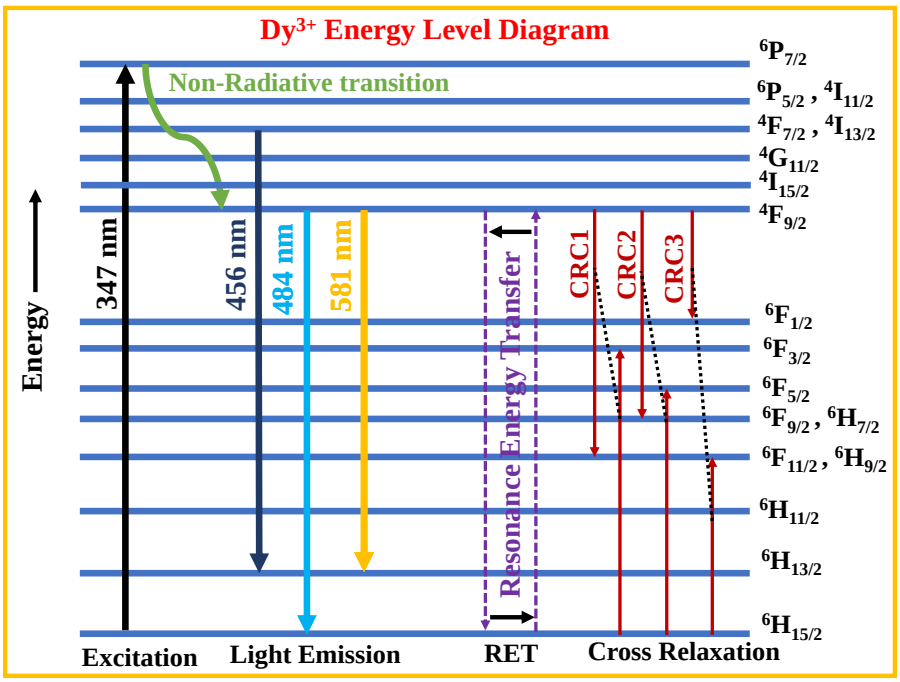

Figure 4.8. *Schematic representation of excitation, emission and energy transfer processes involving in Dy^{3+} substituted GTO.*

4.3.4. CIE Calorimetric Postulate:

The Commission International de L' Eclairage (CIE) chromaticity coordinates are helpful to identify the colour of any luminous material [87], specified on a chromaticity diagram as shown in Figure 4.9, for Dy^{3+} substituted GTO under the excitation wavelength of 347 nm for the current series. The PL results were used to calculate the colour coordinates by calculating α(λ), β(λ) and γ(λ) three essential colour matching functions described in CIE 1931 diagram [157]. For a particular spectral density D(λ), amount of inducement necessary to exactly match the colour of power density D(λ) is explained by the following expressions:

$$X = \int_{\lambda} \alpha(\lambda)\mathrm{D}(\lambda)d\lambda \ldots\ldots\ldots (4.6)$$

$$Y = \int_{\lambda} \beta(\lambda) D(\lambda) d\lambda \ldots\ldots\ldots (4.7)$$

$$Z = \int_{\lambda} \gamma(\lambda) D(\lambda) d\lambda \ldots\ldots\ldots (4.8)$$

Here X, Y, and Z are representing the tristimulus values providing power for red, green and blue colours to match the colour of D(λ). Now to identify the actual colour these dimension X, Y, and Z were used to match the colour of D(λ), done by CIE 1931 diagram. From X, Y and Z values x and y can be measured through the following expressions (4.9 & 4.10) [157];

$$x = \frac{X}{X + Y + Z} \ldots\ldots\ldots (4.9)$$

$$y = \frac{Y}{X + Y + Z} \ldots\ldots\ldots (4.10)$$

The CIE coordinates for the Dy^{3+} substituted GTO for various concentration were calculated from the PL EM-spectra measured under 347 nm excitation wavelength. The value of CIE coordinates is come out to be (0.31730, 0.31024), (0.32988, 0.31403), (0.32780, 0.32651), (0.34959, 0.35381), and (0.34217, 0.34587) for the various doing of Dy^{3+}, 0.5 mol%, 1.0 mol%, 1.5 mol %, 2.0 mol %, and 2.5 mol % respectively, and well depicted in Table 4.5. It was noticed that for all the various concentration the value of CIE coordinates is close to standard equal energy white light coordinates (0.333, 0.333) [145].

The quality of white light can be estimated through chromaticity coordinates using McCamy's approximate expression (4.11) [162];

$$CCT = -449s^3 + 3525s^2 - 6823.3s + 5520.33 \ldots\ldots\ldots (4.11)$$

Here, then term 's' represents the inverse slope line where $s = \frac{x-x'}{y-y'}$. And the term '$x' = 0.332$' and '$y' = 0.186$' are the epicenter coordinates. The values of colour correlated temperature (CCT) calculated through equation (4.11) for Dy^{3+} substituted GTO series with various concentration for excitation at 347 nm were tabulated in Table 4.5, and were lying in the range 4845-6385 and falls in cool-white light region. From many studies it was found that the lamps with CCT < 3200 K emit warm white light whereas the lamp with CCT > 4000 K are tend to give cool white light [157]. For the optimized concentration (2 mol%) of Dy^{3+} substituted GTO value of CCT is 4845, indicating the cool white light emission and it is close to the ideal white colour region in CIE diagram. Higher value of CCT indicating the large brightness and better visual acuity. The value of CCT lying in cool white light region signifies the use of Dy^{3+} substituted GTO pyrochlore oxide for better w-LED applications.

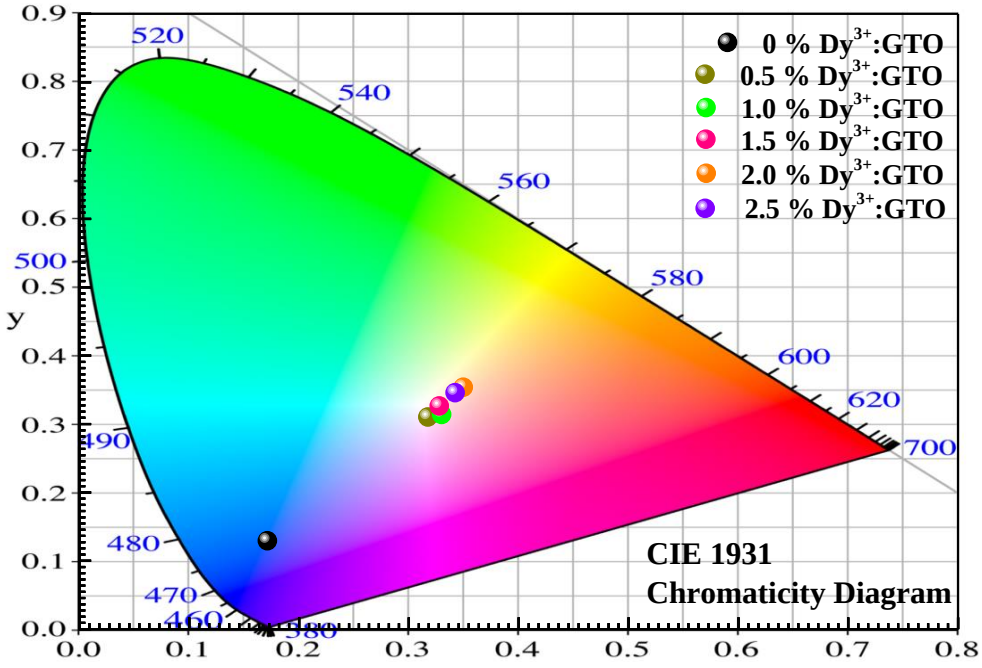

Figure 4.9. *CIE 1931 chromaticity diagram for Dy^{3+} substituted GTO for various concentration.*

4.4. Conclusion:

The GTO and series of Dy^{3+} doped GTO were successfully prepared through standard solid state reaction technique. For the complete series, the structural analysis was done through XRD and Raman analysis. XRD results accompanied with Rietveld refinement analysis suggested that all the samples are crystalline in nature and freeze with single pyrochlore phase. This small substitution is not too significant to produce any structural distortion as observed through XRD. which causes lattice contraction of host GTO with Dy^{3+} substitution. Raman profile indicating the presence of functional group corresponding to active vibrational modes which are in good agreement with XRD results. Unlike XRD, Raman spectroscopy exhibits a very small blue shift as the effect of smaller cationic substitution. The EX-spectra for every sample show the appearance of excitation peak at 347 nm wavelength and the EM-spectra have two sharp intensity bands centered around 484 nm and 581 nm, originating due to the $^4F_{9/2} \rightarrow {}^6H_{15/2}$ and $^4F_{9/2} \rightarrow {}^6H_{13/2}$ transition respectively and the less intense band appeared at wavelength of 456 nm formed due to the $^4I_{13/2} \rightarrow {}^6H_{13/2}$ transition of Dy^{3+} ions. The optimum concentration of Dy^{3+} substituted GTO series is found to be 2.0 mol% after this concentration quenching effect occurs. The Y/B ratio for the complete series of samples were found to close to unity and the combination of both yellow and blue emission bands emit white light with CIE coordinates values for the 2.0 mol % of Dy^{3+} ion in GTO host is (0.34959, 0.35381) with CCT value 4844.95 lying in the standard cool white light calorimetric point. Overall, the Dy^{3+} substituted GTO pyrochlore samples could be used as luminescent material for WLEDs application.

Chapter 5

Effect of $Ce^{4+} \rightarrow Ce^{3+}$ conversion on the structural and luminescence properties of Ce^{4+} doped $Gd_2Ti_2O_7$ pyrochlore oxide

A series of $Gd_2Ti_{2-x}Ce_xO_7$ (with doping concentrations of x = 0, 0.04, 0.08, 0.12, and 0.16) was prepared using solid state reaction technique. Conventional methods like X-ray diffraction and Raman spectroscopy verified that the synthesised samples displayed a pyrochlore structured phase. The main focus of this chapter is to investigate the effect of Ce^{4+} to Ce^{3+} conversion on the structural and luminescence properties. The unit cell expanded more and strain accumulated more in the reduced samples with pyrochlore structures. The oxidation state of the oxygen anions as well as the cations of Gd and Ti was examined using X-ray photoelectron spectroscopy (XPS). In comparison to the unreduced samples, it was observed that the Ce^{4+} to Ce^{3+} conversion produced better PL excitation and emission results. At 4% doping concentration for the cerium dopant, concentration quenching effects is observed. This work offers insightful information on the potential use of Ce^{4+} to Ce^{3+}: $Gd_2Ti_2O_7$ for the synthesis of blue LED chips used in the creation of WLEDs.

5.1. Introduction

Light emitting diodes (LED's) are the successful contender for lighting due to their quickly enhancing durability, reliability, efficiency, flexibility in size, and ecofriendly components [32]. Due to environmental issues, researchers are now more focused on the alternatives to the fossil fuels as energy sources emitting on carbon dioxide gas. White LED's (WLED's) are one of the most efficient and best candidates as WLED's notably reduces global power requirements and the harnessing of fossil fuels. A numerous investigation have been done on WLED's due to their large number of advantages over other LED's such as small size, low energy consumption, long lifetimes, high brightness and reliability, high efficiency etc. [171,172]. WLED's can be produced by two methods; (a) Multi chip-LED method includes the mixing of red, green, and blue LED's light which produces white light. (b) Phosphor conversion method, Phosphor material are deposited on the top layer of LED chip [10]. The mixing of light from the phosphor and the LED chip generates white light. The second approach is currently giving higher efficiency and superior light distribution characteristic compared to the multi color LED chip method [7]. Blue LED usage in the WLED's formation, avoids the formation of ultraviolet (UV) light by a fluorescent lamp. Yum *et al.* synthesized $Y_3Al_5O_{13}$: Ce^{3+} yellow phosphors and used it as blue chip for the fabrication of WLED's with near UV chips with a highly efficient solid-state light [172]. Hence, near ultraviolet phosphor used in WLED's have great interest in the area of solid-state lighting. Thus, it is necessary to develop a new blue phosphor that can be efficiently excited in the ultraviolet range (~ nearly 400 nm) for the luminescence intensity enhancement.

Luminescent materials need two main things for its fabrication: crystalline host and dopant for their production. Pyrochlore ternary oxides, with chemical formula $A_2B_2O_7$ belongs to Fd-3m space group and having face centered cubic structure, were more explored and investigated

structure due to their large variety of physical, chemical, and magnetic properties that depends on the cations substituted at A and B sites with different valency [159]. The larger cation A is generally a trivalent rare earth ion with an inert pair of electrons and cation B is a smaller transition metal with higher valency. Larger cation at A site is eight-fold coordinated with oxygen and situated on the 16c site at position (0.5, 0.5, 0.5) within an elongated cubic polyhedron. B site with smaller sized cation is six-fold coordinated to oxygen (loss of oxygen causes reduction in the coordination of B-site cation from eight to six-fold) on the 16d site at position (0,0,0) and located within a distorted octahedron [90]. Some of the pyrochlore oxides are excellent refractory materials display interesting phosphorescent and fluorescent properties and therefore, used as host matrix in phosphor materials. Hence pyrochlore oxides were explored world-wide as multifunctional materials due to their various use in dielectrics and fast ion conduction [173], electrocatalysts [174], high temperature catalysts [175], magnetic devices [176], in thermal barrier coatings [177], nuclear waste encapsulation [158,178], and in luminescent materials as host matrix [54,83,123,150,179]. The stability of an ordered pyrochlore structure is basically determined by the cationic radii ratio r_A/r_B which must be within 1.46 to 1.78 [150]. Present work focused on the titanate based pyrochlore oxides as they were easily formed at ambient temperatures and are promising candidate for ceramic pigments, fulfilling the basic requirement of high melting temperature (greater than 1600°C), high refractive index, and have the potential to accommodate first row transition metal ions in the crystal lattice at the place of octahedrally coordinated site [66]. Rare earth based pyrochlore ternary oxide, $Gd_2Ti_2O_7$ selected as host lattice in luminescent material for the enhancement of luminescence intensity as $Gd_2Ti_2O_7$ produces high-quality doped material free from defect and would be ideal for practical applications [74,78]. In the present work, the rare earth ion cerium is used as the dopant (impurity) due to its existence in two stable valance states *i.e.,* Ce^{3+}/Ce^{4+} [180].

The most probable electric transition 5d → 4f with tens of nanoseconds decay lifetime in Ce^{3+} ions are responsible for the intense radiative emission. Moreover, there is a large energy gap between 4f and 5d level making it one of the most effective emission centers as this large energy gap reduces the multi-phonon relaxation rate. The cerium in Ce^{3+} valance state is characterized by broad absorption and emission bands due to the high sensitivity of 5d orbitals to the host phosphor matrix [181]. Cerium in the valance state Ce^{4+} has strong UV absorption due to the charge transfer transition from oxygen emission to Ce^{3+} ions and therefore has very less luminescence. Here, CeO_2 is used as the blue light emitting luminescent dopant at the B-site of pyrochlore $Gd_2Ti_2O_7$ host in valance state Ce^{4+}. The cationic radii of Ti^{4+} and Ce^{4+} are 0.605 Å and 0.87 Å, respectively. Therefore, the cationic radii ratio r_{Gd}/r_{Ti} and r_{Gd}/r_{Ce} are obtained as 1.7405 and 1.6816, respectively which means the maximum doping of Ce^{4+} (for 8%) at the place of titanium (B-site) does not affect the basic pyrochlore structure. The first part of the paper presents the structural and optical properties of $Gd_2Ti_2O_7$ doped with Ce^{4+} and the later section focuses on the effect of reduction on optical properties in Ce^{4+} doped $Gd_2Ti_2O_7$. These samples with prior and post reduction were studied by means of XRD, Raman spectroscopy, CIE chromaticity coordinates and photoluminescence (PL) spectroscopy. The reduction is confirmed through X-ray photoelectron spectroscopy.

5.2. Experimental details:

5.2.1. Sample preparation:

5.2.1.1. Ce^{4+} doped $Gd_2Ti_2O_7$:

Series of pure phasic $Gd_2Ti_2O_7$ pyrochlore matrix doped Ce^{4+} samples have been prepared by mixing and grinding of high purity raw powders Gd_2O_3 (CAS No.: 12064-62-9, 99.99% purity, Sigma Aldrich), CeO_2 (CAS No.:1306-38-3, 99.95% purity, Sigma Aldrich), and TiO_2 (CAS No.12188-41-9, 99.99%), *via* conventional multi-step solid-state reaction method. The

systematic process was done during solid-state rection method to produce powdered samples as shown in Figure 5.1. Since lanthanide-based oxides are highly reactive towards water and carbon dioxide, therefore, these oxides easily form hydroxides, carbonates, and oxycarbonates when exposed to the atmospheric environment. That being the case, in the very first step oxide powders Gd_2O_3, CeO_2, and TiO_2 were essentially preheated at a temperature of 850℃ for 4 hours for the removal of excess moisture and volatile impurities. Later preheating step, stoichiometric amounts of all the reagents Gd_2O_3, CeO_2, and TiO_2, were accurately weighted using weighing machine as reported in Table 5.1. Using agate mortar pestle a single collection of 3 gram (g) of all precursors Gd_2O_3, CeO_2, and TiO_2 were mixed well and ground properly for 7.5 hours to construct homogeneity and uniformity in the final experimental product. These finely mixed and grounded powdered products were converted into pellets of ~10 mm diameter and 1.5 nm thickness by applying a pressure of 4.5 torr on the hydraulic press machine using a stainless-steel die set. These pellets were sintered in the alumina boat at a temperature 1200℃ for 24 hours of duration in the air atmosphere by using the high temperature muffle furnace (Nabertherm).

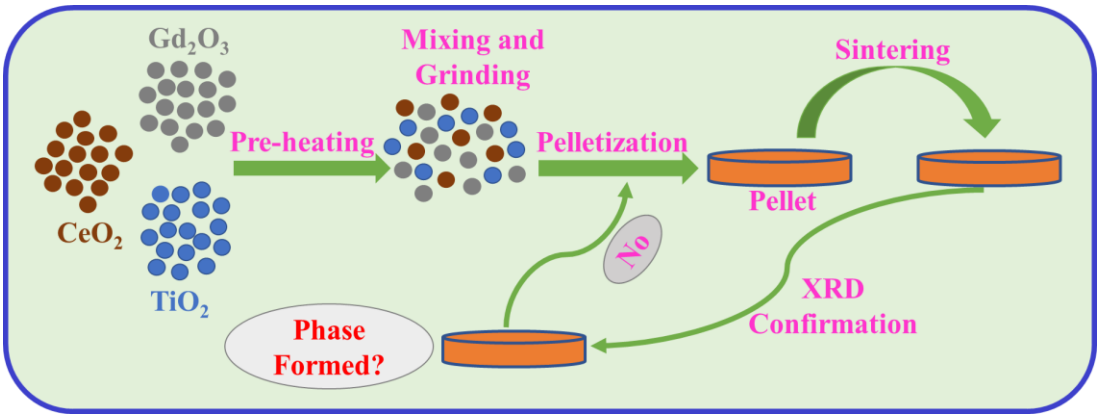

Figure 5.1. *Systematic flow chart for the preparation of Ce^{4+} doped $Gd_2Ti_2O_7$ pyrochlore oxide through solid state method.*

In order to form high density products, the pellets were re-grounded for 3 hours in mortar pestle and pelletized again and were annealed at a final temperature 1300℃ with a heating rate of 5℃/min and for 48 hours and cooling rate 2℃/min. A series of powdered samples of $Gd_2Ti_{2-x}Ce_xO_7$ (x = 0. 0.04, 0.08, 0.12, and 0.16) were prepared using solid state route from the starting precursors Gd_2O_3, CeO_2, and TiO_2 following the below reaction (5.1);

$$Gd_2O_3 + xCeO_2 + (2-x)TiO_2 \xrightarrow{1200℃,24\ h + 1300\ ℃,48\ h} Gd_2Ti_{2-x}Ce_xO_7$$

$$(x = 0, 0.04, 0.08, 0.12, 0.16) \quad \ldots (5.1)$$

Table 5.1. Weight of Gd_2O_3, CeO_2, and TiO_2 precursors used for the synthesis of 3g batch of $Gd_2Ti_{2-x}Ce_xO_7$ series.

Doping (%)	**$Gd_2Ti_{2-x}Ce_xO_7$**	**Gd_2O_3 (g)**	**TiO_2 (g)**	**CeO_2 (g)**
0	$Gd_2Ti_2O_7$	2.0824	0.9176	0
2%	$Gd_2Ce_{0.04}Ti_{1.96}O_7$	2.0678	0.8929	0.0393
4%	$Gd_2Ce_{0.08}Ti_{1.92}O_7$	2.0534	0.8686	0.0780
6%	$Gd_2Ce_{0.12}Ti_{1.88}O_7$	2.0392	0.8446	0.1162
8%	$Gd_2Ce_{0.16}Ti_{1.84}O_7$	2.0252	0.8210	0.1538

5.2.1.2. Reduction of $Ce^{4+} \rightarrow Ce^{3+}$:

All the finally sintered pellets of Ce^{4+} doped $Gd_2Ti_2O_7$ pyrochlore host samples were finely grounded and each composition was placed in different cylindrical alumina crucibles with marking. After that all the cylindrical crucibles containing Ce^{4+} doped $Gd_2Ti_2O_7$ powders were placed in quartz tube of length of 1 meter and heated at a temperature of 1000℃ for the duration of 24 hours in the environment of H_2 and Ar gas at a flow rate of 10% /sccm (standard cubic

centimeter) and 90% /sccm, respectively in the round vacuum sealed tube furnace. Schematic diagram of the setup for cerium reduction was shown in Figure 5.2. The Ce^{4+} get reduced to Ce^{3+} through the following equation (5.2):

$$Ce^{4+} \xrightarrow[1200°C \text{ for } 24 \text{ hours}]{H_2(10\%)+Ar(90\%)} Ce^{3+} \quad \ldots\ldots\ldots (5.2)$$

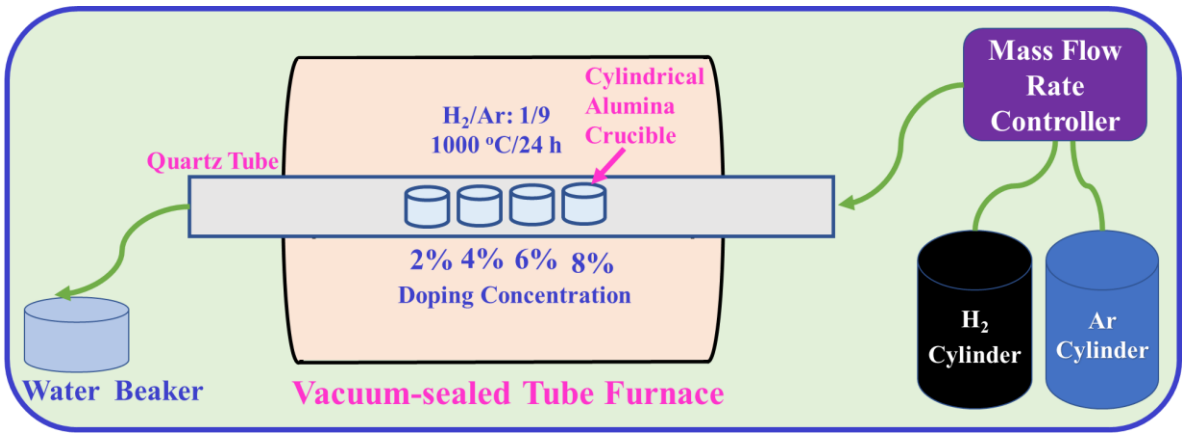

Figure 5.2. *Setup for the reduction of Ce^{4+} into Ce^{3+} through round vacuum sealed tube furnace setup.*

5.2.2. Characterization:

For the structural examination, all unreduced and reduced pellets were evaluated using X ray diffraction characterization. XRD results for both the set of pellets were recorded in the 2θ angle range from 10°-70° using 0.02° step size and scanning rate 0.5° min^{-1} through Bruker company X-ray diffraction machine (Model Number-D8-Advance) using CuK_α radiation source of wavelength λ=1.5406Å at Delhi technological university (DTU), New Delhi. The measurements were carried out for microstructural investigations using field emission scanning electron microscopy (FESEM-MIRA-II, TESCAN) at Inter-University Accelerator Centre (IUAC), New Delhi. Raman patterns for both the set of pellets (unreduced + reduced pellets) were noted by applying laser light of 532 nm using the WITec Alpha 300RA Raman microscopy equipped with a 50× objective lens at Jawaharlal Nehru University (JNU), New

Delhi. X-ray photoemission spectrum for all the elements present in the reduced sample of 6% doping were noted using a monochromatic Al-Kα source with ESCA + Omicron Nano Technology at Materials Research Centre (MRC) in Malaviya National Institute of Technology (MNIT) Jaipur. PL excitation and emission spectrum for all the samples were recorded using a Jasco-8300 fluorescence spectrometer at room temperature using Xenon lamp, at DTU, New Delhi.

5.3. Results and discussion:

5.3.1. Microstructural analysis:

SEM photographs of undoped $Gd_2Ti_2O_7$ sample sintered at a temperature of 1300℃ for 48 hours was depicted in Figure 5.3. The grain size of the undoped host $Gd_2Ti_2O_7$ estimated under the high magnification order of 20,000 times. The captured SEM micrograph contains nearly spherical agglomerated particles and submicron sized pores which were clearly seen at the very compact morphological surface. The diameter of spherical grains was calculated with the help of Image J software program, and the grain size come out to be 1.2 ± 0.006 μm for pristine $Gd_2Ti_2O_7$ host. Average grain size was estimated from the Gaussian fitting size distribution histogram method as shown in Figure 5.3 (b). The elemental mapping through energy dispersive x-ray analysis of pristine host samples shows the uniform distribution of Gd, Ti and O ions throughout the composition shown by Figure 5.3 (c-e).

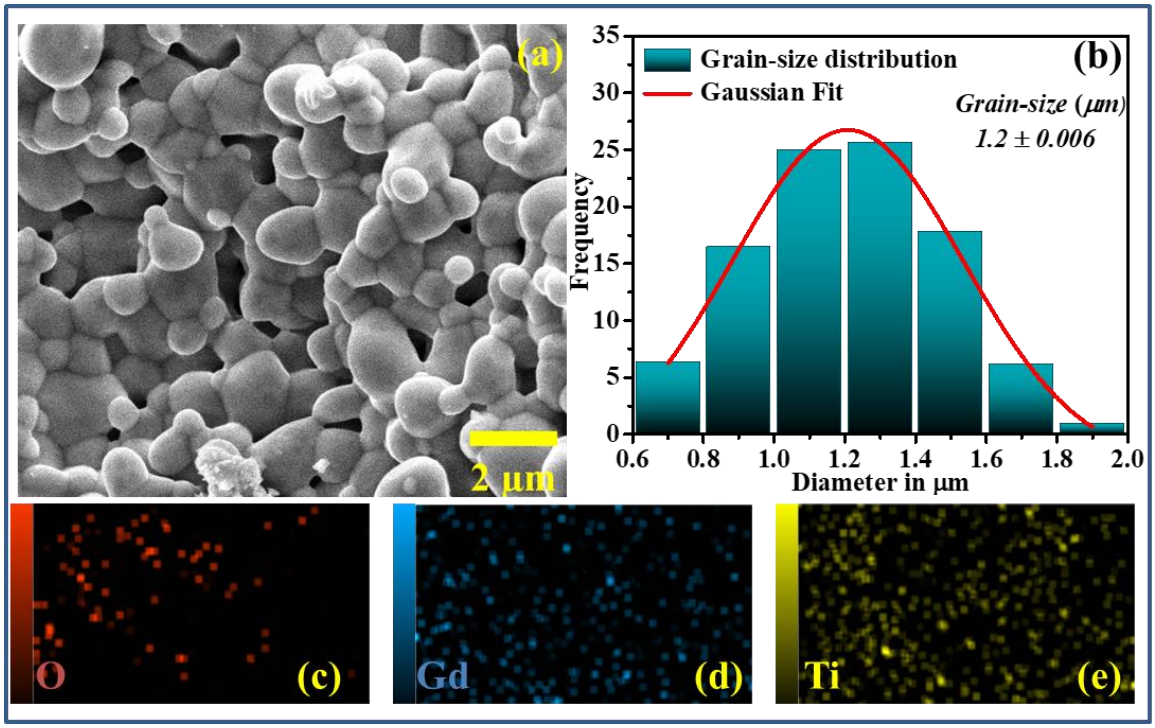

Figure 5.3 *(a). Systematic SEM micrograph of pristine host $Gd_2Ti_2O_7$, (b) Gaussian fitting size distribution histogram, and (c-e) elemental mapping of undoped host.*

5.3.2. Structural analysis using XRD:

5.3.2.1. Ce^{4+} doped $Gd_2Ti_2O_7$

XRD patterns for unreduced Ce^{4+} doped series of $Gd_2Ti_2O_7$ were recorded within 2θ range 10°-70° represented in Figure 5.4 (a) to examine the crystalline nature and phase formation of samples. Two types of diffraction peaks were observed. The first type of high intensity peaks has even order miller indices (222), (400), (440), (622), and (444) belongs to the fluorite basic framework and were found at 2θ values 30.50°, 35.35°, 50.80°, 60.38°, and 63.31°, respectively. Second type of low intensity diffraction peaks with odd miller indices (111), (311), (331), (511), and (531) belongs to ordered pyrochlore superstructure, and were observed at 2θ values 15.15°, 29.17°, 38.63°, 46.4°, and 53.29° respectively (represented by star '*' mark). All the XRD spectra are similar and indicating that the final product has an ordered pyrochlore cubic crystal structure which are in good agreement with the previous studies of $Gd_2Ti_2O_7$ [115,143].

Hence, from the XRD results we found that with the introduction of Ce^{4+} over Ti^{4+} into $Gd_2Ti_2O_7$ does not distort the basic crystal structure of pyrochlore oxide and concluded that the rare earth Ce^{4+} ion have been completely dissolved at B site within the host $Gd_2Ti_2O_7$ lattice.

A series of Ce^{4+} doped $Gd_2Ti_2O_7$ pyrochlore structure can be produced through solid state reaction method and their structural stability can be decided by the cationic radii ratio r_A/r_B, which can be estimated by using the following relation (5.3),

$$\left[\frac{r_{Gd}}{r_{Ce,Ti}}\right] = \left[\frac{r_{Gd}}{r_{Ti} \times \text{atomic } \% + r_{Ce} \times \text{atomic } \%}\right] \ldots\ldots\ldots (5.3)$$

Where r_{Gd} = 1.0530 Å, r_{Ti} = 0.6050 Å and r_{Ce} = 0.8700 Å, are the ionic radius for the trivalent and tetravalent cations of pyrochlore oxide $Gd_2Ti_2O_7$. The cationic radii ratio for the different doping concentrations of Ce^{4+} were calculated and tabulated into the Table 5.2, which decreases from 1.7405 to 1.6816 with increasing Ce^{4+} content. The r_A/r_B ratio for all compositions lies with pyrochlore stability range and XRD results supports these estimations.

The magnified view of the high intensity diffraction peak (222) is plotted from 29.5^o to 31.5^o as shown in Figure 5.4 (b). Here it is clearly observable that this (222) peak is monotonically shifted on lower angle side from 2θ = 30.53^o to 30.47^o on successive doping of Ce^{4+} which is represented by the short dash dotted line in Figure 5.4 (b). As Ce^{4+} doping doesn't affect the peak intensity for all samples indicating, the stability of crystalline texture has prevailed. However, shifting of (222) indexed peak toward lower angle side for all the samples indicates an increase in lattice parameter from 10.1143 Å to 10.1332 Å on increasing doping content of Ce^{4+} due to the expansion of crystalline host lattice, which is attributed due to the substitution of large sized Ce^{4+} (0.87 Å) at relatively smaller sized Ti^{4+}(0.605 Å). A maximum doping of Ce^{3+} into $Gd_2Ti_2O_7$ structure induces a 0.18 % increment in unit cell parameter.

Using Williamson-Hall (W-H) plot [182], the crystallite size for the complete series were calculated and described by the following equation (5.4),

$$\frac{\beta_{h,k,l}\cos\theta}{\lambda} = \frac{K}{D} + \frac{4\varepsilon\sin\theta}{\lambda} \ldots\ldots\ldots (5.4)$$

Here, $\beta_{h,k,l}$ is the width of diffraction maxima (FWHM) for different 2θ values, the parameter 'ε' represents the lattice strain, and 'λ' is the wavelength of X-ray source (1.5046 Å) used in XRD. Here 'K' is the structure factor used for spherical particles having cubic structure and 'D' is the crystallite size. The estimated values of $\beta_{hkl}.\cos\theta$ were plotted as a function of $\sin\theta$ values and fitted with a straight line to calculate the strain and crystallite size, as shown in Figure 5.4 (c) for the complete series. The slope of straight line and y-intercept were further used to calculate strain 'ε' and crystallite size 'D', respectively [126]. These calculated structural parameters from XRD patterns of Ce^{4+} doped samples were represented in Table 5.2.

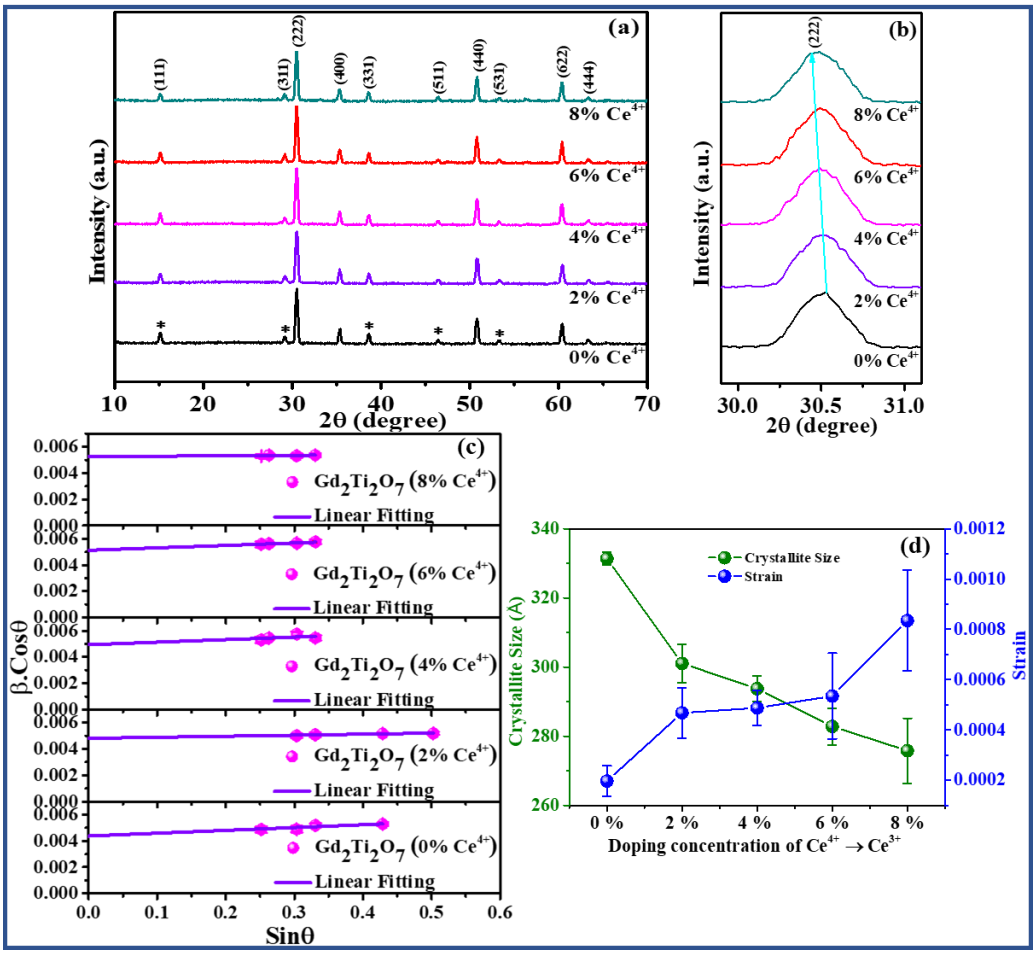

Figure 5.4 *(a). XRD patterns for complete series of Ce^{4+} doped $Gd_2Ti_2O_7$, (b) peak shifting of (222) peak, (c) W-H plot for all the compositions, and (d) crystallite size and strain distribution with cerium doping.*

Figure 5.4 (d) shows a variation in crystallite size and strain as a function of Ce^{4+} doping concentration. A gradual decrement is found in crystallite size from 331.4 ± 1.8 Å to 275.83 ± 9.4 Å with successive doping concentration, respectively. Moreover, it is found that the strain increases from 0.000197 to 0.000835 on replacing Ce^{4+} over Ti^{4+}. It may be noted that the almost ~3.2 times strain is induced into the host lattice by the 8 % doping of a relatively larger cation at the B-site. This decreasing trend in crystallite size with the substitution of relatively larger cation at Ti-site is in accordance with the reported results for $Gd_2Ti_{2-y}Zr_yO_7$ pyrochlore series [115].

Table 5.2. Structural variables calculated for pristine and Ce^{4+} doped samples of $Gd_2Ti_2O_7$ from XRD results.

Doping (%)	$Gd_2Ce_xTi_{2-x}O_7$	r_A/r_B	Crystallite Size (D) in Å	Strain	Lattice Constant (Å)
0%	$Gd_2Ti_2O_7$	1.7405	331.38 ± 1.8	0.000197 ± 0.00006	10.1143 ± 0.0002
2%	$Gd_2Ce_{0.04}Ti_{1.96}O_7$	1.7254	301.07 ± 5.6	0.000468 ± 0.0001	10.1177 ± 0.0001
4%	$Gd_2Ce_{0.08}Ti_{1.92}O_7$	1.7105	293.74 ± 3.7	0.000488 ± 0.00007	10.1208 ± 0.0005
6%	$Gd_2Ce_{0.12}Ti_{1.88}O_7$	1.6959	282.84 ± 5.3	0.000535 ± 0.00017	10.1247 ± 0.0003
8%	$Gd_2Ce_{0.16}Ti_{1.84}O_7$	1.6816	275.83 ± 9.4	0.000835 ± 0.0002	10.1332 ± 0.0001

5.3.2.2. Reduced $Ce^{4+}\rightarrow Ce^{3+}$ doped $Gd_2Ti_2O_7$

To carry out the structural investigation of complete reduced series of cerium doped $Gd_2Ti_2O_7$, the XRD has been executed and were also shown in Figure 5.5 (a). All the reduced samples show perfectly single pyrochlore phase similar to XRD patterns of unreduced samples. There were no additional impurity peaks on the complete reduced series of $Ce^{4+}\rightarrow Ce^{3+}$ doped $Gd_2Ti_2O_7$, indicating that the reduction $Ce^{4+}\rightarrow Ce^{3+}$ has not affected the dissolution of cerium into pyrochlore unit cell. Moreover, it was found that the XRD diffraction peaks of $Ce^{4+}\rightarrow Ce^{3+}$ doped $Gd_2Ti_2O_7$ shifts towards lower 2θ angle side with increasing cerium doping, in

comparison to standard data of pristine host $Gd_2Ti_2O_7$. The most intense XRD peak centered around ~ 30.53^o (with miller indices (222)), is separately plotted for all the compositions and shown in Figure 5.5 (b), to depict peak shifting towards lower 2θ angle side. Since the cationic size of Ce^{3+} (1.01 Å) is larger than the B-site cation *i.e.,* Ti^{4+} (0.605 Å), therefore, unit cell parameter increases as indicated by shifting of diffraction pattern on lower 2θ value. It is noteworthy that the unit cell parameter calculated through (222) diffraction peak increases from 10.1143 Å to 10.1527 Å as reported in Table 5.3. A maximum doping of Ce^{4+} into $Gd_2Ti_2O_7$ structure under reduced environment causes a 0.40 % increment in unit cell parameter. W-H plots deduced from XRD patterns of reduced samples were depicted in Figure 5.5 (c). The crystallite size and strain estimated through W-H plots are reported in Table 5.3 and plotted as a function of $Ce^{4+}\rightarrow Ce^{3+}$ concentration in Figure 5.5 (d). A variation in strain with respect to increasing doping concentration clearly shows that the strain increases on increasing cerium content. The host lattice with maximum doping concentration of reduced cerium is examined as ~4.3 times of that persist in pristine $Gd_2Ti_2O_7$ lattice.

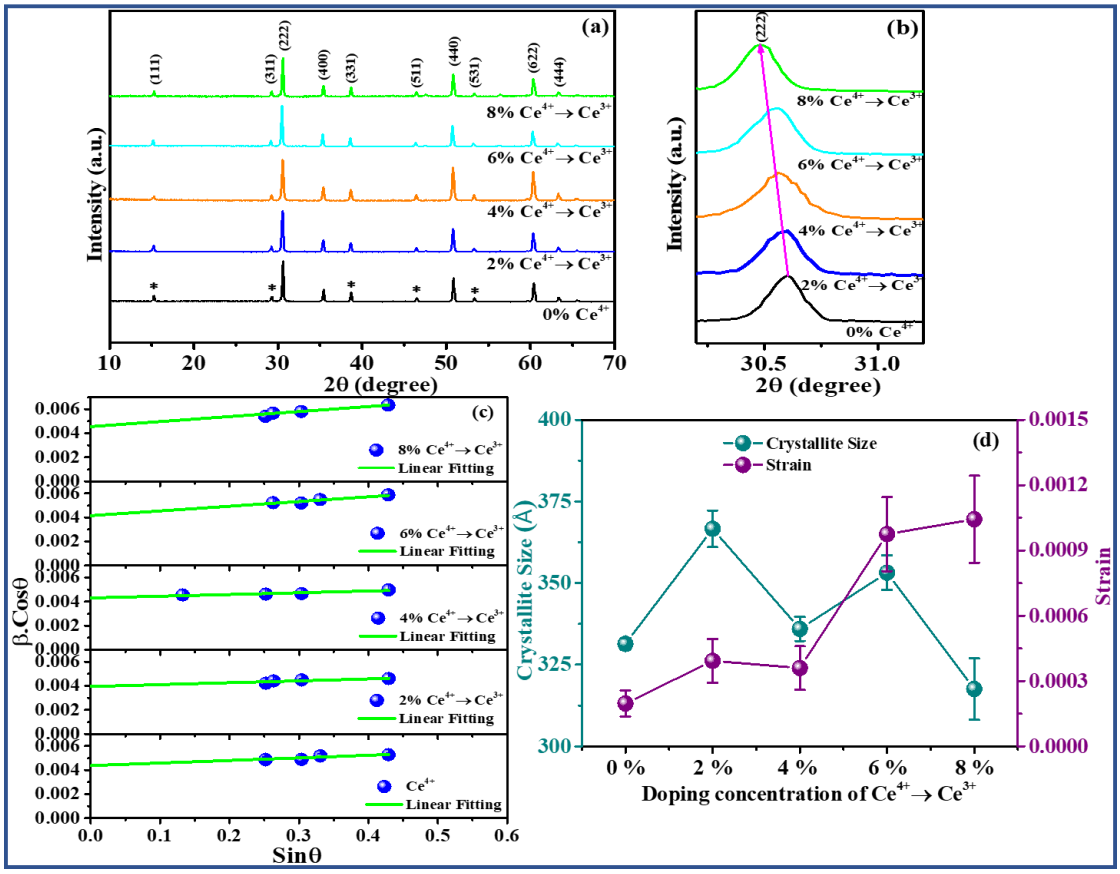

Figure 5.5 *(a). XRD patterns for complete series of* $Ce^{4+}\rightarrow Ce^{3+}$ *doped* $Gd_2Ti_2O_7$*, (b) peak shifting of (222), (c) W-H plot for all the compositions, and (d) Crystallite size and strain distribution with cerium doping.*

The reduction of cerium cation causes a lattice distortion which is shown by increased strain. The crystallite size does not show any significant variation as on increasing doping concentration. A gradual decrement in crystallite size as on increasing Ce^{4+} content is harnessed by reduction of Ce^{4+} to a larger sized Ce^{3+} ion and structural distortion caused unit cell expansion.

5.3.2.3. Effect of $Ce^{4+}\rightarrow Ce^{3+}$ conversion

It was clearly observed from XRD analysis that in case of reduced samples the shifting of diffraction pattern towards lower angle side is more as compared to unreduced samples. This is due to the reason that the size of Ce^{3+} (1.01 Å) is more as compared to Ce^{4+} (0.87 Å). Hence

as Ce^{4+} converted to Ce^{3+}, then due to the bigger size of Ce^{3+} as compared to Ti^{4+} (0.605 Å), the host lattice expands more. $Ce^{4+}\rightarrow Ce^{3+}$ reduction generates more strain in the pyrochlore single phasic cell. It is concluded from the reduction caused variation in crystallite size that the $Ce^{4+}\rightarrow Ce^{3+}$ reduction causes an increment in crystallite size which is encountered by a reduction in crystallite size driven by doping. Although, structural investigation through XRD is not produced any structural transformation or significant structural distortion.

Table 5.3. Structural variables calculated for pristine and $Ce^{4+}\rightarrow Ce^{3+}$ doped samples of $Gd_2Ti_2O_7$ through XRD results.

Doping (%)	**$Gd_2Ce_xTi_{2-x}O_7$**	**Crystallite Size (D) in Å**	**Strain**	**Lattice Constant (Å)**
0%	$Gd_2Ti_2O_7$	331.38±1.80	0.000197±0.00006	10.1143 ± 0.0002
2%	$Gd_2Ce_{0.04}Ti_{1.96}O_7$	366.61±16.2	0.000393±0.00015	10.1413 ± 0.0001
4%	$Gd_2Ce_{0.08}Ti_{1.92}O_7$	335.99±7.60	0.000360±0.00009	10.1433 ± 0.0003
6%	$Gd_2Ce_{0.12}Ti_{1.88}O_7$	353.20±27.2	0.000975±0.000033	10.1477 ± 0.0006
8%	$Gd_2Ce_{0.16}Ti_{1.84}O_7$	317.57±12.0	0.001043±0.000174	10.1527 ± 0.0012

5.3.3. Structural analysis using raman spectroscopy

5.3.3.1. Ce^{4+} doped $Gd_2Ti_2O_7$

Principal factor investigation of $A_2B_2O_7$ pyrochlore oxides with Fd-3m space group indicates the presence of six Raman active modes: A_{1g}, E_g, and four T_{2g}. Only oxygen atoms (O_{8b} and O_{48f}) are displaced from their respective position for all these vibrational modes. Out of all the modes, only single T_{2g} mode is appeared due to the O_{8b} oxygen vibrations and other three T_{2g} are present due to the O_{48f} oxygen vibrations [130,183]. Raman spectra for complete set of Ce^{4+} doped $Gd_2Ti_2O_7$ host oxides were shown in Figure 5.6 (a) and de-convoluted Raman spectra were also represented by Figure 5.6 (b-f) for each composition, at room temperature. For the pristine host $Gd_2Ti_2O_7$ sample, the Raman spectra were recorded within 140-800 cm^{-1} wavenumber range, are in good agreement with the previous reports [124,127,150]. Raman spectrum contains two most intense bands; one is due to the combination of E_g and T_{2g} with very close wave number centered around ~310 cm^{-1} is attributed due to the O-Gd-O bending mode; and the second most intense band is centered around ~516 cm^{-1} ascribed as A_{1g} band is assigned due to the presence of internal stretching of Gd-O. The other four bands have weaker intensity. Out of these remaining four weak bands, three bands were presented at ~212 cm^{-1}, ~545 cm^{-1} and ~680 cm^{-1}. The remaining T_{2g} bands appears due to Ti-O stretching. The Raman spectrum for Ce^{4+} doped $Gd_2Ti_2O_7$ samples shows the same pattern as that of pristine host, therefore, we can say that Ce^{4+} ions well dissolved in the pristine host $Gd_2Ti_2O_7$ without introducing much structural distortion. But with the doping of Ce^{4+}, it is found that an extra small intensity peak centered around ~457 cm^{-1} is appeared due to the trace amounts of TiO_2 [130]. From XRD results, it is found that with Ce^{4+} ion doping in $Gd_2Ti_2O_7$ host matrix, the radii ratio of cation A(Gd) and cation B(Ti/Ce) decreases from 1.7405 to 1.6816 and the pyrochlore unit cell experiences lattice expansion from 10.1143 Å to 10.1332 Å. It causes a small decrement in force constant among various Raman active bands. The doping of larger

cation allows an increment in bond length due to loosen Raman modes and is evidenced by a shifting of all Raman peaks towards lower wavenumber side as on increasing Ce^{4+} content. Thus, Raman spectroscopic results are in accordance with XRD results.

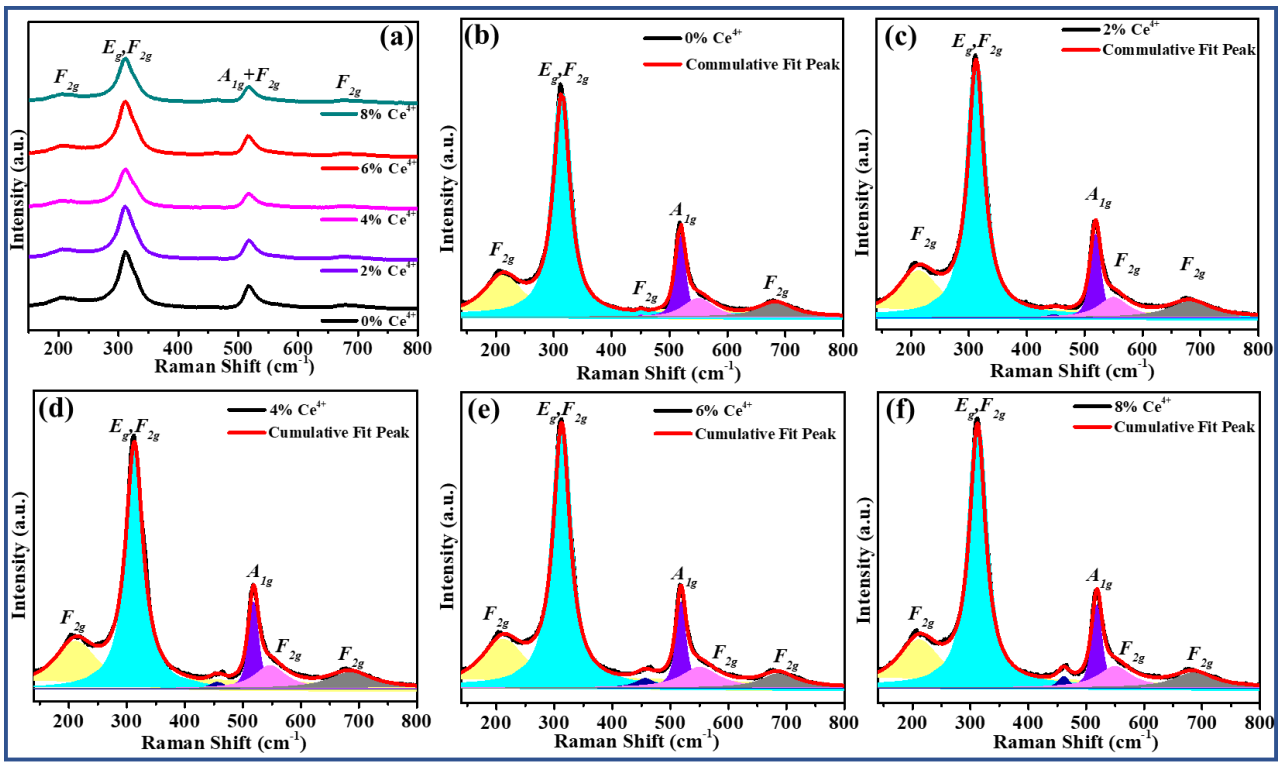

Figure 5.6 *(a). Raman spectra for all the Ce^{4+} doped $Gd_2Ti_2O_7$ host samples and (b-f) Raman de-convolution for each composition of Ce^{4+} doped $Gd_2Ti_2O_7$.*

5.3.3.2. Reduced $Ce^{4+}\rightarrow Ce^{3+}$ doped $Gd_2Ti_2O_7$

Since Raman spectroscopy is useful to probe the vibrations of cations as well as anions, Raman results would show the effect of reduction in cerium ions more prominently than XRD. Raman spectra were recorded for the series of Ce^{4+} doped $Gd_2Ti_2O_7$ annealed at a temperature of 1000°C under the reducing environment. Figure 5.7 (a) represents a series of vibrations recorded for all reduced samples *i.e.*, $Gd_2Ti_2O_7$: $Ce^{4+}\rightarrow Ce^{3+}$ as on increasing doping concentration from bottom to top. Raman data for each sample is deconvoluted into six Raman modes and represented in the Figure 5.7 (b-e) for the doping concentrations of 2%, 4%, 6%, and 8% respectively. A similar Raman spectrum is obtained for the reduced samples except a

small red shift in all vibrations. The reduction of doped cerium does not allow any significant structural distortion as evidenced by XRD results. Like Raman results of unreduced samples, larger size of Ce^{3+} (1.01 Å) ion than Ti^{4+} (0.605 Å) is responsible for the red shift in doped sample $Gd_2Ti_2O_7$: $Ce^{4+} \rightarrow Ce^{3+}$.

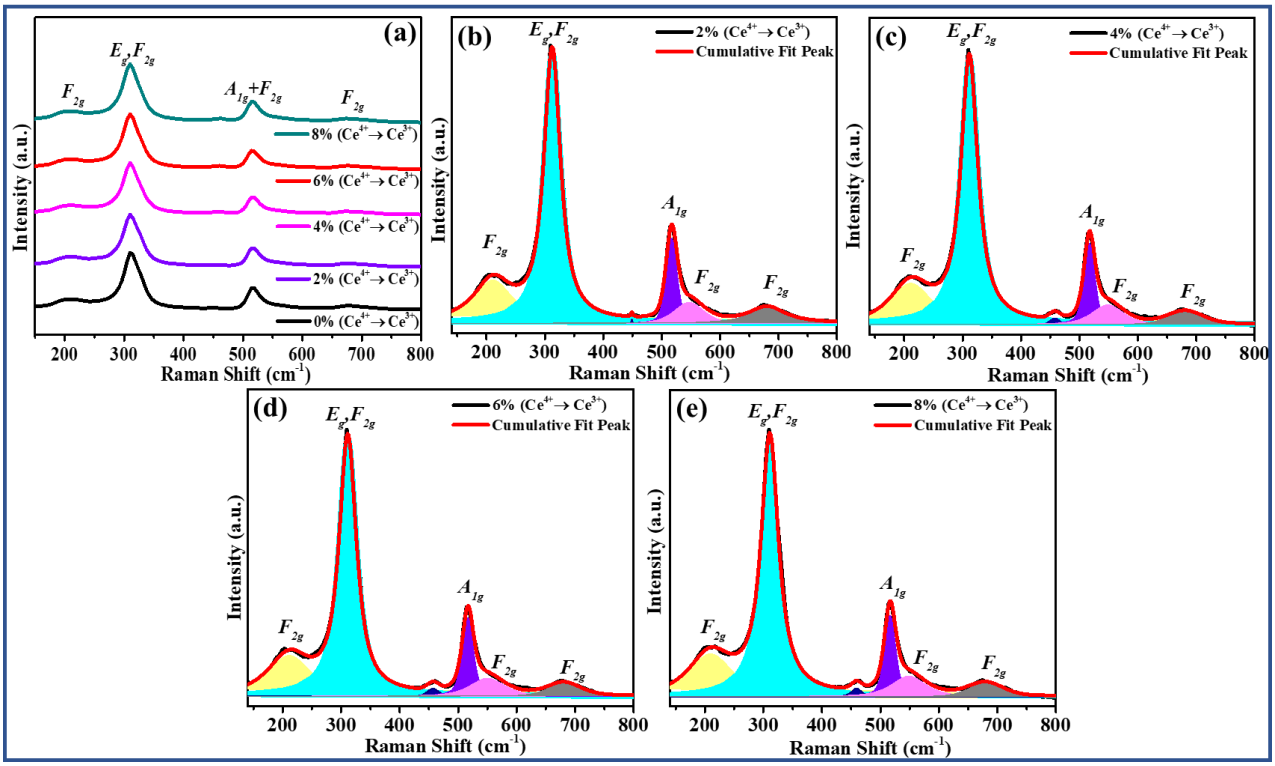

Figure 5.7 *(a). Raman spectrum for all the reduced samples $Gd_2Ti_2O_7$: $Ce^{4+} \rightarrow Ce^{3+}$ with various doping concentration and (b-e) Raman de-convolution for each composition of Ce^{4+} doped $Gd_2Ti_2O_7$.*

5.3.3.3. Effect of $Ce^{4+} \rightarrow Ce^{3+}$ conversion

The effect of reduction of cerium dopants from Ce^{4+} to Ce^{3+} is characterized by a larger red shift in respective composition. This is due to the reason that the size of Ce^{3+} cation (1.01 Å) is bigger as compared to the size of Ce^{4+} cation which is 0.870 Å. So, in the case of Ce^{3+} the lattice expansion is more as well explained by the XRD results also. Therefore, force constant decreases more and bond length increases more. Hence, shifting of 2nd, and 4th most intense Raman vibrational bands are more for the reduced $Ce^{4+} \rightarrow Ce^{3+}$ samples as compared to Ce^{4+}

doped $Gd_2Ti_2O_7$. This shifting in Raman active vibrations were estimated for unreduced and reduced set of samples and tabulated in Table 5.4 and respective red and blue shift are well represented in Figure 5.8 (a) and (b) by subscript R and B. The high intensity Raman band shows the maximum peak shifting *i.e.*, 1.6 cm^{-1} for unreduced sample, but in the case of reduced sample, the maximum shifting for the same Raman band is 2.9 cm^{-1}. The value of the peak shifting in 2nd most intense Raman band is 0.6 cm^{-1} for the Ce^{4+} doped $Gd_2Ti_2O_7$, but for the reduced $Gd_2Ti_2O_7$: $Ce^{4+}\rightarrow Ce^{3+}$ sample, the respective peak shifting is 1.8 cm^{-1}. The maximum shifting of 3.2 cm^{-1} in the peak position was observed for the last vibrational band centered around ~680 cm^{-1} for without reduction, but the same band shows maximum peak shifting of 8.8 cm^{-1} for reduced samples. Thus, reduction of cerium dopant has introduced a small amount of disordering in the lattice of oxygen ions examined by Raman spectroscopy which is not much significant that would allow a phase transformation.

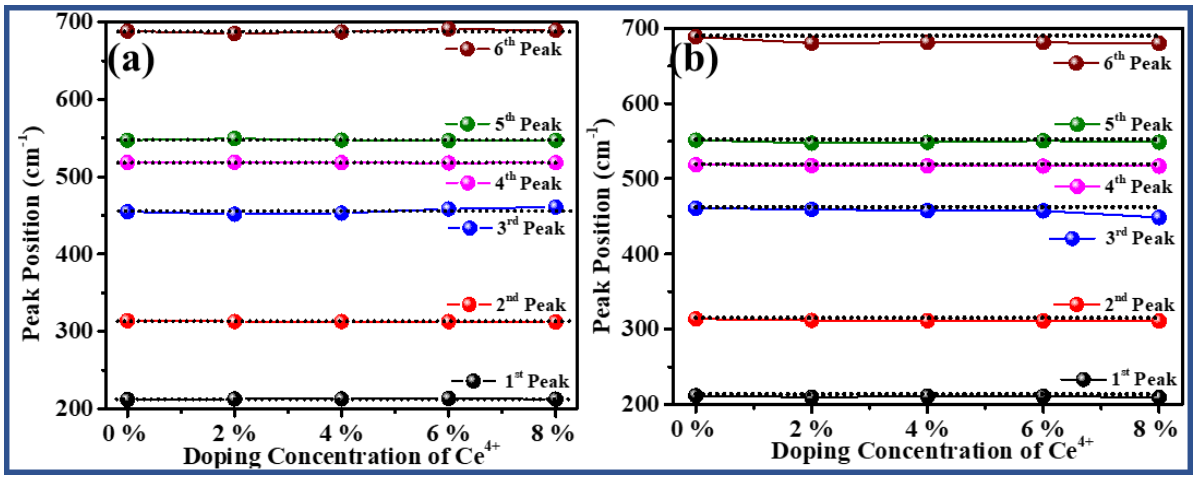

Figure 5.8 *(a). Shifting of all the raman peaks for Ce^{4+} doped $Gd_2Ti_2O_7$ and (b) the reduced samples $Gd_2Ti_2O_7$: $Ce^{4+}\rightarrow Ce^{3+}$ with various doping concentration.*

Table 5.4. Peak shifting in raman modes as a function of doping concentration for both Ce^{4+} doped $Gd_2Ti_2O_7$ and reduced $Gd_2Ti_2O_7$: $Ce^{4+} \rightarrow Ce^{3+}$ samples.

Doping	**Ce^{4+} (Peak Shifting $\Delta\omega$ cm^{-1})**						**$Ce^{4+} \rightarrow Ce^{3+}$ (Peak Shifting $\Delta\omega$ cm^{-1})**					
	1st Peak	2nd Peak	3rd Peak	4th Peak	5th Peak	6th Peak	1st Peak	2nd Peak	3rd Peak	4th Peak	5th Peak	6th Peak
0 %	0.0	0.0	0.0	0.0	0.0	0.0	0.0	0.0	0.0	0.0	0.0	0.0
2 %	0.6 B	1.0 R	3.2 R	0.3 R	2.2 B	3.2 R	2.0 R	2.0 R	6.2 R	1.2 R	4.0 B	8.4 R
4 %	0.6 B	1.2 R	1.9 R	0.3 R	0.1 R	1.0 R	0.8 R	2.4 R	2.9 B	1.4 R	1.1 B	7.3 R
6 %	0.4 B	1.6 R	6.2 B	0.3 R	0.1 R	0.9 B	0.7 R	2.5 R	2.5 B	1.8 R	3.0 B	7.5 R
8 %	1.3 B	1.2 R	3.7 B	0.6 R	0.5 R	2.8 B	3.0 R	2.9 R	4.5 B	1.8 R	1.2 B	8.8 R

5.3.4. X-ray photoemission spectroscopic analysis:

X-ray photoelectron spectroscopy (XPS) is used to confirm the reduction of cerium dopant. The XPS spectrum of Ce^{4+} doped $Gd_2Ti_2O_7$ pyrochlore oxide for 6% cerium doped sample after reduction were analyzed in order to find the charge state of different ions. Figures 5.9 (a-f) show the survey and core level spectra of different elements present in the sample. Each core level spectra were fitted using the Pseudo Voigt peak shape after subtracting the Shirley or linear background. In order to account for the instrumental offset, each spectrum was calibrated using the C 1*s* peak, as shown in Figure 5.9 (a). A reference value of 284.6 eV was used for the C 1*s* binding energy and the corrected difference was then used for each element [118,184]. The charge neutralizer was used during the measurement due to the insulating nature of the sample. Figure 5.9 (b) shows the XPS survey spectra of the 6% Ce^{4+} doped reduced $Gd_2Ti_2O_7$ pyrochlore oxide. All the prominent peaks have been assigned to the respective energy levels

of the different elements present in the sample, which discard the possibility of any elemental impurity in the synthesized sample.

Figure 5.9 (c) show the Gd 3*d* core level spectra, where the two-spin orbit splitted components $3d_{5/2}$ and $3d_{3/2}$ are present at 1187.48 eV and 1219.49 eV and the binding energy difference for these two peaks are 32.01 eV and the area ratio for both the peaks are 2:3, which indicate the 3+ oxidation state of Gd in the compound [185]. Further, the Ti 2p core level spectra for the 6% cerium doped $Gd_2Ti_2O_7$ reduced sample is shown in Figure 5.9 (d), where the two peaks centered around 463.82 eV and 458.25 eV are assigned to the $2p_{1/2}$ and $2p_{3/2}$ components with energy gap 5.57 eV and area ratio of both the peaks are 1:2 indicating the peak positions and the energy separation of the two components indicate the 4+ valence state of TiO_2 in the sample [184,186]. The absence of any distortion/ splitting in the components discard the possibility of the deviation of the Ti atoms from the tetravalent state Further, the presence of cerium ions in the reduced sample (of 6% composition) is confirmed by conducted XPS measurements. As seen in Figure 5.9 (e), the reduced sample was found to contain $Ce^{4+} \rightarrow Ce^{3+}$ equilibrium towards reduction occurred during sample preparation. The low concentration of the Ce ions in the sample results in the weak signal quality, however the analysis of the spectra clearly indicates the presence of the mixed oxidation state of 3+ and 4+ for cerium ions in the sample.

As seen in Figure 5.9 (e), XPS spectrum collected for the reduced sample. Eric Beche et.al., in 2007, studied XPS for Ce 3d for $Ce_xTi_yO_7$ composition. The group study observed that Ce^{3+} and Ce^{4+} oxidation state can be distinguished through the various line shapes corresponding to the final states [187];

$$\mathrm{Ce(III)} = \mathrm{v_o} + \mathrm{v'} + \mathrm{u_o} + \mathrm{u'}$$

$$\mathrm{Ce(IV)} = \mathrm{v} + \mathrm{v''} + \mathrm{v'''} + \mathrm{u} + \mathrm{u''} + \mathrm{u'''}$$

The terms u and v are the multiplets corresponding to the $3d_{5/2}$ and $3d_{3/2}$ core holes. The spin orbit splitting is nearly 18.1 eV for every u and v and the intensity ratio $I(3d_{3/2})/ I(3d_{5/2})$ was fixed to be 2/3. From the reported previous results, we observed that the CeO_2 compound having the six multiplets (v, v", v"', u, u", u"') corresponding to Ce (IV) oxidation state. And for the $Ce_2Ti_2O_7$ compound there were four multiplets (v_o, v', u_o, u') corresponding to the Ce(III) oxidation state [187]. In Figure 5.9 (e), the XPS spectrum collected for the reduced sample contains ten peaks. The high intensity energy states u' (903.3 eV) and v' (885.2 eV) are corresponding to the Ce $3d^9$ $4f^1$ O $2p^6$ final state and the lowest binding energy state u_o (898.1 eV) and v_o (880.0 eV) are observed and are corresponding to the Ce $3d^9$ $4f^2$ O $2p^5$ final state. Hence, the reduced sample contains Ce (III) states [187].

The highest binding energy states u"' (917.2 eV) and v"' (899.1 eV) are corresponding to the Ce $3d^9$ $4f^0$ O $2p^6$ final state and the presence of u"' component is associated with Ce $3d_{3/2}$, located at the 917.2 eV position in the XPS spectrum indicating the presence of Ce (IV) state. The lowest binding energy states u (902.0 eV), v (883.9 eV), and u" (907.2 eV), v" (889.0 eV) are corresponding to the Ce $3d^9$ $4f^2$ O $2p^4$ and Ce $3d^9$ $4f^1$ O $2p^5$ final state states respectively [187]. The low concentration of the Ce ions in the sample results in the weak signal quality, however the analysis of the spectra clearly indicates the presence of the mixed oxidation state of 3+ and 4+ for cerium ions in the sample [188].

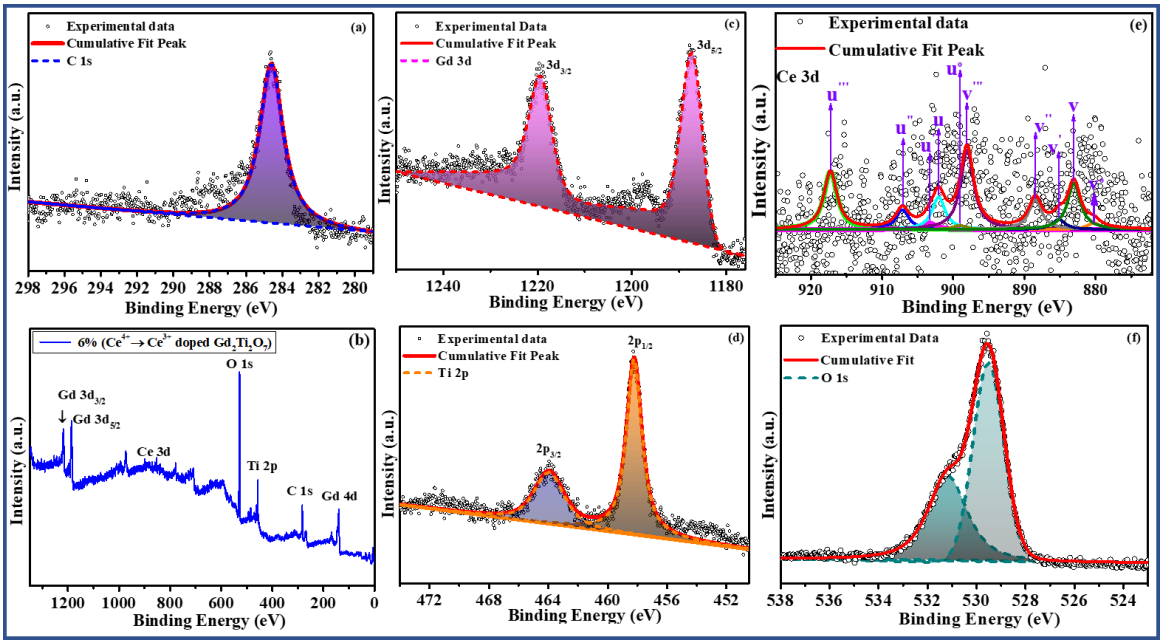

Figure 5.9. *XPS spectrum of 6% Ce^{4+} doped $Gd_2Ti_2O_7$ thermally heated in reduced environment for (a) C 1s, (b) survey spectrum, (c) Gd 4f, (d) Ti 2p, (e) Ce 3d, (f) O 1s, and Here black circles are the measured XPS spectra and red line represents cumulative fit.*

Figure 5.9 (f) represents the deconvoluted O 1s XPS spectrum of 6 % cerium doped $Gd_2Ti_2O_7$, after thermal treatment in reduced environment. The O 1s XPS spectra show the main peak at 529.5 eV, found to be due to the oxygen bounded in lattice (O^{2-}) and the second weak intense component at 531.2 eV corresponds to the surface contamination, i. e., OH-group present on the outermost surface layer of the sample [118]. Also, these two peaks may arise from the two different types of oxygen coordination geometries in the pyrochlore $Gd_2Ti_2O_7$ host. Note that in the pyrochlore structures, two different oxygen environments and cationic disordering between Gd-O and Ti-O site give rise to change of oxygen anion chemical environment. The cation Gd is less electronegative than the Ti cation and hence the Ti-O bond's ionic character is weaker than Gd-O bond. Therefore, the O 1*s* peak with the higher binding energy (531.25 eV) is attributed to the oxygen anions bounded to site cations. On the other hand, O 1s the peak

with at the lower binding energy (529.52 eV) may result from the oxygen atoms bounded to Ti-O bond [189].

5.3.5. Photoluminescence (PL) results:

The Ce^{3+} involves 4f to 5d electric dipole transition which strongly depends on the provincially surrounding of the Ce^{3+} sites present in the host $Gd_2Ti_2O_7$ pyrochlore oxide. This is why trivalent Ce^{3+} ions producing not only strong excitation and emission but also produces slight shifting in both the excitation and emission spectrum over a broad range of wavelength. Up to now, a clear difference between Ce^{3+} and Ce^{4+} emission and excitation bands have not been observed. Reducing conditions are applied to enable a clear difference between the Ce^{3+} and Ce^{4+} emission and excitation bands.

5.3.5.1. Ce^{4+} doped $Gd_2Ti_2O_7$ and effect of reduction:

We report a comparative experimentally observed PL excitation and emission spectrum results of Ce^{4+} doped $Gd_2Ti_2O_7$ pyrochlore samples and for the same samples series annealed at a temperature of 1000℃ for time 24 hours in reducing environment under the flow of gas mixture hydrogen and argon, were well represented in Figure 5.10 (a) and Fig 5.10 (b), at room temperature. The excitation spectrum in Fig 5.10 (a) shows two broad bands centered around wavelength of 255 nm and 360 nm similar to earlier report [190]. The excitation broad band from 320 nm to 400 nm with peak at nearly 360 nm is ascribed due to the band-to-band absorption of the undoped $Gd_2Ti_2O_7$ host lattice which give rise to excitation of luminescent centers [78]. Tetravalent cation Ce^{4+} does not perform 4d → 5f transition emission and excitation, therefore in Figure 5.10 (a) all the unreduced samples of Ce^{4+} doped $Gd_2Ti_2O_7$, shows that with increasing Ce^{4+} ion doping in host $Gd_2Ti_2O_7$, reduces the excitation intensity of host material $Gd_2Ti_2O_7$ which is also represented by inset enlarged view for the unreduced samples. But for the reduced samples, these bands at 255 nm and 360 nm were appeared due

to the 4f → 5d transition of the cerium trivalent (Ce^{3+}) ion presence as Ce^{4+} ions reduced to Ce^{3+} and at the 360 nm excitation peak of host $Gd_2Ti_2O_7$ also appeared and the peak intensity increases with the reduction and doping. The emission spectrum for fixing excitation wavelength λ_{ex} = 255 nm were recorded and represented in Figure 5.10 (b) shows that the emission band nearly around ~ 400 nm wavelength were observed due to the 5d to 4f transition of Ce^{3+} ions. But as the excitation wavelength spectrum has high intensity band at 360 nm as compared to 255 nm, so we have taken into consideration the emission spectrum at λ_{ex} = 360 nm [191].

The emission spectrum at fixed excitation wavelength λ_{ex} = 360 nm, for the complete series with or without reduction were presented in Figure 5.10 (c). For the host, emission spectrum was recorded at excitation wavelength of 360 nm, it was observed that an emission peak around 425 nm is attributed due to host $Gd_2Ti_2O_7$ containing gadolinium ion [150]. As tetravalent cation Ce^{4+} does not perform 4d → 5f transition emission, therefore it is charge transfer (CT) emission in case of reduced samples. The band in case of reduced samples exhibits a broad band centered around 425 nm can be attributed due to the transition from lowest 5d state to $^2F_{5/2}$ and $^2F_{7/2}$ components of the ground state as shown in Fig 5.10 (b). Thus, we can say that CT emission might occur in the same place as 4d → 5f in case of Ce^{3+} emission. In the excitation spectra, the reduced samples have tail from the lower energy side suggesting few constituents. According to crystal field splitting of d^1 orbital of Ce^{3+} ions in a cubic symmetry ($Gd_2Ti_2O_7$), the T_{2g} energy level always lying below the E_g. As we know Ce^{3+} has $4f^1$ ground state having only one electron and this electron is excited to 5d level and it produces excitation peak at 360 nm. This excitation peak is due to the radiative transition from 5d (T_{2g}) level to the $^2F_{5/2}$ and $^3F_{7/2}$ levels of the ground state causing emission peak doublet around 425 nm. We observed that the PL spectrum shows blue shifting of Ce^{3+} emission peaks in cubic crystal structure of $Gd_2Ti_2O_7$ host. When cerium entering in the cubic host lattice $Gd_2Ti_2O_7$, the

electron shell of cerium expands and therefore, decreases electrostatic interaction between the electrons due to which the excited state energy reduces from their free ion values. This blue shift in the emission spectrum is interpreted in terms of chemical bonding properties of ligands like oxygen, which affects the absorption band position [192]. Moreover, it was clearly observed from the emission results of all the cerium doped samples with or without reduction show bright blue emission and the emission intensity depends on the concentration of cerium ion.

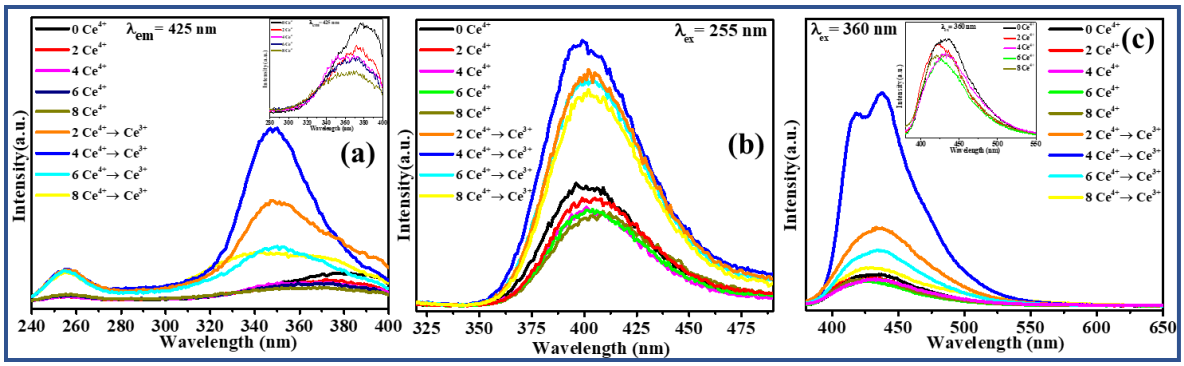

Figure 5.10. *Comparative (a) excitation, (b) emission spectrum (for λ_{ex}= 255), and (c) emission spectrum (for λ_{ex}= 360) for Ce^{4+} doped $Gd_2Ti_2O_7$ pyrochlore host and reduced $Ce^{4+} \rightarrow Ce^{3+}$ samples.*

Overall, it is found for the series of Ce^{4+} doped samples that the emission intensity decreases with increasing doping of Ce^{4+} ion in the host as Ce^{4+} does not show emission due to 4f → 5d transition. But for the reduced samples firstly the intensity goes on maximum up to doping concentration of 4% after that it again decreases due to the effect of concentration quenching [144]. Therefore, the emission intensity increases under reducing environment as a result of reduction of Ce^{4+} ions to Ce^{3+}, for the complete series of samples at room temperature. This is because in comparison to the closed shell of Ce^{4+}, the trivalent Ce^{3+} is having single optically active electron which is associated with the $^2F_{7/2} \rightarrow {}^2F_{5/2}$ electronic transition within the $4f^1$ orbital in the ground state configuration of Ce^{3+} [193].

5.3.6. CIE chromaticity coordinates:

The exact information about the emission color and the color purity of the prepared samples can be measured using chromaticity diagram and CIE coordinates [145]. Customary Commission International de I'Eclairage (CIE) 1931 diagram is used to estimate the emission color and color coordinates (x, y) of $Gd_2Ti_2O_7$ doped Ce^{4+} and simultaneously for the same set of samples sintered at high temperature in reduced environment under the excitation wavelength of 360 nm. In Figure 5.11, the CIE coordinates (x = 0.1544, y = 0.0590) and (x = 0.1562, y = 0.0079) represented by the green- and yellow-colored spherical balls for both the unreduced ($Gd_2Ti_2O_7$: Ce^{4+}) and reduced ($Gd_2Ti_2O_7$: $Ce^{4+}\rightarrow Ce^{3+}$) samples respectively, for the optimized concentration (*i.e.*, 4% doping of cerium). The calculated CIE coordinates for both the samples are found to present in the pure blue region of the CIE color plot suggesting that the prepared samples may be used as blue emitting phosphors for the further production of WLED's.

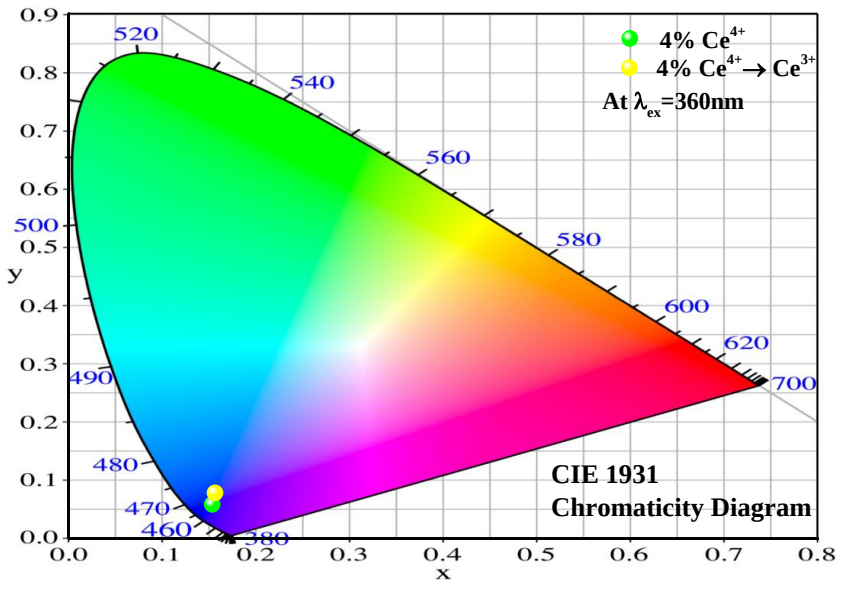

Figure 5.11. *Schematic CIE 1931 diagram for the cerium doped $Gd_2Ti_2O_7$ reduced and unreduced samples.*

The quality of the color emission has been calculated through Corelated Color Temperature (CCT) using CIE coordinates. And the CCT has been measured using McCamy empirical formula which is given by the following equation (5.5) [144];

$$\mathrm{CCT} = -449u^3 + 3525u^2 - 6823.3u + 5520.33 \ldots\ldots\ldots (5.5)$$

Here, $u = \frac{x-x_e}{y-y_e}$; is the inverse slope line. And the $x_e = 0.3320$, $y_e = 0.1858$ are the epicenter coordinates. The values of CCT calculated from equation (4) were found to be 1779 K and 2021 K for the $Gd_2Ti_2O_7$: Ce^{4+} and reduced ($Gd_2Ti_2O_7$: $Ce^{4+} \rightarrow Ce^{3+}$) samples respectively, for the optimum doping concentration of 4% of cerium, which could be useful for the production of WLEDs.

5.4. Conclusion:

A series of Ce^{4+} doped $Gd_2Ti_2O_7$ pyrochlore oxides with a doping concentration; namely 2%, 4%, 6%, and 8% were successfully formed *via* high temperature solid state reaction route. The crystal structure and disordering driven luminescence properties were investigated for all the samples. XRD analysis along with Raman vibrational spectroscopy confirms the formation of single phasic pyrochlore oxide structure. SEM micrographs confirms the formation of nearly spherical agglomerated particles having average grain size ~1.2 ± 0.006 μm in the synthesized highly dense materials. The doping of bigger sized Ce^{4+} ion over Ti^{4+} at the B-site results in lattice expansion and introduction of lattice strain. All the Raman vibrational bands show a red-shifts caused by increasing bond-length or decreasing force constant on the compositional substitution of Ce^{4+} atoms at the place of Ti^{4+} with mismatched ionic radii causing disordering in the crystal structure. The Ce^{4+} cationic oxidation state was converted to Ce^{3+} oxidation state by heating in reduced environment of H_2 (10%) and argon (90%) flow at a temperature of

1000℃ for 24 hours duration. The reduction of cerium ion *i.e.*, $Ce^{4+} \rightarrow Ce^{3+}$ is confirmed through XPS analysis. XPS results for the 6% cerium doped pyrochlore sample showed a mixed oxidation state of 3+ and 4+ for cerium ion in the reduced sample. The effect of $Ce^{4+} \rightarrow Ce^{3+}$ conversion is effectively studied *via* XRD, Raman, and Photoluminescence results. Diffraction patterns of reduced samples show a relatively larger shifting towards lower 2θ value as compared to unreduced samples due to the conversion of Ce^{4+} (0.87 Å) into Ce^{3+} (1.01 Å). The reduction has also induced more strain in the pyrochlore lattice structure. Like XRD results, Raman spectra of all the reduced samples also show relatively more vibrational band shifting (red shift) on compositional substitution of cerium cation as comparison to the unreduced samples. The PL excitation (at λ = 425 nm) contains two broad bands at 255 nm (4f to 5d transition of the cerium trivalent ion) and 360 nm (due to band-to-band absorption of host $Gd_2Ti_2O_7$ and due to the 4f to 5d transition of the cerium trivalent ion). PL intensity goes on increasing up to a doping of 4% of cerium after that again decreases due to the concentration quenching effect. PL emission (at λ = 360 nm) exhibits a broad band centered around 425 nm can be attributed due to the transition from lowest 5d state to $^2F_{5/2}$ and $^2F_{7/2}$ components of the ground state. This radiative transition from 5d (T_{2g}) level to the $^2F_{5/2}$ and $^3F_{7/2}$ levels of the ground state causing emission peak at doublet around 425 nm. The Photoluminescence results for both the reduced and unreduced series shows that on reduction of Ce^{4+} into Ce^{3+} state, reduced samples show blue shifting of Ce^{3+} emission peaks in cubic crystal structure of $Gd_2Ti_2O_7$ host, due to the expansion of crystal size of cerium in Ce^{3+} state. It was clearly observed from the emission results of all the ceria doped samples with or without reduction that bright blue emission and the emission intensity depends on the concentration of cerium ion. Hence, reduced samples of Ce^{4+}: $Gd_2Ti_2O_7$ would have a potential application in the mass production of blue LED chips for the further, fabrication of WLED's.

Chapter 6

Influence of Al^{3+} co-doped ions for the improvement of orange reddish light emitting photoluminescence characteri-stics of $Gd_2Ti_2O_7:Eu^{3+}$ pyrochlore

In this chapter main focus is to study the enhanced luminescence emission and corelation of structural and optical properties for a series of powdered samples of $Gd_{1.92}Ti_{2-x}O_7:Eu_{0.08}Al_x$ with Al^{3+} doping (where x = 0, 0.02, 0.04, 0.06, & 0.08). Raman spectroscopy analysis revealed that high intensity vibrational bands displayed a blue shift upon the introduction of Al^{3+} substitution in the $Gd_{1.92}Eu_{0.08}Ti_2O_7$ host lattice, the purity of the produced samples was confirmed using X-ray diffraction analysis. Photoluminescence results show that the Al^{3+} doped $Gd_{1.92}Eu_{0.08}Ti_2O_7$ pyrochlore oxides have prominent orange-reddish emission spike at 588 nm caused by the $^5D_0 \rightarrow {}^7F_1$ transition, as well as emission peaks at 612 nm coming from the trivalent europium ions' $^5D_0 \rightarrow {}^7F_2$ transition. The measured CIE coordinates (x = 0.622 and y = 0.351), which are dependent on the emission profile under 322 nm excitation, closely matched those of the commercial phosphor $Y_2O_2S:Eu^{3+}$. The results show that the Al^{3+} doped $Gd_{1.92}Eu_{0.08}Ti_2O_7$ pyrochlore oxides used as orange-reddish emitting components in luminous devices.

6.1. Introduction:

Rare earth ion-doped inorganic compounds are a significant family of phosphor materials that have been used in various applications like plasma display panels (PDPs), field emission displays (FEDs), efficient white light emitting diodes (WLEDs), optical communication, in addition to other bio-medical applications (PDP) [112,194–196]. WLEDs are serving as a viable replacement for conventional incandescent, xenon, halogen, and fluorescent lights today, due to their extraordinary luminous efficiency, low energy consumption, low gas emissions, reliability, great brightness, compact design, quick switching, environmental friendliness, and long working lifetime [197–202]. One of the crucial methods for creating effective commercial WLEDs is phosphor conversion (pc) emission, which combines blue LEDs and yellow phosphor ($Y_3Al_5O_{12}$:Ce^{3+}) [140,203]. There are primarily two methods that have been used to create WLEDs. The first option uses monochromatic red, green, and blue LED light that is directly combined to produce white light emission using phosphor-free RGB-LEDs [204,205]. For each embedded LED to emit steady white light, it requires a different driving current, which makes it more challenging to obtain and these are less available. Another strategy to achieve white light emission is through mixing a blue light-emitting InGaN chip with a yellow phosphor (YAG: Ce^{3+}), a material that is already useful in many commercial WLEDs [206–208]. However, due to the lack of red light in these commercial WLEDs, PL spectral profiles results in a small colour rendering index and a high value for correlated colour temperature (CCT) [209]. Therefore, a red-light emitting phosphor using UV, near-UV, or blue light stimulation is needed, can solve the problem of red element, to improve the colour rendering index, light colour tolerance and CCT values. White light emission through an individual host structure is made through (a) substituting a single rare earth ion, (b) adding multiple rare earth ions, (c) co-doping multiple ions & governing emission through energy transfer mechanism, & (d) managing the defect generation through ion level [145,179].

Crystalline host and dopant are the two major ingredients needed to produce luminescent materials. As the high melting point and excellent mixing of rare-earth ions regardless of their chemical & physical characteristics, ternary pyrochlore oxides are regarded as appropriate hosts for more efficient luminous active ions [150]. Because of the superior optical [74], magnetic [52], electrical [126], and dielectric characteristics [189], pyrochlore oxide structures with the general formula $A_2B_2O_7$ have shown to be satisfactory host materials for the intensification of luminescence characteristics of fluorescent centres in different domains of scientific technology and mechanisms. These applications include ionic/electric conductors [147], catalysts [174], radioactive waste management [173,182], and several others. The ternary oxides have general formula $A_2B_2O_7$ include pyrochlores. The derived pyrochlore architecture differs from the parent structure (fluorite, or AX_2) in that it includes two different types of cations and lacks one-eighth of an oxygen ion. Eight molecules make up each unit cell of the cubic pyrochlore oxide $A_2B_2O_7$, which is a variant of the fluorite structure with the Fd3m space group and two different variety of cations at the A- and B-sites. Large-sized rare earth ions with a 3+ covalency make up the cations at site A, while smaller-sized cations with a 4+ covalency are found at site B [159,173]. Due to the removal of oxygen atoms, the B-site cations are 6-fold coordinated and are situated within a distorted octahedron, which includes six anions at equivalent distance from the central cation. The A-site cations are 8-fold coordinated to the oxygen anion & are placed within a distorted cubic coordination polyhedron (consist of 6 equi-spaced anion oxygens at a somewhat diminished distance from the central cation) [72].

Two different sorts of oxygen sites 48f and 8b for pyrochlore structures known as Wyckoff locations. The positions of oxygen and the rare earth cations A^{3+} and B^{4+} are coordinated within Wyckoff notation 48f at (x, 0.5, 0.5). In a tetrahedron coordinated to solely rare earth A^{3+} cations, oxygen is placed at (0.375, 0.375, 0.375) for the other 8b Wyckoff notation [173].

Pyrochlore structures have a single positional parameter, x, whose value ranges from 0.309 to 0.355 and a nearly ~10 Å unit lattice parameter. In order to explain the phase strength of pyrochlore structures, the relative cationic radii ratio of cations A and B, or r_A/r_B, was used. The range of the cation radii ratio for stable pyrochlore oxide structures is 1.460-1.780 [150]. Several ternary pyrochlore oxide compositions ($Gd_2Ti_2O_7$, $Ln_2Ti_2O_7$, $Gd_2Zr_2O_7$, $Nd_2Zr_2O_7$, and $Ho_2Ti_2O_7$ etc.) were successfully prepared and reported as they show excellent optical properties when doped with trivalent rare earth ions like Eu^{3+}, Tb^{3+}, Sm^{3+}, and Er^{3+} etc. [93,119,121,150,210]. The current study concentrated on titanate-based pyrochlore oxides because they could be produced easily at room temperature and also a potential applicant for ceramic pigments as they meet the key criteria of high melting temperature (>1600 °C), higher refractive index, also the ability to hold 1st row transition metal ions in the crystal at the location of octahedrally coordinated site [119,178]. In order to increase the luminescence intensity for the fabrication of WLEDs, the rare earth-based pyrochlore ternary oxide $Gd_2Ti_2O_7$ was chosen as the host lattice in the luminous material. This is because $Gd_2Ti_2O_7$ generates high-quality substituted element that is defect-free and can be excellent for practical applications. $Gd_2Ti_2O_7$ possesses a structurally robust pyrochlore framework, due to its larger cationic radii ratio of 1.75, which enables the accommodation of various trivalent lanthanide ions without undergoing phase transformation or segregation [211]. Alongside its structural and chemical adaptability, $Gd_2Ti_2O_7$ offers a favourable localized environment that exhibits strong luminescent, optical, magnetic, and electrical properties [82,116,118,212,213].

For the creation of optoelectronic equipment's, which mostly require red light element, Eu^{3+} active red phosphors are commonly used as the favourable red-emitting elements of WLEDs due to significant orange-reddish emission spectrum resulting from the 4f→4f transition of Eu^{3+} [40,41]. M.L. Pang et. al, prepared Eu^{3+} doped $Gd_2Ti_2O_7$ thin films through sol gel method and reported its photoluminescent properties and observed that the optimised level for Eu^{3+}

were found to be 9 at.%. of Gd^{3+} for $Gd_2Ti_2O_7$ film host. [79]. M. Saif, prepared ($Gd_2Ti_2O_7$:Ln^{3+}) [Ln^{3+}=Eu^{3+} or Dy^{3+}] through sol-gel technique and study its luminescent characteristics on the basis of energy transfer mechanism and the optimum concentration is 5 mol% for Eu^{3+} rare earth cation in $Gd_2Ti_2O_7$ host lattice [74]. Sanja Culubrk et. al., prepared rare earth (Sm^{3+} and Eu^{3+}) doped $Gd_2Ti_2O_7$ composition through the combined metal–citric acid complex procedure and study its luminescent properties and observed strong emission results are formed for the doping concentration of 5 mol % Eu^{3+} for the host $Gd_2Ti_2O_7$ [54]. Zhang Ying et.al., prepared Eu^{3+}/V^{5+} co-doped nanocrystalline $Gd_2Ti_2O_7$ samples using sol gel method and studied their role of annealing temperature on luminescent characteristics of host lattice for the optimum doping concentration of Eu^{3+} (4 mol%) and this study provides more detailed information about the doping level, as in this study it contains a series of samples $Gd_{2(1-x)}Eu_{2x}Ti_2O_7$ with x = 0.01, 0.02, 0.03, 0.04, 0.05, and 0.06, out of these samples the 4 mol% doping Eu^{3+} give the best photoluminescence results while in the other studies only single doping composition was considered. Therefore, this study provides a clear idea about the best doping concentration of Eu^{3+} in the $Gd_2Ti_2O_7$ for better luminescence results [78].

However, the low efficiency of $Gd_2Ti_2O_7$:Eu^{3+} phosphors also restrict their use. To increase the luminous efficacy of phosphors, a straightforward and effective technique is to dope them with some other metal elements. The activated ions can effectively receive photon energy from the inserted metal ions, increasing the luminescence intensity of the ions. The cation Al^{3+} is a widely recognised sensitizer, useful for enhancing the Eu^{3+} luminescence qualities in numerous crystals as the luminescence intensity of the activated ions is increased through incorporation of Al^{3+} metal ions [84]. Hence according to the previous reported luminescence results the best optimised doping level of the Eu^{3+} cation is 4 mol% for the host $Gd_2Ti_2O_7$ lattice. A modified solid state reaction approach was used in this study to create a series of $Gd_{1.92}Ti_{2-x}O_7$:$Eu_{0.08}Al^{3+}_x$

(x = 0, 0.02, 0.04, 0.06, and 0.08) powders. The final product series was produced and their structural characteristics, morphology, and photoluminescence spectra were all thoroughly examined.

The current study integrates optical investigations with structural analysis, revealing that the optimal doping concentration for the $Gd_{1.92}Ti_{2-x}O_7:Eu_{0.08}$ series doped with Al^{3+} is determined to be 2.0 mol%. This particular concentration maintains the integrity of the pyrochlore structure, and the corresponding CIE coordinate set for this pyrochlore composition aligns with in the standard orange-reddish light calorimetric point.

6.2. Experimental section:

6.2.1. Sample preparation:

A traditional multi-step solid-state approach was utilized to create a series of pure phasic Al^{3+} doped $Gd_{1.92}Ti_{2-x}O_7:Eu_{0.08}Al^{3+}_x$ (where x = 0, 0.02, 0.04, 0.06, & 0.08) pyrochlore powdered samples via mixing and grinding high-purity raw powders of Gd_2O_3 (CAS No.:12064-62-9, 99.9% purity, Sigma Aldrich), TiO_2 (CAS No.:1306-38-3, 99.95% purity, Sigma Aldrich), Eu_2O_3 (CAS No.:1308-96-9, 99.9% purity, Sigma-Aldrich) and Al_2O_3 (CAS No.:1344-28-1, 99.5% purity, Sigma-Aldrich). For the creation of series of final powdered samples, the systematic procedure was carried out during the solid-state technique which is depicted in Figure 6.1. Lanthanide-based oxides readily generate hydroxides, carbonates, and oxycarbonates when unprotected to the atmosphere because these oxides are extremely reactive with water and carbon dioxide [86]. As a result, firstly, the powders Gd_2O_3, TiO_2, Eu_2O_3 & TiO_2 were substantially warmed at high temperature of 900 ^oC for 4 h to remove extra moisture and volatile impurities [158].

Following the preheating stage, the precise weights, are shown in Table 6.1, of stoichiometric amounts for each reagent Gd_2O_3, TiO_2, Eu_2O_3 and Al_2O_3 were measured using weighing

machine. Three grams of each of the precursor materials, Gd_2O_3, TiO_2, Eu_2O_3 and Al_2O_3, were combined and thoroughly milled for 7 hours to create homogeneity and uniformity in the experimental final product.

Table 6.1: The 3-g batch of $Gd_{1.92}Ti_{2-x}O_7:Eu_{0.08}Al^{3+}_x$ series was made using parent materials of Gd_2O_3, Eu_2O_3, Al_2O_3 and TiO_2.

Al^{3+} (in %)	Composition	Gd_2O_3 (gram)	Eu_2O_3 (gram)	Al_2O_3 (gram)	TiO_2 (gram)
0 %	$Gd_{1.92}Eu_{0.08}Ti_2O_7$	1.3338	0.0540	0	0.6122
1 %	$Gd_{1.92}Eu_{0.08}Ti_{1.98}Al_{0.02}O_7$	1.3353	0.0540	0.0039	0.6068
2 %	$Gd_{1.92}Eu_{0.08}Ti_{1.96}Al_{0.04}O_7$	1.3368	0.0541	0.0078	0.6013
3 %	$Gd_{1.92}Eu_{0.08}Ti_{1.94}Al_{0.06}O_7$	1.3383	0.0541	0.0118	0.5958
4 %	$Gd_{1.92}Eu_{0.08}Ti_{1.92}Al_{0.08}O_7$	1.3398	0.0542	0.0157	0.5903

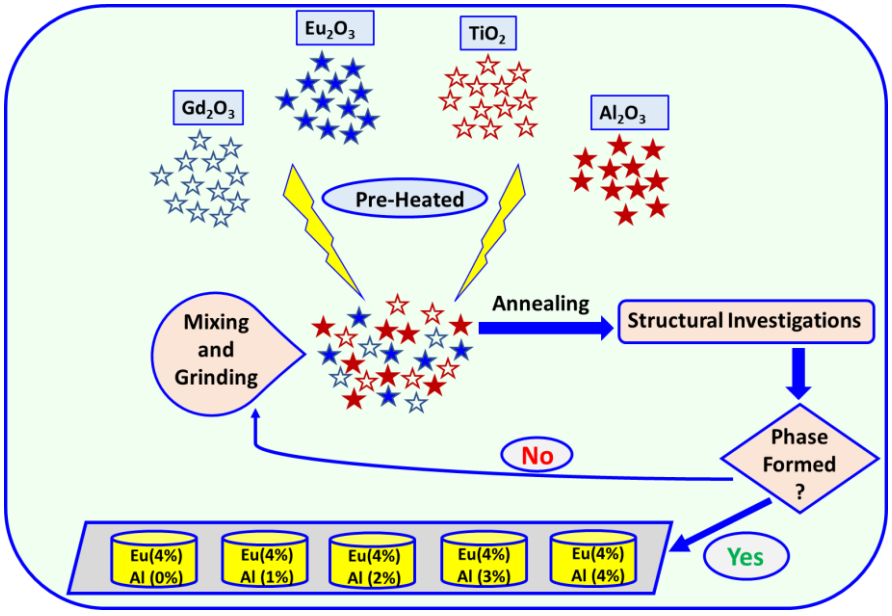

Figure 6.1. *Schematic diagram of $Gd_{1.92}Ti_{2-x}O_7:Eu_{0.08}Al^{3+}_x$ (x = 0, 0.02, 0.04, 0.06, and 0.08) powders.*

By exerting a 4.2 torr pressure on hydraulic press tool using a stainless-steel die set, all powders are finely combined and ground, were transformed into pellets of approximately 10 mm diameter and 1.5 nm thickness.

Using a high temperature muffle furnace, the pellets were sintered in an alumina boat for 36 hours at a temperature 1150 ^{o}C. The pellets were again ground for four hours in mortar and pestle, pelletized, and annealed at a final temperature of 1250°C for 45 hours following heating rate of 3°C/min & cooling rate at 1°C/min to create high density products. Using the starting precursors Gd_2O_3, TiO_2, Eu_2O_3 and Al_2O_3 utilising the solid-state technique, a succession of powdered series of $Gd_{1.92}Ti_{2-x}O_7$:$Eu_{0.08}Al^{3+}{}_x$ (x = 0, 0.02, 0.04, 0.06, and 0.08) were produced as follows the equation (6.1):

$$0.96\ Gd_2O_3 + 0.04\ Eu_2O_3 + (2-x)TiO_2 + \frac{x}{2}Al_2O_3 \rightarrow\ Gd_{1.92}Eu_{0.08}Ti_{2-x}Al_xO_{7-\delta} \ldots\ldots (6.1)$$

6.2.2. Sample characterization of Al^{3+} doped $Gd_{1.92}Eu_{0.08}Ti_2O_7$ oxide composition:

All pellets were analysed through X-ray diffraction characterisation for the structural phase compositions of the acquired samples. All the pellets were subjected to XRD measurements at Delhi Technological University (DTU), New-Delhi, using an X-ray diffraction equipment made by Bruker Company (Model Number-D8-Advance) and a CuK_α radiation source with a wavelength of 1.5406 and 0.01671 step size. At Jawaharlal Nehru University, Raman plots for complete series of powders were observed by using laser light of 532 nm in the WITec Alpha 300RA Raman microscope outfitted with 50-objective lens. All the sample's PL excitation and emission spectra was captured using a Jasco-8300 fluorescence spectrometer at ambient temperature using a Xenon lamp light source at the DTU in New Delhi. The life time decay

measurements were done at Jamia Milia Islamia (JMI) using Time-Resolved Fluorescence Lifetime measurement spectrometer machine of Horiba company with model DeltaFlex01-DD.

6.3. Results and discussion:

6.3.1. Structural investigations:

6.3.1.1. XRD results:

The as-synthesised sample has undergone structural analysis for the complete series of Al^{3+} doped GTO, utilising X-ray diffraction (XRD) technique. For all five sets of samples of $Gd_{1.92}Ti_{2-x}O_7$:$Eu_{0.08}Al^{3+}_x$ (x = 0, 0.02, 0.04, 0.06, and 0.08) XRD figure were plotted in the 2θ dimension 10^o to 90^o, all the XRD patterns are same and miller indices for each peak were marked as shown in Figure 6.2 (a). The background and diffraction peaks were fitted using the six-coefficient polynomial function and the pseudo-Voigt function, respectively. It displays two separate sets of diffraction peaks, the first of that has a higher intensity and corresponds to the fluorite sub-cell for the set of planes (222), (400), (440), (622), (444), (800), (662), and (840) located at 30.67^o, 35.50^o, 50.94^o, 60.48^o, 63.45^o, 74.72^o, 82.72^o, and 85.36^o, respectively. The second set of intensity peaks has a lower intensity and corresponds to the highly ordered pyrochlore superstructure for the planes (111), (311), (331), (511), (531), (551), and (731) situated at 15.36^o, 29.33^o, 38.77^o, 46.56^o, 53.43^o, 65.64^o, and 71.26^o, respectively, depicted by an symbol diamonds (♦) in Figure 6.2 (a) [173,182].

The X-ray diffraction study includes a reference comparison with the JCPDS No.23-0259 for $Gd_2Ti_2O_7$ phase [82]. The XRD patterns produced showed a good match between all diffraction peaks and the standard card, confirming the presence of a single phase free of impurities and with good crystallinity for the $Gd_{1.92}Eu_{0.08}Al_xTi_{2-x}O_7$ phosphors. These XRD data revealed that the Al^{3+} ions could fully incorporate into the host lattice, resulting in a crystal structure similar to $Gd_2Ti_2O_7$. The substitution of Ti^{4+} ions by Al^{3+} ions resulted in no notable phase alterations.

Therefore, based on the XRD results, we deduced that the transition ion Al^{3+} ion has been entirely dissolved at B site inside the host $Gd_{1.92}$ $Eu_{0.08}Ti_2O_7$ lattice and the incorporation of Al^{3+} over Ti^{4+} into $Gd_{1.92}$ $Eu_{0.08}Ti_2O_7$ doesn't change fundamental crystal architecture of pyrochlore oxide.

A modest variation in the lattice cell parameter can be used to explain the minor shift in peak location to higher angles that is seen with increased Al^{3+} content at the place of Ti^{4+} site. Since Al^{3+} has a smaller cationic radius (r_{Al} = 0.535 Å) than Ti (r_{Ti} = 0.605 Å), when Al^{3+} is substituted for Ti at the B-site, the lattice parameter decreases, shifting the peak location of the XRD spectrum along the higher 2θ angle side. According to Fig 6.2 (b), the immense intensity diffraction peak (222) is amplified and plotted from 30.2 to 31.2. On serial doping of Al^{3+}, which is depicted by the solid green line in Figure 6.2 (b), it can be easily seen that this (222) peak is gradually displaced on the higher angle side (from 2θ = 30.67º to 30.74º). Since Al^{3+} doping had no effect on the peak intensity for any of the powders, the stability of the crystalline texture was able to prevail out. The (222) indexed peak, however, has shifted for all samples towards the higher angle side, suggesting a decrease in lattice parameter (from 10.0438 Å to 10.0376 Å) on adding Al^{3+} level, by virtue of the shrinkage of the crystalline lattice, which is associated to the doping of smaller size Al^{3+} (0.535 Å) at comparatively large size Ti^{4+} (0.605 Å). The unit cell parameter decreases by 0.06% when Al^{3+} is maximally incorporated into the $Gd_{1.92}$ $Eu_{0.08}Ti_2O_7$ structure.

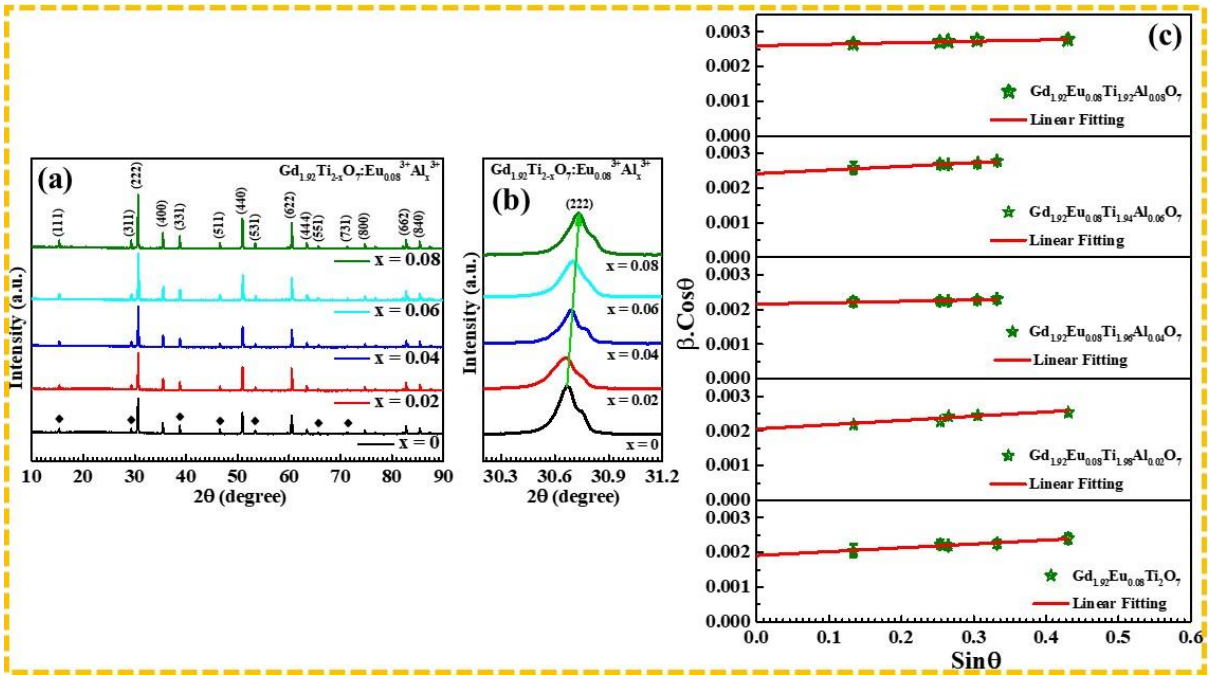

Figure 6.2; *(a) Patterns of XRD for the entire set of Al^{3+} doped $Gd_{1.92}$ $Eu_{0.08}Ti_2O_7$, (b) Peak shift for the (222) peak, and (c) W-H plot for each sample.*

Williamson-Hall Plot (WHP) formula given by equation (6.2) [121,215], was used to compute the strain and crystallite size for each sample of Al^{3+} doped $Gd_{1.92}$ $Eu_{0.08}Ti_2O_7$, and the results are shown in Table 6.2.

$$\frac{\beta_{h,k,l} * \cos\theta}{\lambda} = \frac{0.94}{D} + \frac{4\varepsilon * \sin\theta}{\lambda} \ldots\ldots\ldots (6.2)$$

Here, the parameters 'ε' and 'λ' stands for the host strain and the wavelength of the X-ray source (1.5046 Å) employed in XRD diffraction, respectively. Parameter '$\beta_{h,k,l}$' is the width of diffraction maximum (FWHM) for various 2θ standards. Here, the mathematical value 0.94 is the structural factor applied to spherical particles with a cubic structure, and 'D' refers to the size of the crystallite. To determine the strain and crystallite size, the calculated amount of '$\beta_{h,k,l} \times \cos\theta$' were drawn as a function of 'sinθ' values and fitted using a straight line [216], as depicted in Figure. 6.2 (c) for entire series. The strain 'ε' and crystallite size 'D' were further determined using the slope of a straight line and the y-intercept, respectively. The structural

parameters that were determined from the XRD patterns of the Al^{3+} doped $Gd_{1.92}$ $Eu_{0.08}Ti_2O_7$ samples were displayed by Table 6.2. In order to determine an estimation of FWHM and peak position for the W-H formalism, the pseudo-Voigt profile polynomial was fitted for the five strongest peaks.

Table 6.2: Structural characteristics for Al^{3+} doped $Gd_{1.92}$ $Eu_{0.08}Ti_2O_7$ pyrochlore for all compositions via XRD data.

Degree of doping 'x'	**Composition**	**Intercept**	**Slope**	**Crystallite size 'D' (Å)**	**Strain 'ε'**
x = 0	$Gd_{1.92}Eu_{0.08}Ti_2O_7$	0.0019 ± 0.0001	0.0011 ± 0.0002	758.1814 ± 15.6	0.00028 ± 0.00004
x = 0.02	$Gd_{1.92}Eu_{0.08}Ti_{1.98}Al_{0.02}O_7$	0.0021 ± 0.0001	0.0021 ± 0.0004	702.9740 ± 3.08	0.00031 ± 0.00001
x = 0.04	$Gd_{1.92}Eu_{0.08}Ti_{1.96}Al_{0.04}O_7$	0.0022 ± 0.0000	0.0022 ± 0.0001	673.5472 ± 10.4	0.00099 ± 0.00004
x = 0.06	$Gd_{1.92}Eu_{0.08}Ti_{1.94}Al_{0.06}O_7$	0.0024 ± 0.0001	0.0024 ± 0.0002	600.8823 ± 10.07	0.00026 ± 0.00005
x = 0.08	$Gd_{1.92}Eu_{0.08}Ti_{1.92}Al_{0.08}O_7$	0.0026 ± 0.0000	0.0026 ± 0.0001	556.9717 ± 2.86	0.00011 ± 0.00001

The diffraction plots for all samples were further analysed through the Rietveld refinement programme Fullprof-2005 [159] for additional structural investigation. Change in the structural variables derived from the Rietveld refinement of $Gd_{1.92}$ $Eu_{0.08}Ti_2O_7$ with increasing Al^{3+} content at the place of Ti^{4+}-site, is depicted in Figure 6.3, and the observed values are given in Table 6.3. Linear interpolation was used to fit the background while the pseudo-voigt function

was used for the fitting of experimental data. The rise in Al^{3+} in $Gd_{1.92}$ $Eu_{0.08}Ti_2O_7$ causes the lattice parameter to linearly decrease due to the contraction of the host lattice, as is seen from Table 6.3.

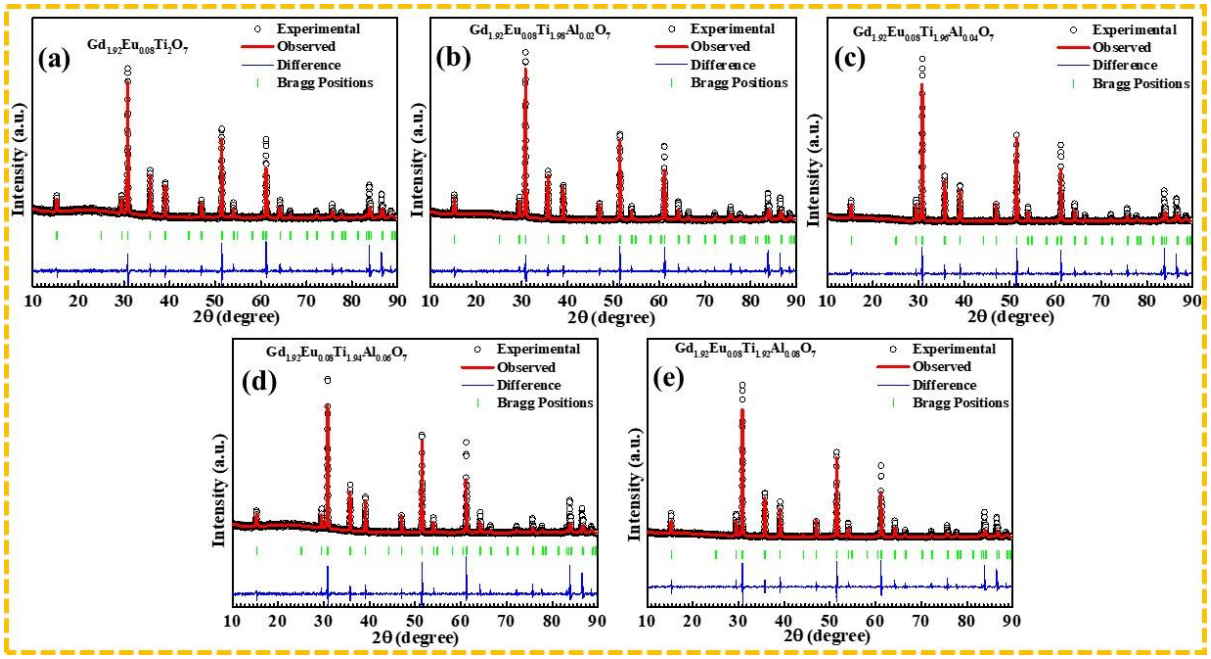

Figure 6.3. *Refined XRD plots for the $Gd_{1.92}Ti_{2-x}O_7$:$Eu_{0.08}Al^{3+}{}_x$ samples with x = 0.0, 0.02, 0.04, 0.06, and 0.08.*

In Table 6.3, the lattice parameter, Braggs component (R_B), volume (V), weight components R_{wp} and R_e, and quality of fitting (χ^2) for all samples with adding amounts of Al^{3+} ions at the position of Ti^{4+} were listed. In the refined plot for each composition, the red line indicating the refined intensity/observed intensity, the blue line shows the difference between the empirically noticed and measured intensities, the green vertical line symbol denotes the locations of Bragg's peaks and the black loop reflects experimental intensity data.

Table 6.3. Full-Prof Suite structural parameters for the diffraction patterns of $Gd_{1.92}Ti_{2-x}O_7:Eu_{0.08}Al^{3+}_x$ powdered samples with x = 0.0, 0.02, 0.04, 0.06, and 0.08.

Al^{3+} 'x'	**Composition $Gd_{1.92}Ti_{2-x}O_7:Eu_{0.08}Al^{3+}_x$**	**Lattice parameter (Å)**	**R_p, R_e, R_{wp}, χ^2**	**Volume $(Å)^3$**
x = 0	$Gd_{1.92}Eu_{0.08}Ti_2O_7$	10.0438	54.1, 16.7, 35.9, 4.6	1013.200
x = 0.02	$Gd_{1.92}Eu_{0.08}Ti_{1.98}Al_{0.02}O_7$	10.0423	48.0, 16.1, 33.4, 4.3	1012.732
x = 0.04	$Gd_{1.92}Eu_{0.08}Ti_{1.96}Al_{0.04}O_7$	10.0420	49.6, 15.4, 36.3, 5.6	1012.668
x = 0.06	$Gd_{1.92}Eu_{0.08}Ti_{1.94}Al_{0.06}O_7$	10.0397	59.8, 40.5, 17.4, 5.4	1011.953
x = 0.08	$Gd_{1.92}Eu_{0.08}Ti_{1.92}Al_{0.08}O_7$	10.0376	49.4, 14.8, 36.9, 6.2	1011.326

6.3.1.2. Raman spectroscopic results:

The technique of Raman spectroscopy is essential for analysing the short-range structural dynamics of all specimens, including deformations, flaws, ordering, phonon-phonon and electron-phonon interactions. The Raman bands of $Gd_{1.92}Ti_{2-x}O_7:Eu_{0.08}Al^{3+}_x$ with (x = 0.0, 0.02, 0.04, 0.06, and 0.08) pyrochlore compounds are displayed in Figure 6.4. According to previous research, the pyrochlore phonon modes containing thirteen bands which are; 1 E_g + 4 F_{2g}+A_{1g}+ 7F_{1u}, in which one E_g, four F_{2g}, and one A_{1g} are six actively Raman modes, and 7 F_{1u} are infrared active mode [216]. For the samples having (a) x = 0, (b) x = 0.02 , (c) x = 0.04, (d) x = 0.06, and (e) x = 0.08 of Al^{3+}, the spectrum of Raman was deconvoluted into six Raman strong bands, and the locations are tabulated in Table 6.4.

Table 6.4. The locations of the deconvoluted Raman active bands for all the five samples.

Sample	Peak location				
	F_{2g} band (cm^{-1})	**F_{2g}+E_g band (cm^{-1})**	**A_{1g} band (cm^{-1})**	**F_{2g} band (cm^{-1})**	**F_{2g} band (cm^{-1})**
0% Al^{3+}	212.8±0.5	312.3±0.1	518.2±0.1	547.3±2.3	689.2±1.6
1 % Al^{3+}	213.1±0.5	312.5±0.1	517.9±0.1	546.0±2.0	689.1±1.6
2 % Al^{3+}	213.1±0.5	312.5±0.1	518.3±0.1	549.2±2.2	689.7±1.8
3 % Al^{3+}	212.8±0.6	313.6±0.1	518.4±0.1	546.4±2.3	690.4±1.9
4 % Al^{3+}	213.4±0.6	313.9±0.1	518.6±0.1	550.4±3.3	686.5±1.7

It was noticed that the existence of an extremely weak band at 447 cm^{-1}, denoted by an asterisk (*) symbol, was caused by the small quantity of titanium dioxide by adding Al^{3+} ions into the host [130]. In the case of undoped $Gd_{1.92}Eu_{0.08}Ti_2O_7$ composition, the spike at the wave number 312.3 cm^{-1} could be due to the F_{2g} and E_g vibrational modes, whereas F_{2g} relates to bending vibrational modes O_{48f}-Gd-O_{48f}, and E_g correlates to the sublattice of O_{48f}. The stretching band Gd-O_{48f} is associated with the mode A_{1g} at wavenumber 518.2 cm^{-1}. At 212.8 cm^{-1}, the weakest wavenumber's peak, F_{2g}, has a connection to the sublattice O_{8b} of the lattice. The blue shift in these two high intensity vibrational bands (from 312.3 to 313.9 cm^{-1} and 518.2 to 518.6 cm^{-1}) is indicative of an increase in Al^{3+}-doping concentration.

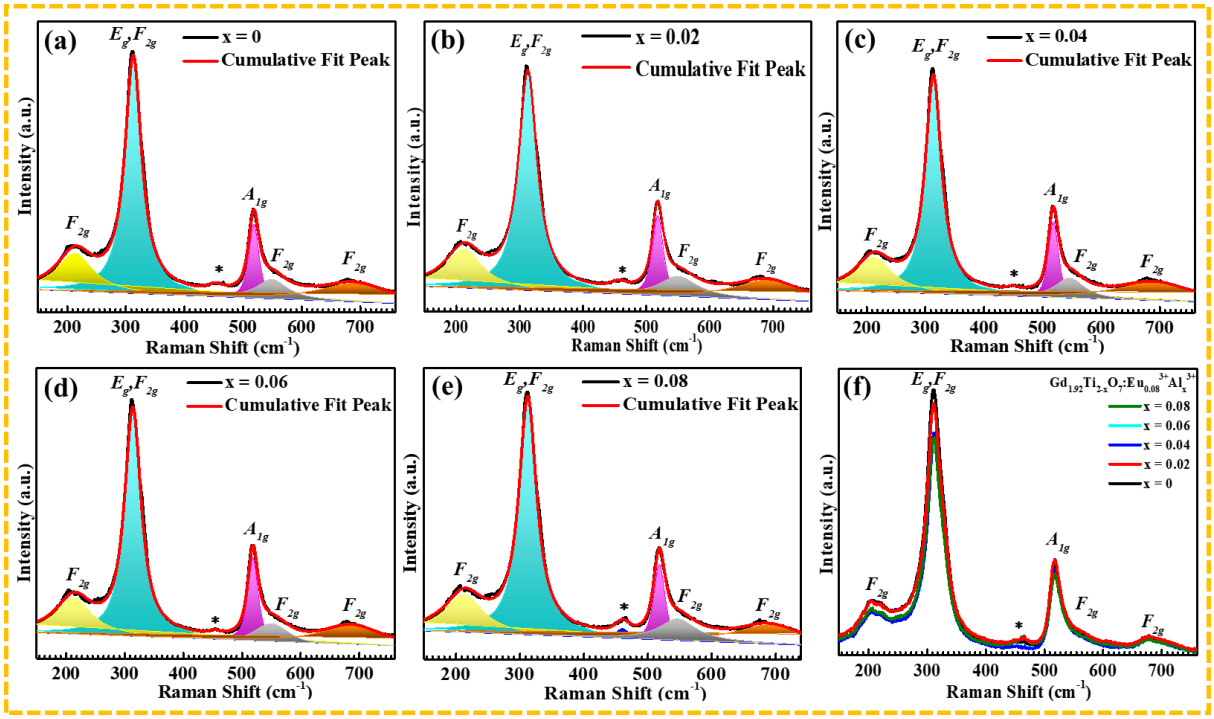

Figure 6.4. *(a-e) Deconvoluted Raman bands for x = 0, 0.02, 0.04, 0.06 and 0.08.x = 0, 0.1, and 0.2 compositions of* $Gd_{1.92}Ti_{2-x}O_7:Eu_{0.08}Al^{3+}{}_x$*, and (f) Comparable Raman active modes for* Al^{3+}*-doping level for complete series.*

The decrease in bond length or increasing force constant caused by the doping of a smaller sized Al^{3+} ion over Ti^{4+} are related to the displacement of phonon vibration along the higher wave-number side. In the current study, the last two Raman modes F_{2g} are located at wavenumbers of 549.2 cm^{-1} and 689.7 cm^{-1}. Surprisingly, Al^{3+} ion implantation on the Ti-site confirms a single-phase pyrochlore composition in every sample in both Raman and XRD analyses.

6.3.2. Optical investigations:

6.3.2.1. Photoluminescence results:

The photoluminescence excitation (PLEx) profiles for the $Gd_{1.92}Eu_{0.08}Ti_{2-x}Al_xO_7$ (with $0 \leq x \leq 0.08$) configurations annealed at 1250°C in atmosphere for 45 hours of duration, are displayed in Figure 6.5 (a), at the emission wavelength λ_{em} = 588 nm for ambient temperature.

The intra 4f transitions of the Eu^{3+} ions in the spectrum result five distinct peaks and one broad band within 250 nm to 510 nm range. Amongst these bands, broad excitation band between 278 and 350 nm centered around ~ 322 nm wavelength, can be considered due to the charge-transfer band, which might have developed via an electron shift from an oxygen binding site 2p orbital to a vacant 4f orbital of europium ion [84]. The intramolecular 4f-4f transitions $^7F_0 \rightarrow {}^5D_4$, $^7F_0 \rightarrow {}^5G_2/{}^5L_7$, $^7F_0 \rightarrow {}^5L_6$, $^7F_0 \rightarrow {}^5D_3$, and $^7F_0 \rightarrow {}^5D_2$ of Eu^{3+} ions are responsible for the five peaks centered at nearly ~ 362 nm, 383 nm, 394 nm, 416 nm, and 466 nm [198,214]. The $Gd_{1.92}Eu_{0.08}Ti_{2-x}Al_xO_7$ with x = 0, 0.02, 0.04, 0.06 and 0.08 samples have shown two high intensity prominent excitation peaks at 322 nm and 394 nm.

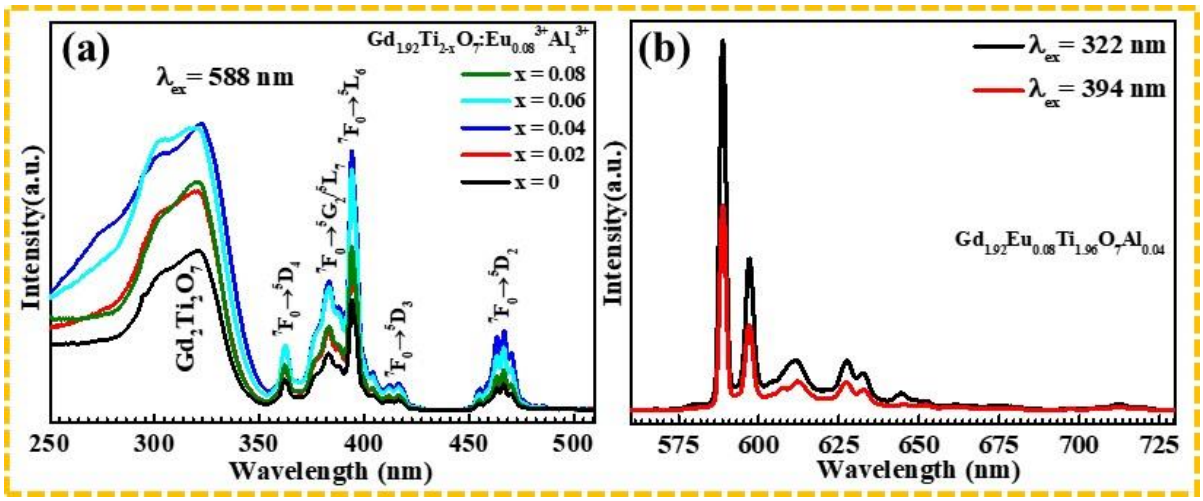

Figure. 6.5 *(a) PLEx spectrum of $Gd_{1.92}Eu_{0.08}Ti_{2-x}Al_xO_7$ with x = 0, 0.02, 0.04, 0.06 and 0.08 samples, (b) Comparative PLEm spectrum of $Gd_{1.92}Eu_{0.08}Ti_{1.96}Al_{0.04}O_7$ for both the excitation wavelengths 322 nm and 394 nm.*

In Figure 6.5 (b), the photoluminescence emission (PLEm) bands of $Gd_{1.92}Eu_{0.08}Ti_2O_7$ pyrochlore doped with 2 mol% Al^{3+} ions activated at two different excitation wavelength 322 nm and 394 nm are compared. The comparison of the emission spectrum reveals that for both the excitations at 322 nm and 394 nm, the Al^{3+} doped $Gd_{1.92}Eu_{0.08}Ti_2O_7$ pyrochlore structure

exhibit same 4f-4f transitions of Eu^{3+} ions. Also, for 322 nm excitation, the $Gd_{1.92}Eu_{0.08}Ti_2O_7$ pyrochlore host exhibits maximal intensity peaks for 4f-4f transitions of the Eu^{3+} ions. The insertion of Al^{3+} within $Gd_{1.92}Eu_{0.08}Ti_2O_7$ host doesn't affect the locations of the excitation peaks but may significantly improve their intensity. This outcome illustrates the viability of improving this material's luminous efficacy.

Additionally, such pyrochlore structures have the characteristics that are required to be used in the manufacturing of white light producing gadgets, including the ability to excite effectively in the near-UV and blue regions. The PLEm characteristics of $Gd_{1.92}Eu_{0.08}Ti_{2-x}Al_xO_7$ with x = 0, 0.02, 0.04, 0.06 and 0.08 pyrochlore oxide samples have been plotted in the wavelength range from 565 nm to 730 nm, for both the excitation wavelengths of 322 nm and 394 nm and displayed in Figure 6.6 (a) and 6.6 (b), correspondingly. The PLEm spectra of all samples, excited at 322 nm and 394 nm, exhibit identical emission peak positions. On comparing both the images of Figure 6.6 (a) and Figure 6.6 (b), it becomes evident that the intensity of each peak in the spectrum is influenced by the amount of Al^{3+} doping. Firstly, the excitation intensity goes on increasing upto the maximum doping concentration of 2 mol% of Al^{3+}, but after that the intensity decreases due to the well-known concentration quenching effect [10].

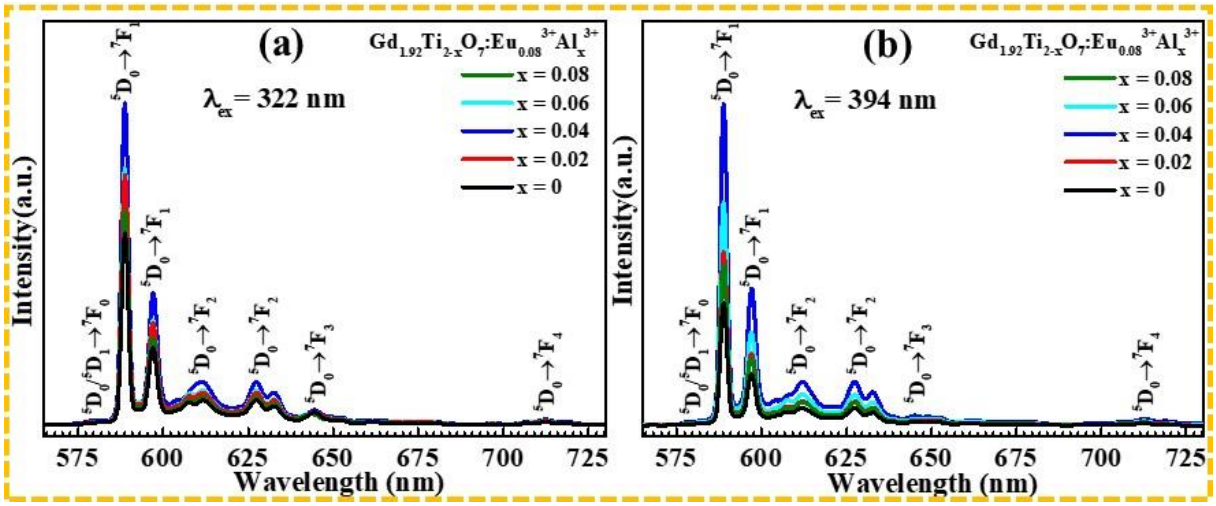

Figure 6.6. *PLEm profiles for $Gd_{1.92}Eu_{0.08}Ti_{2-x}Al_xO_7$ with x = 0, 0.02, 0.04, 0.06 and 0.08 samples under the excitation wavelength (a) 322nm, and (b) 394 nm.*

The PLEm spectra contains seven emission peaks which are centred at nearly ~ 579 nm, 588 nm, 596 nm, 612 nm, 627 nm, 644 nm, and 712 nm wavelengths that corresponds to the transitions between Eu^{3+} ion energy levels $^5D_0 \rightarrow {}^7F_0$ (579 nm), $^5D_0 \rightarrow {}^7F_1$ (588 nm, 596nm), $^5D_0 \rightarrow {}^7F_2$ (612 nm, 627nm), $^5D_0 \rightarrow {}^7F_3$ (644 nm), $^5D_0 \rightarrow {}^7F_4$ (712 nm), respectively [120,196,211,217,218] . The high intensity emission peak at wavelength 588 nm ($^5D_0 \rightarrow {}^7F_1$) lies in the orange-reddish region which corresponds to the magnetic dipole allowed transition (MDAT) of Eu^{3+} trivalent ion, and the emission peak at wavelength 612 nm ($^5D_0 \rightarrow {}^7F_2$) lies in the red region corresponding to the electric dipole allowed transition (EDAT) of Eu^{3+} ions. The luminescence behaviour of Eu^{3+} ions is strongly dependent on the crystal field environment and the symmetry of the host lattice. The results reveal that the former MDAT and the latter EDAT contribute significantly to the emission spectrum. The dominance of emission energy in the orange-reddish region indicates that Eu^{3+} ions involve symmetry sites with an inversion center [78].

The location of the Eu^{3+} emission spikes are unaffected by Al^{3+} doping, but Al^{3+} can substantially improve the luminescence intensity of Eu^{3+} in $Gd_{1.92}Eu_{0.08}Ti_2O_7$. The level of Al^{3+}

loading also affects the luminescence intensity. Figure. 6.6 (a & b) demonstrates that the intensity of the emission peak at 588 nm grows quickly using the excitation wavelength of 322 nm and 394 nm, with raising the Al^{3+} concentration at first, attaining its highest level at an Al^{3+} level of 2.0 mol%, after that dramatically decreasing with further doping as a result of the concentration quenching mechanism [3]. Hence, the optimized concentration of Al^{3+} ions in $Gd_{1.92}Eu_{0.08}Ti_2O_7$ pyrochlore is found to be 2.0 mol%. This fluorescence quenching at higher activator concentration occurs because of decreased distance between luminescent centers, leading to feasible non-radiative energy transfer encompassed by activator ions rather than emitting the excitation energy radiatively. Non-radiative energy transfers can be related by either resonance energy transfer (RET) or cross relaxation among Eu^{3+} ions [168]. The critical distance (M_c), between Eu^{3+} ions, which mainly determines the non-radiative energy transfer, could be calculated using the formula (6.3) provided [145];

$$M_c = 2 * \left\{\frac{3\times V}{4\pi\alpha_c n}\right\}^{\frac{1}{3}} \ldots\ldots\ldots (6.3)$$

where 'V' is volume of the unit cell of the crystalline lattice, 'M_c' is the critical doping level above which quenching occurred, and n is the efficient no. of cations in a unit cell. For the optimum concentration of Al^{3+} in the $Gd_{1.92}Eu_{0.08}Ti_2O_7$ host lattice, the calculated critical distance is 17.81 Å, and the value of factors V = 1012.67 $Å^3$, α_c = 0.04, & n = 8. Energy transfer over exchange interaction typically occurs when M_c is nearly 5 Å [145]. For the current study, non-radiative energy transfer occurs via multipolar interaction as the critical distance value is bigger than 5 Å.

The luminescence intensity (I) is related to the concentration of dopant ions (x) by the following equation (6.4) [198];

$$\log\left[\frac{I}{x}\right] = \mathrm{M} - \frac{Q}{3}\log(x) \ldots\ldots\ldots (6.4)$$

where M is a constant and Q represents the type of multipolar interaction. The values of Q for electric dipole-dipole, dipole-quadruple, & quadruple-quadruple interactions are 6, 8, and 10, correspondingly [144]. Figure 6.7 shows a plot of log(I/x) on y-axis & log(x) on x-axis for all the compositions based on the emission plot of $Gd_{1.92}Eu_{0.08}Ti_2O_7$ excited using 322 nm. The calculated slope of the graph is 1.5847, and value for the factor Q is 4.75, lies near to 6. This explains that the energy transfer mechanism in the current study formed because of the electric dipole-dipole interaction.

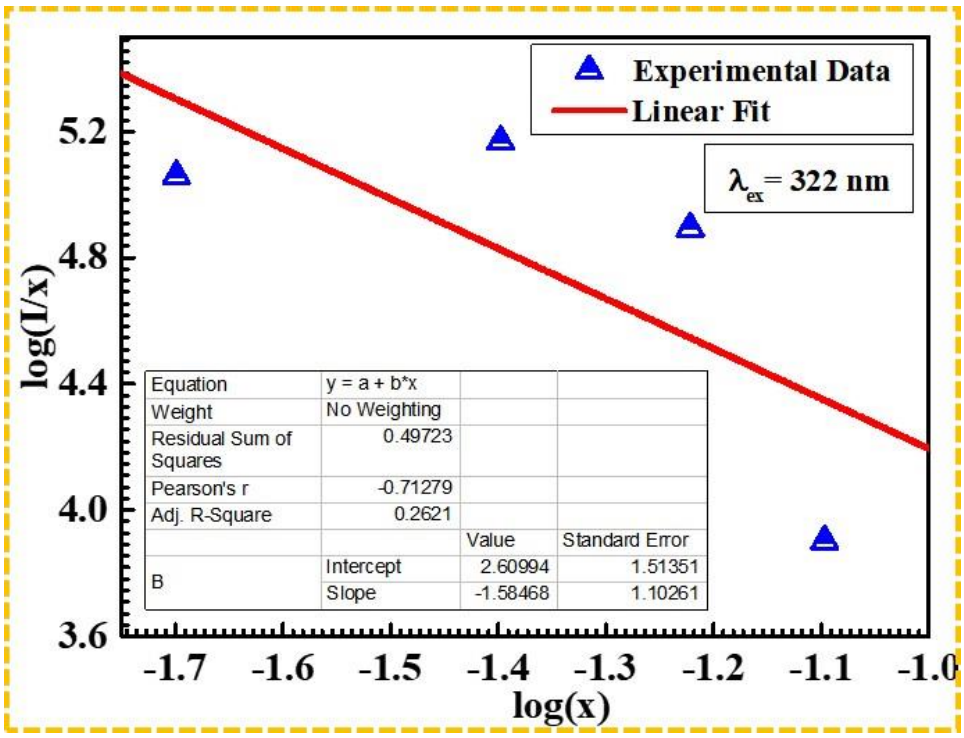

Figure 6.7. *Correlation between log(I/x) and log(x) for the entire series of Al^{3+} doped $Gd_{1.92}Eu_{0.08}Ti_2O_7$, excited under 322 nm.*

The planned energy scale distribution for Al^{3+} doped $Gd_{1.92}Eu_{0.08}Ti_2O_7$ is shown in Figure 6.8, and includes the mechanisms of excitation, emission, energy transfer, and non-radiative transitions. Seven visible light emission lines represented by downward vertical dotted arrows

at wavelengths of 579 nm ($^5D_0 \rightarrow {}^7F_0$), 588 nm and 596 nm ($^5D_0 \rightarrow {}^7F_0$), 612 nm and 627 nm ($^5D_0 \rightarrow {}^7F_0$), 644 nm ($^5D_0 \rightarrow {}^7F_0$), and 712 nm ($^5D_0 \rightarrow {}^7F_0$) are released from $^5D_0$ energy levels by the radiation after it has excited the Eu^{3+} ions using energy of 322 nm and 394 nm (vertical black solid line represents excitation line).

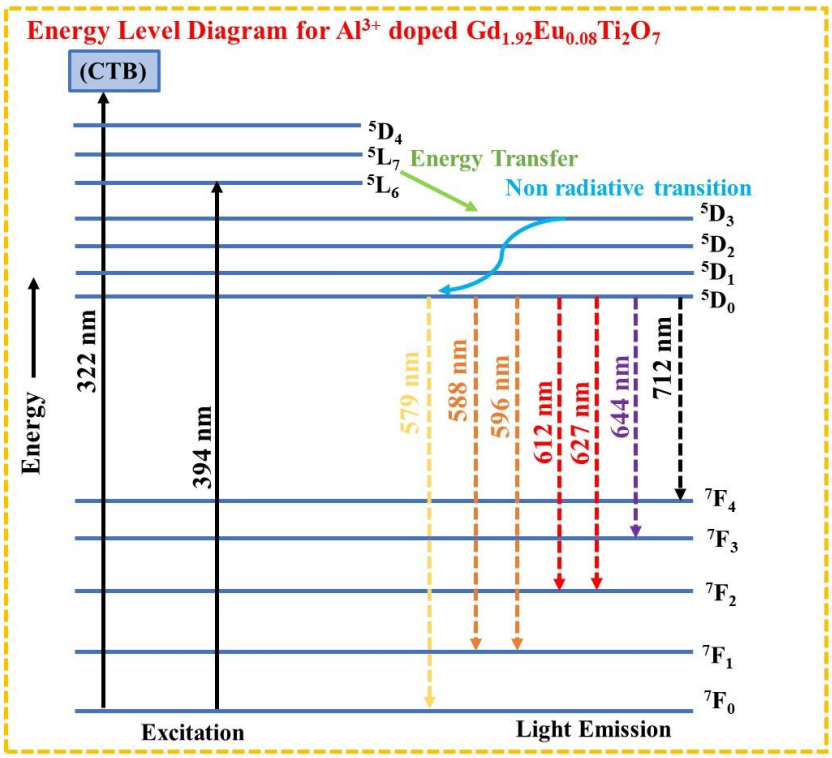

Figure 6.8. *Excitation, emission, and energy transfer processes employing Al^{3+} doped $Gd_{1.92}Eu_{0.08}Ti_2O_7$ are represented graphically.*

6.3.2.2. CIE results:

The Commission Internationale de I'Eclairage (CIE), is an international organization that establishes standards and recommendations concerning light and colour measurement. The CIE is responsible for defining various colour spaces, including the widely used CIE colour space (coordinates x, y), as well as for developing standards for measuring and specifying the colour rendition of light source.

To achieve an exact colour match for a given spectral density α(λ), the required amount of stimulation can be determined using the following expressions (6.5), (6.6), and (6.7) [179];

$$A = \int_{\lambda} X(\lambda).\alpha(\lambda)\, d\lambda \ldots\ldots\ldots (6.5)$$

$$B = \int_{\lambda} Y(\lambda).\alpha(\lambda)\, d\lambda \ldots\ldots\ldots (6.6)$$

$$C = \int_{\lambda} Z(\lambda).\alpha(\lambda)\, d\lambda \ldots\ldots\ldots (6.7)$$

In these equations, A, B, and C represent the tristimulus values that contribute to the power of the red, blue, and green colours, respectively, in order to match the colour of α(λ). To describe the real colour, the CIE 1931 diagram is used, where the A, B, and C values are employed. This system is a worldwide method of representing all possible colours through a combination of three primary colours, and the chromaticity coordinates were determined using equations (6.8) and (6.9) from the tristimulus values, given below [179];

$$x = \frac{A}{A+B+C} \ldots\ldots\ldots (6.8)$$

$$y = \frac{B}{A+B+C} \ldots\ldots\ldots (6.9)$$

The standard x and y coordinates for white light emission are fixed at (x=0.33, y=0.33) and situated at the center of CIE 1931 chromaticity diagram. The Al^{3+} doped $Gd_{1.92}Eu_{0.08}Ti_2O_7$ oxides were analysed in this study, and their colour chromaticity diagram was generated and depicted in Figure 6.9. The all samples exhibited x, y chromaticity coordinates of (0.607, 0.39), (0.606, 0.391), (0.605, 0.392), (0.604, 0.393), and (0.6, 0.395), corresponding to the $Gd_{1.92}Eu_{0.08}Ti_{2-x}Al_xO_7$ with x = 0. 0.02, 0.04, 0.06, and 0.08, respectively, using excitation wavelength of 322 nm.

The National Television Standard Committee (NTSC) coordinates, represented by x = 0.670 and y = 0.330 [214], serve as a reference point. The quality of light can be assessed by utilizing chromaticity coordinates and McCamy's approximate expression (6.10) [219];

$$CCT = -449\,m^3 + 3535\,m^2 - 6823.3\,m + 5520.33 \ldots\ldots\ldots (6.10)$$

In this equation, the term 'm' represents the inverse slope line, here $m = \frac{x-\overline{x}}{y-\overline{y}}$. The values of '$\overline{x}$' and '$\overline{y}$' used in this expression are 0.332 and 0.186, corresponding to the epicenter coordinates [144]. Table 6.5 tabulates the calculated CIE chromaticity coordinates, colour correlated temperatures (CCT), for Al^{3+} doped $Gd_{1.92}Eu_{0.08}Ti_2O_7$ series with various concentrations, excited at 322 nm. These CCT values range from 1750 to 1726, falling within the orange-reddish light region. For the optimized concentration of Al^{3+} substitution (2 mol%) in $Gd_{1.92}Eu_{0.08}Ti_2O_7$, the CCT value is 1738, indicating orange-reddish light emission.

Table 6.5. The (x, y) coordinates and CCT parameter for the entire series of Al^{3+} doped $Gd_{1.92}Eu_{0.08}Ti_2O_7$.

Sample	**Under 322 Excitation**	
	(x, y) coordinates	**CCT**
$Gd_{1.92}Eu_{0.08}Ti_2O_7$	(0.607, 0.39)	1749.694325
$Gd_{1.92}Eu_{0.08}Ti_{1.98}Al_{0.02}O_7$	(0.606, 0.391)	1744.915649
$Gd_{1.92}Eu_{0.08}Ti_{1.96}Al_{0.04}O_7$	(0.605, 0.392)	1738.064152
$Gd_{1.92}Eu_{0.08}Ti_{1.94}Al_{0.06}O_7$	(0.604, 0.393)	1734.056865
$Gd_{1.92}Eu_{0.08}Ti_{1.92}Al_{0.08}O_7$	(0.600, 0.395)	1725.681371

Notably, the CIE coordinates measured for emission spectra are found to be in close proximity to those of the economical phosphor Y_2O_2S: Eu^{3+} (x=0.622 and y=0.351)[214]. Therefore, the

optimized series mentioned earlier holds great potential as a viable choice for the orange-reddish component in WLEDs when illuminated by a blue light-emitting excitation source.

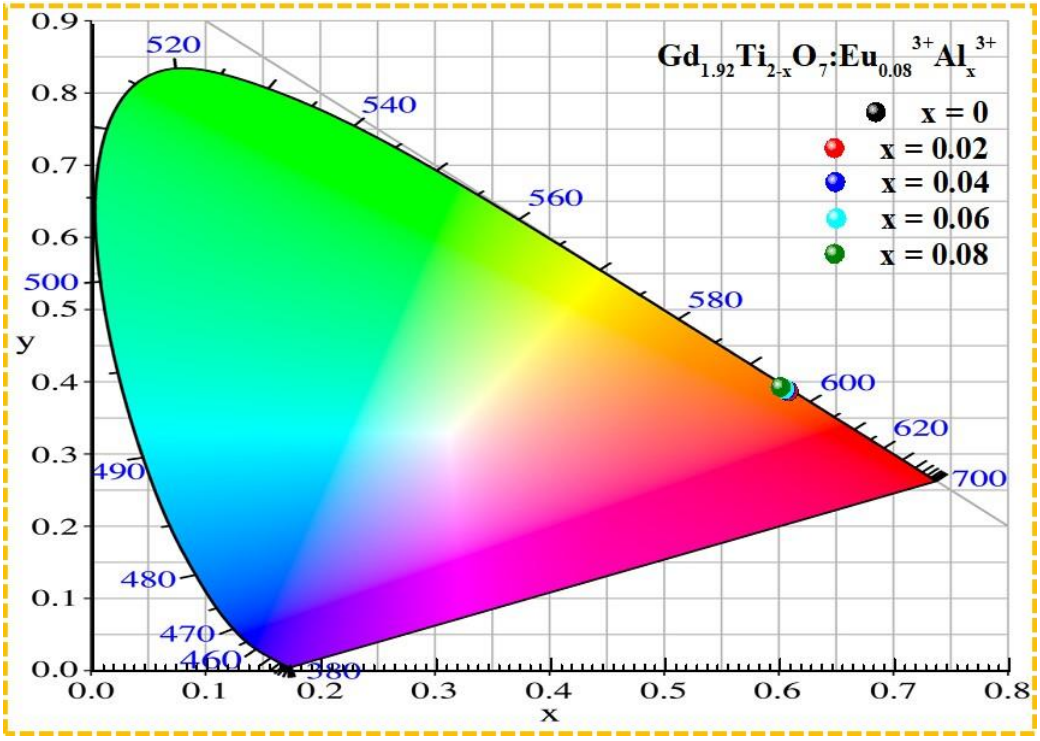

Figure 6.9. *CIE chromaticity plot for Al^{3+} doped $Gd_{1.92}Eu_{0.08}Ti_2O_7$ pyrochlore oxide.*

6.3.2.3. Life-time decay results:

The decay behaviour of the luminescence intensity over time, known as lifetime decay, was investigated for the $^5D_0$ excited level of Eu^{3+} ions in the prepared $Gd_{1.92}Eu_{0.08}Ti_{2-x}Al_xO_7$ with x = 0, 0.02, 0.04, 0.06 and 0.08 pyrochlore oxide samples. Decay curve profiles were obtained by measuring the $^5D_0 \rightarrow {}^7F_1$ transition at 588 nm wavelength under 322 nm excitation wavelength, as shown in Figure 6.10. To analyse the luminescence decay behaviour, the decay curve was fitted using various equations, and the good fit was found using a bi-exponential equation (6.11) [198];

$$U = \alpha_1 e^{\frac{-t}{\tau_1}} + \alpha_2 e^{\frac{-t}{\tau_2}} \dots\dots\dots (6.11)$$

In this equation, 'U' represents the luminescence intensity, 't' is time, 'τ_1' and 'τ_2' are the decay times for the exponential components, and 'α_1', 'α_2' are the fitting parameter constants.

To determine the average lifetime in the case of bi-exponential fit, the following equation is used (6.12) [145];

$$\tau_{Avg} = \frac{\alpha_1 {\tau_1}^2 + \alpha_2 {\tau_2}^2}{\alpha_1 \tau_1 + \alpha_2 \tau_2} \ldots\ldots\ldots (6.12)$$

The optimized phosphor sample exhibited a fluorescent lifetime of approximately 1.17 ms for the $^5D_0$ level. In general, the decay curves of photoluminescence (PL) could be affected by energy transfer among Eu^{3+} ions. In case of no interaction among the rare-earth ions, the decay profiles are typically described by a single exponential function. However, the bi-exponential fit observed in this study suggests the potential interaction between Eu^{3+} ions in the $Gd_{1.92}Eu_{0.08}Ti_2O_7$ lattice, as discussed in previous sections. The average lifetime comes out to be 1.05 ms (x = 0.02), 1.17 ms (x = 0.04), 1.19 ms (x = 0.06), 1.28 ms (x = 0.08) for Al^{3+} doping concentration. The introduction of small quantity of Al^{3+} enhances the asymmetry of Eu^{3+} and increases the likelihood of energy transfer to Eu^{3+}, thereby reducing the rate of nonradiative relaxation [84].

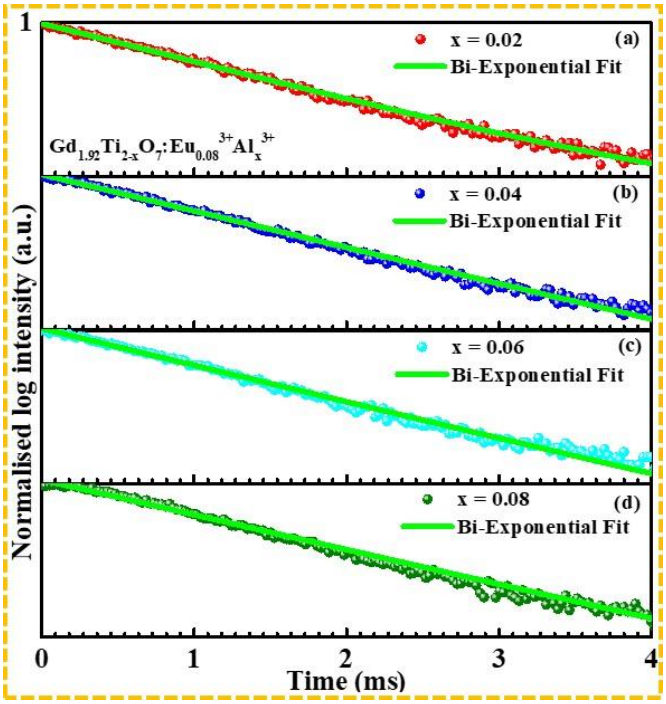

Figure 6.10. *Under 386 nm excitation, the luminescence decay curve of the* $Gd_{1.92}Eu_{0.08}Ti_{2-x}Al_xO_7$ *with x = 0, 0.02, 0.04, 0.06 and 0.08 pyrochlore oxide samples.*

6.4. Conclusion:

Using the solid-state reaction method, successfully prepared monophasic Al^{3+} doped $Gd_{1.92}Eu_{0.08}Ti_2O_7$ pyrochlore oxides. XRD patterns validate pure phase production with a cubic structure and average crystallite size ranging from 758.18 ± 15.6 Å to 556.97 ± 2.86 Å. The Raman profile of the material shows the existence of functional groups that correspond to active vibrational modes, and this observation is consistent to the obtained XRD results. Raman spectroscopy reveals a slight blue shift, which can be attributed to the smaller cationic substitution that takes place in the material. The Al^{3+} doped $Gd_{1.92}Eu_{0.08}Ti_2O_7$ pyrochlore oxides exhibited colour tunability with changing rare earth Al^{3+} doping amount and immense orange-reddish emission under excitation of 322 nm and 394 nm respectively. Concentration quenching occurred above 2.0 mol% of Al^{3+} ion doping because of the dipole-dipole interaction within Eu^{3+} ions. The average lifetime factor for $^5D_0$ energy state of Eu^{3+} trivalent ions with different amount of doping in Al^{3+} substituted $Gd_{1.92}Eu_{0.08}Ti_2O_7$ pyrochlore oxides come out

to be in milliseconds when excited by 322 nm. The calculated CIE chromaticity coordinates (0.605, 0.392) for the highly intense Al^{3+} substituted $Gd_{1.92}Eu_{0.08}Ti_2O_7$ pyrochlore oxides sample when excited with wavelength of 322 nm were occupying the orange-reddish region of CIE 1931 plot, which is close to economical red phosphor $Y_2O_2S:Eu^{3+}$ (x= 0.622 and y= 0.351) and through the coordinates determined by NTSC. The outcomes suggest that the synthesized Al^{3+} doped $Gd_{1.92}Eu_{0.08}Ti_2O_7$ pyrochlore oxide samples have potential for application as an orange-reddish element in WLEDs and other luminescent tools.

Chapter 7

Summary and future scope

In this chapter, significant outcomes of this thesis are presented. This chapter provides an overview of the fundamental concept behind the structural and optical outcomes. Lastly, future scope of this work is discussed in detail as rare earth ion doped $Gd_2Ti_2O_7$ hold immense potential for usage in the production of WLEDs.

7.1. Summary:

This thesis is primarily concerned with synthesising and characterising a variety of pyrochlore oxide structures doped with different rare earth ions, with a focus on their optical and structural characteristics for use in solid-state lighting applications. Using the solid-state reaction technique, we have successfully synthesised monophasic $Gd_2Ti_2O_7$ pyrochlore structures doped with single rare earth ions (Tb^{3+}, Dy^{3+}, Ce^{3+}, and Eu^{3+}). Furthermore, we study how various doping ion concentrations affects the rare earth ion emission characteristics.

As discussed in previous chapters, white light-emitting diodes, are a dominant force in solid-state lighting technology because of their special qualities. These include their long lifespan, energy efficiency, environmental friendliness, and exceptional luminous efficiency, which make them ideal for their use in displays, medical equipment, sensors, and artificial lighting. Using traditional solid-state reaction approach, we successfully produced Tb^{3+}-doped $Gd_2Ti_2O_7$ pyrochlore structures in this study. According to our findings, Tb^{3+} doping in $Gd_2Ti_2O_7$ at a maximum concentration of 6 mol% exhibits potential as a bright luminescent material. Moreover, white light can be produced by combining the green light-emitting Tb^{3+}-doped $Gd_2Ti_2O_7$ pyrochlore with red and blue emissions. The colour rendering index (CRI) of commercial white light-emitting diodes based on YAG: Ce^{3+} coupled with blue LEDs is generally lower since they lack a red component. By combining an effective red phosphor with YAG: Ce^{3+} and putting the combination on a blue LED chip, this restriction can be removed. However, due to their low chemical stability and absorption characteristics, red phosphors that are sold commercially frequently have feeble emission. Therefore, $Gd_2Ti_2O_7$ phosphors doped with Ce^{4+} were successfully synthesized by solid state reaction method and the Ce^{4+} cationic oxidation state was converted to Ce^{3+} oxidation state by heating in reduced environment of H_2 (10%) and argon (90%) flow at a temperature of 1000℃ for 24 hours duration. Moreover, by converting the cerium doping level and transforming it into the Ce^{3+} state, we are able to

achieve enhanced red emission in reduced $Ce^{3+} \rightarrow Ce^{4+}$-doped $Gd_2Ti_2O_7$ phosphors. We performed a thorough examination of the structural and luminous characteristics of reduced and unreduced cerium doped $Gd_2Ti_2O_7$ host lattice, which were produced using the solid-state reaction technique. In comparison to the unreduced Ce^{4+}-doped $Gd_2Ti_2O_7$ samples, the reduced $Ce^{4+} \rightarrow Ce^{3+}$ doped $Gd_2Ti_2O_7$ pyrochlore samples exhibited better luminosity, according to the results.

We used the solid-state reaction approach to synthesise Al^{3+}/Eu^{3+}-doped and Dy^{3+}-doped $Gd_2Ti_2O_7$ phosphors in the search for single-phase phosphors that could produce white light. We investigated their morphology, structure, and photoluminescence properties in detail.

Important findings of research work:

The heating protocol in solid state reaction method synthesis of $Gd_2Ti_2O_7$ pyrochlore oxide was accomplished to analyse the crystallization of the various rare earth ion doped pyrochlore structure. The crystallization of $Gd_2Ti_2O_7$ phosphor began beyond 1000 °C. Therefore, these samples were sintered at 1300 ^oC to achieve pure phase of $Gd_2Ti_2O_7$. The structural properties of differently synthesized $Gd_2Ti_2O_7$ phosphor doped with various rare earth ions were investigated to analyse crystallinity, phase purity, and crystallite size by using XRD and Rietveld refinement for phase confirmation. The XRD patterns for all the prepared samples were in complete agreement with the standard phase of $Gd_2Ti_2O_7$ pyrochlore structure signifies the pure phase formation of with cubic structure and fd3m space group. The morphological analysis of rare earth doped $Gd_2Ti_2O_7$ was accomplished by recording SEM/FESEM images. The synthesis methods discussed in the previous chapters, solid state reaction method, show spherical agglomerated particles.

The photoluminescence study reveals that the Tb^{3+} doped $Gd_2Ti_2O_7$ pyrochlore structures have four emission bands with the intense emission at 545 nm ($^5D_4 \rightarrow {}^7F_5$ transition), when pumped

at 375 nm wavelength. The concentration quenching has been obtained beyond 6.0 mol% of Tb^{3+}. Further for 6% terbium doping, an electron under excitation of 375 nm goes into the 5d localised band first and returns to $^5D_3$ energy level non-radiatively. All these results indicate that the prepared Tb^{3+} doped $Gd_2Ti_2O_7$ pyrochlore structures with 6 mol% of Tb^{3+} ion doping serve as an efficient green emitting phosphor for display and solid-state lighting devices.

The photoluminescence study shows that for the Dy^{3+} doped $Gd_2Ti_2O_7$ phosphors, excitation spectra for every sample show the appearance of excitation peak at 347 nm wavelength and the emission spectra have two sharp intensity bands centered around 484 nm and 581 nm, originating due to the $^4F_{9/2} \rightarrow {}^6H_{15/2}$ and $^4F_{9/2} \rightarrow {}^6H_{13/2}$ transition respectively and the less intense band appeared at wavelength of 456 nm formed due to the $^4I_{13/2} \rightarrow {}^6H_{13/2}$ transition of Dy^{3+} ions. The optimum concentration of Dy^{3+} substituted $Gd_2Ti_2O_7$ series is found to be 2.0 mol% after this concentration quenching effect occurs. The Y/B ratio for the complete series of samples were found to close to unity and the combination of both yellow and blue emission bands emit white light with CIE coordinates values for the 2.0 mol % of Dy^{3+} ion in GTO host is (0.34959, 0.35381) with CCT value 4844.95 lying in the standard cool white light calorimetric point. Overall, the Dy^{3+} substituted $Gd_2Ti_2O_7$ pyrochlore samples could be used as luminescent material for WLEDs application.

The PL excitation (at λ = 425 nm) contains two broad bands at 255 nm (4f to 5d transition of the cerium trivalent ion) and 360 nm (due to band-to-band absorption of host $Gd_2Ti_2O_7$ and due to the 4f to 5d transition of the cerium trivalent ion). PL intensity goes on increasing up to a doping of 4% of cerium after that again decreases due to the concentration quenching effect.

The luminescent analysis of Ce^{4+} doped $Gd_2Ti_2O_7$ phosphor recorded under different excitation wavelengths reveal red emission with photoluminescence emission (at λ = 360 nm) exhibits at 425 nm due to the transition from lowest 5d state to $^2F_{5/2}$ and $^2F_{7/2}$ components of the ground state. This radiative transition from 5d (T_{2g}) level to the $^2F_{5/2}$ and $^3F_{7/2}$ levels of the ground state

causing emission peak at doublet around 425 nm. The Photoluminescence results for both the reduced and unreduced series shows that on reduction of Ce^{4+} into Ce^{3+} state, reduced samples show blue shifting of Ce^{3+} emission peaks in cubic crystal structure of $Gd_2Ti_2O_7$ host, due to the expansion of crystal size of cerium in Ce^{3+} state. It was clearly observed from the emission results of all the ceria doped samples with or without reduction that bright blue emission and the emission intensity depends on the concentration of cerium ion. Hence, reduced samples of Ce^{4+}: $Gd_2Ti_2O_7$ would have a potential application in the mass production of blue LED chips for the further, fabrication of WLEDs.

The photoluminescence results of monophasic Al^{3+} doped $Gd_{1.92}Eu_{0.08}Ti_2O_7$ pyrochlore oxides exhibited immense orange-reddish emission under excitation of 322 nm and 394 nm respectively. Concentration quenching occurred above 2.0 mol% of Al^{3+} ion doping because of the dipole-dipole interaction within Eu^{3+} ions. The average lifetime factor for $^5D_0$ energy state of Eu^{3+} trivalent ions with different amount of doping in Al^{3+} substituted $Gd_{1.92}Eu_{0.08}Ti_2O_7$ pyrochlore oxides come out to be in milliseconds when excited by 322 nm. The calculated CIE chromaticity coordinates (0.605, 0.392) for the highly intense Al^{3+} substituted $Gd_{1.92}Eu_{0.08}Ti_2O_7$ pyrochlore oxides sample when excited with wavelength of 322 nm were occupying the orange-reddish region of CIE 1931 plot, which is close to economical red phosphor $Y_2O_2S:Eu^{3+}$ (x= 0.622 and y= 0.351) and through the coordinates determined by NTSC. The outcomes suggest that the synthesized Al^{3+} doped $Gd_{1.92}Eu_{0.08}Ti_2O_7$ pyrochlore oxide samples have potential for application as an orange-reddish element in WLEDs and other luminescent tools.

The results confirm that various rare earth ions doped $Gd_2Ti_2O_7$ pyrochlore structures developed in this thesis, possess significant potential for solid-state lighting applications, especially when considering white light-emitting diodes (WLEDs).

7.2. Future scope:

- It would be interesting to investigate alternative strategies for making these pyrochlore compounds, including the Sol-gel and co-precipitation approaches, and compare the results with those from solid-state reaction method.
- To fabricate prototype pc-WLEDs using optimized pyrochlore host $Gd_2Ti_2O_7$ for the UV/n-UV/blue LED chip.
- A cation even smaller than titanium, might be substituted into the pyrochlore B-site via high-pressure elevated temperature synthesis and study the effect on the optical behaviour.
- In contrast to $Gd_2Ti_2O_7$, the introduction of various rare earth inside different host like as $Gd_2Zr_2O_7$ and $Dy_2Ti_2O_7$, would be greatly improved the luminescence behaviour for different applications.
- It would be beneficial to carry out temperature-dependent time photoluminescence studies to further investigate the optical data. Using this method, it is possible to examine how optical and structural changes alter with temperature. It is feasible to observe any changes in the crystal structure within the material by creating defects studies at various temperatures. By validating and supporting the results of the optical measurements, this additional approach would aid in developing a thorough understanding of the optical properties.
- It would be better to study the further effect of both annealing temperature and time on the optical behaviour of the rare earth ion doped pyrochlore oxide structures for various luminescence devices.
- To extend the utility of this phosphor for versatile applications such as agricultural lighting, solar cells, thermal and fingerprint sensing etc.

References:

[1] L.Y. Zhou, F.Z. Gong, J.X. Shi, M.L. Gong, H. Bin Liang, A novel red phosphor Na2Ca4Mg2Si4O15:Eu3+ for plasma display panels, Mater. Res. Bull. 43 (2008) 2295–2299. https://doi.org/10.1016/j.materresbull.2007.08.014.

[2] D. Manzani, J.F.D.S. Petruci, K. Nigoghossian, A.A. Cardoso, S.J.L. Ribeiro, A portable luminescent thermometer based on green up-conversion emission of Er3+/Yb3+ co-doped tellurite glass, Sci. Rep. 7 (2017) 1–11. https://doi.org/10.1038/srep41596.

[3] V. V. Shinde, R.G. Kunghatkar, S.J. Dhoble, UVB-emitting Gd3+-activated M2O2S (where M = La, Y) for phototherapy lamp phosphors, Luminescence. 30 (2015) 1257–1262. https://doi.org/10.1002/bio.2889.

[4] L. Ozawa, M. Itoh, Cathode Ray Tube Phosphors, Chem. Rev. 103 (2003) 3835–3855. https://doi.org/10.1021/cr0203490.

[5] A. Vecht, C. Gibbons, D. Davies, X. Jing, P. Marsh, T. Ireland, J. Silver, A. Newport, D. Barber, Engineering phosphors for field emission displays, J. Vac. Sci. Technol. B Microelectron. Nanom. Struct. 17 (1999) 750. https://doi.org/10.1116/1.590633.

[6] Y. Fujimoto, M. Nakatsuka, Infrared luminescence from bismuth-doped silica glass, Japanese J. Appl. Physics, Part 2 Lett. 40 (2001) 14–17. https://doi.org/10.1143/jjap.40.l279.

[7] C. Feldmann, T. Jüstel, C.R. Ronda, P.J. Schmidt, Inorganic luminescent materials: 100 Years of research and application, Adv. Funct. Mater. 13 (2003) 511–516. https://doi.org/10.1002/adfm.200301005.

[8] M. Gaft, G. Panczer, R. Reisfeld, E. Uspesnsky, Laser-induced time-resolved luminescene as a tool for rare-earth element identification in minerals, Phys. Chem. Miner. 28 (2001) 347–363. https://doi.org/10.1007/s002690100163.

[9] S. Babu, V. Reddy Prasad, D. Rajesh, Y.C. Ratnakaram, Luminescence properties of

Dy3+ doped different fluoro-phosphate glasses for solid state lighting applications, J. Mol. Struct. 1080 (2015) 153–161. https://doi.org/10.1016/j.molstruc.2014.09.080.

[10] R.-J. Xie, Y.Q. Li, N. Hirosaki, H. Yamamoto, Nitride Phosphors and Solid-State Lighting, 2016. https://doi.org/10.1201/b10939.

[11] W.Z. Wu, Z.R. Zheng, W.L. Liu, J.P. Zhang, Y.X. Yan, Q.H. Jin, Y.Q. Yang, W.H. Su, Upconversion luminescence of CdTe nanocrystals by use of near-infrared femtosecond laser excitation, Opt. Lett. 32 (2007) 1174. https://doi.org/10.1364/ol.32.001174.

[12] J. Thirumalai, Luminescence: An Outlook on the Phenomena and their Applications, 1994.

[13] G. Annadurai, S.M.M. Kennedy, V. Sivakumar, Luminescence properties of a novel green emitting Ba2CaZn2Si6O17:Eu2+ phosphor for white light - Emitting diodes applications, Superlattices Microstruct. 93 (2016) 57–66. https://doi.org/10.1016/j.spmi.2016.02.045.

[14] B. Valeur, M.N. Berberan-Santos, A brief history of fluorescence and phosphorescence before the emergence of quantum theory, J. Chem. Educ. 88 (2011) 731–738. https://doi.org/10.1021/ed100182h.

[15] H. Search, C. Journals, A. Contact, M. Iopscience, I.P. Address, No Title, 369 (n.d.).

[16] F. Demichelis, S. Schreiter, A. Tagliaferro, E , 51 (1995).

[17] J.R. Lakowicz, Introduction to Fluorescence, (1999).

[18] G. Baryshnikov, B. Minaev, H. Ågren, Theory and Calculation of the Phosphorescence Phenomenon, (n.d.). https://doi.org/10.1021/acs.chemrev.7b00060.

[19] X. Liu, C. Yan, J.A. Capobianco, Chem Soc Rev, Chem. Soc. Rev. (2015). https://doi.org/10.1039/C5CS90009C.

[20] J. Mckittrick, L.E. Shea-rohwer, Review : Down Conversion Materials for Solid-State Lighting, 26 (2014) 1–26. https://doi.org/10.1111/jace.12943.

[21] S. Zhu, Y. Song, X. Zhao, J. Shao, J. Zhang, B. Yang, The photoluminescence mechanism in carbon dots (graphene quantum dots , carbon nanodots , and polymer dots): Current state and future perspective, 8 (2015) 355–381. https://doi.org/10.1007/s12274-014-0644-3.

[22] A. Manuscript, Ac ce d M us pt, (2018).

[23] A.J.J. Bos, Theory of thermoluminescence, 41 (2007) 45–56. https://doi.org/10.1016/j.radmeas.2007.01.003.

[24] P. Taylor, A.J. Walton, Advances in Physics Sonoluminescence, (n.d.) 37–41.

[25] C. Dodeigne, L. Thunus, R. Lejeune, Chemiluminescence as diagnostic tool . A review, 51 (2000) 415–439.

[26] J.W. Hastings, Th´ er` ese Wilson and J. Woodland Hastings, (1998) 197–230.

[27] N.A. Atari, Ii wi., 90 (1982) 93–96.

[28] H. Search, C. Journals, A. Contact, M. Iopscience, I.P. Address, Fractoluminescence Spectra in Crystalline Quartz, 1892 (1892).

[29] K.V.R. Murthy, H.S. Virk, Luminescence Phenomena : An Introduction, 347 (2014) 1–34. https://doi.org/10.4028/www.scientific.net/DDF.347.1.

[30] C. Kltck, H. Schulman, Luminescence in Solids, (n.d.) 97–172.

[31] C. Ronda, A. Srivastava, Luminescence Science and Display Materials, (2006).

[32] C.C. Lin, R. Liu, Advances in Phosphors for Light-emitting Diodes, (2011) 1268–1277.

[33] R. Reisfeld, structure and bonding 22, Royal Society of Chemistry, 2016. https://doi.org/10.1039/c6ra19584a.

[34] B. di Bartolo, Advances in nonradiative processes in solids, 2013.

[35] D.J. Robbins, P.J. Dean, Advances in Physics The effects of core structure on radiative and non-radiative recombinations at metal ion substituents in semiconductors and phosphors, (n.d.) 37–41.

[36] Q. Peng, Q. Shi, Y. Niu, Y. Yi, S. Sun, W. Li, Z. Shuai, Understanding the efficiency drooping of the deep blue organometallic phosphors : a computational study of radiative and non-radiative decay rates for triplets †, J. Mater. Chem. C. 4 (2016) 6829–6838. https://doi.org/10.1039/C6TC00858E.

[37] H. Nikol, Rare earth phosphors: fundamentals and applications ¨, 277 (1998) 669–676.

[38] A. Manuscript, Materials Chemistry C, (2016). https://doi.org/10.1039/C6TC02258H.

[39] C.J. Summers, B. Wagner, H. Menkara, Solid State Lighting : Diode Phosphors, 5187 (2004) 123–132. https://doi.org/10.1117/12.514075.

[40] T. Review, Chem Soc Rev, (2014). https://doi.org/10.1039/c3cs60314h.

[41] K. Hentschel, Russell-Saunders Coupling., (2009).

[42] G.K. Woodgate, Elementary Atomic Structure., (1970).

[43] B. Barnett, R. Englman, Quantitative theory of luminescent centres in a configurational diagram model. II. Results and their interpretation, J. Lumin. 3 (1970) 55–73. https://doi.org/10.1016/0022-2313(70)90007-4.

[44] A.S. Coolidge, H.M. James, R.D. Present, A study of the franck-condon principle, J. Chem. Phys. 4 (1936) 193–211. https://doi.org/10.1063/1.1749818.

[45] S.D. Meetei, S. Dorendrajit, Effects of crystal size , structure and quenching on the photoluminescence emission intensity , lifetime and quantum yield of ZrO 2 : Eu 3 þ nanocrystals, J. Lumin. 147 (2014) 328–335. https://doi.org/10.1016/j.jlumin.2013.11.064.

[46] M.J. Weber, I11 relaxation phenomena in rare-earth luminescence, (1976).

[47] G. Blasse, Luminescence of rare earth ions at the end of the century, J. Alloys Compd. 192 (1993) 17–21. https://doi.org/10.1016/0925-8388(93)90172-J.

[48] M.A. Subramanian, G. Aravamudan, G.V.S. Rao, OXIDE REVIEW, 15 (1983).

[49] N. Nabihah, M. Yusof, A. Idris, H. Zainal, RSC Advances White light employing

luminescent engineered large (mega) Stokes shift molecules : a review, (2021) 13409–13445. https://doi.org/10.1039/d1ra00129a.

[50] Y. Gyu, J. Hyok, Local-field correction for intra-4 f -configurational transitions of rare earth ions embedded in amorphous chalcogenide solids, Chem. Phys. Lett. 467 (2009) 323–326. https://doi.org/10.1016/j.cplett.2008.11.016.

[51] R. Kolesov, K. Xia, R. Reuter, A. Zappe, J. Meijer, P.R. Hemmer, J. Wrachtrup, Optical detection of a single rare-earth ion in a crystal, (2012). https://doi.org/10.1038/ncomms2034.

[52] M. Hirayama, N. Sonoyama, A. Yamada, R. Kanno, Relationship between structural characteristics and photoluminescent properties of (La1-xEux)2M2O7 (M=Zr, Hf, Sn) pyrochlores, J. Lumin. 128 (2008) 1819–1825. https://doi.org/10.1016/j.jlumin.2008.05.005.

[53] M. Hatanaka, S. Yabushita, Mechanisms of f – f hypersensitive transition intensities of lanthanide trihalide molecules : a spin – orbit configuration interaction study, (2014) 219–220. https://doi.org/10.1007/s00214-014-1517-2.

[54] M. Marinovic, Synthesis and luminescent properties of rare earth (Sm 3 + and Eu 3 +) Doped Gd 2 Ti 2 O 7 pyrochlore nanopowders ˇ eljka Antic, 37 (2014) 598–606. https://doi.org/10.1016/j.optmat.2014.08.001.

[55] H. Li, R. Zhao, Y. Jia, W. Sun, J. Fu, L. Jiang, S. Zhang, R. Pang, C. Li, Photoluminescence Properties, (2014) 1–7.

[56] S. Kuck, Laser-related spectroscopy of ion-doped crystals for tunable solid-state lasers, Appl. Phys. B-Lasers Opt. 72 (2001) 515–562. https://doi.org/10.1103/PhysRevB.24.5.

[57] P.A.M. Berdowski, M.J.J. Lammers, G. Blasse, 5D3-5D4 cross-relaxation of Tb3+ in α-GdOF, Chem. Phys. Lett. 113 (1985) 387–390. https://doi.org/10.1016/0009-2614(85)80387-0.

[58] A. Herrmann, H.A. Othman, A.A. Assadi, M. Tiegel, C. Rüssel, Spectroscopic properties of cerium-doped aluminosilicate glasses, 5 (2015) 720–732. https://doi.org/10.1364/OME.5.000720.

[59] W. Li, X. Qian, J. Li, Phase transitions in 2D materials, Nat. Rev. Mater. 6 (2021) 829–846. https://doi.org/10.1038/s41578-021-00304-0.

[60] N.R. Glavin, R. Rao, V. Varshney, E. Bianco, A. Apte, A. Roy, E. Ringe, P.M. Ajayan, Emerging Applications of Elemental 2D Materials, Adv. Mater. 32 (2020) 1–22. https://doi.org/10.1002/adma.201904302.

[61] P.A. Tanner, Some misconceptions concerning the electronic spectra of tri-positive europium and cerium, Chem. Soc. Rev. 42 (2013) 5090–5101. https://doi.org/10.1039/c3cs60033e.

[62] G. Boulon, Fifty years of advances in solid-state laser materials, Opt. Mater. (Amst). 34 (2012) 499–512. https://doi.org/10.1016/j.optmat.2011.04.018.

[63] J. Yang, Y. Su, J. Li, Novel tube-like Y2Sn2O7:Tb3+ crystals: Hydrothermal synthesis and photoluminescence properties, Chem. Lett. 39 (2010) 182–183. https://doi.org/10.1246/cl.2010.182.

[64] J. Zeng, H. Wang, Y.C. Zhang, M.K. Zhu, H. Yan, Hydrothermal synthesis and photocatalytic properties of pyrochlore la 2Sn2O7 nanocubes, J. Phys. Chem. C. 111 (2007) 11879–11887. https://doi.org/10.1021/jp0684628.

[65] J. Wang, J. Wang, Y. Zhang, Y. Li, Y. Teng, Z. Wang, H. Tan, Flux synthesis and chemical stability of Nd and Ce co-doped (Gd1−xNdx)2(Zr1−xCex)2O7 ($0 \leq x \leq 1$) pyrochlore ceramics for nuclear waste forms, Ceram. Int. 43 (2017) 17064–17070. https://doi.org/10.1016/j.ceramint.2017.09.121.

[66] F. Matteucci, G. Cruciani, M. Dondi, G. Baldi, A. Barzanti, Crystal structural and optical properties of Cr-doped Y2Ti2O7 and Y2Sn2O7 pyrochlores, Acta Mater. 55 (2007)

2229–2238. https://doi.org/10.1016/j.actamat.2006.11.008.

[67] M.R. Díaz-Guillén, K.J. Moreno, J.A. Díaz-Guillén, A.F. Fuentes, K.L. Ngai, J. Garcia-Barriocanal, J. Santamaria, C. Leon, Cation size effects in oxygen ion dynamics of highly disordered pyrochlore-type ionic conductors, Phys. Rev. B - Condens. Matter Mater. Phys. 78 (2008) 1–7. https://doi.org/10.1103/PhysRevB.78.104304.

[68] T. Yanagida, G. Okada, Characterizations of optical properties and radiation induced luminescence of Bi-doped La2Zr2O7 transparent ceramics, J. Ceram. Soc. Japan. 124 (2016) 564–568. https://doi.org/10.2109/jcersj2.15237.

[69] D. Mohr, A.S.S. de Camargo, J.F. Schneider, T.B. Queiroz, H. Eckert, É.R. Botero, D. Garcia, J.A. Eiras, Solid state NMR as a new approach for the structural characterization of rare-earth doped lead lanthanum zirconate titanate laser ceramics, Solid State Sci. 10 (2008) 1401–1407. https://doi.org/10.1016/j.solidstatesciences.2008.01.001.

[70] J. Lian, L.M. Wang, S.X. Wang, J. Chen, L.A. Boatner, R.C. Ewing, Nanoscale Manipulation of Pyrochlore : New Nanocomposite Ionic Conductors, (2001) 3–6. https://doi.org/10.1103/PhysRevLett.87.145901.

[71] J. Lian, K.B. Helean, B.J. Kennedy, L.M. Wang, A. Navrotsky, R.C. Ewing, Effect of Structure and Thermodynamic Stability on the Response of Lanthanide Stannate Pyrochlores to Ion Beam Irradiation, (2006) 2343–2350.

[72] K.E. Sickafus, K.E. Sickafus, L. Minervini, R.W. Grimes, J.A. Valdez, Radiation Tolerance of Complex Oxides, 748 (2013). https://doi.org/10.1126/science.289.5480.748.

[73] C.G. Liu, J. Zhang, L.J. Chen, J. Wen, L.Y. Dong, D.Y. Yang, Y.H. Li, The structural parameters, structural stability and bulk modulus in RE 2 Sn 2 O 7 by first-principles calculations, 31 (2017) 1–14. https://doi.org/10.1142/S0217979217501843.

[74] M. Saif, Luminescence based on energy transfer in silica doped with lanthanide titania

(Gd2Ti2O7:Ln3+) [Ln3+ = Eu3+ or Dy3+], J. Photochem. Photobiol. A Chem. 205 (2009) 145–150. https://doi.org/10.1016/j.jphotochem.2009.04.020.

[75] T.S.G. Raja, K. Dheebikha, S. Balamurugan, N. Palanisami, A. Reshma, Enhanced Band Gap , Optical and Near-Infra-Red Reflecting Properties of Environmentally Benign, 20 (2020) 2277–2285. https://doi.org/10.1166/jnn.2020.17359.

[76] K. Hu, Z. Liu, J. Wang, T. Wang, J. Ouyang, Synthesis and photoluminescence properties of Eu 3 þ -doped Gd 2 Zr 2 O 7, Mater. Lett. 89 (2012) 276–278. https://doi.org/10.1016/j.matlet.2012.08.138.

[77] A.A. Saleh, H.Z. Hamamera, H.K. Khanfar, A.F. Qasrawi, G. Yumusak, Materials Science in Semiconductor Processing Gd and Tb doping e ff ects on the physical properties of Nd 2 Sn 2 O 7, 88 (2018) 256–261. https://doi.org/10.1016/j.mssp.2018.08.017.

[78] ȝ Z.Y., D. Linghong, P. Xinling, Z. Weifeng, Influence of annealing temperature on luminescent properties of Eu 3 + / V 5 + co-doped nanocrystalline Gd 2 Ti 2 O 7 powders, J. Rare Earths. 27 (2009) 900–904. https://doi.org/10.1016/S1002-0721(08)60359-2.

[79] M.L. Pang, J. Lin, J. Fu, Z.Y. Cheng, Luminescent properties of Gd 2 Ti 2 O 7 : Eu 3 þ phosphor films prepared by sol – gel process, 39 (2004) 1607–1614. https://doi.org/10.1016/j.materresbull.2004.05.016.

[80] K. Lin, C. Lin, C. Hsiao, Y. Li, Synthesis of Gd 2 Ti 2 O 7 : Eu 3 + , V 4 + phosphors by sol – gel process and its luminescent properties, 127 (2007) 561–567. https://doi.org/10.1016/j.jlumin.2007.03.010.

[81] Y. Zhang, C. Jia, Z. Su, W. Zhang, The enhanced and color-tunable photoluminescence of Eu 3 + / V 5 + co-doped Gd 2 Ti 2 O 7 nanocrystals, 479 (2009) 381–384. https://doi.org/10.1016/j.jallcom.2008.12.066.

[82] J. Xia, L. Lei, X. Dai, J. Ling, Y. Li, S. Xu, Excitation-dependent multi-color emissions in Yb / Er / Eu : Gd 2 Ti 2 O 7 pyrochlore for anti-counterfeiting, Mater. Res. Bull. 107 (2018) 213–217. https://doi.org/10.1016/j.materresbull.2018.07.027.

[83] A. Kumar, Structural and optical properties of highly thermally active - Gd 2 Zr 2 O 7 : Dy 3 + phosphors for lighting applications, J. Mater. Sci. Mater. Electron. 0 (2019) 0. https://doi.org/10.1007/s10854-018-0509-8.

[84] Y. Yang, Y. Shi, J. Duan, K. Lu, G. Cheng, Y. Zhao, Photoluminescence enhancement of Gd 2 Zr 2 O 7 : Eu 3 + red phosphor sensitized by co-doped Al 3 + ions, Ceram. Int. (2021) 1–7. https://doi.org/10.1016/j.ceramint.2021.01.171.

[85] L. Gao, H. Zhu, L. Wang, G. Ou, Hydrothermal synthesis and photoluminescence properties of Gd 2 Zr 2 O 7 : Tb 3 + phosphors, Mater. Lett. 65 (2011) 1360–1362. https://doi.org/10.1016/j.matlet.2011.02.004.

[86] W. Zhao, K. Zhang, W. Li, T. Deng, B. Luo, H. Zhang, Solid-state reactive sintering of La 2-x Gd x Zr 2 O 7 transparent ceramics and their optical properties, Ceram. Int. 45 (2019) 20078–20083. https://doi.org/10.1016/j.ceramint.2019.06.272.

[87] S.K. Gupta, C. Reghukumar, K. Sudarshan, P.S. Ghosh, N. Pathak, R.M. Kadam, Journal of Physics and Chemistry of Solids Orange-red emitting Gd 2 Zr 2 O 7 : Sm 3 þ : Structure-property correlation , optical properties and defect spectroscopy, J. Phys. Chem. Solids. 116 (2018) 360–366. https://doi.org/10.1016/j.jpcs.2018.01.031.

[88] V. Singh, V.K.R.H. Gao, N.S.J. Li, A.K. Srivastava, Visible upconversion luminescence of Yb co-doped Gd 2 Zr 2 O 7 : Er prepared by a solution combustion reaction, (2016) 310–315. https://doi.org/10.1007/s10854-015-3755-z.

[89] Z. Liu, K. Hu, Y. Jin, J. Ouyang, Y. Zhou, Preparation and photoluminescence properties of Er 3 þ -doped La 2 Zr 2 O 7 nanocrystals, J. Alloys Compd. 653 (2015) 122–125. https://doi.org/10.1016/j.jallcom.2015.08.266.

[90] Y.T.H. O, S.A. Annamma, J. Jijimon, K.T. Sam, S. Solomon, Structural and optical characterization of -, J. Mater. Sci. Mater. Electron. 0 (2017) 0. https://doi.org/10.1007/s10854-017-7797-2.

[91] X-ray diffraction and Raman spectroscopy on Gd2(Ti2−yTey)O7 prepared at high-heredia2010.pdf, (n.d.).

[92] G. Blasse, B.C. Grabmaier, Energy transfer, in: Lumin. Mater., Springer, 1994: pp. 91–107.

[93] J. Yang, Y. Su, H. Li, X. Liu, Z. Chen, Hydrothermal synthesis and photoluminescence of Ce3+ and Tb 3+ doped La2Sn2O7 nanocrystals, J. Alloys Compd. 509 (2011) 8008–8012. https://doi.org/10.1016/j.jallcom.2011.05.082.

[94] G.H. Dieke, R.A. Satten, Spectra and energy levels of rare earth ions in crystals, Am. J. Phys. 38 (1970) 399–400.

[95] Y. Zhang, D. Linghong, P. Xinling, W. Zhang, Influence of annealing temperature on luminescent properties of Eu3+/V5+ co-doped nanocrystalline Gd2Ti2O7 powders, J. Rare Earths. 27 (2009) 900–904.

[96] A. Garbout, M. Férid, Influence of Eu substitution for Gd on the structure and photoluminescent properties of (Gd1− xEux) 2Ti2O7 pyrochlore solid solutions, Adv. Powder Technol. 28 (2017) 1382–1390.

[97] M.L. Pang, J. Lin, J. Fu, Z.Y. Cheng, Luminescent properties of Gd2Ti2O7: Eu3+ phosphor films prepared by sol–gel process, Mater. Res. Bull. 39 (2004) 1607–1614.

[98] Applicability of Pick's Law to Gas Diffusion 1 D. B. JAYNES AND A. S. RooowsKi 2, (1983).

[99] G.A.S. Transport, I.N. Unsaturated, a): Vei, (1989).

[100] A. Panghal, P.K. Kulriya, Y. Kumar, F. Singh, Investigations of atomic disorder and grain growth kinetics, Appl. Phys. A. 125 (2019) 1–11. https://doi.org/10.1007/s00339-

019-2720-8.

[101] X.D. Techniques, X-Ray Diffraction Techniques, 9 (1986) 331–362.

[102] P. Taylor, A.A. Bunaciu, E. Gabriela, U.Ş. Tioiu, H.Y. Aboul-enein, Critical Reviews in Analytical Chemistry X - RAY DIFFRACTION : Instrumentation and Applications, (n.d.) 37–41. https://doi.org/10.1080/10408347.2014.949616.

[103] A.K. Vishwakarma, M. Jayasimhadri, Signi fi cant enhancement in photoluminescent properties via fl ux assisted Eu 3 þ doped BaNb 2 O 6 phosphor for white LEDs, J. Alloys Compd. 683 (2016) 379–386. https://doi.org/10.1016/j.jallcom.2016.05.052.

[104] A.K. Kunti, K.C. Sekhar, M. Pereira, M.J.M. Gomes, S.K. Sharma, Synthesis, Structural and Luminescence Studies of Pyrochlore Phase Free TiO2:Dy3+ Produced by Solid-state Reaction Method, Int. J. Appl. Ceram. Technol. 13 (2016) 1139–1148. https://doi.org/10.1111/ijac.12573.

[105] A. Garbout, I. Ben Taazayet-Belgacem, M. Férid, Structural, FT-IR, XRD and Raman scattering of new rare-earth-titanate pyrochlore-type oxides LnEuTi2O7 (Ln = Gd, Dy), J. Alloys Compd. 573 (2013) 43–52. https://doi.org/10.1016/j.jallcom.2013.03.279.

[106] S.P. Mulvaney, C.D. Keating, Raman Spectroscopy, 72 (2000) 145–158.

[107] A. Mohammed, A. Abdullah, SCANNING ELECTRON MICROSCOPY (SEM): A REVIEW, (2018) 77–85.

[108] B.J. Inkson, 2 - Scanning electron microscopy (SEM) and transmission electron microscopy (TEM) for materials characterization, Elsevier Ltd, 2016. https://doi.org/10.1016/B978-0-08-100040-3.00002-X.

[109] J.D. Andrade, (XPS), (1985) 105–106.

[110] M.P. Seah, The Quantitative Analysis gf Surfaces by XPS :, (1980).

[111] F. Swinehart, The Beer-Lambert, J. Chem. Educ. 39 (1962) 333–335.

[112] A.N. Belsky, J.C. Krupa, Luminescence excitation mechanisms of rare earth doped

phosphors in the VUV range, 19 (1999) 185–196.

[113] E. Procedure, silicon dioxide, 35 (1987) 2972–2979.

[114] G. Blasse, B.C. Grabmaier, A general introduction to luminescent materials, in: Lumin. Mater., Springer, 1994: pp. 1–9.

[115] A. Kumar, P.K. Kulriya, S.K. Sharma, V. Grover, A.K. Tyagi, V.K. Shukla, Structural and compositional effects on the electronic excitation induced phase transformations in Gd 2 Ti 2-y Zr y O 7 pyrochlore, J. Nucl. Mater. 539 (2020) 152278. https://doi.org/10.1016/j.jnucmat.2020.152278.

[116] J.E. Greedan, Frustrated rare earth magnetism: Spin glasses, spin liquids and spin ices in pyrochlore oxides, J. Alloys Compd. 408–412 (2006) 444–455. https://doi.org/10.1016/j.jallcom.2004.12.084.

[117] H. MATSUSHITA, S. NOMURA, S. ANDO, S. ENDO, T. IRIE, Study on the crystal structure of CdInGas, Jpn. J. Appl. Phys. 29 (1990).

[118] N. Cioatera, E.A. Voinea, E. Panaintescu, A. Rolle, S. Somacescu, C.I. Spinu, R.N. Vannier, Changes in structure and electrical conductivity of rare-earth titanate pyrochlores under highly reducing atmosphere, Ceram. Int. 42 (2016) 1492–1500. https://doi.org/10.1016/j.ceramint.2015.09.095.

[119] J.M. Farmer, L.A. Boatner, B.C. Chakoumakos, M.H. Du, M.J. Lance, C.J. Rawn, J.C. Bryan, Structural and crystal chemical properties of rare-earth titanate pyrochlores, J. Alloys Compd. 605 (2014) 63–70. https://doi.org/10.1016/j.jallcom.2014.03.153.

[120] K. Prashanthi, S. Culubrk, T. Thundat, Applied Surface Science Effect of annealing conditions on structural and luminescencent properties of Eu 3 + -doped Gd 2 Ti 2 O 7 thin films ˇ eljka Anti c, 364 (2016) 273–279. https://doi.org/10.1016/j.apsusc.2015.12.137.

[121] C.-C. Ting, Y.-C. Chien, W.-F. Sung, Erbium Doping Effects on the Structural and

Infrared Luminescence Properties of Gd 2 Ti 2 O 7 Nanocrystals , ECS J. Solid State Sci. Technol. 2 (2013) R105–R110. https://doi.org/10.1149/2.015306jss.

[122] Ć. Sanja, V. Lojpur, S.P. Ahrenkiel, J.M. Nedeljkovi, M.D. Drami, Non-contact thermometry with Dy 3 þ doped Gd 2 Ti 2 O 7 nano-powders, 170 (2016) 395–400. https://doi.org/10.1016/j.jlumin.2015.06.006.

[123] V. Lojpur, Ć. Sanja, M.D. Drami, Ratiometric luminescence thermometry with different combinations of emissions from Eu 3 þ doped Gd 2 Ti 2 O 7 nanoparticles, 169 (2016) 534–538. https://doi.org/10.1016/j.jlumin.2015.01.027.

[124] P.K. Kulriya, T. Yao, S.M. Scott, S. Nanda, J. Lian, In fl uence of grain growth on the structural properties of the nanocrystalline Gd 2 Ti 2 O 7, J. Nucl. Mater. 487 (2017) 373–379. https://doi.org/10.1016/j.jnucmat.2017.02.032.

[125] S.K. Gupta, P.S. Ghosh, C. Reghukumar, N. Pathak, R.M. Kadam, Experimental and theoretical approach to account for green luminescence from Gd2Zr2O7 pyrochlore: Exploring the site occupancy and origin of host-dopant energy transfer in Gd2Zr2O7:Eu3+, RSC Adv. 6 (2016) 44908–44920. https://doi.org/10.1039/c6ra05113h.

[126] G.M. Mustafa, S. Atiq, S.K. Abbas, S. Riaz, S. Naseem, Tunable structural and electrical impedance properties of pyrochlores based Nd doped lanthanum zirconate nanoparticles for capacitive applications, Ceram. Int. 44 (2018) 2170–2177. https://doi.org/10.1016/j.ceramint.2017.10.172.

[127] N.J. Hess, B.D. Begg, S.D. Conradson, D.E. McCready, P.L. Gassman, W.J. Weber, Spectroscopic investigations of the structural phase transition in Gd2(Ti1-yZry)2O7 pyrochlores, J. Phys. Chem. B. 106 (2002) 4663–4677. https://doi.org/10.1021/jp014285t.

[128] M. Glerup, O.F. Nielsen, F.W. Poulsen, The Structural Transformation from the

Pyrochlore Structure , A 2 B 2 O 7 , to the Fluorite Structure , A O 2 , Studied by Raman Spectroscopy and Defect Chemistry Modeling, 32 (2001) 25–32. https://doi.org/10.1006/jssc.2000.9142.

[129] A. Garbout, T. Turki, M. Férid, Structural and photoluminescence characteristics of Sm 3 + activated RE 2 Ti 2 O 7 (RE = Gd , La) as orange-red emitting phosphors, J. Lumin. 196 (2018) 326–336. https://doi.org/10.1016/j.jlumin.2017.12.066.

[130] G. Sattonnay, S. Moll, L. Thoḿ, C. Decorse, C. Legros, P. Simon, J. Jagielski, I. Jozwik, I. Monnet, Phase transformations induced by high electronic excitation in ion-irradiated Gd2(ZrxTi1-x)2O 7 pyrochlores, J. Appl. Phys. 108 (2010). https://doi.org/10.1063/1.3503452.

[131] H. Gupta, J. Singh, R.N. Dutt, S. Ojha, S. Kar, R. Kumar, V.R. Reddy, F. Singh, Defect-induced photoluminescence from gallium-doped zinc oxide thin films: Influence of doping and energetic ion irradiation, Phys. Chem. Chem. Phys. 21 (2019) 15019–15029. https://doi.org/10.1039/c9cp02148e.

[132] J. Jassi, V. Biju, A. Shajan, Structural and optical properties of zinc oxide nanoparticles, AIP Conf. Proc. 2263 (2020) 503–508. https://doi.org/10.1063/5.0017263.

[133] J. Ballato, E. Snitzer, concentrations for Faraday isolator applications, Appl. Opt. (1995) 1–7.

[134] B. Jacquier, Laser spectroscopy of rare earth-doped glass waveguides, J. Alloys Compd. 225 (1995) 15–19. https://doi.org/10.1016/0925-8388(94)07111-X.

[135] T. Welker, Recent developments on phosphors for fluorescent lamps and cathode-ray tubes, J. Lumin. 48–49 (1991) 49–56. https://doi.org/10.1016/0022-2313(91)90075-7.

[136] Z. Chen, X. Yang, L. Song, X. Wang, Q. Xiao, H. Xu, Q. Feng, S. Ding, Extraction and complexation of trivalent rare earth elements with tetraalkyl diglycolamides, Inorganica Chim. Acta. 513 (2020) 119928. https://doi.org/10.1016/j.ica.2020.119928.

[137] H. Jiao, Y. Wang, Ca[sub 2]Al[sub 2]SiO[sub 7]:Ce[sup 3+], Tb[sup 3+]: A White-Light Phosphor Suitable for White-Light-Emitting Diodes, J. Electrochem. Soc. 156 (2009) J117. https://doi.org/10.1149/1.3097191.

[138] M. Luo, B. Chen, X. Li, J. Zhang, S. Xu, X. Zhang, Y. Cao, J. Sun, Y. Zhang, X. Wang, Y. Zhang, D. Gao, L. Wang, Fluorescence decay route of optical transition calculation for trivalent rare earth ions and its application for Er3+-doped NaYF4phosphor, Phys. Chem. Chem. Phys. 22 (2020) 25177–25183. https://doi.org/10.1039/d0cp04379f.

[139] S.H. Park, K.H. Lee, S. Unithrattil, H.S. Yoon, H.G. Jang, W. Bin Im, Melilite-structure CaYAl3O7:Eu3+ phosphor: Structural and optical characteristics for near-UV LED-based white light, J. Phys. Chem. C. 116 (2012) 26850–26856. https://doi.org/10.1021/jp307192y.

[140] H.S. Jang, W. Bin Im, D.C. Lee, D.Y. Jeon, S.S. Kim, Enhancement of red spectral emission intensity of Y3Al5O12:Ce3+ phosphor via Pr co-doping and Tb substitution for the application to white LEDs, J. Lumin. 126 (2007) 371–377. https://doi.org/10.1016/j.jlumin.2006.08.093.

[141] L. Ighting, The promise and challenge of solid-state lighting T HE P ROMISE AND C HALLENGE OF S OLID -S TATE, 54 (2001). https://doi.org/10.1063/1.1445547.

[142] M.H. Crawford, LEDs for Solid-State Lighting : Performance Challenges and Recent Advances, 15 (2009) 1028–1040.

[143] X. Wang, Y. Wang, Synthesis , Structure , and Photoluminescence Properties of Ce 3 + - Doped Ca 2 YZr 2 Al 3 O 12 : A Novel Garnet Phosphor for White LEDs, (2015). https://doi.org/10.1021/acs.jpcc.5b01552.

[144] H. Kaur, M. Jayasimhadri, M.K. Sahu, P.K. Rao, N.S. Reddy, Synthesis of orange emitting Sm3+ doped sodium calcium silicate phosphor by sol-gel method for photonic device applications, Ceram. Int. (2020). https://doi.org/10.1016/j.ceramint.2020.04.224.

[145] A. Manuscript, adjust margins, (2015). https://doi.org/10.1039/C5DT02436F.

[146] N. Vijaya, K. Upendra Kumar, C.K. Jayasankar, Dy3+-doped zinc fluorophosphate glasses for white luminescence applications, Spectrochim. Acta - Part A Mol. Biomol. Spectrosc. 113 (2013) 145–153. https://doi.org/10.1016/j.saa.2013.04.036.

[147] J.A. Díaz-Guillén, A.F. Fuentes, M.R. Díaz-Guillén, J.M. Almanza, J. Santamaría, C. León, The effect of homovalent A-site substitutions on the ionic conductivity of pyrochlore-type Gd2Zr2O7, J. Power Sources. 186 (2009) 349–352. https://doi.org/10.1016/j.jpowsour.2008.09.106.

[148] S.F. Weng, H.C. Hsieh, C.S. Lee, Hydrogen production from oxidative steam reforming of ethanol on nickel-substituted pyrochlore phase catalysts, Int. J. Hydrogen Energy. 42 (2017) 2849–2860. https://doi.org/10.1016/j.ijhydene.2016.11.181.

[149] C. Meng, X. Ding, W. Li, J. Zhao, H. Yang, Phase structure evolution and chemical durability studies of Ce-doped zirconolite–pyrochlore synroc for radioactive waste storage, J. Mater. Sci. 51 (2016) 5207–5215. https://doi.org/10.1007/s10853-016-9822-x.

[150] U. Berwal, V. Singh, R. Sharma, Key role of Tb3+ doping on structural and photoluminescence properties of Gd2Ti2O7 pyrochlore oxide, Ceram. Int. (2022). https://doi.org/10.1016/j.ceramint.2022.04.231.

[151] P.H. Crystal, S. Fujihara, K. Tokumo, Cebc3Bdc56E9C3Cade247932C565B7Cc.Pdf, (2005) 5587–5593.

[152] J. Nair, P. Nair, G.B.M. Doesburg, J.G. Van Ommen, J.R.H. Ross, A.J. Burggraaf, F. Mizukami, Sintering of lanthanum zirconate, J. Am. Ceram. Soc. 82 (1999) 2066–2072. https://doi.org/10.1111/j.1151-2916.1999.tb02042.x.

[153] M. Zekri, A. Herrmann, R. Turki, C. Rüssel, R. Maâlej, K. Damak, Experimental and theoretical studies of Dy3+ doped alkaline earth aluminosilicate glasses, J. Lumin. 212

(2019) 354–360. https://doi.org/10.1016/j.jlumin.2019.04.041.

[154] C. Bouzidi, M. Ferhi, H. Elhouichet, M. Ferid, Structural and luminescence properties of (Ba1−xEux)MoO4 powders, J. Lumin. 179 (2016) 230–235. https://doi.org/10.1016/j.jlumin.2016.07.014.

[155] A. Moadhen, C. Bouzidi, H. Elhouichet, R. Chtourou, M. Oueslati, Concentration and temperature dependence of visible up-conversion luminescence in sol-gel SnO2 doped with erbium, Opt. Mater. (Amst). 31 (2009) 1224–1227. https://doi.org/10.1016/j.optmat.2009.01.002.

[156] G. Amira, B. Chaker, E. Habib, Spectroscopic properties of Dy3 + doped ZnO for white luminescence applications, Spectrochim. Acta - Part A Mol. Biomol. Spectrosc. 177 (2017) 164–169. https://doi.org/10.1016/j.saa.2017.01.039.

[157] P. Suthanthirakumar, K. Marimuthu, Investigations on spectroscopic properties of Dy3+ doped zinc telluro-fluoroborate glasses for laser and white LED applications, J. Mol. Struct. 1125 (2016) 443–452. https://doi.org/10.1016/j.molstruc.2016.06.080.

[158] A. Panghal, Y. Kumar, P.K. Kulriya, P.M. Shirage, N.L. Singh, Structural assessment and irradiation response of La2Zr2O7 pyrochlore_ Impact of irradiation temperature and ion fluence, J. Alloys Compd. 862 (2021) 158556. https://doi.org/10.1016/j.jallcom.2020.158556.

[159] S.K. Sharma, V. Grover, R. Shukla, A. Hussain, A. Mishra, R.C. Meena, P.K. Kulriya, Evidence of improved tolerance to electronic excitation in nanostructured Nd2Zr2O7, J. Appl. Phys. 129 (2021). https://doi.org/10.1063/5.0039390.

[160] T.T.A. Lummen, I.P. Handayani, M.C. Donker, D. Fausti, G. Dhalenne, P. Berthet, A. Revcolevschi, P.H.M. Van Loosdrecht, Phonon and crystal field excitations in geometrically frustrated rare earth titanates, Phys. Rev. B - Condens. Matter Mater. Phys. 77 (2008) 1–11. https://doi.org/10.1103/PhysRevB.77.214310.

[161] M. Gökçe, D. Koçyiğit, Spectroscopic investigations of Dy3+ doped borogermanate glasses for laser and wLED applications, Opt. Mater. (Amst). 89 (2019) 568–575. https://doi.org/10.1016/j.optmat.2019.02.004.

[162] R. Liu, M. Chen, X. Zhu, Y. Zhou, F. Zeng, Z. Su, Luminescent properties and structure of Dy3+ doped germanosilicate glass, J. Lumin. 226 (2020) 117378. https://doi.org/10.1016/j.jlumin.2020.117378.

[163] K. Linganna, C.S. Rao, C.K. Jayasankar, Optical properties and generation of white light in Dy3+-doped lead phosphate glasses, J. Quant. Spectrosc. Radiat. Transf. 118 (2013) 40–48. https://doi.org/10.1016/j.jqsrt.2012.12.002.

[164] S.M. Wang, Z.L. Xiu, M.K. Lü, A.Y. Zhang, Y.Y. Zhou, Z. Sen Yang, Combustion synthesis and luminescent properties of Dy3+-doped La2Sn2O7 nanocrystals, Mater. Sci. Eng. B Solid-State Mater. Adv. Technol. 143 (2007) 90–93. https://doi.org/10.1016/j.mseb.2007.07.070.

[165] Q. Su, Z. Pei, L. Chi, H. Zhang, Z. Zhang, F. Zou, The yellow-to-blue intensity ratio (Y/B) of Dy3+ emission, J. Alloys Compd. 192 (1993) 25–27. https://doi.org/10.1016/0925-8388(93)90174-L.

[166] Z. Ci, Q. Sun, S. Qin, M. Sun, X. Jiang, X. Zhang, Y. Wang, Warm white light generation from a single phase Dy3+ doped Mg2Al4Si5O18 phosphor for white UV-LEDs, Phys. Chem. Chem. Phys. 16 (2014) 11597–11602. https://doi.org/10.1039/c4cp00357h.

[167] G. Blasse, Energy transfer in oxidic phosphors, Philips Res. Reports. 24 (1969) 131.

[168] Q. Xu, J. Sun, D. Cui, Q. Di, J. Zeng, Synthesis and luminescence properties of novel Sr3Gd(PO4)3:Dy3+ phosphor, J. Lumin. 158 (2015) 301–305. https://doi.org/10.1016/j.jlumin.2014.10.034.

[169] L.G. Van Uitert, Characterization of Energy Transfer Interactions between Rare Earth

Ions, J. Electrochem. Soc. 114 (1967) 1048. https://doi.org/10.1149/1.2424184.

[170] D.L. Dexter, A theory of sensitized luminescence in solids, J. Chem. Phys. 21 (1953) 836–850. https://doi.org/10.1063/1.1699044.

[171] S. Dalmasso, B. Damilano, C. Pernot, A. Dussaigne, D. Byrne, N. Grandjean, M. Leroux, J. Massies, Injection dependence of the electroluminescence spectra of phosphor free GaN-based white light emitting diodes, Phys. Status Solidi Appl. Res. 192 (2002) 139–143. https://doi.org/10.1002/1521-396X(200207)192:1<139::AID-PSSA139>3.0.CO;2-G.

[172] J. Yum, S.-Y. Seo, S. Lee, Y.-E. Sung, Y[sub 3]Al[sub 5]O[sub 12]:Ce[sub 0.05] Phosphor Coatings on Gallium Nitride for White Light Emitting Diodes, J. Electrochem. Soc. 150 (2003) H47. https://doi.org/10.1149/1.1535207.

[173] S.K. Sharma, H.S. Mohanty, D.K. Pradhan, A. Kumar, V.K. Shukla, F. Singh, P.K. Kulriya, Structural, dielectric and electrical properties of pyrochlore-type Gd2Zr2O7 ceramic, J. Mater. Sci. Mater. Electron. 31 (2020) 21959–21970. https://doi.org/10.1007/s10854-020-04699-4.

[174] J.B. Goodenough, R.N. Castellano, Defect Pyrochlores as Catalyst Supports, 112 (1982) 108–112.

[175] Y. Ma, X. Wang, X. You, J. Liu, J. Tian, X. Xu, Nickel-Supported on La 2 Sn 2 O 7 and La 2 Zr 2 O 7 Pyrochlores for Methane Steam Reforming : Insight into the Difference between Tin and Zirconium in the B Site of the Compound, 330013 (2014) 3366–3376. https://doi.org/10.1002/cctc.201402551.

[176] Bi2−xCaxIr2O6+y Pyrochlore Phases Structure and Properties with varied ir ixidation state from 3+ to 4+.pdf, (n.d.).

[177] H. Zhang, K. Haule, D. Vanderbilt, Metal-Insulator Transition and Topological Properties of Pyrochlore Iridates, 026404 (2017) 1–6.

https://doi.org/10.1103/PhysRevLett.118.026404.

[178] R.C. Ewing, W.J. Weber, J. Lian, W.J. Weber, Nuclear waste disposal — pyrochlore (A2B2O7): Nuclear waste form for the immobilization of plutonium and " minor " actinides APPLIED PHYSICS REVIEWS — FOCUSED REVIEW Nuclear waste disposal — pyrochlore „ A 2 B 2 O 7 … : Nuclear waste form for the immobi, 5949 (2010). https://doi.org/10.1063/1.1707213.

[179] U. Berwal, V. Singh, R. Sharma, Structural and optical studies on Dy3+ doped Gd2Ti2O7 pyrochlore as white light emission, Ceram. Int. (2022). https://doi.org/10.1016/j.ceramint.2022.11.045.

[180] H.E. Liying, S.U. Yumin, J. Lanhong, S.H.I. Shikao, Recent advances of cerium oxide nanoparticles in synthesis , luminescence and biomedical studies : a review, J. Rare Earths. 33 (2015) 791–799. https://doi.org/10.1016/S1002-0721(14)60486-5.

[181] Cerium doped glasses containing reducing agent for enhanced luminescence, 222 (2020) 15–17. https://doi.org/10.1016/j.jlumin.2020.117175.

[182] S.K. Sharma, V. Grover, A.K. Tyagi, D.K. Avasthi, U.B. Singh, P.K. Kulriya, Probing the temperature effects in the radiation stability of Nd2Zr2O7 pyrochlore under swift ion irradiation, Materialia. 6 (2019) 100317.

[183] Probing the Short-Range Ordering of Ion Irradiated Gd2Ti2-yZryO7 (0.0≤ y≤ 2.0) Pyrochlore under Electronic Stopping Regime.pdf, (n.d.). https://doi.org/https://doi.org/10.1016/j.jnucmat.2022.153682.

[184] G. Greczynski, L. Hultman, X-ray photoelectron spectroscopy: towards reliable binding energy referencing, Prog. Mater. Sci. (2019) 100591. https://doi.org/10.1016/j.pmatsci.2019.100591.

[185] D. Raiser, J.P. Deville, Study of XPS photoemission of some gadolinium compounds, 57 (1991) 91–97.

[186] X. Photoelectron, O ,, peaks . These measurements have shown that the number of satellites is higher than found from previous to the main peak were deconvofuted with a gaussian (b) A moIecu ~ ar-orbital caIcuIation on metal octahe- draBy coordinated with oxygen developed, 61 (1979) 453–456.

[187] E. Bêche, P. Charvin, D. Perarnau, S. Abanades, G. Flamant, Ce 3d XPS investigation of cerium oxides and mixed cerium oxide (Ce xTiyOz), Surf. Interface Anal. 40 (2008) 264–267. https://doi.org/10.1002/sia.2686.

[188] H.A.A.S. Ahmed, W.D. Roos, O.M. Ntwaeaborwa, H.C. Swart, R.E. Kroon, Effect of annealing on the Ce 3 + / Ce 4 + ratio measured by XPS in luminescent SiO 2 : Ce, SAIP Proc. (2011) 4–8. events.saip.org.za/materialDisplay.py?contribId=132&sessionId.

[189] Z. Fang, L. Gao, H. Chen, K. Liang, Z. Liu, Z. Guan, J. Zhang, XPS study of probing evidence for displacive disorder in Ni-doped bismuth magnesium niobate pyrochlore, Mater. Sci. Eng. B Solid-State Mater. Adv. Technol. 259 (2020) 114601. https://doi.org/10.1016/j.mseb.2020.114601.

[190] Y.M. Sgibnev, N. V Nikonorov, A.I. Ignatiev, Luminescence of silver clusters in ion-exchanged cerium-doped photo-thermo-refractive glasses, J. Lumin. 176 (2016) 292–297. https://doi.org/10.1016/j.jlumin.2016.04.001.

[191] R. Yu, J. Wang, M. Zhang, J. Zhang, H. Yuan, Q. Su, A new blue-emitting phosphor of Ce 3 + -activated CaLaGa 3 S 6 O for white-light-emitting diodes, 453 (2008) 197–201. https://doi.org/10.1016/j.cplett.2008.01.039.

[192] A. Bahadur, Y. Dwivedi, S.B. Rai, Spectrochimica Acta Part A : Molecular and Biomolecular Spectroscopy Optical properties of cerium doped oxyfluoroborate glass, Spectrochim. Acta Part A Mol. Biomol. Spectrosc. 110 (2013) 400–403. https://doi.org/10.1016/j.saa.2013.03.066.

[193] C. Ce, SOLID IOIilCS conversion in ceria-doped zirconia single crystals induced by

oxido-reduction treatments, 72 (1994) 224–231.

[194] M. Leskela, Rare earths in electroluminescent and field emission display phosphors ¨, 277 (1998) 702–708.

[195] J.H. Oh, S.J. Yang, Y.R. Do, Healthy , natural , efficient and tunable lighting : four-package white LEDs for optimizing the circadian effect , color quality and vision performance, (2014). https://doi.org/10.1038/lsa.2014.22.

[196] J.Y. Choe, D. Ravichandran, S.M. Blomquist, D.C. Morton, K.W. Kirchner, M.H. Ervin, U. Lee, Alkoxy sol-gel derived Y 3x Al 5 O 12 : Tb x thin films as efficient cathodoluminescent phosphors Alkoxy sol-gel derived Y 3 À x Al 5 O 12 : Tb x thin films as efficient cathodoluminescent phosphors, 3800 (2013) 3–6. https://doi.org/10.1063/1.1378313.

[197] M.K. Sahu, H. Kaur, B. V Ratnam, J.S. Kumar, M. Jayasimhadri, Structural and spectroscopic characteristics of thermally stable Eu 3 + activated barium zinc orthophosphate phosphor for white LEDs, Ceram. Int. 46 (2020) 26410–26415. https://doi.org/10.1016/j.ceramint.2020.07.263.

[198] H. Kaur, M. Jayasimhadri, Color tunable photoluminescence properties in Eu3+ doped calcium bismuth vanadate phosphors for luminescent devices, Ceram. Int. (2019). https://doi.org/10.1016/j.ceramint.2019.05.034.

[199] G. Li, Y. Tian, Y. Zhao, J. Lin, Chem Soc Rev, Chem. Soc. Rev. (2015). https://doi.org/10.1039/C4CS00446A.

[200] L. Properties, T. Lamgal, Luminescence Properties and Energy-Transfer Behavior of a Novel and Color- Tunable LaMgAl 11 O 19 :Tm 3+ , Dy 3+ Phosphor for White Light-Emitting Diodes, 7 (2014) 1–7. https://doi.org/10.1111/jace.13346.

[201] X. Min, Z. Huang, M. Fang, Y. Liu, C. Tang, X. Wu, Energy Transfer from Sm 3 + to Eu 3 + in Red-Emitting Phosphor LaMgAl 11 O 19 : Sm 3 + , Eu 3 + for Solar Cells and

Near-Ultraviolet White Light-Emitting Diodes, (2014) 4–9.

[202] C. He, H. Ji, Z. Huang, T. Wang, X. Zhang, Phosphor for Blue Light Pumped White Light Emitting Diodes Red-shifted Emission in Y 3 MgSiAl 3 O 12 : Ce 3 + Garnet Phosphor for Blue Light Pumped White Light Emitting Diodes, (2018). https://doi.org/10.1021/acs.jpcc.8b03940.

[203] S. Xu, L. Sun, Y. Zhang, H. Ju, S. Zhao, D. Deng, H. Wang, B. Wang, Effect of fluxes on structure and luminescence properties of, J. Rare Earths. 27 (2009) 327–329. https://doi.org/10.1016/S1002-0721(08)60244-6.

[204] A. David, L.A. Whitehead, Comptes Rendus Physique Les sources de lumière blanche à base de LED, Comptes Rendus Phys. 19 (2018) 169–181. https://doi.org/10.1016/j.crhy.2018.02.004.

[205] N. Thejokalyani, S.J. Dhoble, Novel approaches for energy ef fi cient solid state lighting by RGB organic light emitting diodes – A review, Renew. Sustain. Energy Rev. 32 (2014) 448–467. https://doi.org/10.1016/j.rser.2014.01.013.

[206] R. June, C.A.W. Sleight, 1038 Spectral Properties of the Luminescence of CdNb206 and CaNb206 Maximum excitation band (nm) Maximum emission band (nm) Stokes shift Maximum additional excitation band (nm)* Maximum additional emission band (nm)* quenched at 300K ; in CaNb206 , 20 (1985) 1037–1045.

[207] S. Nakamura, Blue-Green Diodes and Violet Laser Diodes, (n.d.) 19–20.

[208] K. Li, C. Shen, Optik White LED based on nano-YAG : Ce 3 + / YAG : Ce 3 + , Gd 3 + hybrid phosphors, 123 (2012) 621–623. https://doi.org/10.1016/j.ijleo.2011.06.005.

[209] Q. Xu, J. Sun, D. Cui, Q. Di, J. Zeng, Synthesis and luminescence properties of novel Sr 3 Gd (PO 4) 3 : Dy 3 þ phosphor, J. Lumin. 158 (2015) 301–305. https://doi.org/10.1016/j.jlumin.2014.10.034.

[210] A. Zhang, M. Lü, G. Zhou, S. Wang, Y. Zhou, Combustion synthesis and

photoluminescence of Eu3+, Dy3+-doped La2Zr2O7 nanocrystals, J. Phys. Chem. Solids. 67 (2006) 2430–2434. https://doi.org/10.1016/j.jpcs.2006.05.004.

[211] M.G. Nikolic, M.S. Rabasovic, J. Krizan, S. Savic-Sevic, M.D. Rabasovic, B.P. Marinkovic, A. Vlasic, D. Sevic, Luminescence thermometry using Gd2Zr2O7:Eu3+, Opt. Quantum Electron. 50 (2018) 1–8. https://doi.org/10.1007/s11082-018-1529-6.

[212] G. Sattonnay, S. Moll, L. Thomé, C. Legros, M. Herbst-Ghysel, F. Garrido, J.M. Costantini, C. Trautmann, Heavy-ion irradiation of pyrochlore oxides: Comparison between low and high energy regimes, Nucl. Instruments Methods Phys. Res. Sect. B Beam Interact. with Mater. Atoms. 266 (2008) 3043–3047. https://doi.org/10.1016/j.nimb.2008.03.161.

[213] F.Y. Guo, W.H. Zhang, M. Ruan, J.B. Kang, J.Z. Chen, Czochralski growth of Gd2Ti2O7single crystals, J. Cryst. Growth. 402 (2014) 94–98. https://doi.org/10.1016/j.jcrysgro.2014.05.011.

[214] A.K. Vishwakarma, K. Jha, M. Jayasimhadri, A.S. Rao, K. Jang, B. Sivaiah, D. Haranath, Red light emitting BaNb2O6: Eu3+ phosphor for solid state lighting applications, J. Alloys Compd. (2014). https://doi.org/10.1016/j.jallcom.2014.10.016.

[215] A. Kumar, S. Babu, A.S. Karakoti, A. Schulte, S. Seal, Luminescence properties of europium-doped cerium oxide nanoparticles: Role of vacancy and oxidation states, Langmuir. 25 (2009) 10998–11007. https://doi.org/10.1021/la901298q.

[216] K. Chandra, V. Singh, S.K. Sharma, P.K. Kulriya, La3+ substitution effect on structural and magnetic properties of frustrated Ho2Ti2O7 pyrochlore, J. Alloys Compd. 937 (2023) 168311. https://doi.org/10.1016/j.jallcom.2022.168311.

[217] M.S. Rabasovic, D. Sevic, J. Krizan, M. Terzic, J. Mozina, B.P. Marinkovic, S. Savic-sevic, M. Mitric, Characterization and luminescent properties of Eu 3 + doped Gd 2 Zr 2 O 7 nanopowders, J. Alloys Compd. 622 (2015) 292–295.

https://doi.org/10.1016/j.jallcom.2014.10.072.

[218] X. Min, Y. Sun, L. Kong, M. Guan, M. Fang, X. Wu, Dyes and Pigments Novel pyrochlore-type La 2 Zr 2 O 7 : Eu 3 + red phosphors : Synthesis , structural , luminescence properties and theoretical calculation, Dye. Pigment. 157 (2018) 47–54. https://doi.org/10.1016/j.dyepig.2018.04.045.

[219] U. Berwal, V. Singh, R. Sharma, Effect of $Ce^{4+} \rightarrow Ce^{3+}$ conversion on the structural and luminescence properties, Journal of Luminescence, Volume 257, May 2023, 119687, https://doi.org/10.1016/j.jlumin.2023.119687.